

Time Resolved Fluorescence of CdSe Nanocrystals using Single Molecule Spectroscopy

by

Brent R. Fisher

B.A. Chemistry, Integrated Science
Northwestern University, 2000

Submitted to the Department of Chemistry
in Partial Fulfillment of the Requirements
for the Degree of

DOCTOR OF PHILOSOPHY

at the

MASSACHUSETTS INSTITUTE OF TECHNOLOGY

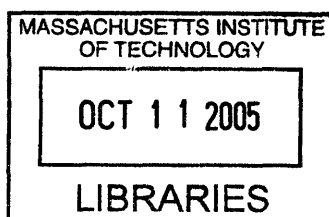
September 2005

© 2005 MASSACHUSETTS INSTITUTE OF TECHNOLOGY
All rights reserved

Signature of Author _____
Department of Chemistry
June 22, 2005

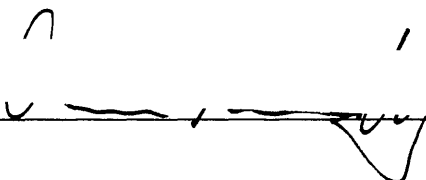
Certified by _____
Moungi G. Bawendi
Professor of Chemistry
Thesis Supervisor

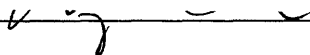
Accepted by _____
Robert W. Field
Chairman, Departmental Committee on Graduate Students

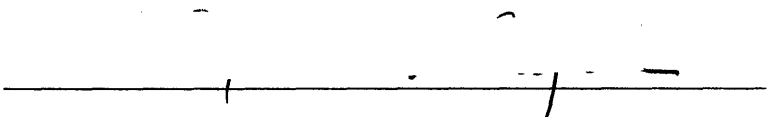


ARCHIVES

This doctoral thesis has been examined by a committee of the Department of Chemistry as follows:

Professor Andrei Tokmakoff  Chairman

Professor Mounji Bawendi  Thesis Advisor

Professor Sylvia Ceyer 

Time Resolved Fluorescence of CdSe Nanocrystals using Single Molecule Spectroscopy

by

Brent R. Fisher

A wide variety of spectroscopic studies of CdSe nanocrystals (NCs) are presented in this thesis, all studying some aspect of the temporal evolution of NC fluorescence under different conditions. In particular the methods of single molecule spectroscopy are used in many experiments allowing the behavior of individual NCs to be resolved from the blurring effect of averaging over the ensemble. Studies of the excited state lifetime of band edge fluorescence from single NCs reveal multiexponential relaxation dynamics that stem from fluctuations of non-radiative decay rates for the band edge exciton. Analysis of these fluctuations allows us to extract single exponential dynamics by sampling only “maximum-intensity” photons, and we find that this single exponential decay is remarkably uniform across a wide variety of NC samples and sizes. We also investigate luminescence from multiexciton (e.g. biexciton and triexciton) states of nanocrystals at both the ensemble and single NC level. Energy splittings, size and temperature dependencies, quantum yields and lifetimes of multiexciton states are measured and discussed. We show for the first time direct resolution of biexciton emission from single exciton emission using two different techniques, fluorescence line narrowing and single NC spectroscopy. We also study the non-classical light emission properties of single NCs and show how multiexciton emission leads to radiative quantum cascades of single photons in the emission of a single NC. Time resolved studies of fluorescence from NCs in solution environments conclude the thesis. The relationship between lifetime and quantum yield for non-homogenous ensembles like NCs is studied in chapter 8. We show that a sub-population of non-luminescent nanocrystals can reduce the quantum yield of an ensemble of NCs even though the measured lifetime stays constant. A study of NCs in solution fluorescence correlation spectroscopy (FCS) is presented last. We find that FCS is a capable tool for distinguishing small differences in hydrodynamic radius of NCs in solution. We also find that blinking of NCs may have a significant impact on these FCS measurements. An appendix to this thesis presents a general summary the lifetime of various samples CdSe and CdTe NCs.

Thesis Supervisor: Mounqi Bawendi

Title: Professor of Chemistry

For Rachel and my Mom and Dad

TABLE OF CONTENTS

Title Page	1
Signature Page	3
Abstract	5
Dedication	7
Table of Contents	9
Chapter 1: Optical Properties of CdSe Nanocrystals	13
1.1 Motivation and Background	13
1.2 Introduction to Colloidal Semiconductor Nanocrystals	16
1.3 Basic Electronic Structure of Nanocrystals	20
1.4 Refinements of Electronics Structure: Band Edge Fine Structure	27
1.5 Optical Spectroscopy of CdSe Nanocrystals	31
1.6 Overview of Thesis	34
1.7 References	35
Chapter 2: Methods of Fluorescence Microscopy	39
2.1 Introduction	39
2.2 Wide Field v. Confocal Microscopies	39
2.3 General Description of the Fluorescence Microscope	41
2.4 Wide Field Microscopy Techniques	43
2.5 Confocal Microscopy Techniques	48
2.6 Two-Photon Microscopy	55
2.7 Conclusions	57
2.8 References	57
Chapter 3: Single Nanocrystal Lifetimes	59
3.1 Introduction	59
3.2 Methods	63
3.3 Multiexponential and Fluctuating Lifetimes from Single Nanocrystals	65
3.4 Single Exponential Decays	69
3.5 Uniformity of Maximum-intensity PL Decay	73
3.6 Quantum Yield Fluctuations and Blinking in Single Nanocrystals	76
3.7 Size Dependence of Nanocrystal Lifetimes	80
3.8 Conclusions	82
3.9 References	82
Chapter 4: Multiexciton Emission from CdSe Nanocrystals	85
4.1 Introduction	85
4.2 Methods	86
4.3 Transient Spectra of CdSe Nanocrystals at Room Temperature	88
4.4 Assignment of Biexciton and Triexciton	90
4.5 Multiexciton Lifetimes	95
4.6 Quantum Yield of Multiexciton States	98
4.6 Multiexciton Emission from CdSe Nanocrystals at Low Temperature	99

4.7 Conclusions	107
4.8 Addendum: Poisson Statistics for Probability of Multiexciton Generation	108
4.9 References	109
Chapter 5: Multiexciton Emission from Single CdSe Nanocrystals	111
5.1 Introduction	111
5.2 Methods	112
5.3 Multiexciton Emission in Single Nanocrystal Emission Spectra	113
5.4 Multiexciton Emission in Single Nanocrystal Lifetime	114
5.5 Quantum Yield of Multiexciton Emission from Power Dependence	118
5.6 Blinking and Multiexciton Emission in Single Nanocrystals	120
5.7 Conclusion	122
5.8 References	123
Chapter 6: Non-classical Light Generation by Single Nanocrystals	125
6.1 Introduction	125
6.2 Methods	126
6.3 Antibunching and Single Photon Emission from Single CdSe Nanocrystals	128
6.4 Quantum Cascaded Emission from Multiexciton States	133
6.5 Modeling Single Photon Correlation Measurements	136
6.6 Ordered Emission of Photons via Radiative Quantum Cascades	138
6.7 Photon Pair Generation Using Nanorods	139
6.8 Conclusion	140
6.9 Addendum: Summary of Results for Various Single Nanocrystal Samples	141
6.10 References	142
Chapter 7: Resolution of Biexciton Emission from CdSe Nanocrystals	145
7.1 Introduction	145
7.2 Detection of Biexciton Emission: Signal Intensity	147
7.3 Detection of Biexciton Emission: Spectral Resolution	152
7.4 Methods	154
7.5 Biexciton Emission in single Nanocrystal Fluorescence	158
7.6 Biexciton Emission in FLN Spectra	163
7.7 Conclusions	168
7.8 References	169
Chapter 8: Lifetime and Quantum Yield of Nanocrystals	171
8.1 Introduction	171
8.2 General Relationship between Quantum Yield and Lifetime	172
8.3 Methods	175
8.4 Quenching Experiments	177
8.5 Discussion	181

8.6 Temperature Dependent Quantum Yield of TiO ₂ -Nanocrystal Composites Films	184
8.7 Conclusions	186
8.8 References	187
Chapter 9: Fluorescence Correlation Spectroscopy of CdSe Nanocrystals	189
9.1 Introduction	189
9.2 Theory of FCS	192
9.3 Methods: Software Autocorrelation	197
9.4 Methods: Optical Setup and Hardware	202
9.5 Preliminary FCS measurements	205
9.6 Measurement of R_H of CdSe Nanocrystals in Aqueous Solution	210
9.7 FCS of Nanocrystals in High Viscosity Aqueous Solutions	216
9.8 Conclusions	222
9.9 References	223
Appendix 1	225
A1.1 Introduction	225
A1.2 Size Dependence of CdSe Lifetimes	226
A1.3 Shape Dependence of CdSe lifetimes – Nanorods	227
A1.4 Lifetime of Type 2 Emission from CdTe/CdSe Nanocrystals	228
A1.5 Effect of Amines on CdSe NC Lifetime and Quantum Yield	230
A1.6 Effect of Overcoating on Nanocrystal Lifetimes	231
A1.7 Lifetime of Closed Packed Films of Bare CdSe Nanocrystals	233
A1.8 References	234
Appendix 2	235
A2.1 Introduction	235
A2.2 Verification of Hanbury-Brown and Twiss Setup by Imaging	236
A2.3 Verification of triexciton in single nanocrystal emission	238
A2.4 Triexciton blinking is correlated to band-edge emission blinking	239
A2.5 Use of a band-pass filter on channel 1 should result in 80% of its signal being from triexciton	244
A2.6 Expected relative count rates match observations for the two channels	246
A2.7 Lifetime data for a single nanocrystal shows 50% of channel 1 is triexciton emission	247
A2.8 Power dependence of triexciton and biexciton emission from a single nanocrystal	255
A2.9 Emission intensity of single nanocrystals in the “off” state	258
Appendix 3	263
A3.1 Introduction: FCS for fluctuations driven only by diffusion	263
A3.2 Relate $G(t)$ to the autocorrelation of a solution containing a single molecule	264
A3.3 Separate the contribution of blinking and diffusion	266

A3.4 Re-assemble the pieces	268
A3.5 References	270
Curriculum Vitae	271
List of Publications	273
Acknowledgement	274

Chapter 1: Optical Properties of CdSe Nanocrystals

- 1.1 Motivation and Background
- 1.2 Introduction to Colloidal Semiconductor Nanocrystals
- 1.3 Basic Electronic Structure of Nanocrystals
- 1.4 Refinements of Electronic Structure: Band Edge Fine Structure
- 1.5 Optical Spectroscopy of CdSe Nanocrystals
- 1.6 Overview of Thesis
- 1.7 References

1.1 Motivation and Background

The past decade has seen a great proliferation of nanomaterials and nanotechnology. An important driver of interest in these materials is the change in physical and chemical properties that occurs when the physical size of these materials is made very small. In many cases the change in properties is related to a greater surface to volume ratio (e.g. nanostructured heterogeneous catalysts). Semiconductor nanocrystals (NCs) on the other hand are interesting because the fundamental *optical and electronic properties* of the semiconductor are altered from their bulk behavior through a quantum mechanical effect, when the physical size of the NC is small enough¹. The origin of this change, so-called quantum confinement, occurs when the dimension of the crystal become so small that photoexcited carriers feel the boundaries. “Small” in this case is defined with reference to the characteristic size of a bound electron-hole pair, or exciton, in the semiconductor material. This value is called the Bohr radius of the exciton, a_B , and its value is 5.6nm for CdSe², the semiconductor of interest in this thesis.

The 1970s saw some of the first explicit studies of size dependent quantum effects in semiconductors when improved epitaxial growth techniques allowed the fabrication of thin films of semiconductor material sandwiched between insulating layers^{3,4}. Quantum

wells, as they are called, confine photoexcited carriers in the direction normal to the plane of the semiconductor thin film. The effect is to modify the density of states such that there are fewer band edge states and the oscillator strength of optical absorption is shifted to the blue. Figure 1.1 illustrates the transition from bulk to quantum well and ultimately to three-dimensionally confined nanoscale materials along with the associated change in basic electronic structure and density of states that accompanies the reduction of material size.

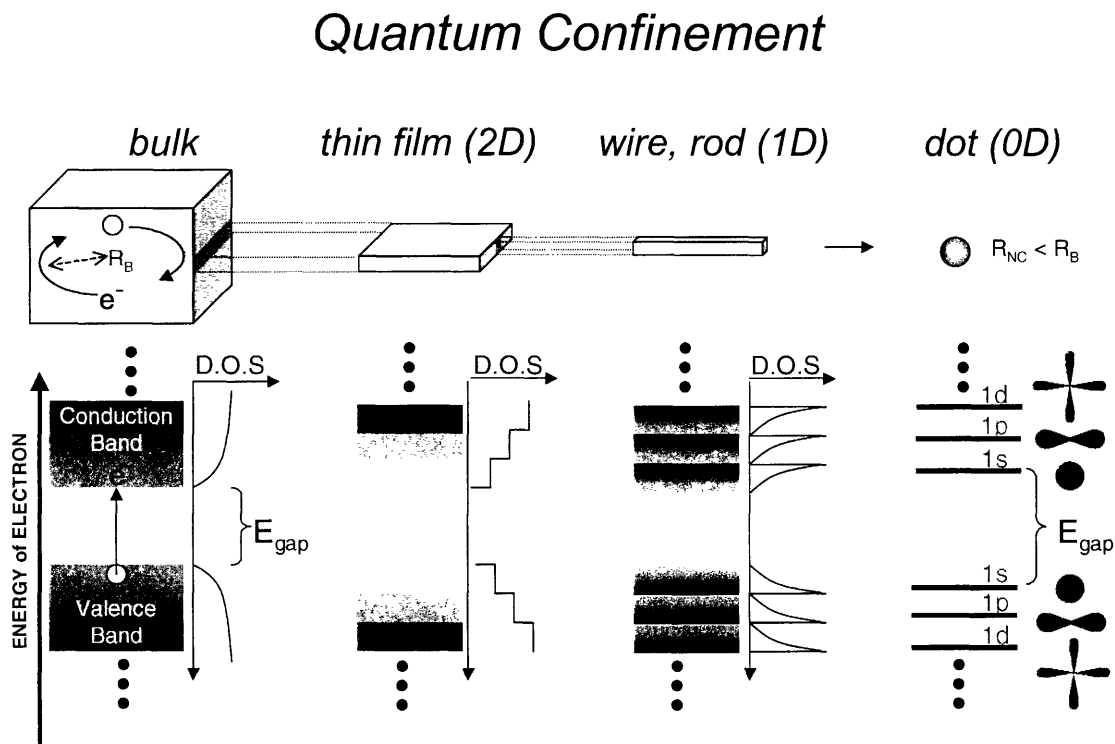


Figure 1.1 As the motion of photo-excited, delocalized carriers is restricted in each dimension, the effects of quantum confinement become more pronounced. On the left the unrestricted motion of carriers in bulk is associated with the usual band structure with a density of states proportional to $E^{1/2}$ for each band. In thin films (i.e. quantum wells), motion of the carriers is restricted to two dimensions leading to a constant density of states for each band. In quantum wires the carriers are confined in all but one dimension and the density of states begins to sharpen. NCs represent the ultimate limit of quantum confinement with carriers restricted in all three dimensions and atomic like states.

It was realized in the 1980s that the same quantum effect could explain the behavior of small crystallites embedded in glass matrices^{1,5}. Semiconductor-doped glasses were known to have a variety of colors despite the fact that they contained the same kind of semiconductor material. The different colors of various glasses were attributed to the size of the semiconductor crystallites embedded in the glass. Quantum confinement of carriers meant that the semiconductor crystallites would have different band edge absorption energies, which would color the glasses differently. Glasses containing very small semiconductor crystallites would appear blue because the confinement of carriers in the crystallites was greatest and the band gap energy was largest. Conversely, red colored glasses contained larger crystallites with weaker quantum confinement.

Advances in chemistry and preparation methods since the initial studies of semiconductor doped glasses allow us to now work with semiconductor NCs in a colloidal suspension. The narrower size distributions of colloidal samples and their availability in a solution form has enabled the development of many applications for these NCs ranging from biological labeling to solid state devices like lasers and LEDs⁶⁻¹⁰. The advent of higher quality samples has driven more incisive studies of the optical and electronic properties of these nanocrystals as well. The last 10-15 years of spectroscopy research on these materials in our group has provided sweeping advances in our understanding of carrier behavior in these quantum-confined nanostructures. Early optical studies determined the fundamental electronic structure of CdSe nanocrystals for sizes ranging from a few nm to 10s of nm^{1, 11-13}. Subsequent studies revealed perturbations on the basic electronic structure that lead to fine structure of atomic like

states at the band edge¹⁴⁻¹⁶. More recently studies of *single* nanocrystals using fluorescence microscopy techniques have revealed a new dimension of physical behavior and a deeper understanding of the optical properties of CdSe nanocrystals¹⁷.

The central questions of this thesis revolve around temporal dynamics of fluorescence from CdSe nanocrystals. Both ensemble and single nanocrystal microscopy techniques are used, but the common thread of the studies is the temporal evolution of fluorescence over a wide range of time scales (10^{-9} s to 10^2 s – 11 orders of magnitude!) to learn a great deal about the nanocrystals' physical behavior. Before explaining these experiments though, we begin with a review of CdSe nanocrystal spectroscopy and electronic structure.

1.2 Introduction to Colloidal Nanocrystals

Colloidal semiconductor nanocrystals are fundamentally just a little (very little!) chunk of semiconductor material suspended in a solid or liquid matrix or solution. The material of primary interest in this thesis is CdSe, and the nanocrystal sizes range from a few nm in diameter to over 10nm. The smallest nanocrystals contain only a few hundred atoms, while the largest contain tens of thousands of atoms. In order to stabilize and improve the optical behavior, CdSe nanocrystals are often epitaxially overcoated with a higher bandgap material like ZnS or CdS. Whether the nanocrystal is overcoated or not, all colloidal nanocrystals are surrounded by surface bound organic ligands. These ligands serve to passivate the surface of the nanocrystal and make it soluble in a given solvent. Typically long chain phosphines or phosphine oxides like trioctylphosphine (TOP) and trioctylphosphine oxide (TOPO) are used to “cap” the nanocrystal, although

long chain amines and ethers among others are often used as well. Figure 1.2 illustrates the composition, size and shapes of colloidal nanocrystals with both cartoons and actual transmission electron microscope (TEM) micrographs.

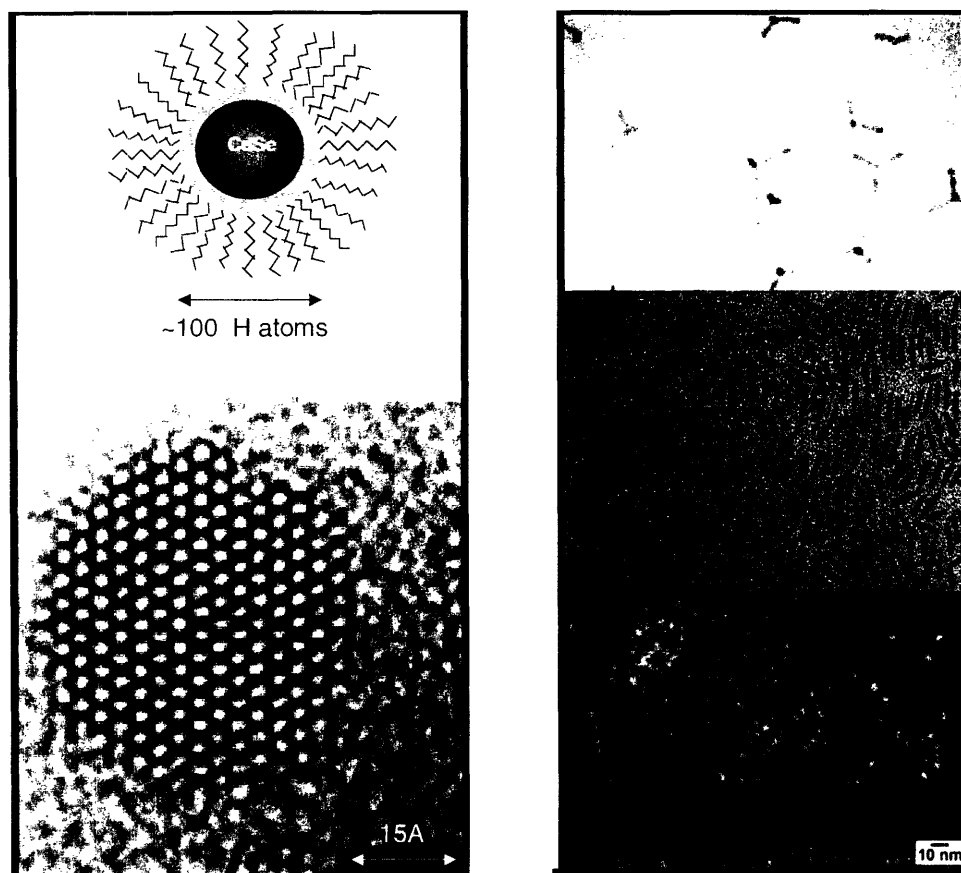


Figure 1.2 Cartoon and transmission Electron Micrographs (TEM) images of CdSe nanocrystals. The cartoon shows the CdSe core, ZnS overcoating shell and long-chain organic capping ligands. In the lower left a high resolution TEM image of CdSe shows the crystallinity of the samples with individual lattice planes clearly present¹⁸. On the right three low resolution TEM images show the various shapes accessible by wet chemical synthesis of nanocrystals: spheres, rods, and tetrapods¹⁹.

Many different sizes and shapes of nanocrystals can be synthesized using a variety of materials, as illustrated by the spherical¹⁸, rod-shaped²⁰, and tetrapod¹⁹ shaped nanocrystals shown in this figure. Our lab has developed synthetic methods for producing rod-shaped nanocrystals as well as nanocrystals of various materials including CdSe, InAs, Co, PbSe, CdS, InSb, and Fe₂O₃ among others. Spherical shaped CdSe

nanocrystals, usually with a 2 to 5 monolayer ZnS overcoating, are the primary focus of the optical studies in this thesis.

The general synthetic procedure for producing these CdSe nanocrystals is high temperature pyrolysis of precursor compounds in a high boiling solvent that can also act as a surface cap for the nanocrystal during its growth process. The first highly successful example of this synthetic method used organometallic precursors (dimethyl cadmium and trioctylphosphine selenide) that were injected into a solvent mixture of TOPO and TOP¹⁸.

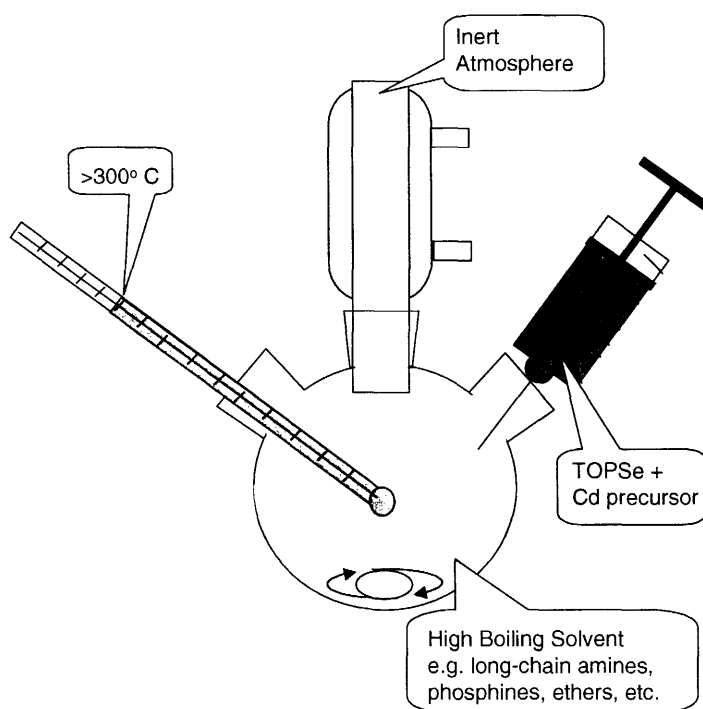


Figure 1.3 The basic procedure and components used for wet chemical synthesis of a batch of CdSe nanocrystals. A solvent with high boiling point is brought to high temperature under an inert atmosphere before injecting a solution of organometallics or inorganic salt precursors, which precipitate and grow into colloidal nanocrystals.

More recently developed procedures deliver improved results using less toxic, reactive precursors like cadmium hydroxide and different solvents like hexadecyl amine or dioctyl ether²¹. An illustration of basics of this synthetic procedure are given in figure 1.3.

Epitaxial overcoating of colloidal nanocrystals follows a very similar synthetic procedure, whereby inorganic precursors are slowly added, dropwise to nanocrystal cores that are brought to a high temperature in a high-boiling solvent^{22, 23}. Despite a small lattice mismatch for ZnS growth on CdSe, up to 5 or 6 monolayers can be grown on the CdSe nanocrystals which serves to passivate dangling bonds and surface traps on the CdSe surface that would otherwise ruin its optical properties.

The ability to synthesize and manipulate colloidal NCs using wet chemical techniques distinguishes them from their cousins, epitaxial quantum dots (QDs) fabricated by Stranski-Krastanow growth. Quantum dots are made using high vacuum, ultra clean deposition techniques whereby a sub-monolayer thick film of the desired material is grown on a substrate with a significant lattice mismatch^{24, 25}. The lattice mismatch strongly affects the wetting properties of the deposited material causing its constituent atoms to “puddle” together like water on a newly waxed car. These oblate shaped nanometer sized crystals are usually only a few nanometers thick, but may be up to 100nm in diameter, and their size distribution cannot be controlled as well as colloidal nanocrystals. Also because they are significantly larger than colloidal nanocrystals, their quantum confinement effects are usually less pronounced. One advantage of quantum dots over nanocrystals, however, is that their surfaces are usually far better passivated than colloidal nanocrystals leading to superior optical properties on a single nanocrystal basis. The elimination of trap states with good surface passivation in quantum dots stems

from their ultra clean growth conditions. Nanocrystals by comparison are synthesized in very “dirty” wet chemical conditions with numerous contaminating species present. The foregoing differences are important to keep in mind when comparing experimental results of colloidal nanocrystals against quantum dots.

1.3 Basic Electronic Structure of Nanocrystals

One of the most fascinating results of quantum confinement on nanocrystals is its effect on the optical absorption and fluorescence properties, i.e. the color, of CdSe nanocrystals. Figure 1.4 shows the wide range of band-edge absorption and fluorescence wavelengths that can be realized simply by changing the size of the CdSe nanocrystals.

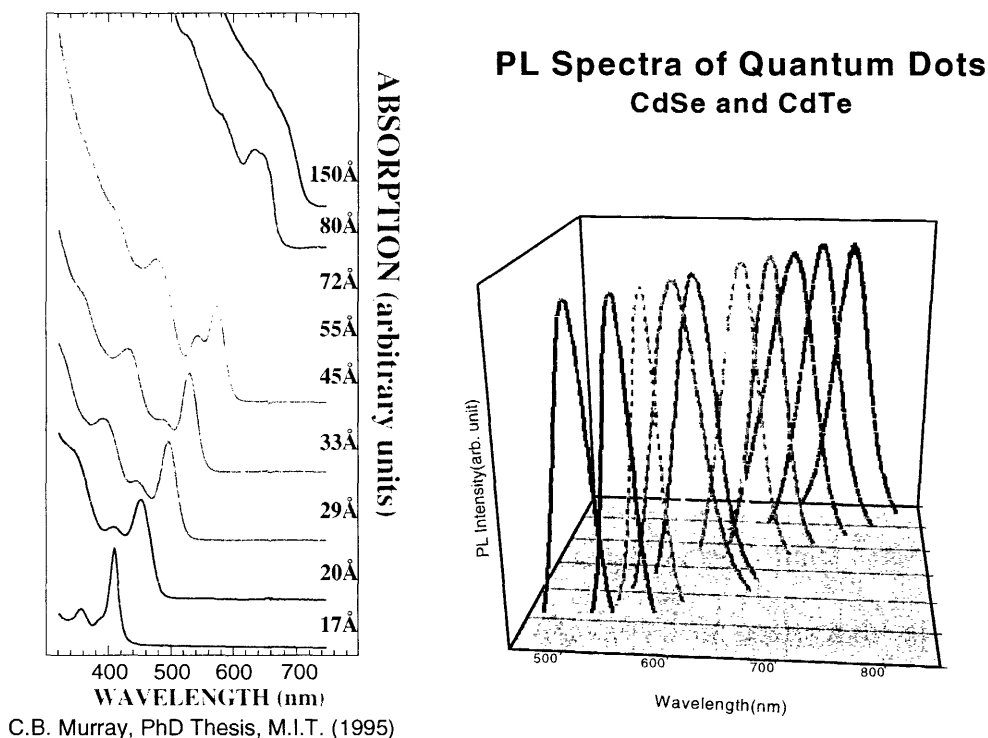


Figure 1.4 Left: optical absorption spectra of nanocrystals of various sizes. **Right:** band-edge photoluminescence spectra for a size series of CdSe nanocrystals¹⁸

Figure 1.1 gave a fundamental summary of how quantum confinement ultimately leads to the tunable absorption and fluorescence spectra shown in figure 1.4. The basis for these size dependent changes in band gap energy is the simple particle in a sphere model^{1, 5, 26}, which gives the wave functions and energy levels of an empty sphere of radius, a , with walls of infinite potential. Solutions of the Schrödinger equation for this problem are given by Flügge²⁷. The wavefunction of a particle in a sphere with infinite potential walls is proportional to the product of an l^{th} order spherical Bessel function in the radial direction and a spherical harmonic in the angular directions:

$$\Phi(r, \theta, \phi) = C \frac{j_l(k_{n,l}r)Y_l^m(\theta, \phi)}{r} \quad (1.1)$$

where C is a normalization constant and $k_{n,l} = \alpha_{n,l}/a$ with $\alpha_{n,l}$ the n^{th} root of the Bessel function. The quantized energy states of a particle in an infinite spherical potential are given by,

$$E_{n,l} = \frac{\hbar^2 k_{n,l}^2}{2m} = \frac{\hbar^2 \alpha_{n,l}^2}{2ma^2} \quad (1.2)$$

which are formally the same as the kinetic energy of a free particle except with the wavevector, $k_{n,l}$, quantized by the boundary conditions. Note that the energy is inversely proportional to the square of the radius of the sphere (a), analogous to the well known L^{-2} energy dependence for a particle in a one-dimensional infinite well of width L .

Equations 1.1 and 1.2 are clean results for a particle in a sphere, but a nanocrystal is not an empty sphere – it is filled with a lattice of atoms. We want to marry the solutions for a particle in a sphere to the solutions for a delocalized carrier (i.e. electron) a bulk crystal lattice. The Hamiltonian for an electron in an atomic lattice is just the

particle's kinetic energy operator, $-\hbar^2\nabla^2/2m$, added to a periodic potential, $U(r+R)=U(r)$, where R is the lattice spacing of the crystal. $U(r)$ represents a lattice of ions including the nuclei plus the core(not valence) electrons, which are considered localized. The solution to the Schrödinger wave equation for this general Hamiltonian gives the wave functions for delocalized valence electrons in the crystal lattice and is one of the fundamental results of solid state physics, Bloch's theorem:

$$\Psi_{nk}(\vec{r}) = u_{nk}(\vec{r}) \exp(i\vec{k} \cdot \vec{r}) \quad (1.3)$$

This result states that the wavefunction, Ψ , of an electron in a periodic potential can be expressed as a plane wave envelope times a periodic function, $u_{nk}(r)$, the so-called Bloch function. Simple proofs of this theorem are available in most solid state texts²⁸. In the tight binding approximation²⁸, the functions $u_{nk}(r)$ are generated from linear superpositions of the atomic orbitals containing the valence electrons.

$$u_n(\vec{r}) = \sum_i C_{n,i} \varphi(r - r_i) \quad (1.4)$$

The summation is over all lattice points, i . By their definition the Bloch functions automatically have the periodicity of the ionic lattice. Note that equation 1.4 makes an approximation from the rigorous definition of Bloch functions by neglecting the k -dependence of $u_n(r)$. The vector of coefficients, $C_{n,i}$ defines a particular wavefunction for a state that is generated from atomic orbitals designated 'n'. If the energies of the states $\Psi_{n,k}$ are plotted against k , then states with common n group together to form a band as shown in figure 1.5. This plot, called the band structure, shows the energy dispersion (k -dependence) of electron states. Each band contains many states that exist only at discrete values of k , separated by dk , where $dk = 2\pi/L$ (L = length of the entire crystal).

Each state is two-fold spin degenerate. The band structure of many band structures can be extremely complicated, but we can simplify matters greatly by restricting our focus to the point in k -space with the smallest energy difference between bands that are filled with electrons (valence band) and bands that are not (conduction band).

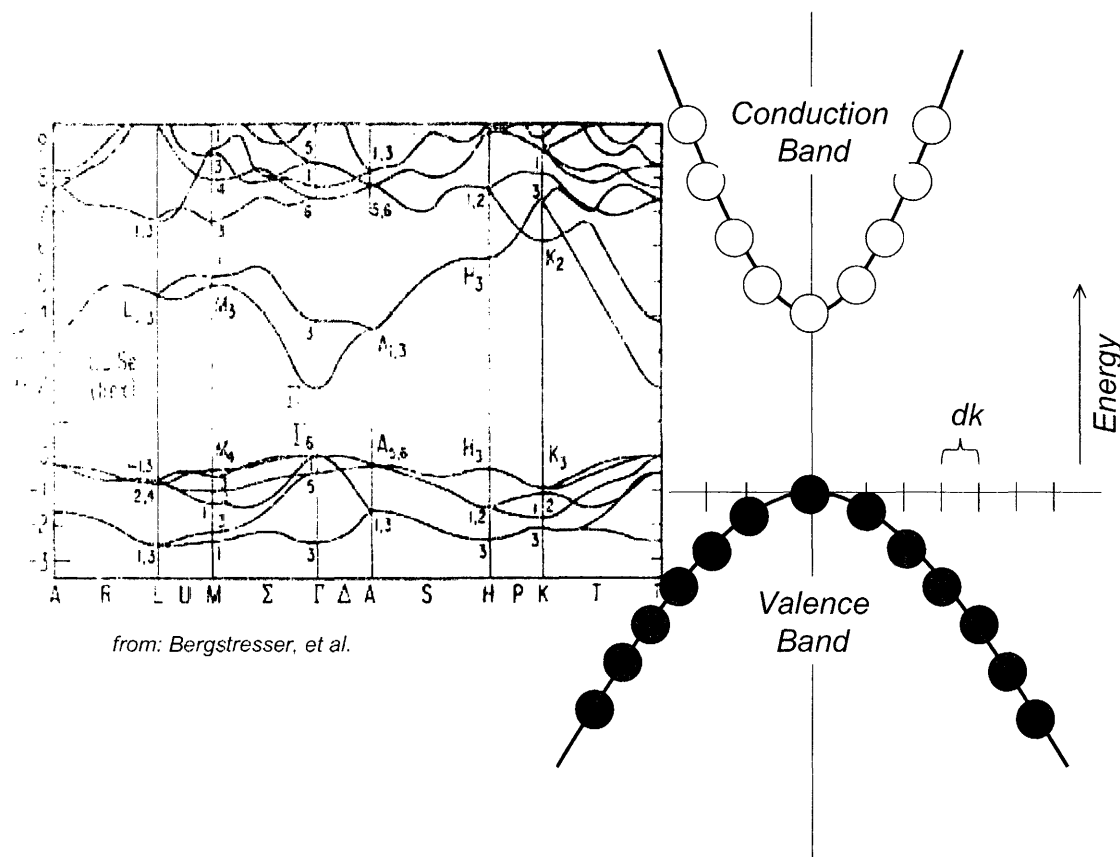


Figure 1.5 Left: band structure for bulk CdSe with a wurtzite crystal structure, calculated using the empirical pseudopotential method²⁹. **Right:** simplified representation of the conduction and valence bands at the band edge (Γ for CdSe, $k=0$). The filled circles represent states occupied by electrons and open circles represent unoccupied electron states.

For many semiconductors, including CdSe, this is at $k=0$, the so-called Γ -point. Near this point we can make the *effective mass approximation* for $E_n(k)$ – we assume that the bands' energy dispersion approximates a parabola. The energies of the conduction and valence bands are then approximated as,

$$E_c(k) = \frac{\hbar^2 k^2}{2m_{eff}^c} + E_g, \quad E_v(k) = -\frac{\hbar^2 k^2}{2m_{eff}^v} \quad (1.5)$$

The degree of curvature in the parabolic approximation of the band structure is represented by the effective mass, m_{eff} , which is defined as is the opposite of the second derivative of $E(k)$: $m_{eff} = -\hbar^2 \left(\frac{d^2}{dk^2} E(k) \right)^{-1}$. Higher effective masses correspond to more gradually changing, wide bands with high density of states (e.g. valence band), while lower effective masses correspond to highly concave bands with lower density of states (e.g. conduction band).

To a first approximation, the wavefunctions and energies of carrier states in nanocrystals are obtained by imposing the boundary conditions of the nanocrystal and hence the particle in a sphere solutions onto the bulk wavefunctions. In general when boundaries are imposed on a bulk crystal, a super position of Bloch functions is used to define the new functions. The Bloch functions can be excluded from the sum because of weak k dependence,

$$\Psi_n(\vec{r}) = u_{n0}(\vec{r}) \sum_k \exp(ik \cdot r) = u_{n0}(\vec{r}) f(r) \quad (1.6)$$

$f(r)$ is an envelope function for a single particle defining the extent of delocalization of the wave function given the boundary conditions. Of course we have already calculated the envelope functions, which fit the boundary conditions of the spherical nanocrystal – they are the solutions of particle in a sphere. Substitution of the particle in a sphere wavefunctions for $f(r)$ is valid when the radius of the nanocrystal, a , is much greater than the lattice constant, and is known as the *envelope function approximation*³⁰.

Optical spectroscopy uses the behavior of photoexcited electron-hole pairs (excitons) to study the electronic structure of the nanocrystals. Since we have calculated

the wave functions for individual carriers in a nanocrystal, we can now construct the wavefunction of the total exciton. To first order we assume no interaction between the electron and hole, so the exciton Hamiltonian is just the sum of the Hamiltonians of the individual carriers, and the wave equation is completely separable. Therefore the wave function of the exciton is just the product of the wave functions for the electron and the hole,

$$\Psi_{ch}(\vec{r}_e, \vec{r}_h) = \Psi_e(\vec{r}_e)\Psi_h(\vec{r}_h) = u_e f_e(\vec{r}_e)u_v f_h(\vec{r}_h) \quad (1.7)$$

The energy levels of the exciton are simply the sum of the energies for each confined carrier,

$$E_{chp}(k) = E_g + \frac{\hbar^2 \alpha_{n_e, l_e}^2}{2m_{eff}^e a^2} + \frac{\hbar^2 \alpha_{n_h, l_h}^2}{2m_{eff}^h a^2} \quad (1.8)$$

Note that the second two terms on the right hand side of equation 1.8 account for the change in the bandgap with nanocrystal radius, a .

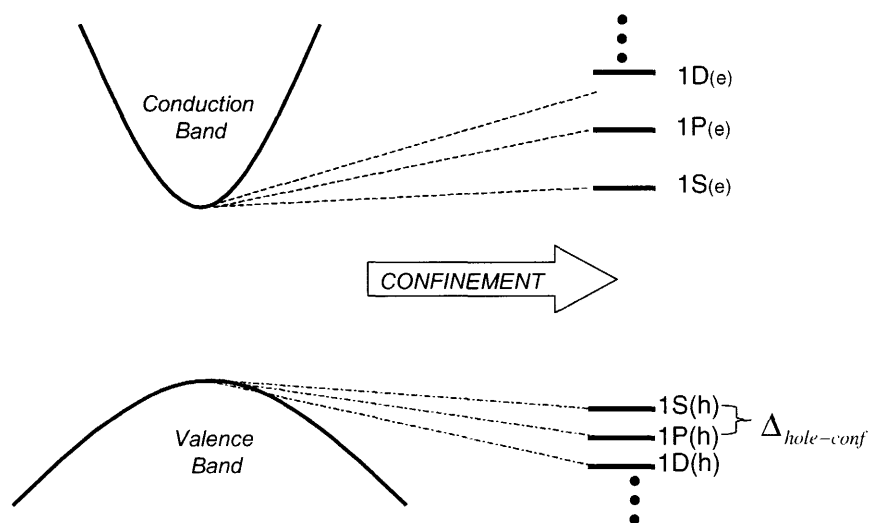


Figure 1.6 Illustration of the effect of confinement on electronic states at the conduction and valence band edge. The labels of the quantum confined states are taken from the states of a particle in a sphere, characterized by quantum numbers n (1, 2, 3 ...) and l (S, P, D, F ...). Photoexcited electrons occupy quantum-confined states of the conduction band while the photoexcited holes occupy states of the valence band. This is the reason for the labels 'e' and 'h' on the quantum confined states.

Transition probabilities and oscillator strengths depend on the dipole matrix element that optically couples the exciton wave function with the ground state (no exciton), $|0\rangle$. This operator, $\hat{e} \cdot \hat{p}$, can be approximated to act only on the Bloch functions, $u(r)$, so the transition probabilities are proportional to the bra-ket of the envelope functions which are orthonormal solutions of the particle in the sphere. Simple selection rules for the envelope functions are the result ($\Delta n=0$, and $\Delta L=0$)³⁰.

1.4 Refinements of Electronic Structure: Band Edge Fine Structure

Significant refinements can and have been made to the wavefunctions and energies for excitons given by equations 1.7 and 1.8. The results of these refinements lead to some of the most interesting optical properties of the nanocrystals, beyond their size dependent band gap. The most important refinements can be summarized as follows:

- Spin Orbit Coupling
- Crystal Field Splitting
- Valence band mixing
- Prolate shape of the nanocrystal
- Exchange coupling between photoexcited electron and hole
- Band-Band Mixing, Non-parabolicity of bands, Crystal Inversion Symmetry

Spin Orbit Coupling Using the zeroth order picture described in section 1.3 the valence band of CdSe would be six-fold degenerate because its Bloch functions are composed primarily of 4p atomic orbitals from selenium (three-fold degenerate), each of which is two-fold spin degenerate. When spin-orbit coupling is taken into account the energy of an electron depends on the total angular momentum, J , where $J = l + s$. States with $J=1/2$ have higher energy. The result is a so-called split-off band in the valence band corresponding to Bloch functions with $J=1/2$, that is separated by about 420meV from the valence band-edge²

Crystal Field Splitting The actual crystal structure of CdSe nanocrystals is uniaxial wurtzite. The orientation of atomic orbitals relative to this preferred axis affects the energy of the bands associated with these orbitals. The result is that the energy of the

$J=3/2$ valence bands are split based on their z-projection of J (M_J): $M_J = \pm 1/2$ is higher energy than $M_J = \pm 3/2$.

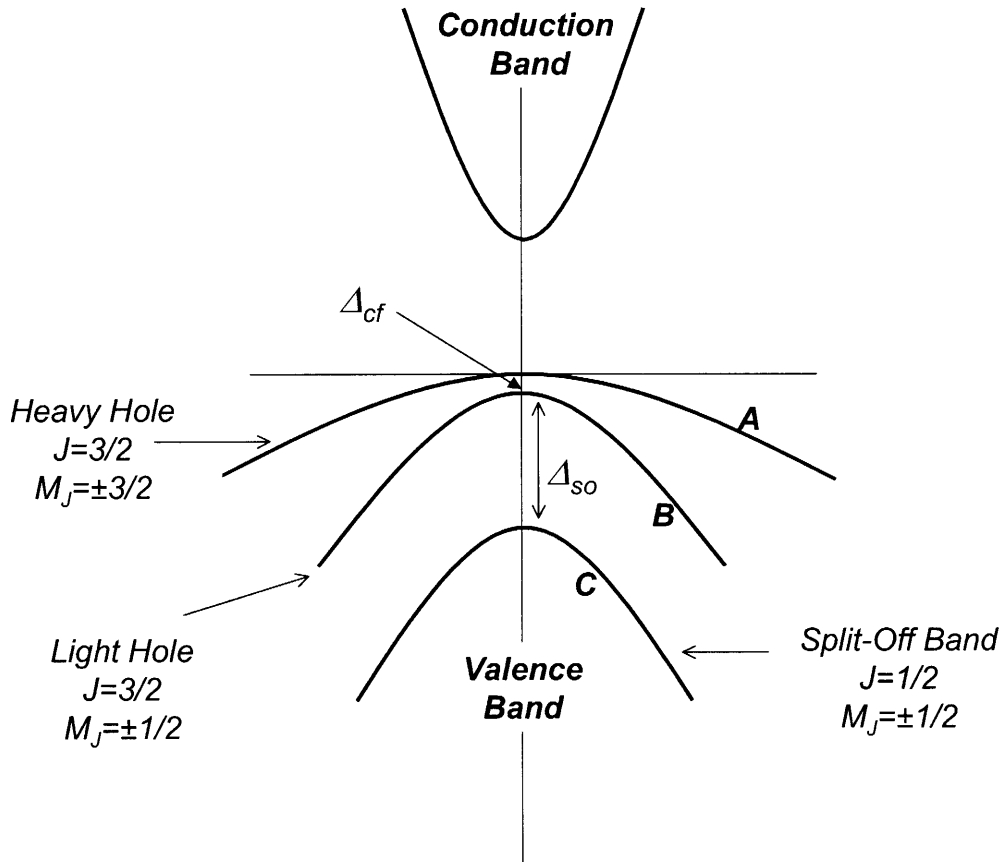


Figure 1.7 Refinement of the bulk band structure of CdSe at the band-edge when spin-orbit coupling and crystal field splitting are accounted for. The spin orbit coupling splits the three valence bands based on the quantum number J for the Bloch functions. The effect of the crystal field anisotropy in wurtzite CdSe splits the bands based on their quantum number M_J , the z-projection of J .

The refined band structure, after both spin-orbit coupling and crystal field splitting are accounted for, is shown in figure 1.7.

Valence Band Mixing If quantum confinement is applied to the band structure of figure 1.7, each of the three subbands, A , B , and C will generate a ladder of hole states, where the hole Bloch function angular momentum of the state is dictated by the subband from which it originated. These ladders of states are not independent of one another. Instead they are coupled together by valence band mixing – the quantum number of

Bloch function angular momentum, J , is not conserved and instead, the good quantum number is F , the sum of J (the total Bloch function angular momentum) and L (from the envelope wavefunction).

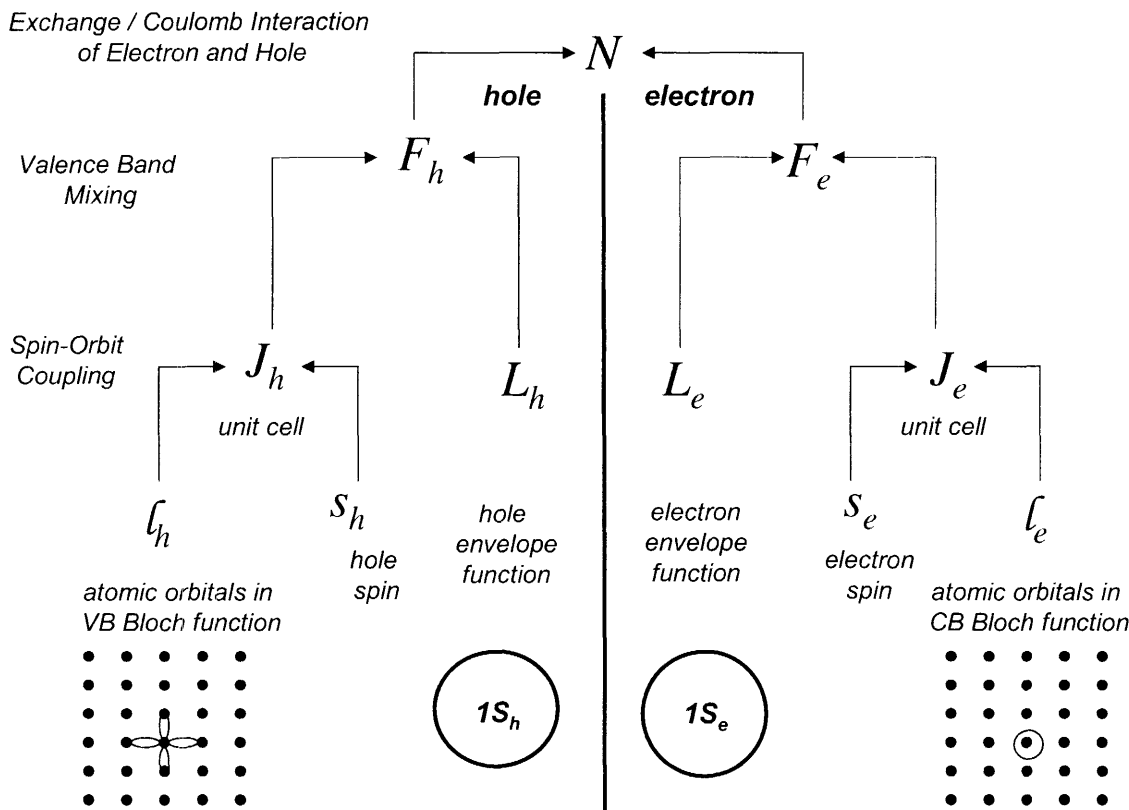


Figure 1.8 Graphical illustration of the meaning of various quantum numbers used to describe carrier states and excitonic states of nanocrystals. This figure adapted from a previous work³⁰.

This coupling explains avoided crossings observed in the size-dependence of energies in these ladders of hole states¹³. A diagram that shows the relationship of the various angular momentum quantum numbers to one another is shown in figure 1.8, which was adapted from a previous work³⁰.

Prolate Shape Although we have modeled the envelope wave functions using the solutions for a particle in a sphere, the reality is of course different. Nanocrystals are usually slightly prolate with an aspect ratio of about 1.1¹⁸. The long axis of the prolate shape generally is parallel to the z-axis of the uniaxial crystal. The effect of the shape

anisotropy has been calculated and causes the excitonic levels to split based on the projection, N , of F on the z-axis³¹.

Exchange coupling Exchange coupling between two particles is highly dependent on the overlap of their wavefunctions (i.e. their separation distance)³². Because a nanocrystal confines electron-hole pairs to a small volume, the exchange coupling energy can split the excitonic levels. This was calculated for CdSe nanocrystals³³⁻³⁵.

When all of these refinements are included in the electronic structure of CdSe nanocrystals the band-edge transition between 1S electron and 1S hole states is split into a five-level fine structure. The energy levels are dependent on the z projection of the total exciton angular momentum, N , which is the sum of the individual electron and hole total angular momenta as shown in figure 1.8. Band edge fine structure states with 1 unit of angular momentum are optically active producing circularly polarized radiative emission, whereas the lowest state of the band edge is optically inactive because its total angular momentum is ± 2 .

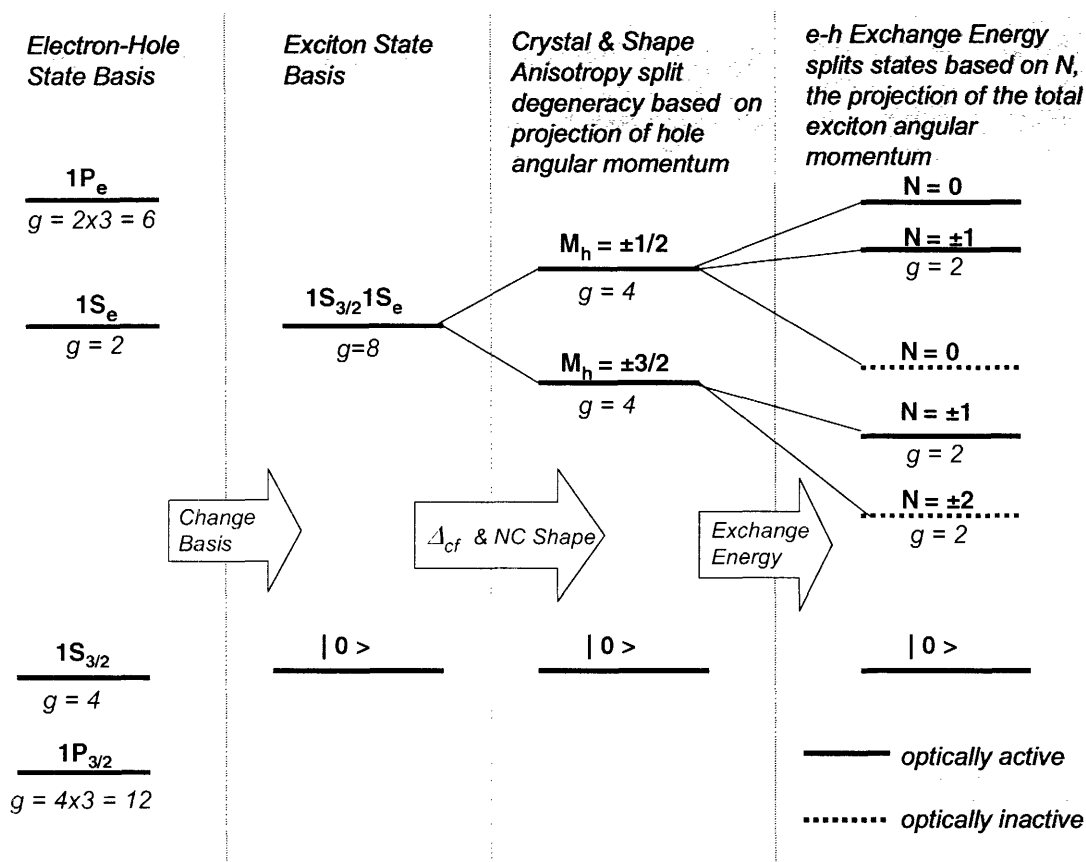


Figure 1.9 The origin of the manifold of fine structure states at the band-edge of CdSe nanocrystals. On the far left the ladder of quantum-confined states of an electron are shown. Changing basis to excitonic states gives a two level system for a single exciton, but the first exciton state is eight-fold degenerate ($g=8$) since it consisted of the four-fold degenerate $1S_{3/2}$ and two-fold degenerate $1S_e$ states. This eight-fold degeneracy is broken first by crystal field and shape anisotropy and finally by the exchange interaction into a ladder of five states designated by the only remaining good quantum number N (see figure 1.8 for description of quantum numbers).

1.5 Optical Spectroscopy of CdSe Nanocrystals

Optical spectroscopy is the single most important experimental tool for confirming the theoretical electronic structure described in the previous section. Photoluminescence Excitation (PLE) and fluorescence line narrowing (FLN) techniques were integral to the studies which elucidated the energy levels at the band edge, particularly the fine structure of the $1S_e1S_{3/2}$ transition¹⁴. Both resonant and non-resonant Stokes shifts as well as a phonon progression in the FLN emission spectrum attest to the

band edge fine-structure of CdSe nanocrystals. In the time domain, the lifetime of the single exciton has been observed to be much longer³⁶ than the lifetime of a single exciton in bulk CdSe which is between 200ps and ~3ns depending on temperature and excitation intensity^{2,37}. A long lifetime runs counter to what one might expect based on the enhanced e-h overlap and oscillator strength induced by quantum confinement, but the long lifetime is nonetheless supported by the fact that the lowest state of the exciton fine structure is optically inactive. This so-called dark exciton has been confirmed in magnetic field dependent lifetime studies at low (cryogenic) temperatures¹⁶ as well as single nanocrystal studies³⁸.

One observation that is of specific relevance to this thesis is the multiexponential character of the excited state lifetime of luminescence from ensembles³⁶. Relaxation that follows a single path with a single rate exhibits a single exponential decay that is linear in a log-linear plot. Excitons at the band-edge of a nanocrystal ought to relax by only a single path, yet ensembles of nanocrystals rarely display single exponential decays. Chapter 3 of this thesis addresses the question of why multiexponential decays are observed in ensembles CdSe nanocrystals.

Another dynamical process observed in nanocrystals that is critical to experiments in this thesis is Auger recombination³⁹⁻⁴¹, which is illustrated in Figure 1.10. Auger relaxation pathways are very fast (10-100ps^{42,43}), and they involve the transfer of relaxation energy from an exciton to another excited, delocalized carrier in the nanocrystal. After accepting the energy, the carrier (electron or hole) is excited to high energy in its band (conduction or valence) before ultrafast (~1ps) intraband relaxation brings it back to the band-edge^{44,45}.

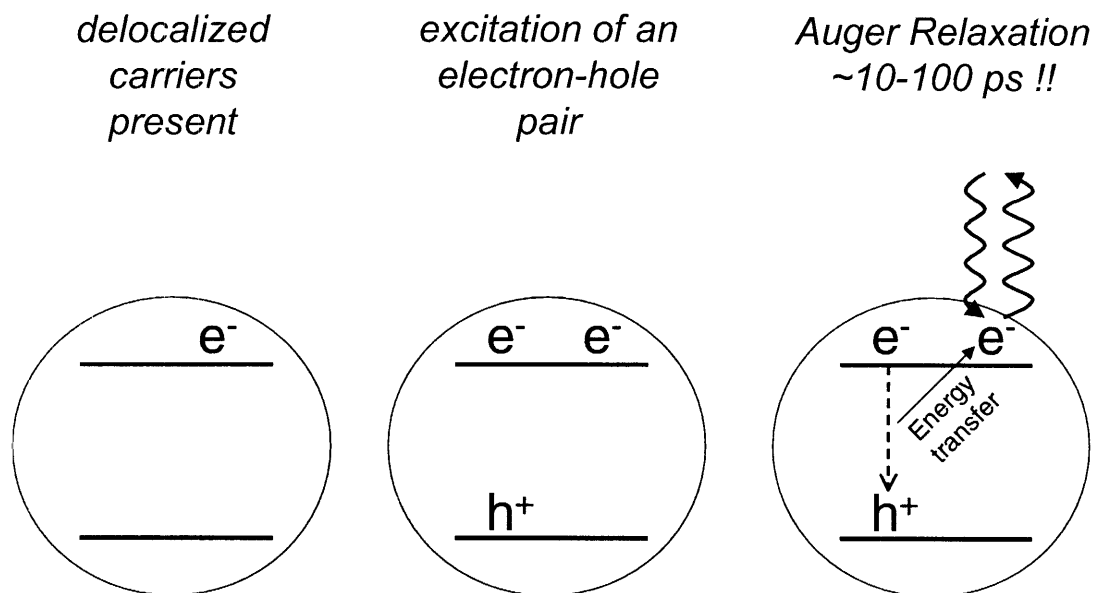


Figure 1.10 The Auger recombination process involves the transfer of an exciton's energy of relaxation to another delocalized carrier. Here the process illustrates energy transfer to an electron by the Auger process, however a hole can also act as an acceptor. Constituent carriers of a neutral exciton can also accept energy by the Auger mechanism. For this reason multiexciton as well as charged exciton states of NCs have ultrashort lifetimes.

Auger relaxation is important because of the dominant role it plays in quenching emission from excitons whenever other photo-excited carriers are present. These "other carriers" may be either lone electrons or holes in a charged NC or constituent carriers in other excitons. One consequence of efficient Auger relaxation is that multiexciton lifetimes are ultrafast compared to radiative relaxation, and multiexciton quantum yield is negligible compared to a neutral single exciton state. Also the Auger mechanism renders charged nanocrystals non-luminescent and is thought to be responsible for off states in the fluorescence intermittency or blinking of single nanocrystals⁴⁶.

Blinking represents just one of many interesting phenomena^{17, 47-53} that were discovered when nanocrystal spectroscopy was finally brought to the single nanocrystal level⁵⁴. The primary motivation behind single nanocrystal spectroscopy is to see the optical physics of nanocrystals without the blurring effects of non-uniformly sized nanocrystals. For instance, the full-width at half-maximum of the band-edge emission from an ensemble of nanocrystals is non-homogenously broadened by the size distribution of the nanocrystals in the ensemble⁵⁵. By looking at single nanocrystals much narrower lines can be obtained with very clear phonon progressions⁵⁶. Single nanocrystal spectroscopy is the method of choice for a majority of the studies in this thesis.

1.6 Overview of Thesis

Because of the heavy use of microscopy in this thesis to isolate fluorescence from individual nanocrystals, we begin in Chapter 2 with a detailed description of the microscopy methods used. In particular this thesis represents the first extensive use of confocal microscopy in our lab so details on the development of this method are given. In chapter 3 confocal microscopy combined with time-correlated single photon counting (TCSPC) is used to study the excited state lifetime of nanocrystals at the single nanocrystal level. In chapter 4 a study of multiexciton emission from ensembles of nanocrystals is presented, and in chapter 5 this work is extended to single nanocrystals. The focus of chapter 6 is the use of single photon correlation experiments on single nanocrystals to study both single and multiexcitonic emission from single nanocrystals. Radiative quantum cascades and various states of nonclassical light generation by single

nanocrystals are observed with possible applications in fields like quantum cryptography⁵⁷. The successful observation of multiexciton emission in chapters 4-6 motivated a fundamental study aimed at directly spectrally resolving biexciton emission from single exciton emission. Such a measurement gives a direct measure of the biexciton Coulombic binding energy, which has never before been directly obtained. Chapters 8 and 9 returns to the realm of experiments on ensemble fluorescence. The relationship between the fluorescence quantum yield and excited state of nanocrystals is studied in Chapter 8. It is found that lifetime cannot be taken as a reliable indicator of quantum yield in nanocrystals if the experimental time resolution is not sufficient to capture the dynamics of all subpopulations of nanocrystals. Finally, in chapter 9 the development and preliminary results of two-photon fluorescence correlation spectroscopy (FCS) measurements on nanocrystals are reported. FCS is successfully used to distinguish identical nanocrystals with different capping ligands in a solution environment based on their different diffusion coefficients. Also, novel dynamics at short times are revealed for FCS experiments on nanocrystals.

1.7 References

- 1 L. E. Brus, *Journal of Chemical Physics* **79**, 5566 (1983).
- 2 K. H. Hellwege, *Landolt-Bornstein Numerical Data and Functional Relationships in Science and Technology* (Springer-Verlag, Berlin, 1982).
- 3 D. S. Chemla, *Physics Today*, 46 (1993).
- 4 D. S. Chemla and D. A. B. Miller, *Journal of the Optical Society of America B* **2**, 1155 (1985).
- 5 A. L. Efros and A. L. Efros, *Soviet Phys. Semicond.* **16**, 772 (1982).
- 6 H. J. Eisler, V. C. Sundar, M. G. Bawendi, et al., *Applied Physics Letters* **80**, 4614 (2002).
- 7 S. Kim, Y. T. Lim, E. G. Soltesz, et al., *Nature Biotechnology* **22**, 93 (2004).
- 8 S. Coe, W. K. Woo, M. Bawendi, et al., *Nature* **420**, 800 (2002).

- 9 M. V. Jarosz, V. J. Porter, B. R. Fisher, et al., *Physical Review B* **70**, 195327 (2004).
- 10 V. Sundar, Eisler, H.J., Bawendi, M.G., *Advanced Materials* **14**, 739 (2002).
- 11 L. E. Brus, *Journal of Chemical Physics* **90**, 2555 (1986).
- 12 A. I. Ekimov, F. Hache, M. C. Schanne-Klein, et al., *Journal of the Optical Society of America B* **10**, 100 (1993).
- 13 D. J. Norris and M. G. Bawendi, *Physical Review B* **53**, 16338 (1996).
- 14 D. J. Norris, A. L. Efros, M. Rosen, et al., *Physical Review B* **53**, 16347 (1996).
- 15 A. L. Efros, M. Rosen, M. Kuno, et al., *Physical Review B* **54**, 4843 (1996).
- 16 M. Nirmal, D. J. Norris, M. Kuno, et al., *Physical Review Letters* **75**, 3728 (1995).
- 17 S. A. Empedocles, R. G. Neuhauser, K. T. Shimizu, et al., *Advanced Materials* **11**, 1243 (1999).
- 18 C. B. Murray, et al., *Journal of the American Chemical Society* **115**, 8706 (1993).
- 19 L. Manna, D. Milliron, A. Meisel, et al., *Nature Materials* **2**, 382 (2003).
- 20 Z. A. Peng and X. G. Peng, *Journal of the American Chemical Society* **124**, 3343 (2003).
- 21 B. R. Fisher, H. J. Eisler, N. E. Stott, et al., *Journal of Physical Chemistry B* **108**, 143 (Supplemental Information 2004).
- 22 B. O. Dabbousi, J. Rodriguez-Viejo, F. V. Mikulec, et al., *Journal of Physical Chemistry B* **101**, 9463 (1997).
- 23 M. A. Hines, Guyot-Sionnest, P., *Journal of Physical Chemistry* **100**, 468 (1996).
- 24 I. N. Stranski and L. Krastanow, *Akademische Wissenschaft Literatur, Mainz Abh Math. Naturwiss. Kl.* **146**, 767 (1939).
- 25 B. A. Joyce and D. D. Vvedensky, *Materials Science and Engineering Reviews - Reports* **46**, 127 (2004).
- 26 L. E. Brus, *Journal of Chemical Physics* **80**, 4403 (1984).
- 27 S. Flugge, *Practical Quantum Mechanics* (Springer-Verlag, Berlin, 1971).
- 28 N. W. Ashcroft and N. D. Mermin, *Solid State Physics* (Harcourt College Publishers, Fort Worth, Philadelphia, San Diego, New York, Orlando, Austin, San Antonio, Toronto, Montreal, London, Sydney, Tokyo, 1976).
- 29 T. K. Bergstresser and M. L. Cohen, *Physical Review* **164**, 1069 (1967).
- 30 D. J. Norris, 2000), p. 65.
- 31 A. L. Efros and A. V. Rodina, *Physical Review B* **47**, 10005 (1993).
- 32 D. J. Griffiths, *Introduction to Quantum Mechanics* (Prentice Hall, Upper Saddle River, NJ, 1995).
- 33 P. D. J. Calcott, K. J. Nash, L. T. Canham, et al., *Journal of Luminescence* **57**, 257 (1993).
- 34 S. Nomura, Y. Segawa, and T. Kobayashi, *Physical Review B* **49**, 13571 (1994).
- 35 T. Takagahara, *Physical Review B* **47**, 4569 (1993).
- 36 M. G. Bawendi, P. J. Carroll, W. L. Wilson, et al., *Journal of Chemical Physics* **96**, 946 (1991).
- 37 J. Erland, B. S. Razbirin, K.-H. Pantke, et al., *Physical Review B* **47**, 3582 (1993).
- 38 O. Labeau, P. Tamarat, and B. Lounis, *Physical Review Letters* **90**, 257404 (2003).

- 39 D. I. Chepic, A. L. Efros, A. I. Ekimov, et al., *Journal of Luminescence* **47**, 113
(1990).
- 40 A. L. Efros, in *Archives* (Naval Research Laboratory, 2002).
- 41 V. A. Kharchenko and M. Rosen, *Journal of Luminescence* **70**, 158 (1996).
- 42 V. I. Klimov, *Journal of Physical Chemistry B* **104**, 6112 (2000).
- 43 V. I. Klimov, A. A. Mikhailovsky, D. W. McBranch, et al., *Science* **287**, 1011
(2000).
- 44 V. I. Klimov, D. W. McBranch, C. A. Leatherdale, et al., *Physical Review B* **60**,
13740 (1999).
- 45 V. I. Klimov, A. A. Mikhailovsky, D. W. McBranch, et al., *Physical Review B*
61, 13349 (2000).
- 46 A. L. Efros, *Physical Review Letters* **78**, 1110 (1997).
- 47 S. A. Empedocles and M. G. Bawendi, *Journal of Physical Chemistry B* **103**,
1826 (1999).
- 48 S. A. Empedocles, *Science* **278**, 2114 (1997).
- 49 S. A. Empedocles, R. G. Neuhauser, and M. G. Bawendi, *Nature* **399**, 126 (1999).
- 50 M. Kuno, D. P. Fromm, H. F. Hafmann, et al., *Journal of Chemical Physics* **115**,
1028 (2001).
- 51 R. G. Neuhauser, K. T. Shimizu, W. K. Woo, et al., *Physical Review Letters* **85**,
3301 (2000).
- 52 K. T. Shimizu, Fisher, B.R., Woo, W.K., Bawendi, M.G., *Physical Review Letters*
89, 117401 (2002).
- 53 K. T. Shimizu, R. G. Neuhauser, C. A. Leatherdale, et al., *Physical Review B* **63**,
205316 (2001).
- 54 S. A. Empedocles, D. J. Norris, and M. G. Bawendi, *Physical Review Letters* **77**,
3873 (1996).
- 55 S. A. Empedocles and M. G. Bawendi, *Accounts of Chemical Research* **32**, 389
(1999).
- 56 S. A. Empedocles, in *Chemistry* (Massachusetts Institute of Technology,
Cambridge, 1999), p. 204.
- 57 N. Gisin, G. Ribordy, W. Tittle, et al., *Reviews of Modern Physics* **74**, 145
(2002).

Chapter 2: Methods of Fluorescence Microscopy

- 2.1 Introduction
- 2.2 Wide Field versus Confocal Microscopy
- 2.3 General Descriptions of the Fluorescence Microscope
- 2.4 Wide Field Microscopy Techniques
- 2.5 Confocal Techniques – Image Acquisition
- 2.6 Two-Photon Microscopy
- 2.7 Conclusions
- 2.8 References

2.1 Introduction

At the beginning of this thesis work the primary microscopy technique used in our research group was wide-field fluorescence imaging of single nanocrystals using charge-coupled devices (CCDs) for detection^{1,2}. Part of the challenge of this thesis was the development and implementation of techniques that were new to our lab, particularly confocal and two-photon microscopies. These techniques are gaining widespread use in the field of single molecule spectroscopy and are the basis for a majority of the single nanocrystal experiments presented in this thesis. This chapter will give a description of the fundamental differences between wide field and confocal microscopy. It will also describe in some detail the methods we developed to generate images of single nanocrystals using confocal microscopy, and conversely, methods to isolate the emission of a single NC when wide-field excitation is used. The chapter finishes with an introduction to two-photon microscopy, which is fundamental to fluorescence correlation spectroscopy (FCS) experiments in chapter 9.

2.2 Wide-Field versus Confocal Microscopy

We begin by discussing the similarities and differences between confocal and wide-field fluorescence microscopy methods. In figure 2.1 the key elements of the two

methods are illustrated in a simplified manner showing their basic optical paths, illumination and collection. In the confocal geometry, the illumination optical path images a point source of light onto the sample (object) plane. The distribution of illumination intensity for this single point of light in the sample plane is described by the point spread function (PSF) of the illumination optical path, $I_{PSF}(x,y,z)$. The collection path of the confocal microscope collects light from a single point in the sample plane and

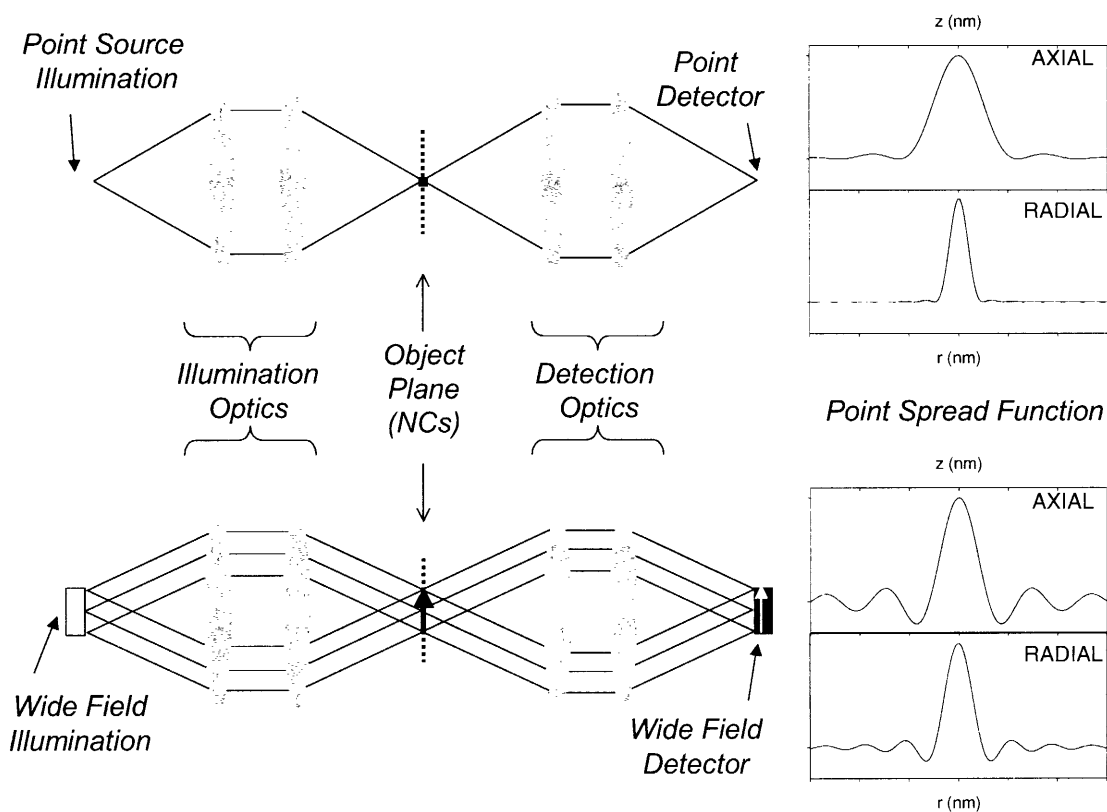


Figure 2.1 Comparison of confocal and widefield microscopy. Confocal microscopy focuses a point source of light to a single point in the sample which is itself detected by a point detector. Wide-field microscopy by contrast illuminates a wide field of points on the sample and collects each point simultaneously with a wide field detector. The difference in the point spread functions (PSFs) for the two methods is shown on the right. Both are based on Airy functions, but the PSF for confocal microscopy is narrower because it is the convolution of both the excitation and illumination PSFs.

sends it to a point detector. Conversely, one can say that the collection optics image the point detector onto the sample plane with a PSF of detection efficiency, $D_{PSF}(x,y,z)$. One

would like the illumination PSF and the detection PSF to overlap at the sample. The term *confocal* microscopy itself refers to the fact that the foci of both optical paths overlap.

Wide field microscopy is completely analogous to confocal microscopy, except that “point” is replaced by “wide-field.” A wide field light source is imaged onto the sample plane by the illumination optics, and the wide-field of fluorescence from the sample is collected and sent to a wide-field detector such as a CCD. A wide-field CCD is like a massively parallel version of the confocal microscope – each point in the illumination plane corresponds to a point in the sample plane, which corresponds to a point in the detector plane, and all are collected simultaneously by the wide field detector. The efficiency of this parallel operation is the primary advantage of wide-field microscopy. As we shall see, however, confocal microscopy has a number of different advantages to boast.

2.3 General Description of the Fluorescence Microscopes

In figure 2.1 the illumination optical path is shown with completely separate optics from the collection path. For the optical microscopes used in this thesis, however, the diagrams in 2.1 are folded over onto themselves so that some optics (the objective in particular) are shared by the illumination and collection optical paths. This general optical layout is given by figure 2.2. A beam splitter that passes red wavelengths but reflects blue wavelengths (e.g. dichroic or ND filter plus band pass or notch filters) couples the excitation laser into the same path as the collected fluorescence, allowing the same objective to be used for excitation and fluorescence collection. Of course, the

selection of beam splitter dictates whether the illumination path follows the right angle reflection or vice versa.

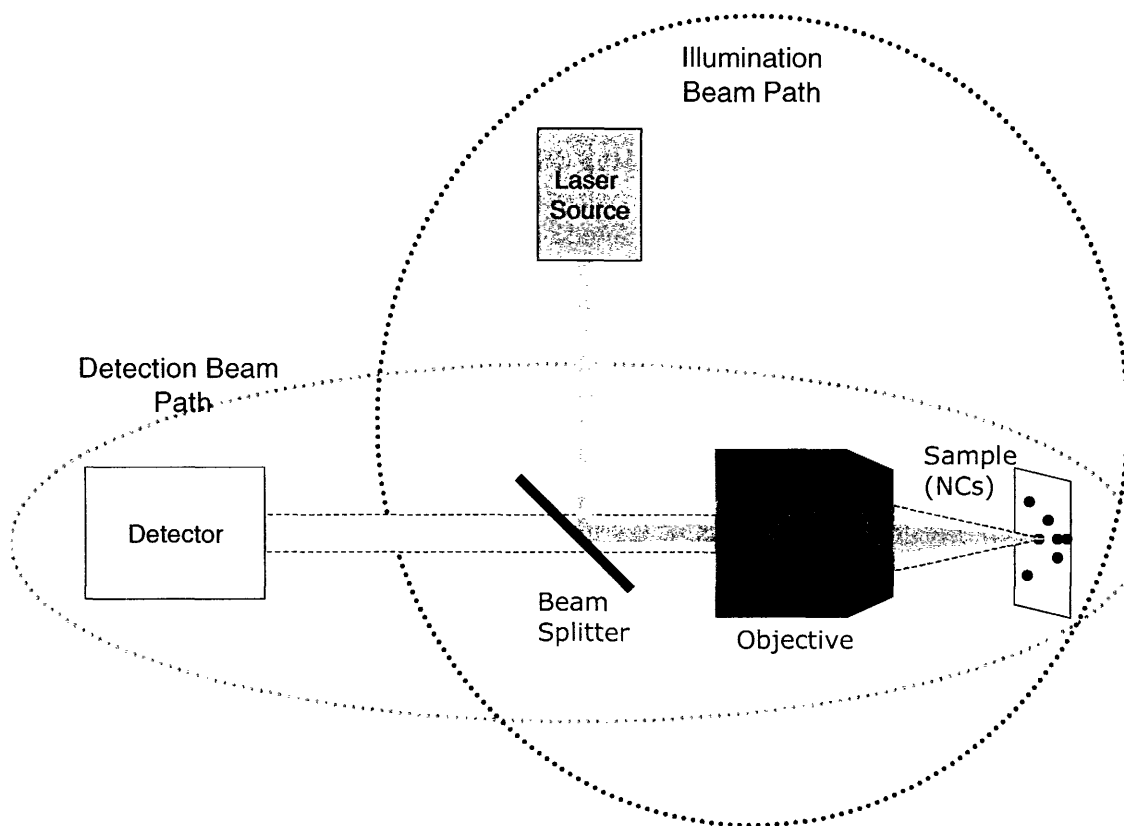


Figure 2.2 The basic layout of all microscopes used in this thesis. The same objective is used both to focus the illumination and to collect fluorescence from the sample. A beamsplitter couples the illumination and collection optical paths.

The objective is the most important individual optic in the microscope so understanding it is essential. There are many defining parameters for microscope objectives including magnification and numerical aperture (NA). Good descriptions of these metrics as well as various corrections of objectives (e.g. spherical aberration, chromatic, etc.) are available in literature³. Because so-called “infinity corrected” objectives are not well described in literature that we read and because the understanding of them is critical to scanning confocal microscopes, we discuss them here. Figure 2.3

shows the difference between traditional objectives that adhere to the DIN (Deutsche Industrie Norm) and newer infinity corrected objectives.

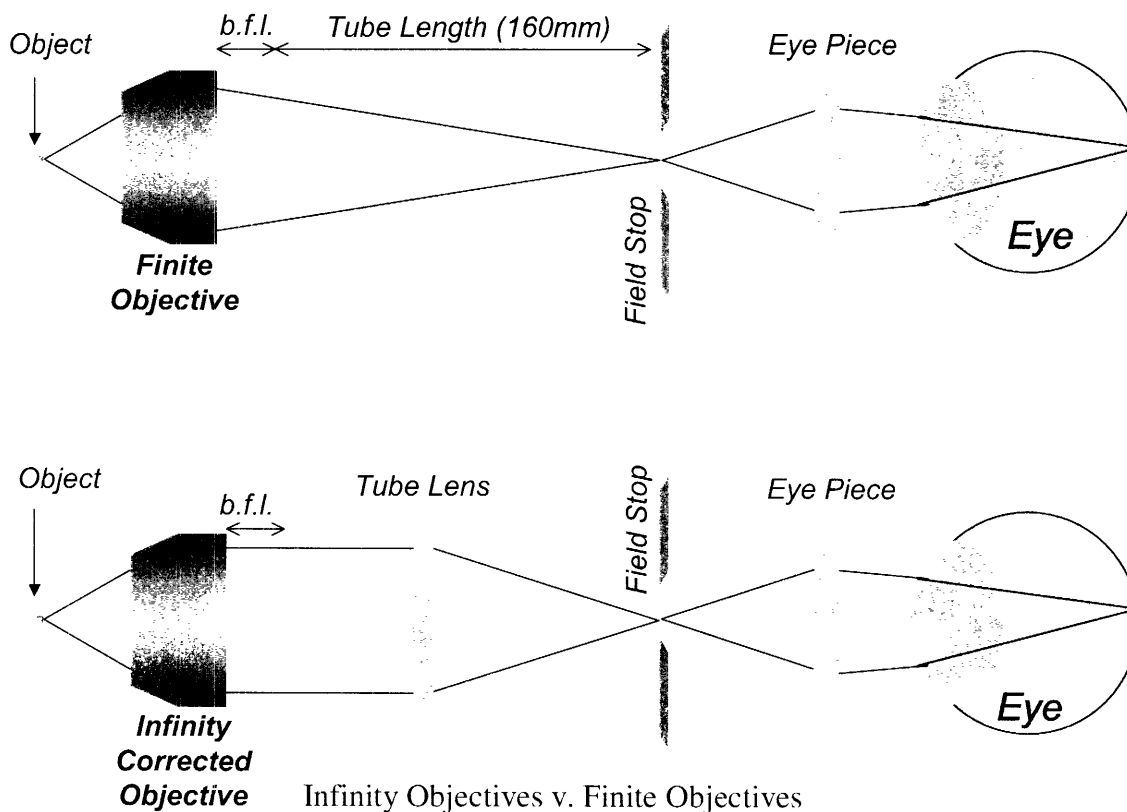


Figure 2.3 The difference between infinity corrected objectives and conventional DIN finite objectives. DIN objectives are standardized to form an image of the object in focus at 160mm behind its back focal length. Infinity corrected objectives by contrast form the image at infinity – collimated light from the sample emerges from the objective and a tube lens is necessary to form an image. Note that here the word “objective” refers to the entire set of optical elements contained in the steel barrel and not just the first hemispherical lens.

The DIN standardized the distance behind the objective at which the image would be formed as 160mm plus the back focal length (b.f.l). Use of DIN finite objectives therefore requires that the sample and the image plane be at well-defined positions in order to achieve optimum performance. Because this requirement limits how many optics can be added to the collection path, and because aberrations are introduced when such optics are placed in a non-collimated beam path, infinity corrected objectives were

introduced. For these objectives the image is formed at infinity, meaning that a tube lens is required to form the image at the field stop. A user can either place a detector at the image plane or use an eyepiece to look through the microscopy using his own eyes. The collimated light emerging from the back of the infinity corrected objective allows optical elements to be added without aberration and it confers more design flexibility in the microscope. The difference between these objectives is simple but it was critical to the understanding and design of microscopes in this thesis.

2.4 Wide-field Microscopy Techniques

In figure 2.4 the most basic setup for wide field spectroscopy is shown for use

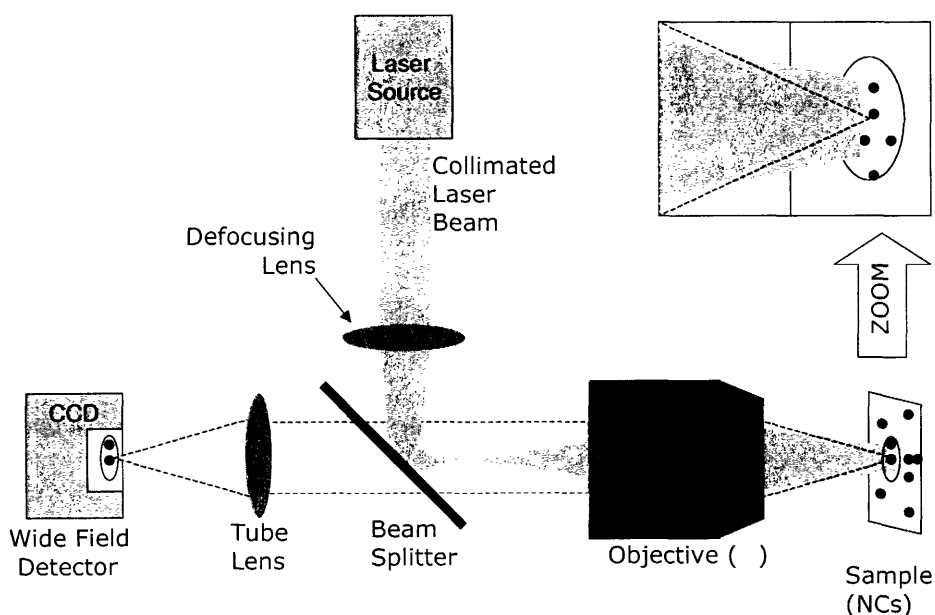


Figure 2.4 Wide field microscope setup used for CCD imaging of single nanocrystals in this thesis. Note that a defocusing lens serves to cause a wide field of the sample to be illuminated when the sample is in the focal plane of the objective. Also, since a wide field detector is used, a wide field of points in the sample plane are collected and measured simultaneously to generate the image.

with an infinity corrected objective. It adheres closely to the general design of figure 2.2 but a few details are critical. First, a defocusing lens is added to the illumination path so that the excitation light entering the objective is not collimated and hence does not focus to a diffraction-limited point at the sample. Instead, since the excitation is diverging as it enters the objective it does not focus completely at the sample and illuminates a wide region. For 100x magnification, high NA (>1) objectives and a spherical defocusing lens of $\sim 100\text{mm}$ focal length, the illuminated region of the sample plane is about $30\ \mu\text{m}$ in diameter.

The second detail to notice is the use of wide-field detection, which collects light from all of the illuminated points on the sample as discussed earlier. If the detector is placed one focal length away from the tube lens, then it is assured to collect light from the proper focal plane in front of the objective. (For clarity, the light path of just one of the many points is drawn explicitly.) We note another advantage of infinity corrected objectives here as well: since collimated light emerges from the back of the objective, the distance from objective to tube lens does not greatly impact performance and the objective itself may be moved to focus the sample. Only the relative distance between the tube lens and the detector dictate the distance between the front of the objective and the sample plane that is in focus.

In figure 2.5 we show how the use of apertures to perform transverse sectioning of the image gives added flexibility to wide-field microscopy. On the left side of the diagram is a simplified collection path showing fluorescence collected from three different points on the sample. An aperture that is placed in the primary image plane allows only specific points to pass on to another optical system and be detected. The

secondary optical system on the right side takes the image at the aperture and projects it to the detector on the right. If the optical element between the lenses is a plain, reflective mirror, then the transversely sectioned image is detected (figure 2.5(c)).

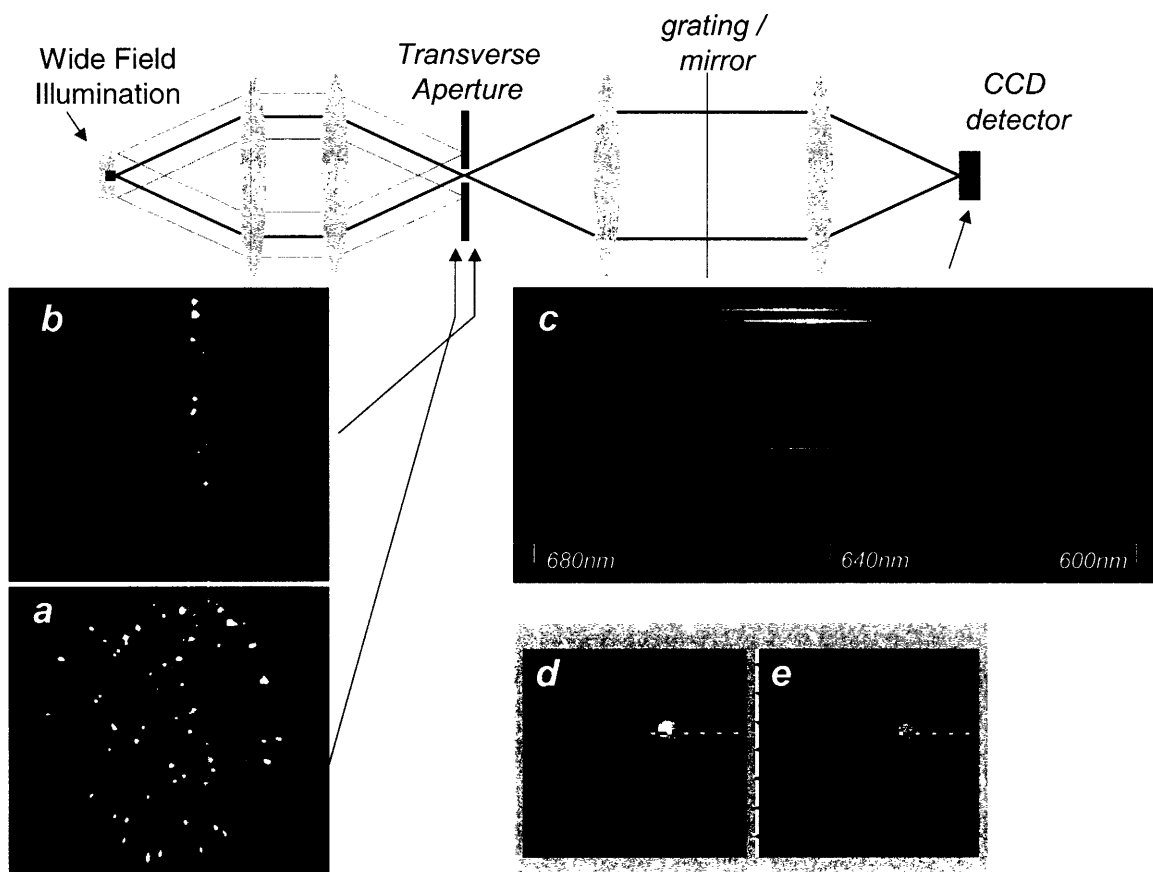


Figure 2.5 Illustration: diagram of transverse sectioning of images using wide-field microscopy. (a) fluorescence image of single nanocrystals as seen without an aperture used (i.e. as the image appears immediately before the aperture). (b) same as (a) except that a one-dimensional aperture is applied. The image is transferred to the CCD detector using a mirror. (c) spectra of the single nanocrystals shown in (b) obtained by reflecting the image of (b) off of a diffraction grating. (d) and (e) two-dimensional transverse sectioning of a wide field image such that only the light from a single nanocrystal is collected. In image (d) the nanocrystal is blinked “on” and in image (e) it is blinked “off.”

If the a diffraction grating is used between the lenses of the secondary optical system then a spectrum of the points of light that passed the aperture is generated on the detector. The application of this scheme to single nanocrystal spectroscopy is illustrated by the images at the bottom of the figure. On the left (figure 2.5(b)) is a wide field image of single

nanocrystals generated by the collection optics and sent to the CCD detector with no aperture at the image plane. The second image (figure 2.5(c)) shows the effect of imposing a one-dimensional aperture (i.e. slit) at the primary image plane. Only a few nanocrystals are visible along the vertical dimension. The third image shows the image generated when the light from these nanocrystal point sources passes the diffraction grating before detection on the CCD – the spectrum of each individual nanocrystal is recorded. This technique was developed in our group for the purpose of measuring PL spectra from single nanocrystals² and is used widely in this thesis.

For some applications like single photon counting, a point detector such as an avalanche photodiode (APD) is required. In these cases we would like to know precisely the location within the image where the detected light originates (e.g. from which single nanocrystal). Transverse sectioning allowed us to do this even when wide-field microscopy was used and light from a wide field with numerous nanocrystals was collected by the objective. In this case a two-dimensional aperture (i.e. pinhole) was placed in the primary image plane allowing only a single point of light to pass. To illustrate this, a 2 dimensionally sectioned image was detected using a CCD and the images are shown in the lower right of figure 2.5. In one image the dot has blinked “off” and in the other the dot has blinked “on.” To acquire these images the aperture was positioned so that the fluorescence of a single nanocrystal could pass. This light could then be sent to an APD for single photon counting.

2.5 Confocal Microscopy Techniques

Although the use of pinholes for two-dimensional transverse sectioning of wide field images of single nanocrystals was successful at selecting emission from only one nanocrystal for detection on the APD, it was highly inefficient in practice. Use of a pinhole required repositioning of it and the APD (in order to maintain alignment of the collection path) for each nanocrystal of interest. A much better option is to use confocal microscopy where only a single point of the sample is excited and light from the same single point is collected.

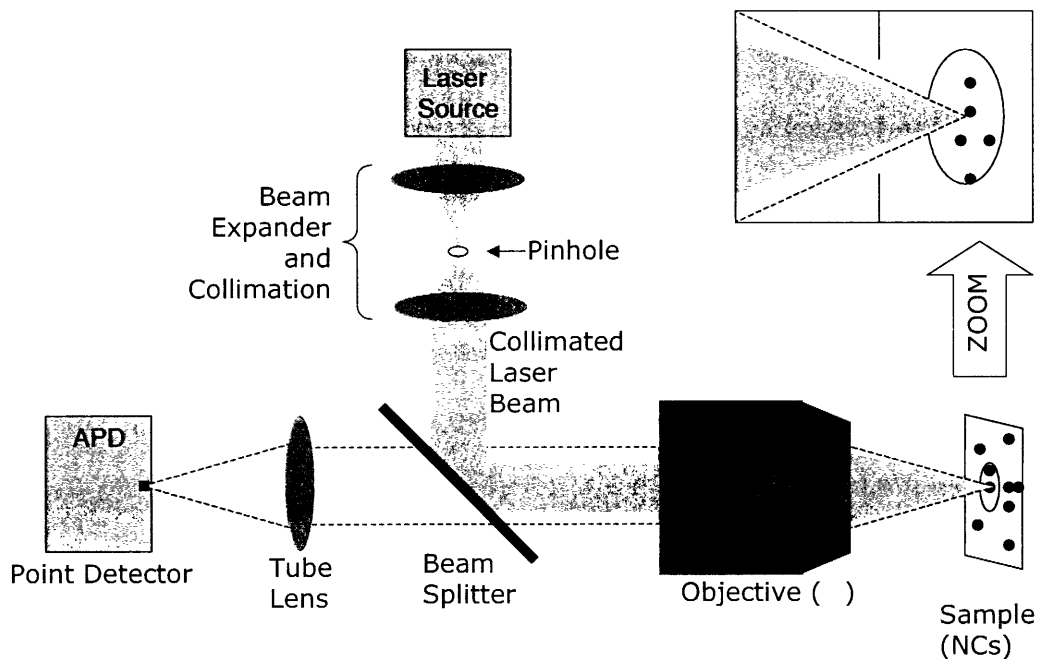


Figure 2.6 Illustration of basic confocal microscope design used in this thesis. Note that a point source of light (pinhole) is focused to a point in the sample. Meanwhile the point detector is imaged by the collection optics onto the same single point in the sample plane.

The fundamental differences between confocal and wide field microscopies were described in figure 2.1.

The basic setup of the confocal microscope used in our single photon counting experiments, shown in figure 2.6, has two main differences from the wide-field setup that was shown in figure 2.4. First, there is no defocusing lens in the illumination path, and a collimated laser beam enters the infinity corrected objective so that the excitation light is focused to a single point. Second, the light emitted from the single point on the sample is focused to a single point detector rather than a wide-field CCD detector. Most commercial confocal microscopes use a photomultiplier tube (PMT) for detection with a pinhole in the image plane to define the single point of the image that is detected since a PMT has a wide area of sensitivity. In our case we used an APD for detection of single photons. The APD serves as a point detector with an area of sensitivity that is about $175\mu\text{m}$ in diameter.

We mentioned earlier (figure 2.1) that the transverse PSF of confocal microscopes is significantly sharper than that for wide field microscopy. In the axial direction the PSF of the confocal microscope enjoys an even greater advantage, leading to the ability to perform depth sectioning with it. The basis for the depth sectioning ability of confocal microscopes is shown in figure 2.7. Light that originates from the sample plane at the front focal length of the objective is focused to a point in the image plan and can pass through the pinhole efficiently. However, light that originates from different axial positions (dashed lines) is not in focus at the pinhole and is not efficiently passed or detected. Because only thin film samples are studied in this thesis, depth sectioning is not required and our experiments do not specifically take advantage of this property. Still,

depth sectioning illustrates one advantage of the much more focused PSF available from confocal microscopy.

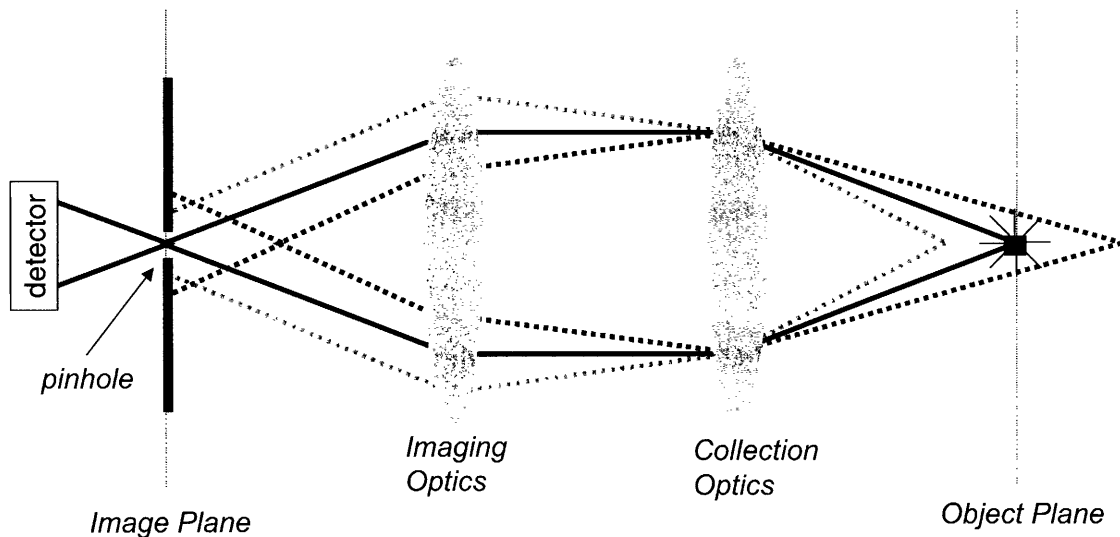


Figure 2.7 Origin of the depth sectioning capability of confocal microscopy. Only light originating from the image plane is efficiently passed through the pinhole in the primary image plane.

The microscope setup as shown in figure 2.6 does not have imaging capabilities, rather it is a sampling device, providing detection of light from a specific point in the sample. In order to generate an image of the sample, the point of the specimen that is sampled must be serially raster-scanned over the specimen using software to reconstruct the image. The most straightforward way to achieve this is to raster-scan the sample in the x-y plane relative to the focused point sampled by the confocal microscope. In this thesis a piezo stage with 200 μ m of x-y range and 5nm precision was used (Physik Instruments). A Labview program was written to perform the scanning, whereby each

cycle of a nested for-loop (one loop each for x and y directions) measures the intensity of light at a given point and then moves the sample to its next position.

The use of a piezo stage for sample scanning has the advantage of simplicity and high precision, however it is slow, and it is limited to moving only very small samples that can be carried by the small piezo stage. For low-temperature experiments where the sample is contained inside of a large cryostat weighing several kilograms, scanning with the piezo stage is impractical. In this case laser scanning is the method of choice.

Laser scanning uses movable mirrors to change the angle of the illumination path so that the PSF is raster scanned across the sample, which is held stationary. Confocal laser scanning microscopy (CLSM) can generate images much more quickly than sample scanning^{4,5}. Using resonantly driven galvanometer controlled mirrors (galvo-mirrors), images can be generated at TV rates (>20Hz). In our setup galvo-mirrors were used, but the emission intensity of single nanocrystals limited the speed at which scanning was practical – one must integrate on each pixel long enough that the signal significantly outweighs shot noise. For a single nanocrystal the maximum count rate typically achievable is about 200kcps meaning that a 0.5ms/pixel integration time still only gives 100 counts with S/N ratio of 10. At that scan rate a single frame still takes 50 seconds, which does not capitalize on the scan speed capabilities of the galvo-mirrors. The ability to scan the PSF of the confocal microscope focus on a *stationary* sample (in a cryostat), not speed, is the motivation for using scanning mirrors

The main disadvantage of CLSM is that the microscope setup is more complex[†]. Figure 2.8 illustrates the added complexity, showing how the system should be arranged for two cases, one using an infinity-corrected objective and the other using a finite (DIN)

objective. The first point to notice is the positioning of the scanning mirror: the scanning mirror should be positioned so that its motion affects the illumination and the collection paths in the same way - this is called “descanning” the collected light. If the scanning mirror only altered the illumination path, then scanning would move the illumination PSF but not the collection PSF and the system would not remain *confocal*. In practice this means that the scanning mirrors should be between the beamsplitter and the objective as shown in both setups of figure 2.8. The second important issue is telecentric corrections of the optics in the system. A telecentric plane is a plane in the system where a change in

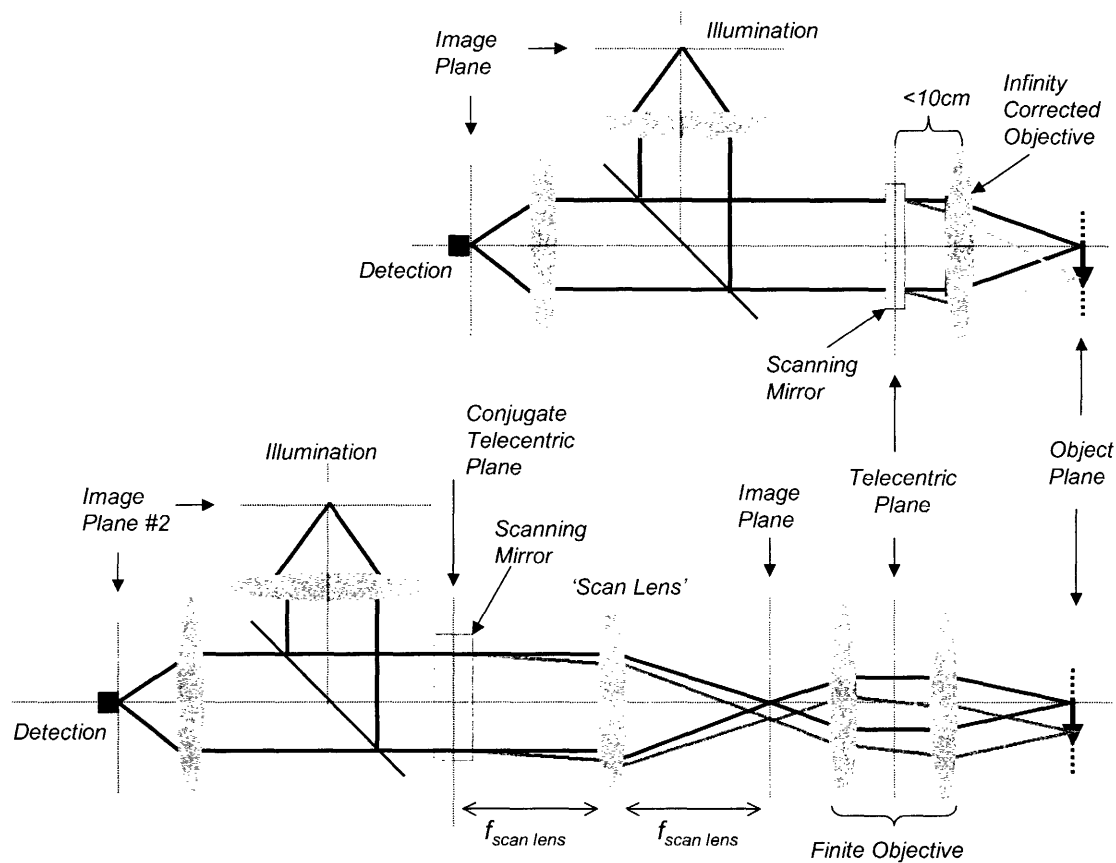


Figure 2.8 Design of laser scanning mirrors for confocal microscopy using a finite objective (bottom) and an infinity corrected objective (top).

angle of the optical path results in the lateral translation of the focus in the focal plane (on the sample)⁴. This means that we would like the scanning mirrors to lie in a telecentric

plane. Here the differences between infinity corrected and finite (DIN) objectives become important.

For finite objectives the telecentric plane is physically within the housing of the objective. Therefore a scan lens is used to create a conjugate telecentric plane, which is an image of the primary telecentric plane (inside the objective). The scanning mirror is placed in the conjugate telecentric plane. Proper positioning of the scan lens to generate the conjugate telecentric plane is one focal length of the scan lens from the image plane of the finite objective. This illustrates a different but equivalent description scanning: collimated excitation light deflected by the scanning mirror is focused by the scan lens to a displaced point in the primary image plane that is projected by the finite objective to a displaced point in the focal plane on the sample. Recall that the light collected from this displaced point follows the same optical path and is “descanned” by the scanning mirror back onto the rest of the collection path, which remains stationary.

In the case of infinity corrected objectives, the image plane is at infinity, so another tube lens plus a scan lens would be required to reproduce the setup shown for the finite objective. In practice we found that by placing the scanning mirrors close enough to the back entrance of the infinity corrected objective, we could approximate positioning in the primary telecentric plane well enough to achieve good images. In general the scanning mirrors were within 100mm of the back of the infinity objective. Although the mirrors were not perfectly positioned in the primary telecentric plane, the small scan angles used (covering only about 20 to 30 μ m of displacement in the sample) tolerated this deficiency – proper positioning in the telecentric plane is much more critical for large scan angles.

The results of imaging a sample of single nanocrystals using CLSM and sample scanning are shown in figure 2.9 along with a CCD image of single nanocrystals for comparison. The great advantage of scanning with a confocal microscope, as mentioned earlier, is the ability to easily focus the spectroscopy experiment inside a single diffraction limited point of the sample (e.g. one single nanocrystal). After generating the image we can direct the scanner to bring any single nanocrystal in the image into the focus using the click of a mouse. This is the single NC spectroscopy technique used to collect light for measurement of lifetimes, spectra, and single photon correlation of emission of individual nanocrystals later in this thesis.

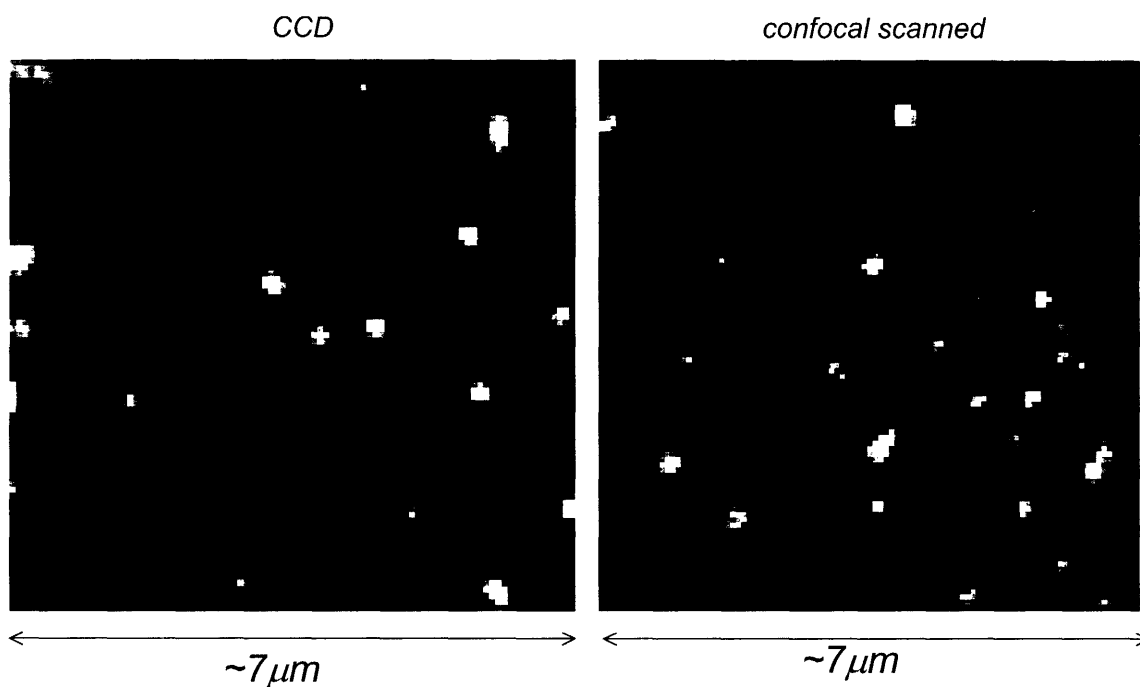
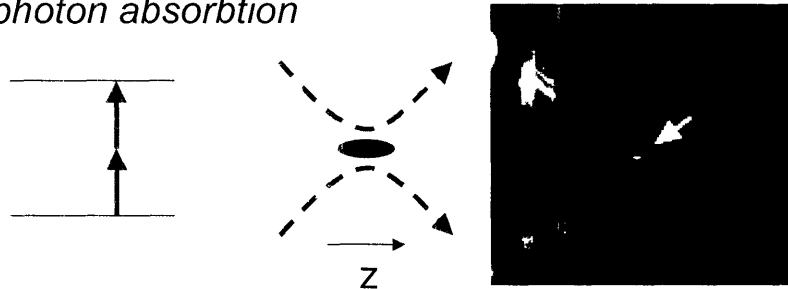


Figure 2.9 Comparison of images of single nanocrystals obtained by widefield CCD detection and by confocal scanning.

2.6 Two-Photon microscopy

The last technique that was significantly developed in our lab for experiments in this thesis is two-photon microscopy. Instead of relying on a single photon whose energy is greater than the nanocrystal band gap for excitation of a single nanocrystal, two-photon microscopy works by focusing laser light whose photon energy is less than the NC bandgap to such high intensities that two photons are simultaneously absorbed by a NC.

Two photon absorption



One photon absorption

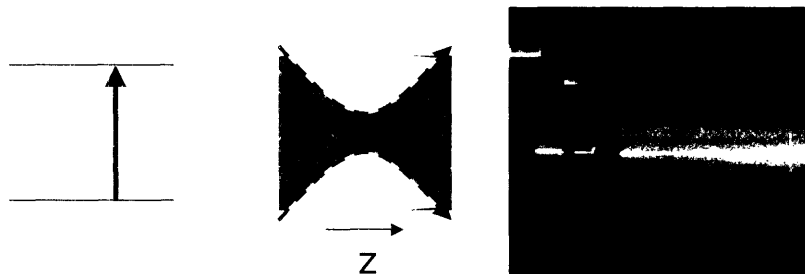


Figure 2.10 One versus two photon excitation. In one-photon absorption processes, each photon incident on the nanocrystal has enough energy to induce an excitation of the nanocrystal. Therefore as the laser excitation beam passes through a solution of NCs it excites essentially every NC in its path and fluorescence is observed all along the beam path. For two-photon excitation two photons must strike a NC simultaneously to generate an excitation. Therefore excitation only occurs at the point of highest intensity, and only a small volume of the sample fluoresces.

The two photons together deposit enough energy to excite the nanocrystal, although either photon by itself would not provide enough energy. Extremely high photon fluxes

are required to achieve simultaneous absorption of two photons, so high NA microscope objectives are used to focus ultra-high intensity femtosecond laser pulses into the sample, usually at about 800nm. Despite the very high photon fluxes of femtosecond pulses, the probability of exciting a nanocrystal is still miniscule - except at the very focal point of the objective. Therein lies the power of two-photon microscopy: excitation of nanocrystals occurs only at the focal point of the objective and nowhere else. On the bottom of figure 2.10, a laser beam of high energy photons is focused through a solution of fluorescent molecules, and although the intensity of the excitation is highest at the focus, light is clearly absorbed at all focal depths. Two-photon excitation on the other hand, which is shown on the top of figure 2.10, excites the sample only at the focus so fluorescence only originates from a tiny point within the solution.

Two-photon excitation has proven particularly useful for deep tissue imaging in biological microscopy⁶⁻⁸. Since the excitation only occurs at the focal depth, background noise is not generated by the intermediate tissue. Furthermore, the intermediate tissue is not damaged. Two-photon microscopy has also proven very useful in fluorescence correlation spectroscopy (FCS), which is the topic of chapter 9. The basis of FCS is the time-correlation of fluctuations in the intensity of fluorescence that originates from a very small region of a solution sample. If the size of the volume from which the fluorescence originates is small enough, the number of molecules residing (and fluorescing) in that volume varies significantly with time, leading to fluorescence intensity fluctuations. One can see that the use of two-photon excitation allows a very small focal volume to be probed so that large fluctuations can be observed.

2.7 Conclusions

In this chapter we have given an overview of the most important microscopy techniques that were used in the work of this thesis. We discussed the fundamental differences between confocal and wide-field microscopy before describing in some detail the actual implementation of both techniques. We showed how wide field images can be transversely sectioned to select specific parts of an image for spectroscopy or detection by an APD. We also addressed the differences between finite and infinity corrected objectives, and we discussed how laser scanning should be properly used in confocal microscopes. Although these techniques were not originally developed by in our lab, their use in this thesis represents their first implementation in our lab, so the details and descriptions given here should aid future researchers in using these techniques.

2.8 References

- ¹ K. Shimizu, in *Chemistry* (Massachusetts Institute of Technology, Cambridge, 2002), p. 128.
- ² S. A. Empedocles, in *Chemistry* (Massachusetts Institute of Technology, Cambridge, 1999), p. 204.
- ³ E. H. Keller, in *Handbook of Biological Confocal Microscopy*, edited by J. B. Pawley (Plenum, New York, 1995), p. 111.
- ⁴ E. H. K. Stelzer, in *Handbook of Biological Confocal Microscopy*, edited by J. B. Pawley (Plenum, New York, 1995), p. 139.
- ⁵ M. Mueller, J. Schmidt, S. L. Mironov, et al., *Journal of Physics D: Applied Physics* **36**, 1747 (2003).
- ⁶ C. Xu, W. Zipfel, J. B. Shear, et al., *Proceedings of the National Academy of Sciences* **93**, 10763 (1996).
- ⁷ D. R. Larson, W. R. Zipfel, R. M. Williams, et al., *Science* **300**, 1434 (2003).
- ⁸ K. Berland, P. T. C. So, and E. Gratton, *Biophysical Journal* **68**, 694 (1995).

Chapter 3: Single Nanocrystal Lifetimes

- 3.1 Introduction
- 3.2 Methods
- 3.3 Multiexponential and Fluctuating Lifetimes from Single Nanocrystals
- 3.4 Single Exponential Decays
- 3.5 Uniformity of Maximum-intensity PL Decay
- 3.6 Quantum Yield Fluctuations and Blinking in Single Nanocrystals
- 3.7 Size Dependence of Nanocrystal Lifetimes
- 3.8 Conclusions
- 3.9 References

3.1 Introduction

Interest in colloidal semiconductor nanocrystals (NCs) has largely centered on their unique size dependent optical properties. Excitons in a NC are quantum confined in all three dimensions, making optical properties like emission and absorption energies strongly size dependent. These properties, when measured from an ensemble, can be masked by size polydispersity and by fluctuating local environments. Fortunately, the advent of these materials has closely followed the development of single chromophore optical microscopy and spectroscopy. These techniques have allowed the study of many NC optical properties without the blurring effects of size distribution. Moreover single molecule spectroscopy has led to the discovery of new phenomena in colloidal NC optical properties, like blinking¹⁻³ and spectral diffusion,⁴ that are not at all resolved on the ensemble level.

The excited state lifetime of colloidal NCs is one optical property that was not yet well understood at the beginning of this thesis. Photoluminescence (PL) decay dynamics of ensembles of colloidal NCs differ from those of traditional organic chromophores in two important ways. First, very long (tens of nanoseconds at room temperature to microseconds at low temperature) lifetimes are observed⁵ in contrast to the much shorter decay time of bulk CdSe (200ps to a few ns depending on temperature and excitation power)^{6, 7} and CdSe

quantum dots (210ps)⁸. This long lifetime has been explained by the band edge fine structure of CdSe nanocrystals whose lowest energy state ($N=\pm 2$) is optically inactive^{9,10}. Radiative relaxation from this so-called dark exciton state to the ground state (no exciton) requires a spin flip, making it very slow compared to bulk CdSe.

The second peculiarity observed in the lifetimes of ensembles of nanocrystals is the multi-exponential dynamics of their PL decay. Standard fluorophores and organic dyes almost invariably exhibit single exponential decay dynamics. Figure 3.1 shows the PL decay for Rhodamine 640, a common organic dye molecule.

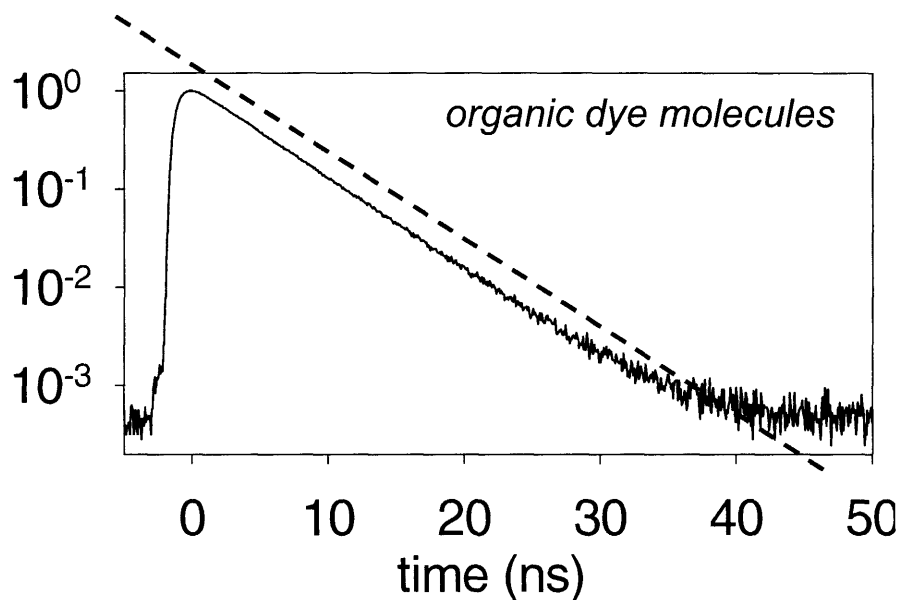


Figure 3.1 PL decay of solution of Rhodamine640 molecules in methanol at room temperature.

Ensembles of nanocrystals (e.g. solutions), on the other hand, are known to exhibit multiexponential decays, which are not linear in a log-linear plot. Moreover the degree to which the lifetime deviates from single exponential decay behavior can vary greatly from sample to sample leading resulting in vastly different lifetime measurements for ensembles of

nanocrystals. The underlying physics of radiative emission is masked by these unpredictable, multiexponential decay dynamics. Figure 3.2 illustrates the deviation of lifetime measurements from two different ensembles of nanocrystals from single exponential behavior.

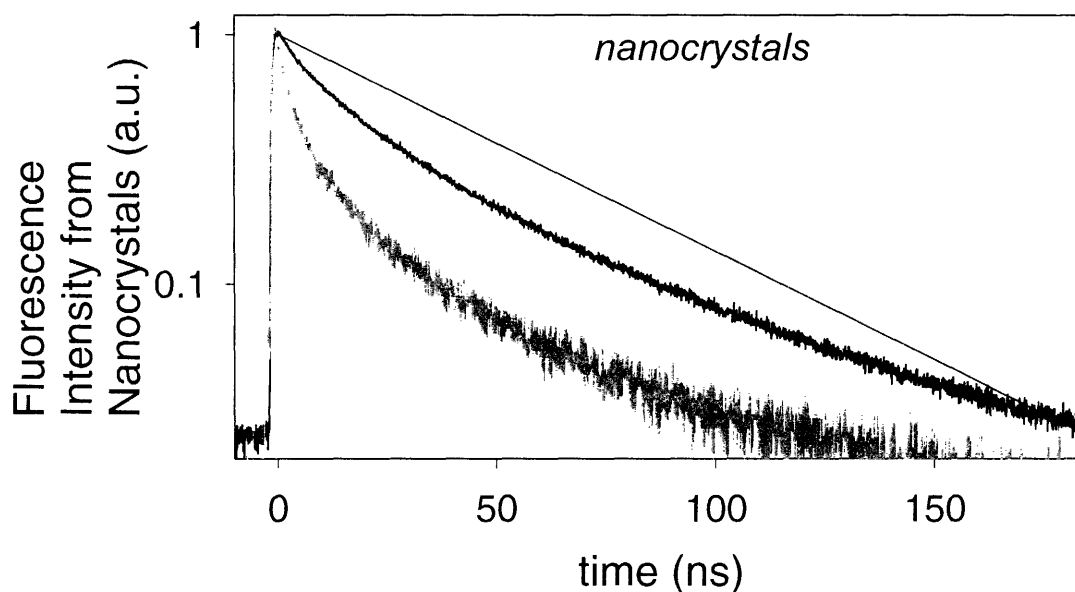


Figure 3.2 solutions of NCs at room temperature exhibit multiexponential PL decays

Three possible explanations for multi-exponential behavior in the NC ensemble PL decay dynamics present themselves: (i) each member of the ensemble has its own unique single-exponential (single rate) lifetime, and the distribution of rates within the ensemble yields a multi-exponential decay; (ii) the PL decay is an inherently complex process for each individual NC, so the decay dynamics of each individual NC are multiexponential; (iii) the PL decay of each member is single exponential at any given moment, but it fluctuates in

time, so that the (time averaged) PL decay of both an individual NC and the ensemble is multi-exponential.

Time resolved single chromophore microscopy makes it possible to probe the nature of this multiexponential behavior on a dot-by-dot basis. Recent Time Correlated Single Photon Counting (TCSPC) experiments showed that the PL decay from single CdSe colloidal NCs is in general multiexponential, and moreover that the PL decay varies during the course of the TCSPC measurement¹¹. The phenomenon of PL decay fluctuations has also been observed in single molecule studies of organic and biological molecules^{12, 13}, but the multi-exponential behavior seen in these studies is caused by fluctuations between different molecular conformational states, a parameter that is not present in the NC system. Instead fluctuations in the local electrostatic environment surrounding the NC should play an important role, as suggested in a study that correlated spectral diffusion with fluorescence blinking events in single NCs¹⁴. These electrostatic fluctuations may also lead to corresponding variations in the fluorescence quantum yield (QY) of each single NC. It was suggested that the QY of an ensemble of NCs may represent an average over widely varying QY values from individual NCs¹⁵; time-dependent fluctuations would add a new dimension to this complex QY behavior.

The experiments presented here demonstrate that PL decay fluctuations from single colloidal CdSe NCs occur on timescales ranging at least up to many seconds. They confirm that variation of the PL decay rate is correlated to variation of the time-averaged emission intensity of the NC, i.e. blinking. We also find that discriminating which photons are counted in TCSPC – for example by selecting only those photons emitted while the emission intensity is above a given threshold – reveals single-exponential PL decays from single NCs.

We propose that these single-exponential decays are a measurement of the radiative lifetime, thus providing a quantitative measure of the single-exponential radiative lifetime of colloidal CdSe NCs at room temperature.

3.2 Methods

Three different samples of ZnS overcoated (4-5 monolayers) CdSe colloidal NCs were studied at room temperature. Each NC sample was synthesized independently using established methods^{16, 17}. Overcoating was carried out using the methods of Dabbousi¹⁸. The samples had mean core radii of 3.1nm, 3.3nm and 3.3nm respectively. The samples were prepared for detection at the single molecule level by spin casting (5000rpm) a solution (~50 nM) of NCs in PMMA/Toluene solution (200mg/20mL) onto a glass coverslip.

The experimental setup consisted of a homebuilt confocal scanning microscope with either 532nm or 414nm pulsed laser excitation. The excitation laser light was focused through a pinhole and recollimated before entering the microscope. A dichroic mirror was used to couple the excitation light into the optical path, and galvanometer driven scanning mirrors were used to generate scanned images of the single NCs. A 100x oil immersion objective (Nikon) with 1.25 NA was used to both focus the collimated laser and to collect the NC emission. Laser excitation at 532nm with a pulse width ~1ps (Coherent MIRA-OPO) was provided by an intracavity frequency doubled optical parametric oscillator (OPO) that was pumped by a Ti:Sapphire laser (MIRA) at 737nm. A pulse picker was used to lower the OPO repetition rate to 4.75 MHz. Laser excitation at 414nm was provided by a GaN diode pumped laser with repetition rate of 5 MHz and pulse width of 90ps (PDL800-LDH400, Picoquant, GmbH). An avalanche photodiode (APD) (EG&G, SPCM-AQR14) was used for

detection. Single photon counting was carried out using a time to digital converter integrated into a PC computer card (Timeharp200, Picoquant, GmbH).

Time-tagged, time-resolved (TTTR) measurements using the Timeharp were performed on each single nanocrystal for a period of 120 or 180 seconds. TTTR measurements differ from traditional TCSPC in that both the start-stop time (time between excitation pulse and single photon emission, τ_p) and the absolute arrival time (time since the start of experiment, t_p) of each photon are measured. The resolution on τ_p was approximately 700ps, and the resolution on t_p was about 200ns. Single NC emission

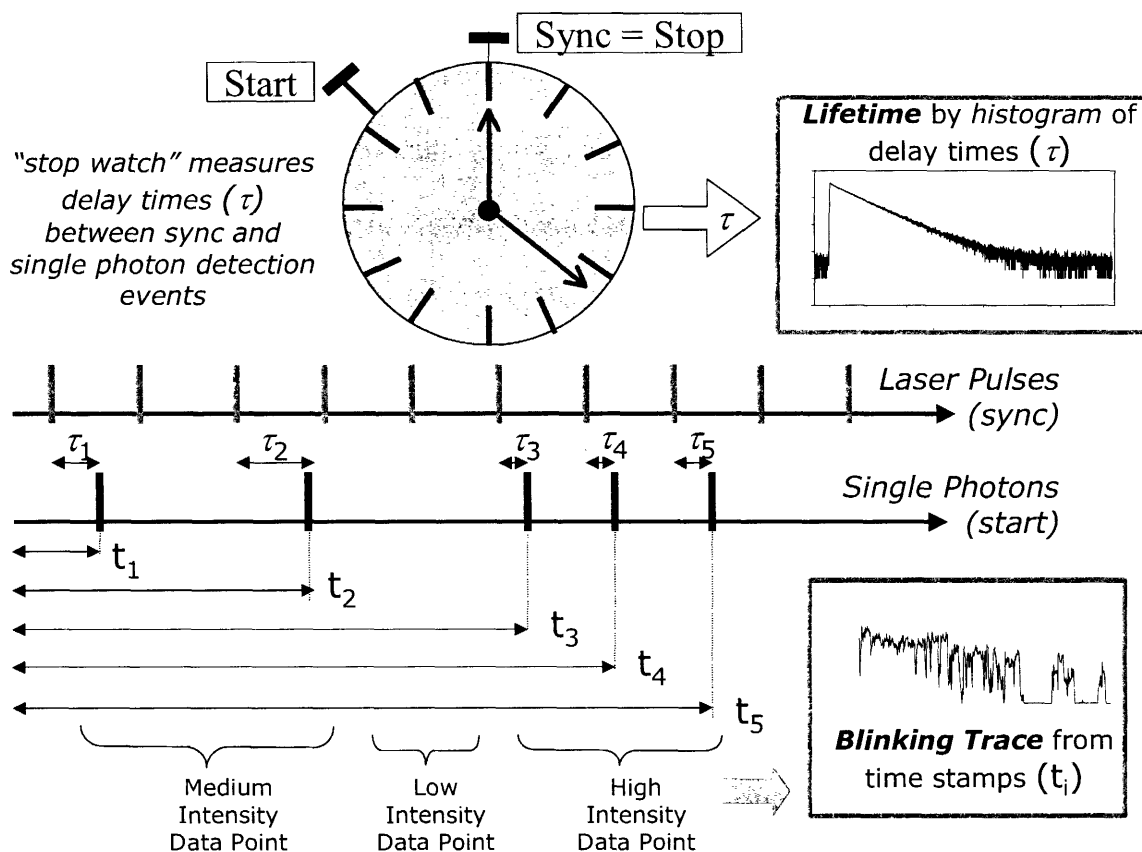


Figure 3.3 Application of Time-Tagged, Time Resolved Single Photon Counting. Both the time between excitation pulse and single photon emission ("start-stop" time, τ) and the absolute arrival time (time stamp, t) of each photon are measured. A histogram of the start-stop times gives the lifetime. The time stamps, on the other hand, tell the absolute time that the photon was emitted during the experiment. By counting the number of photons emitted during each of a sequence of time intervals the intensity trajectory of fluorescence can be recovered (counts per second, cps).

intensity trajectories were generated by binning photons according to t_p , allowing τ_p to be studied as a function of either t_p or average emission intensity. The use of TTTR measurements for these experiments are illustrated in Figure 3.3. After generating PL decays, the data were fit to decay functions in Matlab using the Nelder-Mead Simplex minimization algorithm.

3.3 Multiexponential and fluctuating lifetimes from single nanocrystals

Two examples of typical TCSPC generated PL decays from single NCs are shown in figure 3.4. These PL decays were obtained by conventional TCSPC and will be referred to as

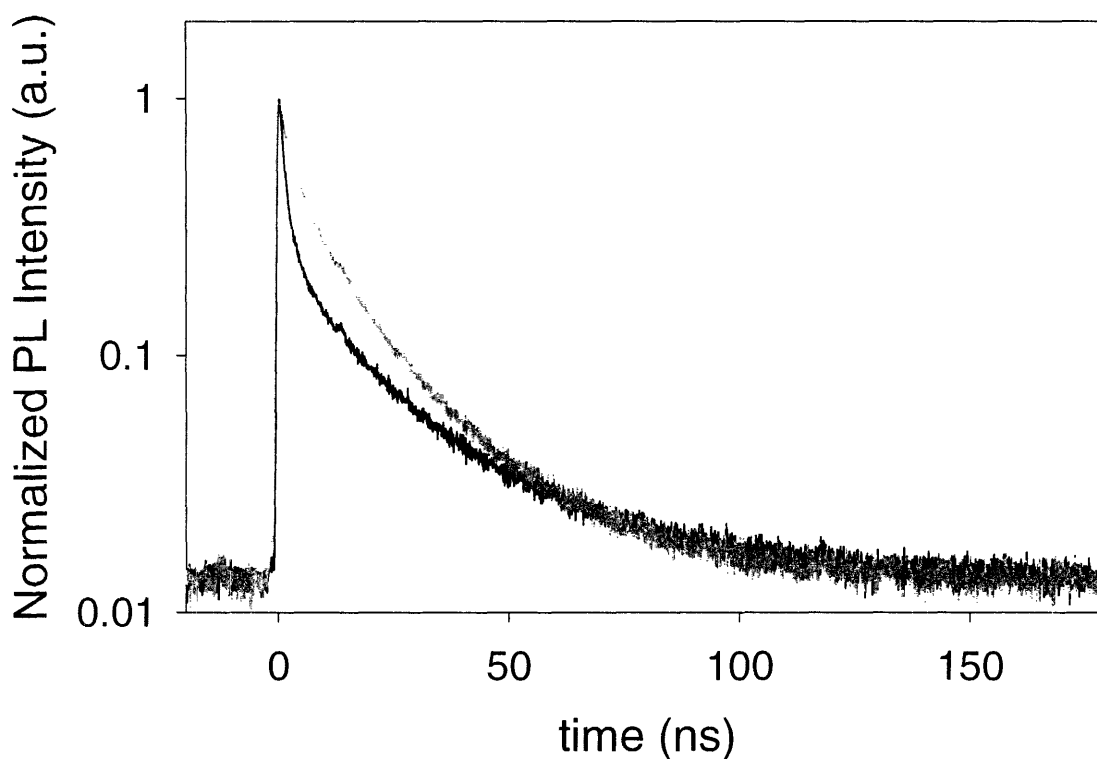


Figure 3.4 PL decays for two different single CdSe NCs (from sample 1) as measured by conventional TCSPC.

“time-averaged” PL decays to distinguish them from “maximum-intensity” decays, which use only some of the photons collected by TTTR measurements and are discussed later. The multiexponential, time-averaged single NC PL decays in figure 3.4 rule out the first suggested explanation for the multiexponential behavior of ensemble PL decay (that the ensemble comprises a distribution of NCs whose decays are single exponential, but whose rates differ from one another). Instead, each individual NC exhibits multiexponential dynamics in TCSPC measurements. However, because TCSPC in figure 3.4 is time-averaged over many seconds (120s), it fails to establish whether the decay is inherently multiexponential or whether it results from time averaging of a fluctuating single exponential decay.

Using the time-stamps obtained in the TTTR measurement, we were able to generate PL decays corresponding to very short intervals of time (~ 1 sec) by histogramming the τ values corresponding to time stamps that fall within a small time interval. The result, shown in figure 3.5, is a 3-dimensional plot of 1-second integrated PL decays over the course of a 120 second measurement. Cross-sections in the τ - z plane give the standard TCSPC generated PL decay corresponding to that value of T . A cursory look at figure 3.5 strongly suggests that the PL decay fluctuates in time, and moreover, that the fluctuation may be correlated to variations of the single NC emission intensity (blinking). Figure 3.6 confirms this observation explicitly. The top of figure 3.6 shows the emission intensity trajectory for the dot in figure 3.5, plotted using 100ms bins. The bottom panel of figure 3.6 illustrates how the lifetime varies with the emission intensity by plotting three different PL decays that were generated by photons collected during short (1 second) periods of low, medium and high count rates. These three PL decays more closely approximate single exponentials

indicating that the single dot multiexponential behavior observed in figure 3.4 is caused primarily by

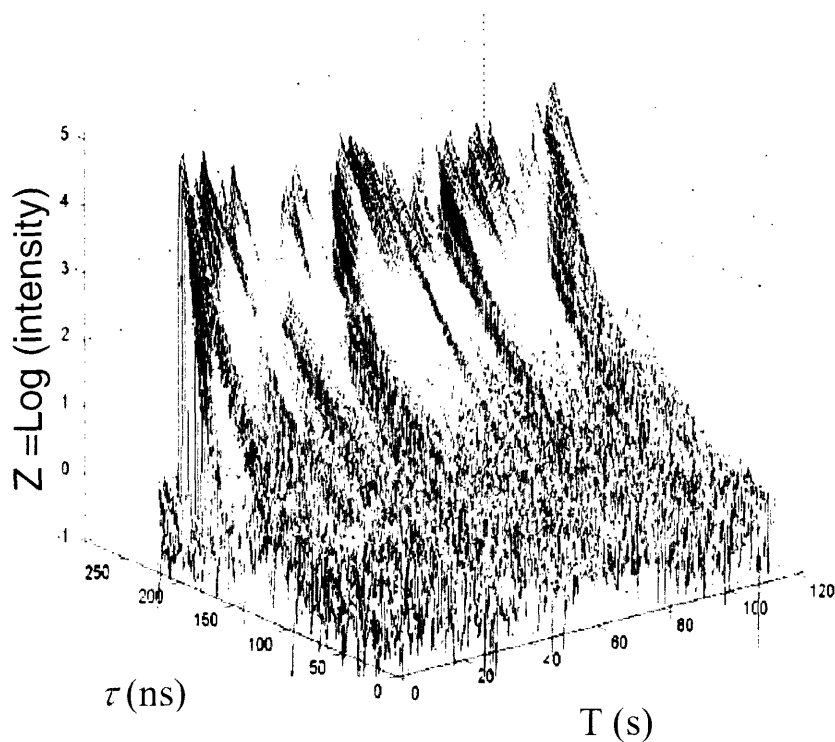


Figure 3.5 Three-dimensional count intensity versus stochastic photon arrival time (start-stop time, τ , in nanoseconds) and collection time (T , in seconds) for a single nanocrystal. The intensity is plotted in logarithmic scale.

fluctuation of the lifetime that is correlated to the emission intensity of the single NC.

Fluctuating lifetimes like this were observed in practically all TTR experiments that we performed on single NCs.

The longer lifetimes associated with higher emission intensities strongly suggest that fluctuations in the non-radiative rate (k_{nr}) dominate (see also chapter 8). If fluctuations of the radiative rate (k_r) were dominant, a decreased lifetime would correspond to an increased

quantum yield (QY) and increased PL intensity. Surface and other external trap states provide a source of non-radiative relaxation pathways for single excitons in colloidal NCs⁵.

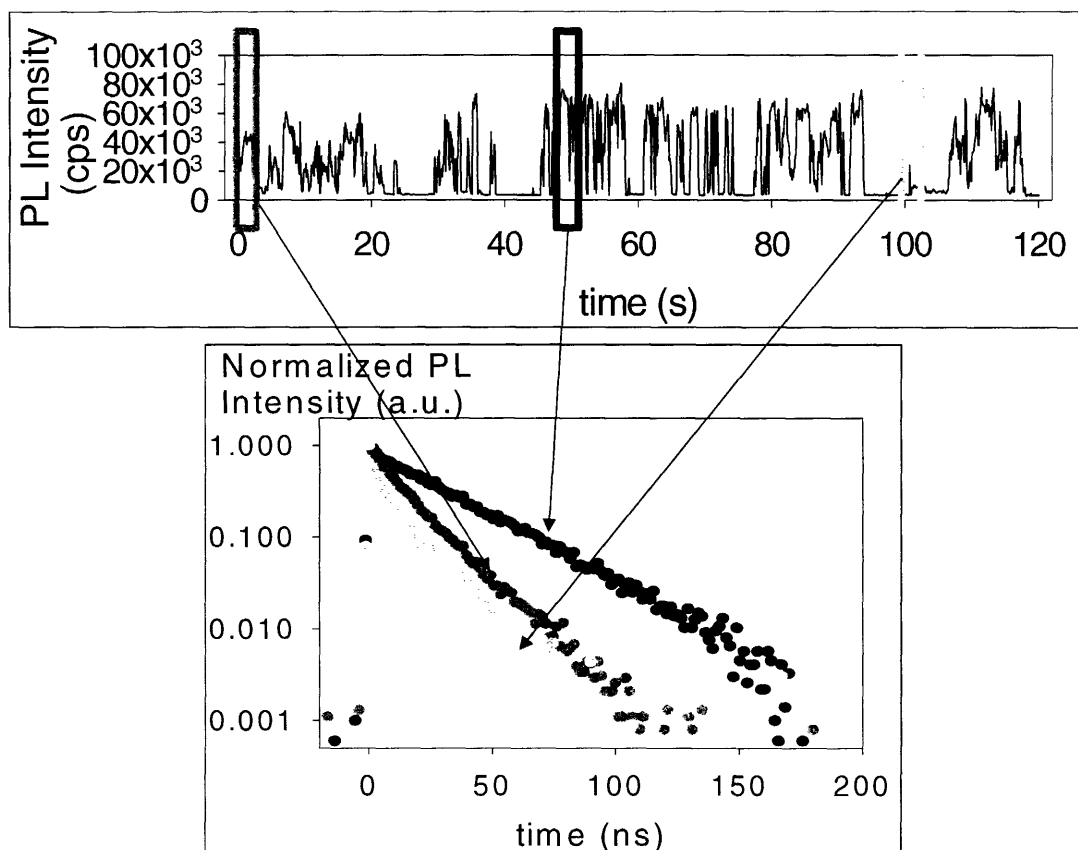


Figure 3.6 *Top:* emission intensity trajectory for the data in figure 3.5. *Bottom:* three different PL decays result from photons collected during three different brief periods of low (light gray), medium (dark gray), and high (black) emission intensities of the trajectory.

However, carrier trapping into NC surface states usually occurs on sub-nanosecond time scales and strongly quenches any NC that has such traps. Thus any fluorescence that we observe must originate from the population of NCs that do not have any strong traps on the CdSe surface. The ZnS overcoating of our samples passivates these immediate ultrafast surface traps on the core CdSe NC. For these reasons, the relaxation mechanism associated

with the variable non-radiative rates we observe probably does not involve carrier traps on the CdSe surface.

Trapping of carriers on the exterior of the ZnS overcoating is an equally unlikely mechanism for the non-radiative pathway. Whereas ultrafast carrier trapping on bare CdSe NCs still yields a neutral NC through deep-trap emission (recombination of surface trapped carriers), any carriers trapped outside of the ZnS shell of our NCs would be quasi-permanently charged, leading to a charged NC. Charged NCs exhibit strong Auger relaxation, which proceeds much faster than the nanosecond time-scale of the non-radiative rates that we observe.

Instead we propose that the physical origin of the fluctuating non-radiative relaxation pathways that we observe may reflect some kind of Coulombic coupling of the exciton to energy acceptor species outside of the ZnS shell. The dynamic variation of the non-radiative pathway indicates that these pathways likely involve the unstable environment of the NC. Lone charges on the ZnS surface or in the organic matrix around the NC represent one possible candidate for the fluctuating energy acceptor pathway involved in the dynamic non-radiative rates. The existence and importance of such charges has been demonstrated in earlier works^{14, 19, 20}.

3.4 Single exponential decays from single nanocrystals

Another way to take advantage of the time-stamp information available from TTTR measurements is shown in figure 3.7 where the collected photons were grouped based on the emission intensity of the single NC for the time bin to which the photons belonged. For each TTTR measurement, an intensity trajectory was generated by grouping photons by their absolute arrival times (t_p) into 100 ms intervals or ‘bins.’ Intensity thresholds were set at

10%, 60% and 90% of the difference between the maximum and minimum emission intensities, $I_{thresh} = I_{min} + \frac{\%}{100}(I_{max} - I_{min})$. All photons were then categorized according to the emission intensity range of their time bin. Separate single photon counting PL decay histograms were generated for each intensity range as shown in the bottom of figure 3.7. The PL decays generated by photons from bins with emission intensity $> 90\%$ are referred to as “maximum-intensity” PL decays, in contrast to the time-averaged PL decays shown in figure 3.4 which counted all of the photons. The results presented in figure 3.7 confirm the

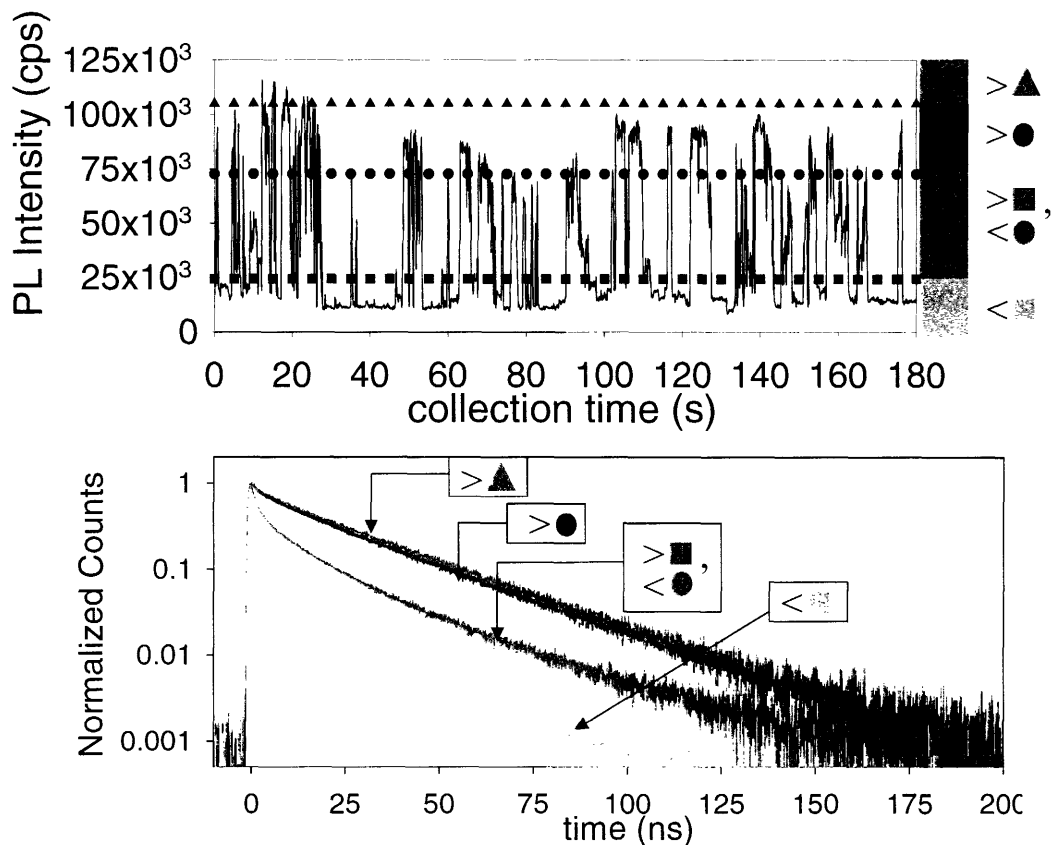


Figure 3.7 *Top*: emission intensity trajectory from single NC with four intensity ranges defined by the three threshold levels of 10% (■), 60%(●), and 90% (▲). *Bottom*: PL decay curves generated by using only photons from time bins of 2d whose emission intensity falls one of the four ranges shown. For instance the black PL decay is generated only by photons from bins whose average emission intensity was above the 60% line (●) in the top panel.

conclusions suggested by figure 3.6. Besides having longer time constants, the maximum-intensity PL decays are also nearly single-exponential.

Fitting the maximum-intensity PL decays to a stretched exponential decay model,

$$y(t) = c + a \cdot \exp\left(-\left(\frac{t}{\tau}\right)^\beta\right) \quad (3.1)$$

quantifies, through the parameter β , how closely the maximum-intensity PL decay approaches single-exponential kinetics. Pure single exponential behavior has $\beta=1$, whereas smaller β values reflect a distribution of decay rates leading to greater multiexponential

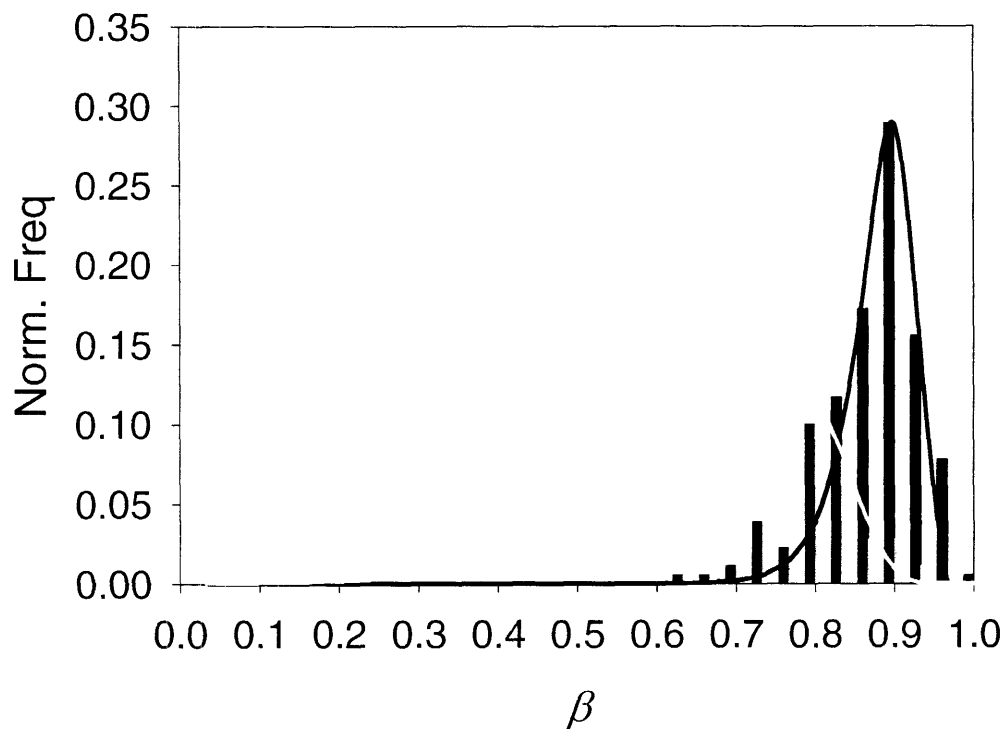


Figure 3.8 Distribution of stretched exponential (equation 1) β parameters when fitting the maximum-intensity PL decay (black) and to the time averaged PL decay (gray). The average β value for the maximum-intensity PL decays was 0.90, whereas the average β for the corresponding time averaged PL decays was 0.75. Log-normal fits to these two β distributions are superimposed for comparison.

character²¹. The results of fitting PL decays to stretched exponentials are shown in figure 3.8 where the distribution of β values over 180 selected single NC measurements is displayed for

the maximum-intensity PL decays (black) versus the time-averaged PL decays (gray). The distributions shown here were fitted to a log-normal distribution.

The distribution of β values shown in figure 3.8 quantitatively demonstrates the degree to which the maximum-intensity PL decay approaches single-exponential behavior, in contrast to the time-averaged, standard TCSPC measurement generated from the same TTTR measurements. Over 90% of the maximum-intensity PL decays have stretched exponential β parameters greater than 0.8 while more than 70% of the time-averaged PL decays have $\beta < 0.8$.

The hypothesis that k_{nr} for the single NC is fluctuating between various values is supported by the fact that whereas the maximum-intensity PL decay is nearly single exponential, PL decays generated from a narrow range of medium intensity data over the entire TTTR measurement are invariably multiexponential. On the other hand, if data from the same medium intensity range but limited to a short time span (e.g. a few seconds) is used to generate the PL decay, nearly single exponential character (with a shorter lifetime) can again be recovered. An instance of this can be seen by comparing the medium intensity PL decay of figure 3.7 (integrated over entire TTTR measurement) against the more single-exponential medium intensity PL decays shown in figure 3.6 (data taken from only a few seconds of the TTTR measurement).

The appearance of single-exponential character for maximum-intensity PL decays reveals an intrinsic property of the NC core that is independent of its surface cap or local environment – factors that can dominate many other single NC measurements. Single-exponential kinetics result from a single rate constant, $k = k_r + k_{nr}$, where k_r is the rate of radiative transition and k_{nr} is the sum of all (varying) non-radiative rates. Given the

fluctuating environment of the QY, it is unlikely that the same non-radiative pathway (i.e. same k_{nr}) will be repeatedly visited by many different NCs during all periods of high emission intensity during a collection period of two or three minutes. It is more probable that the single-exponential decay measured from the maximum intensity photons is dominated by k_r , the radiative lifetime of the single NC. That is, $k_{max} \sim k_r$ (max = maximum-intensity) for a single NC.

3.5 Uniformity of maximum-intensity PL decays

The hypothesis that the maximum-intensity PL decay measures the room temperature radiative lifetime (τ_r) for the NC is supported by the robustness of the measured lifetime value when fit to a single exponential. Figure 3.9 shows the distribution of single exponential fits to the maximum-intensity PL decays for the three different samples used. The mean maximum-intensity lifetimes for samples 1, 2 and 3 were 26.5 ns, 24.6 ns, and 24.6 ns respectively. The inset to figure 3.9 shows the overall distribution of lifetimes for all NCs considered. The mean maximum-intensity lifetime for these 122 NCs was 25.0 ns. The $1/e$ lifetime for time-averaged PL decays was much shorter and less consistent.

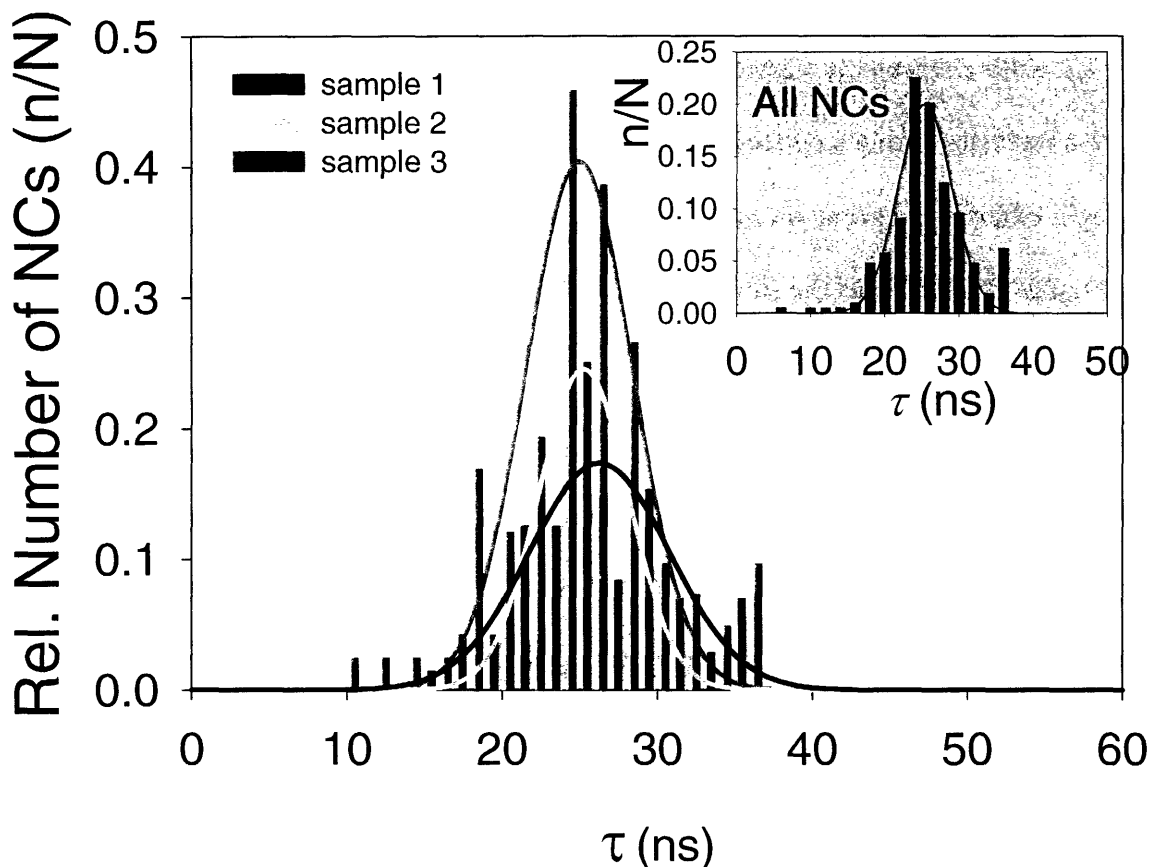


Figure 3.9 Normalized distribution of single exponential lifetime (τ) values from NCs with stretched exponential $\beta > 0.85$ for each of the three samples along with fits to the normal distribution. The mean lifetimes for samples 1 (gray), 2 (dark gray) and 3 (black) were 26.5 ns, 24.6 ns, and 24.6 ns respectively. *Inset:* the normalized distribution for all of the NCs taken together along with a Gaussian fit. The overall mean lifetime is 25.0ns.

These data show that the value of the maximum-intensity lifetime is practically uniform across all NCs, even those originating from different samples and syntheses. Furthermore, the percent standard deviation of maximum-intensity lifetimes about the mean is much less than the percent standard deviation of the corresponding $1/e$ times for time-averaged PL decays taken from the same NCs.

The uniform results obtained for maximum intensity PL decays contrast starkly with the wide variety of results obtained from time-averaged TCSCP measurement of single NC lifetimes. Figure 3.10 shows two pair of PL decays. Each pair represents two successive

measurements on the same NC. The left panel shows two successive maximum-intensity PL decays, while the right panel shows the pair of time-averaged PL decays taken from the same TTTR measurements.

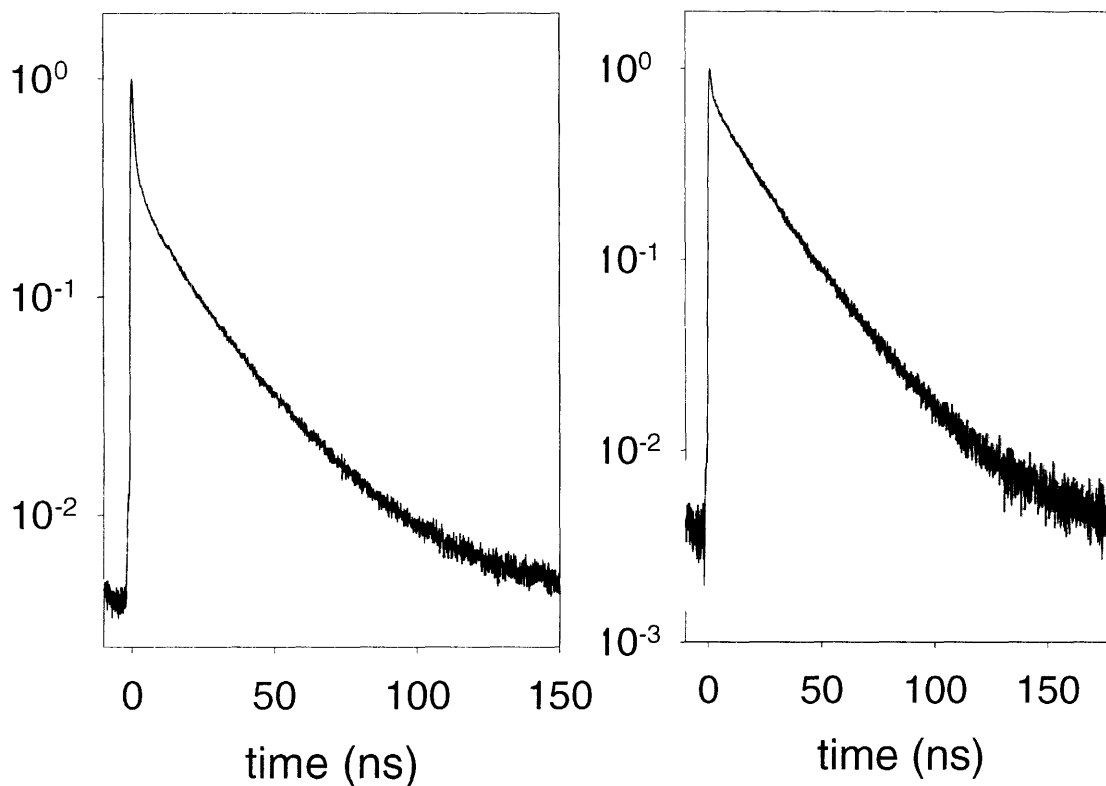


Figure 3.10 Two consecutive PL decay measurements from the same NC. *Left:* the time-averaged PL decays for these same measurements. *Right:* the maximum-intensity PL decays for the two consecutive measurements are shown.

By focusing only on photons emitted during time bins of maximum emission intensity we obtained reproducible decay rates from a single NC, unlike the unstable results of time-averaged PL decays. This is consistent with the idea that the maximum-intensity PL decay represents purely radiative relaxation. We expect the radiative lifetime to remain essentially

constant from measurement to measurement, whereas the time-averaged PL decay integrates all of the varying, environmentally influenced non-radiative components of the lifetime, making it less reproducible in sequential measurements. While the arguments above support our speculation that it is the radiative lifetime that is being measured, a direct measurement of the QY at the single NC level is required to absolutely confirm our hypothesis. Such a measurement was recently reported²² and supports to our hypothesis that the on-state of a NC emits fluorescence with a quantum yield of 100%.

3.6 Quantum yield fluctuations and blinking in single nanocrystals

The observed emission intensity dependence of single NC lifetimes coupled with the hypothesis that the maximum-intensity lifetime approaches a constant value (k_{max}^{-1}) with single-exponential character leads to an important modification of our understanding of the emission-intensity trajectories observed from single NCs: the intensity trajectory is determined not by digital intermittency alone, but also by a fluctuating QY of the on-state. At the beginning of this study the predominant hypothesis stated that fluorescence intermittency or blinking completely determines *all* fluctuations in the intensity trajectory of a single NC (discounting shot noise). Numerous studies^{2, 3, 23, 24} have helped establish a model mechanism for this blinking wherein a NC switches between on and off states via charging events. Charging events turn the NC from on to off (off to on) by opening (closing) highly efficient Auger non-radiative recombination channels. Because the Auger recombination channel has a rate that is orders of magnitude faster than competing processes²⁵⁻²⁷, digital behavior is predicted – either the dot is on with some constant intensity,

or it is completely off²³. Deviations from perfectly digital behavior have usually been attributed to insufficient time resolution of the measurement.

Since the time scale of intermittency has been shown to span up to five decades in time with event times extending down to 10ms or less²⁴, it is difficult to rule out insufficient time resolution as a source of medium intensity data points in the intensity trajectory. We explored the possibility that the intermediate PL decays observed for medium intensity events could result from fast blinking, and that its PL decay would be given by a simple superposition of long lifetime and short lifetime weighted by the amount of time the dot was on and off during each bin. We found that the actual PL decay that was observed for medium

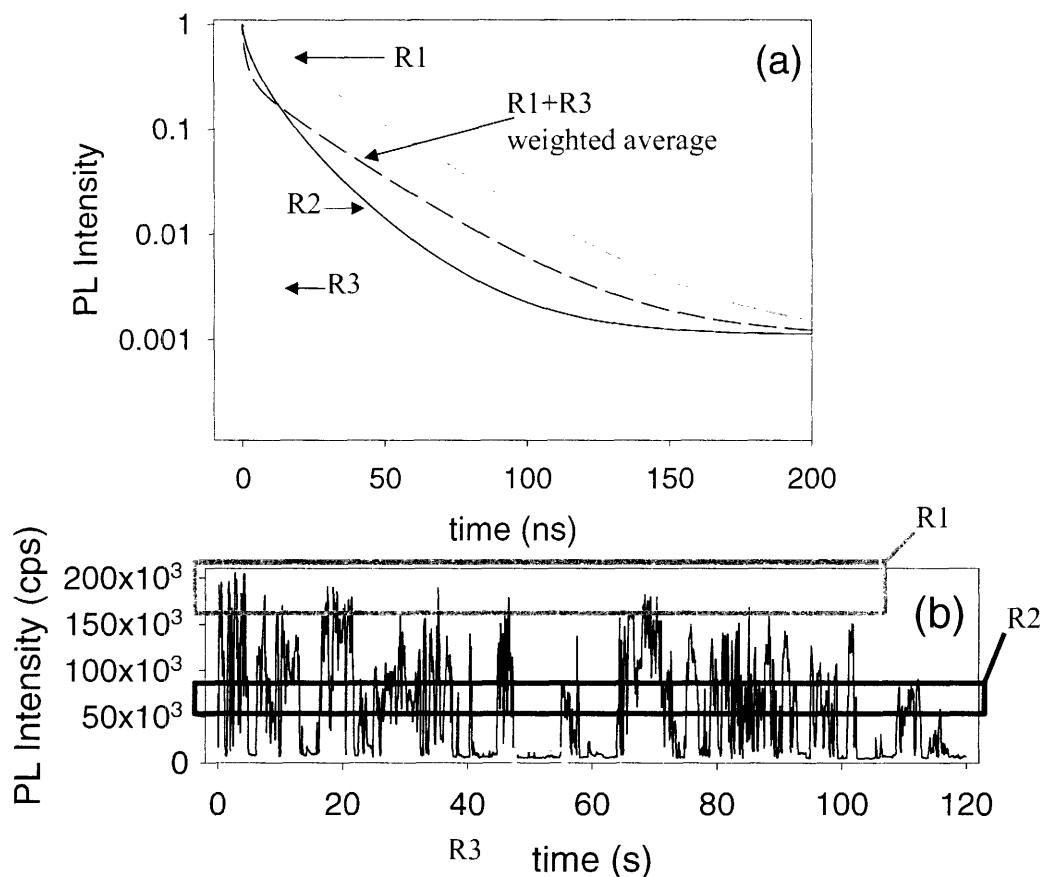


Figure 3.11 The weighted average (dashed line) of maximum-intensity (R1) and off-time (R3) PL decays does not reproduce the medium-intensity PL decay that is measured (R2).

intensity events almost never matched the result of simply calculating the weighted average of maximum-intensity and off-time PL decays. This result is illustrated in figure 3.11.

Moreover, since the maximum intensity lifetime tends to be constant and single exponential, perfectly digital blinking of the NC should lead to a perfect equivalence between the time-averaged PL decay and the maximum intensity PL decay (i.e. either the NC is “on” with the maximum intensity PL decay lifetime or it is “off” and contributing no signal to the lifetime). This is also not observed. Therefore we are convinced that, while fast blinking probably still causes some artificially low intensity data points in the intensity trajectory, fluctuations in the non-radiative relaxation rate dominate medium intensity fluctuations in a single NC emission intensity trajectory.

Changes in k_{nr} imply that the “instantaneous QY” (i.e. the instantaneous probability of radiative rather than non-radiative relaxation) is fluctuating as well. We can relate the fluctuating PL decays to the fluctuating instantaneous QY through the integrated area beneath the intensity normalized PL decay curve, A_N . As discussed in chapter 8, A_N is a generalization of the single exponential decay constant, τ , for cases of multiexponential decays: $Q = k_r \cdot \tau \rightarrow Q = k_r \cdot A_N$. This relationship is based on the definition of QY as the number of photons emitted (n_e) per number of photons absorbed (n_a), that is $QY = n_e/n_a$. Since the number n_e is directly proportional to the area beneath the normalized PL decay curve, it follows that the QY is directly proportional to this PL decay area, assuming constant n_a , collection efficiency, etc.

Figure 3.12 plots the integrated area beneath the intensity normalized PL decay curves for a single NC as a function of its emission intensity. The error bars display the emission intensity range of the bins used. These ranges were defined for this figure by

thresholds of 10, 40, 60, and 90 percent. The symbols (●) in the plot represent the average intensity for that range. A linear relationship as in figure 3.12, explicitly showing the correlation between emission intensity and instantaneous QY, is found for practically all of the individual NCs observed. We conclude that the intensity trajectory observed for a single NC is dictated not only by purely digital intermittency between charged and uncharged states, but also by a fluctuating QY of the emitting state

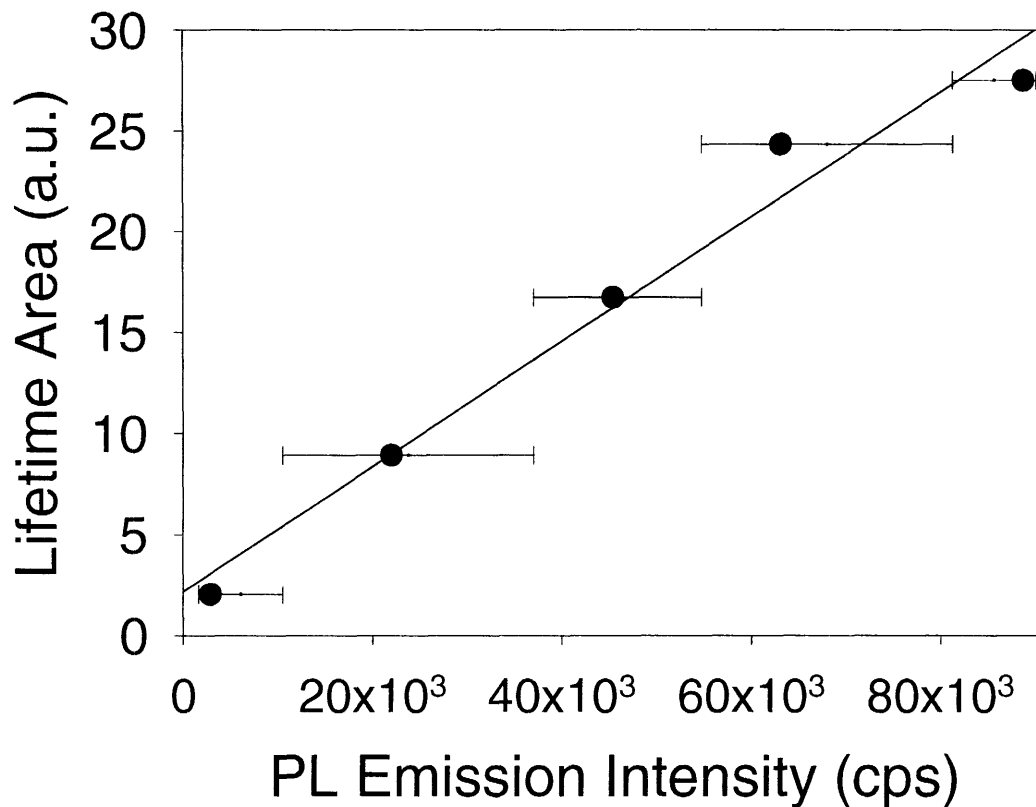


Figure 3.12 The average emission intensity for a particular intensity range of the trajectory is compared to the area beneath the normalized PL decay curve that is generated by photons from bins whose intensity falls in that range. The error bars indicate the range of emission intensity values for the photons used to generate the PL decay whose area is calculated. The linear relationship between emission intensity and PL decay area indicates that the variations of emission intensity can be attributed to QY fluctuations.

3.7 Size Dependence of Nanocrystal Lifetimes

The three samples covered in the preceding experiments were all of similar size (3.1-3.3nm), but it is also of interest to understand how the lifetime of CdSe NCs may vary with the size of the NCs. The dependence of lifetime on size is difficult to qualitatively predict because various known size dependent effects can influence the lifetime in different ways. For instance, as the size of the NC is reduced, the band-edge fine structure splitting energies increase due to the exchange interaction so that the optically inactive $N = \pm 2$ state is more isolated from the optically active $N = \pm 1$ state. A longer lifetime should result from this. In addition, as the NC size decreases, the overall oscillator strength of the NC decreases since there are simply fewer atoms and hence a lower overall absorptive cross section. This could also increase the lifetime. On the other hand, as the NC size is decreased, confinement increases leading to greater overlap of the electron-hole pair, and more concentration of oscillator strength in the band-edge transition. This would also lead to a shorter lifetime. Clearly, without a quantitative approach, it is practically impossible to theoretically predict with certainty the effect of size on lifetime. An experimental approach is of interest.

Having developed a method of stripping away the effects of fluctuations to reveal an intrinsic lifetime (maximum intensity lifetime), we performed a study of the lifetimes of NCs that were smaller than those in our previous studies in order to reveal any strong effects of NC size on single NC lifetime at room temperature. The sample of small NCs were prepared using the same methods as the previous larger samples¹⁷ and were overcoated¹⁸ with ZnS, but had a core radius of 1.9nm corresponding to band edge absorption of 543nm. We measured the maximum-intensity lifetime from approximately 30 NCs from this sample and fit the lifetimes to a stretched exponential. As with the larger samples, the maximum-

intensity lifetimes approached single exponential behavior with beta parameters averaging about 0.93. The distribution of measured lifetimes is given in figure 3.13 for these smaller NCs.

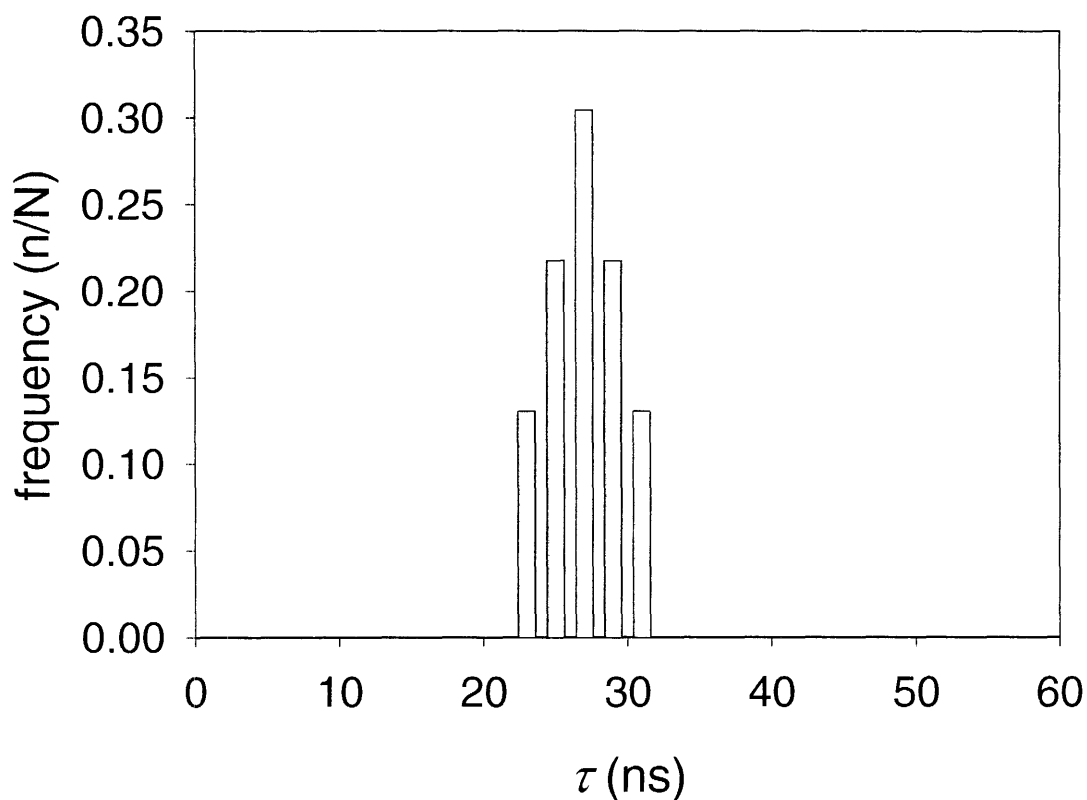


Figure 3.13 Distribution of lifetimes from measurements of single NCs with mean radius of 1.9nm.

The average lifetime value measured from these small NCs was 27ns with a standard deviation of about 3.6ns. These results are very similar to the results obtained for larger NCs, indicating that the size dependence of lifetime at room temperature is practically negligible within this range of sizes. Although our measurements were done at room temperature, leading to an “effective lifetime” for the thermalized manifold of band-edge states, the relative insensitivity of our lifetime measurements to NC size agrees with the results of a low-temperature study (isolating the lowest band-edge fine structure states) of

lifetimes of single CdSe NCs²⁸. These results lead us to conclude that, while the lifetime of CdSe NCs does differ significantly from the exciton lifetime of bulk CdSe, within the quantum confinement regime, the lifetime of CdSe NCs is relatively size insensitive.

3.8 Conclusions

We have presented data that demonstrate the emission intensity dependence of PL decay measurements from single colloidal NCs. We have seen that the maximum-intensity PL decays approach single-exponential behavior, and their lifetimes are nearly constant from NC to NC and even from sample to sample. These observations lead us to speculate on the possibility that the maximum-intensity lifetime is actually the radiative lifetime. Furthermore, these results highlight the important role that QY fluctuations play in determining the emission intensity trajectory of single NCs.

3.9 References

- ¹ S. A. Empedocles, D. J. Norris, and M. G. Bawendi, *Physical Review Letters* **77**, 3873 (1996).
- ² M. Kuno, D. P. Fromm, H. F. Hafmann, et al., *Journal of Chemical Physics* **112**, 3117 (2000).
- ³ K. T. Shimizu, R. G. Neuhauser, C. A. Leatherdale, et al., *Physical Review B* **63**, 205316 (2001).
- ⁴ S. A. Empedocles and M. G. Bawendi, *Journal of Physical Chemistry B* **103**, 1826 (1999).
- ⁵ M. G. Bawendi, P. J. Carroll, W. L. Wilson, et al., *Journal of Chemical Physics* **96**, 946 (1991).
- ⁶ K. H. Hellwege, *Landolt-Bornstein Numerical Data and Functional Relationships in Science and Technology* (Springer-Verlag, Berlin, 1982).
- ⁷ J. Erland, B. S. Razbirin, K.-H. Pantke, et al., *Physical Review B* **47**, 3582 (1993).
- ⁸ G. Bacher, R. Weigand, J. Seufert, et al., *Physical Review Letters* **83**, 4417 (1999).
- ⁹ M. K. Kuno, in *Chemistry* (Massachusetts Institute of Technology, Cambridge, 1998), p. 386.
- ¹⁰ M. Nirmal, D. J. Norris, M. Kuno, et al., *Physical Review Letters* **75**, 3728 (1995).

- 11 G. Schlegel, J. Bohnenberger, I. Potapova, et al., *Physical Review Letters* **88**, 137401
(2002).
- 12 L. Edman, Ulo, M., Rigler, R., *Proceedings of the National Academy of Science,*
USA **93**, 6710 (1996).
- 13 E. A. Geva, Skinner, J. L., *Chemical Physics Letters* **288**, 225 (1998).
- 14 R. G. Neuhauser, K. T. Shimizu, W. K. Woo, et al., *Physical Review Letters* **85**, 3301
(2000).
- 15 Y. Ebenstein, Mokari, T., Banin, U., *Applied Physics Letters* **80**, 4033 (2002).
- 16 M. G. Bawendi and N. E. Stott, (Massachusetts Institute of Technology (Cambridge,
MA), U.S., 2000).
- 17 B. R. Fisher, H. J. Eisler, N. E. Stott, et al., *Journal of Physical Chemistry B* **108**, 143
(2004).
- 18 B. O. Dabbousi, J. Rodriguez-Viejo, F. V. Mikulec, et al., *Journal of Physical*
Chemistry B **101**, 9463 (1997).
- 19 S. A. Empedocles, R. G. Neuhauser, K. T. Shimizu, et al., *Advanced Materials* **11**,
1243 (1999).
- 20 S. A. Empedocles, *Science* **278**, 2114 (1997).
- 21 C. P. Lindsey, Patterson, G.D., *Journal of Chemical Physics* **73**, 3348 (1980).
- 22 X. Brokmann, L. Coolen, M. Dahan, et al., *Physical Review Letters* **93**, 107403
(2004).
- 23 A. L. Efros, *Physical Review Letters* **78**, 1110 (1997).
- 24 M. Kuno, D. P. Fromm, H. F. Hafmann, et al., *Journal of Chemical Physics* **115**, 1028
(2001).
- 25 V. I. Klimov and D. W. McBranch, *Physical Review B* **55**, 13173 (1997).
- 26 V. I. Klimov, *Journal of Physical Chemistry B* **104**, 6112 (2000).
- 27 A. L. Efros, in *Archives* (Naval Research Laboratory, 2002).
- 28 O. Labeau, P. Tamarat, and B. Lounis, *Physical Review Letters* **90**, 257404 (2003).

Chapter 4: Multiexciton Emission from CdSe Nanocrystals

- 4.1 Introduction
- 4.2 Methods
- 4.3 Transient Spectra of CdSe Nanocrystals at Room Temperature
- 4.4 Assignment of Biexciton and Triexciton
- 4.5 Multiexciton Lifetimes
- 4.6 Quantum Yield of Multiexciton States
- 4.6 Multiexciton Emission from CdSe Nanocrystals at Low Temperature
- 4.7 Conclusions
- 4.8 Addendum: Poisson Statistics for Probability of Multiexciton Generation
- 4.9 References

4.1 Introduction

Over the past decade, multiexciton states in semiconductor quantum dots (QDs) have attracted the attention of many investigators. The discrete QD energy levels and the three dimensional quantum confinement of multiple carriers have been exploited, in epitaxially grown quantum dots, to produce strongly correlated photon pairs¹, nonclassical optical field states² or to demonstrate the optical entanglement of excitons³ in a NC.

As mentioned in chapter 1 colloidal semiconductor nanocrystals (NCs) are related to QDs but are distinct. Instead of vacuum deposition techniques, NCs are synthesized by wet chemical methods in organic colloidal suspensions with good size and shape control. NCs are typically smaller and more spherically symmetric than QDs, which can lead to stronger carrier confinement. Unlike in epitaxial QDs, fast non-radiative processes dominate multiexciton relaxation in strongly confined colloidal NCs. The Coulomb mediated Auger mechanism^{4,5} has been proposed as the main non-radiative pathway for multiple carrier relaxation. In particular, for CdSe NCs, high-resolution time resolved

experiments show that multiexciton dynamics depend strongly on the NC radius⁴. For instance, reducing the radius of spherical CdSe NCs from 4.2 to 2.3 nm decreases the biexciton Auger relaxation time by a factor of 8, from 360 ps to 42 ps.

Despite strong Auger relaxation in NCs, two recent reports have shown multiexciton photoluminescence (PL) from ensembles of CdSe NCs using transient detection techniques^{6,7}. In the work of reference 7 an ultra-fast photoluminescence (PL) upconversion technique was used to detect multiexcitonic emission in CdSe colloidal NCs, and a charged biexciton model was introduced to explain the observed higher energy multiexcitonic band at high excitation power. In this chapter and previous work⁶ we also detect such a multiexcitonic band from overcoated colloidal CdSe/ZnS core/shell NCs. Measurement of the power dependence and energy splitting of the multiexcitonic band strongly suggest that it originates from a 3 electron-hole ($e-h$) pair recombination.

In this chapter we present room temperature data from solution phase samples, which allows us to extract fundamental properties of the multiexciton transitions including radiative lifetimes, quantum yields, and energy splittings. In addition, we present a study of multiexciton emission from one sample at cryogenic temperatures. These low temperature data provide additional insight into the nature of the multiexciton transition in CdSe nanocrystals.

4.2 Methods

We used high quantum yield (QY, 30%-80%) CdSe(CdZnS) core(shell) NCs of various sizes (2.5nm - 5nm, core radius) obtained from Quantum Dot Corp. (QDC), (Catalog No.1002-1) or synthesized using methods developed in our laboratory⁸ and

surface passivated by an epitaxial ZnS shell using well-established overcoating procedures^{9,10}. Rod shaped, one-dimensional nanocrystals (nanorods) of aspect ratio 5:1 were synthesized in our lab using procedures adapted from a previously reported direct one-pot synthesis¹¹ with n-tetradecylphosphonic acid and cadmium oxide (99.99%). These were overcoated using procedures analogous to those used for the spherical nanocrystals^{9,10}.

For measurement of transient spectra of room temperature solutions of NC we dispersed NCs into hexane at low concentration in a 1 mm path length quartz cuvette. The NCs were excited by a frequency-doubled regeneratively amplified titanium–sapphire laser, delivering 100 fs pulses at 400 nm with a repetition rate of 1 kHz. Within our pump fluence, up to 10 *e-h* pairs could be generated in a NC on average. The mean number of *e-h* pairs (\bar{n}) generated in a NC by a pulsed laser with repetition rate, *f*, and average power, *P*, is: $\bar{n} = \frac{P \cdot f}{hc \cdot \lambda} \cdot \frac{\sigma}{A} \equiv \alpha P$, where *h*, *c*, λ , σ , and *A* are Planck's constant, the speed of light, the excitation wavelength, the absorptive cross-section, and the cross-sectional area of the excitation beam, respectively. The room temperature PL was collected with a 5 cm focal length lens, dispersed with a 100 grooves/mm grating and directly detected with a streak camera. The time resolution of the detection setup was 18 ps for the shortest experimental time range.

Measurements of transient spectra at liquid helium temperatures were carried out on ensembles of NCs that were dispersed in a thin film polymer matrix by spin coating onto a single crystal quartz substrate. The sample was cooled to liquid helium temperatures (approximately 4.3 K) in a cold finger cryostat and was excited using the frequency doubled, pulse-picked laser emission of a Ti:Sapphire oscillator (400nm,

4.775kHz, 150fs). Although the pulses generated by this laser source would normally be too weak to generate multiexcitons in the nanocrystals, use of a 0.7NA microscope objective to focus the light to a very small (but probably not diffraction limited) point on the sample inside the cryostat allowed us to achieve appreciable multiexciton emission from the samples. For instance, the pulse fluence of just 300 μ W of 400nm light in this experiment was $\sim 200 \mu\text{J}/\text{cm}^2$ at the focus ($\sim 1\text{mm}$ radius spot size), generating on average 7 excitations per NC per pulse (assuming a $1.8 \times 10^{-14} \text{cm}^2$ cross section at 400nm). Transient spectra of emission from the NC film were recorded on an ultrafast gated, intensified CCD (LaVision, PicoStar).

4.3 Transient Spectra of CdSe Nanocrystals at Room Temperature

Figure 4.1(a) shows a three dimensional transient PL spectrum for a 2.3nm radius CdSe NCs sample; 4 $e-h$ pairs are injected into the NCs on average. The PL intensity is coded in a white color, brighter area corresponding to higher PL intensity. Figure 4.1(b) shows PL spectra, extracted from figure 4.1(a), 20ps (black circle) and 800ps (gray circle) after excitation using a 40ps integration window. The transient PL spectra show that, shortly after excitation, a second emission peak is present at higher energy than the usual band edge emission peak. The multiexcitonic origin of the higher energy band is confirmed by its observation only at high excitation intensity. The splitting, Δ , between the two peaks is 0.25eV in figure 4.1(b). Figure 4.1(c) displays the band edge emission spectrum for 2.3 nm radius NCs 20 ps (black circle) and 800 ps (gray circle) after excitation. Since the band edge peak is a mixture of single exciton (X) and biexciton (BX) emission (both $1S_{3/2}-1S_e$ transitions), the observed 20meV positive energy shift

with time is evidence for the negative binding energy of the BX as previously reported⁶.

Transient spectra from larger (5.1 nm radius) NCs at four separate delay values are shown in Figure 4.1(d).

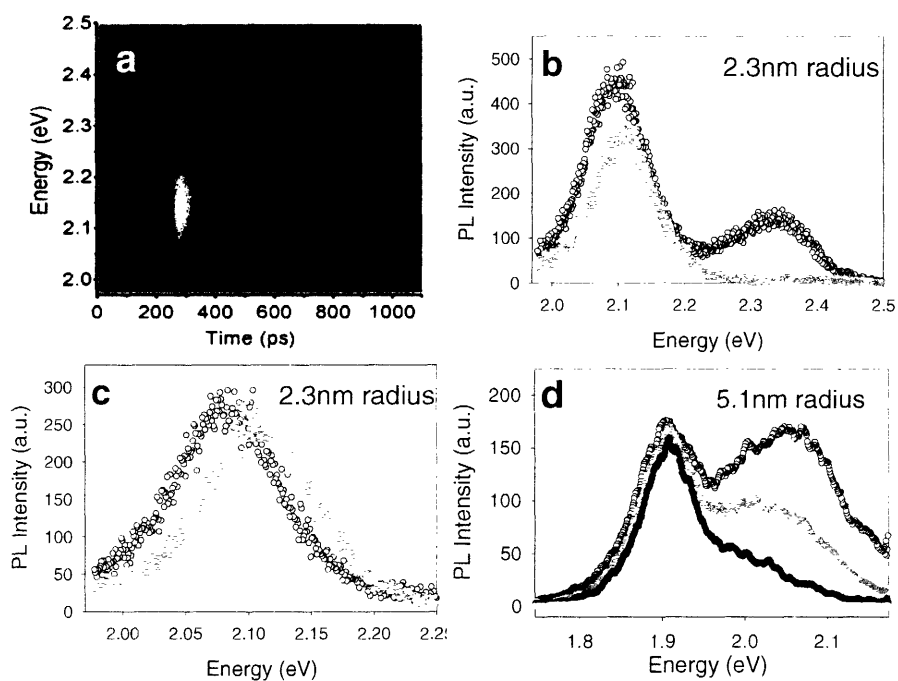


Figure 4.1 (a) 3D transient PL spectrum recorded on a 1.1 ns time window for a 2.3 nm radius NCs sample; the PL intensity is coded in white color; brighter area corresponds to higher PL intensity. (b) transient PL spectra 20 ps (black) and 800 ps (gray) after excitation extracted from Fig. 1(a). (c) 2.3 nm radius NC band edge PL spectra 60 ps (black) and 800 ps (gray) after excitation, the blue shift is due to negative biexciton binding energy. (d) Transient PL spectra of a solution of 5.1 nm NCs taken at various delay ranges: -50–50 ps (black open circles); 50–150 ps (gray open circles); 250–350 ps (black solid circles); 3–4 ns (gray solid circles). Plots (a) through (c) were obtained from previous work⁶.

Increasing the NC's radius from 2.3 nm to 5.1 nm decreases Δ by about a factor of 2, but increased the BX and multiexciton emission intensity. Figure 4.2(a) summarizes the evolution of Δ as a function of the NC size. We note that our samples exhibited band edge Stokes shifts of 10–25 meV, which is consistent with reported non-resonant Stokes

shifts¹². Therefore the observed decrease of Δ with NC size is not caused by a significant variation of the band edge Stokes shift.

4.4 Assignment of Biexciton and Triexciton

To determine the origin of the multiexcitonic band, the size evolution of Δ was first compared with single exciton absorption spectra of CdSe NCs, reported earlier¹³.

Figure 4.2(b) compares Δ (squares) and the position of the $1P_{3/2}-1P_e$ transition (triangles)

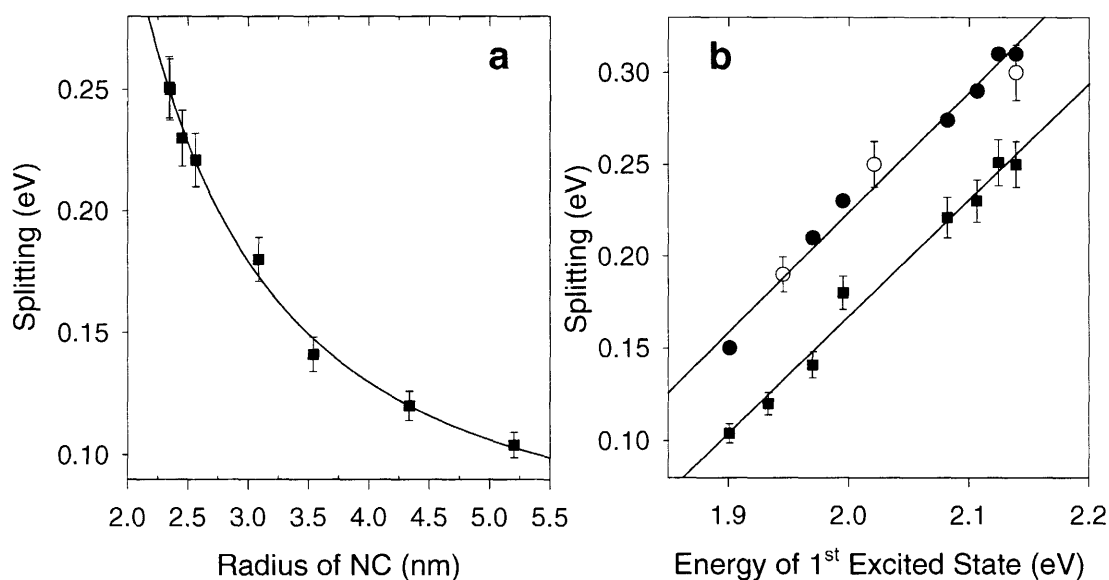


Figure 4.2 (a) Δ versus the NC radius; (b) a comparison between Δ (squares) and the $1P_{3/2}-1P_e$ energy transition (solid circles) relative to the $1S_{3/2}-1S_e$ band edge transition; the notation $1S_{3/2}$, $1P_{3/2}$, $1S_e$ and $1P_e$ of Ref. 20 designates the first two hole and electron levels, respectively; measured $1P_{3/2}-1P_e$ energy position (open circles) for three NC samples at room temperature. These data are taken from earlier work⁶.

relative to the $1S_{3/2}-1S_e$ band edge transition. Since the PLE data in Ref. 14 were obtained at low temperature (10 K), the energy of the first excited state of our NC

samples is used, instead of the NC size, to get the relative energy of the $1P_{3/2}-1P_e$ transition from Ref. 14. By plotting the splitting against the $1S_{3/2}-1S_e$ energy, the temperature dependence of the effective band gap^{14, 15} is built in, and splittings at low temperatures can be compared to splittings at room temperature. For instance, the position of the $1P_{3/2}-1P_e$ transition was measured by performing room temperature linear absorption measurements on three different NC samples (open diamonds in figure 4.2(b)) and obtained a good agreement between the low and room temperature data. Also, the extracted 0.31 eV spacing for the 2.3 nm NCs sample (cf. figure 4.2(b)) is consistent with the room temperature value¹⁶. Within our size range, we obtain an approximately 50 meV energy difference between Δ and the relative position of the $1P_{3/2}-1P_e$ transition.

The $1P_{3/2}-1P_e$ energy transition and Δ track each other closely as shown in figure 4.2(b). This correlation implies that the multiexcitonic band originates from a 3 $e-h$ pair state or triexciton: 2 electrons in the first $1S_e$ electronic state, 2 holes in the first $1S_{3/2}$ state, a third electron in the next $1P_e$ envelope electronic state and a third hole in the $1P_{3/2}$ envelope state. The 50 meV energy offset between Δ and the relative position of the $1P_{3/2}-1P_e$ transition may result from the TX binding energy and a Stokes shift due to the fine structure of the $1P_{3/2}-1P_e$ NC transition, analogous to the non-resonant stokes shift of the $1S_{3/2}-1S_e$ transition.

Analysis of the power dependence of the transient emission bands lent strong support to this hypothesis. Figure 2(c) presents the power dependence of the emission from the X (squares), BX (triangles) and the multiexcitonic (circles) bands in the 2.3 nm radius NC sample, normalized to their intensities at 1 mW excitation power. A Poisson distribution $p(n) = \bar{n}^n e^{-\bar{n}} / n!$ was assumed for the probability of generating a particular

number, n , of e - h pairs by a single, sub-picosecond excitation pulse, where $\bar{n} = \alpha P$ as described above. Justification for the use of a Poisson distribution is given at the end of this chapter (addendum, chapter 4). Since the BX is known to decay much more quickly than a nanosecond, the band edge emission intensity at $t_l \gg 1/\Gamma_2$ ($1/\Gamma_2 \equiv$ BX lifetime) results only from X emission and should follow the Poisson probability of generating more than zero excitons in a single pulse:

$$I_1(P) = C_1(1 - p(0)) = C_1(1 - e^{-\alpha P}) \quad (4.1)$$

Fitting the power dependence of the X emission to this function gave $\alpha = 0.56$ implying a

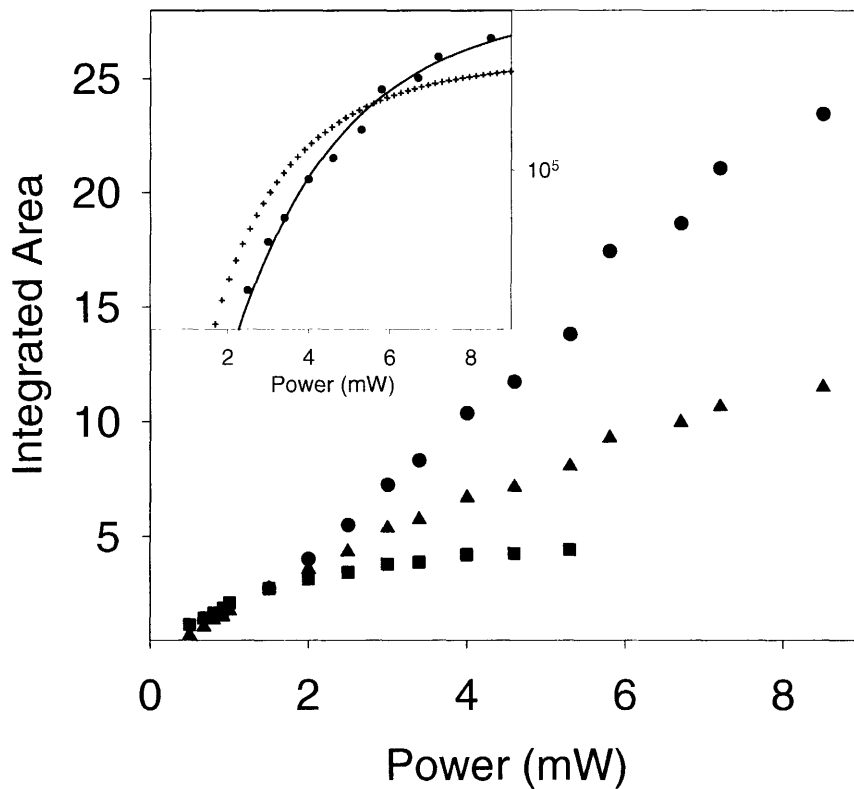


Figure 4.3 Normalized power dependence of the single exciton (squares) biexciton (triangles) and the multiexcitonic band (circles); the 3 different slopes show that the 3 bands originate from 3 different emission processes. (inset) power dependence of multiexcitonic band (circles) and least square fit results using equation (4.2) (crosses) and Eq. (4.3) (solid line), respectively. These data taken from the original work⁶.

cross-section of $6 \times 10^{-15} \text{ cm}^2$ at 400nm for this sample of 2.3nm NCs, in agreement with previous work ¹⁷.

The method for extracting the BX emission from the band edge spectrum was based on solutions of a set of linear differential equations governing decay out of the multiexciton, BX and X states. The time evolution of X decay could then be subtracted from the band-edge spectrum leaving purely BX emission, whose power dependence is shown in figure 4.3(c) (triangles). Details of this procedure are described in the previous work ⁶.

Extracting the power dependence of the multiexciton band, shown in figure 4.3 (circles), was straightforward, since it is spectrally resolved from the band edge. The possibility that the multiexciton emission originates from a *charged biexciton* as reported in one study ⁷ was considered. If this were the case, the power dependence should follow the probability of generating one or more than one exciton in a given pulse,

$$I_2(P) = C_2(1 - p(1) - p(0)) = C_2(1 - (1 + \alpha P) \times e^{-\alpha P}) \quad (4.2)$$

with C_2 as the only fitting parameter. This function was found to fit the power dependence of the multiexciton emission poorly (crosses, inset of figure 4.3). However, by assuming the multiexciton emission originates from a triexciton, according to our hypothesis, the following power dependence is expected,

$$I_3(P) = C_3(1 - p(2) - p(1) - p(0)) = C_3(1 - (1 + \alpha P + \frac{1}{2}(\alpha P)^2) \times e^{-\alpha P}) \quad (4.3),$$

which fits the data almost perfectly, as seen by the solid line of the inset of figure 4.3.

Our analysis of the power dependence and the correlation of Δ to the transition leads us to conclude that the multiexciton band results from 3 *e-h* pair triexciton (TX) recombination. Previously we found this result surprising since the TX's hole was

assumed to relax completely to a band edge state whose envelope had S symmetry – recombination of a 1S hole with a 1P electron is forbidden. We therefore assumed that a combination of thermal population of the 1P hole states at room temperature and relaxed selection rules allowed the TX recombination⁶.

In fact, whether the hole of the TX ends up in a 1S or 1P state after it has relaxed to the band edge depends on how the crystal field splitting energy (Δ_{cf}) compares to the splitting between hole states of 1S and 1P symmetry due to confinement ($\Delta_{hole-conf}$). This is illustrated in figure 4.4.

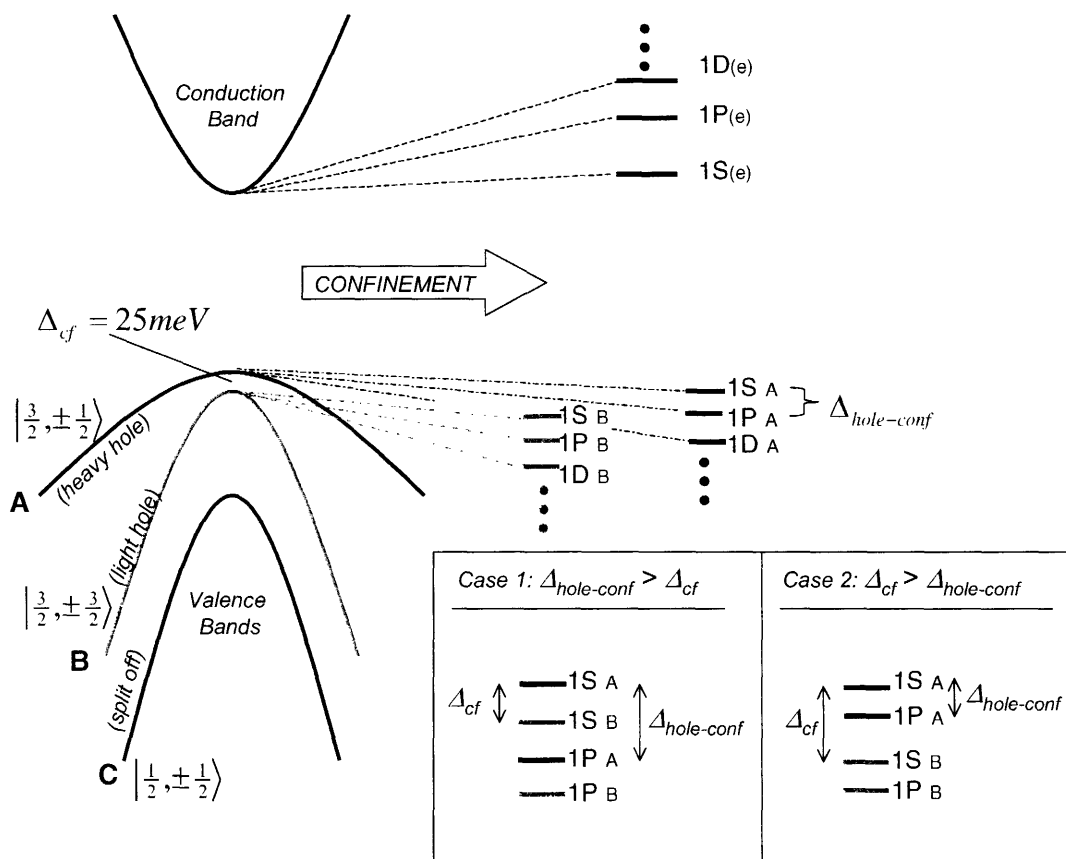


Figure 4.4 Band edge hole states in CdSe nanocrystals. There are three valence bands since they are made up of three-fold degenerate 4p atomic orbitals of Selenium, whereas there is only one conduction band edge because it is made up of 4s orbitals from cadmium. The three valence bands, A, B, and C, are designated by their total angular momentum, J and its projection, M_J : $|J, M_J\rangle$. Spin orbit coupling and crystal field splitting breaks the degeneracy of these bands. *Inset:* the ordering of the lowest energy hole states in a nanocrystal depends on whether the crystal field splitting or the hole confinement energy is dominant. Note that each band (and hence each state) is two-fold spin degenerate.

If the confinement of the hole causes the energy difference between the $1S_h$ and $1P_h$ states to be greater than the crystal field splitting (i.e. $\Delta_{cf} < \Delta_{hole-conf}$), then the lowest energy hole states will be first a two-fold spin degenerate $1S$ state from the heavy hole band followed by another $1S$ state from the light hole. On the other hand, if $\Delta_{cf} > \Delta_{hole-conf}$, then the second highest energy state would be the $1P$ envelope state of the heavy hole band. The bulk Δ_{cf} value is approximately 25meV for CdSe¹⁸. If the confinement energy of the hole is larger than this, then our original assumption should hold and the lowest energy state available to the TX's hole is a $1S$ light hole state whose recombination with its partner $1P$ electron is forbidden. Assuming electron-hole Coulombic interactions do not play a decisive role, this would mean that TX emission should be prohibited at low temperatures. Preliminary results showing weakened TX emission from 2.3nm NC samples at 77K supported this⁶. However, for very large NCs $\Delta_{hole-conf}$ could be smaller than, or at least not much greater than the Δ_{cf} . Hence, the lowest energy envelope state of the TX's hole would have $1P$ symmetry so recombination with the $1P$ electron would be allowed. Indeed, in section 4.7 below we find that TX emission can still be seen from very large NCs, even when cooled to liquid helium temperatures.

4.5 Multiexciton Lifetimes

To further characterize our transient PL data we determined the relaxation time and estimated the quantum yield of each emission band. Figure 4.5 presents the dynamics of the fast decay component, at high power, of the band edge emission peak for 2.3 nm (diamonds), 3.4 nm (circles) and 5.1nm (stars) radius CdSe NCs. The single exciton

lifetime for our solution samples ranged from about 14 to 25 ns, so we assign the fast band edge dynamics, observed on a 1 ns timescale in Fig. 4.5(a), to BX relaxation. After subtracting the “background” X intensity at long times ($t_{long} \gg 1/\Gamma_2$), the measured BX lifetimes, $1/\Gamma_2$, are 50 ps (2.3 nm NC radius), 150 ps (3.4 nm radius NCs), and 790 ps (5.1 nm radius). Figure 4.6 summarizes these times along with previously reported values showing that they are consistent with the linear dependence of the BX Auger decay on volume⁴. Figure 4.7 shows PL decays of the TX in 3.4 nm and 5.1 nm radius samples with 50ps and 230ps relaxation times respectively. The 230ps decay constant was obtained from the slow component of a double-exponential fit, where the fast component likely arises from n -exciton ($n>3$) components.

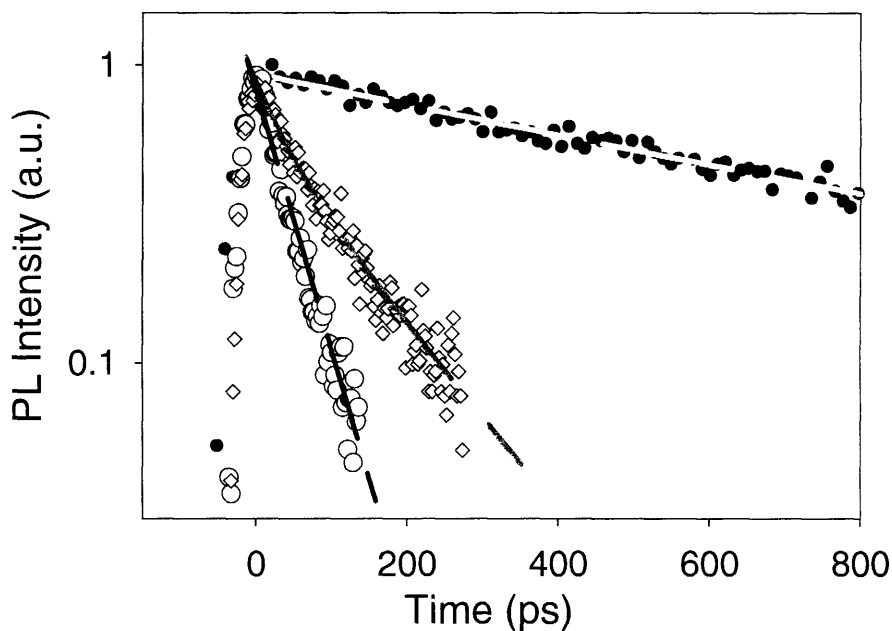


Figure 4.5 Biexciton PL decay curves for solutions of 2.3 nm (open circles), 3.4 nm (open diamonds), and 5.1 nm (solid circles) radius NCs with lifetimes of 50ps, 150ps, and 790ps respectively.

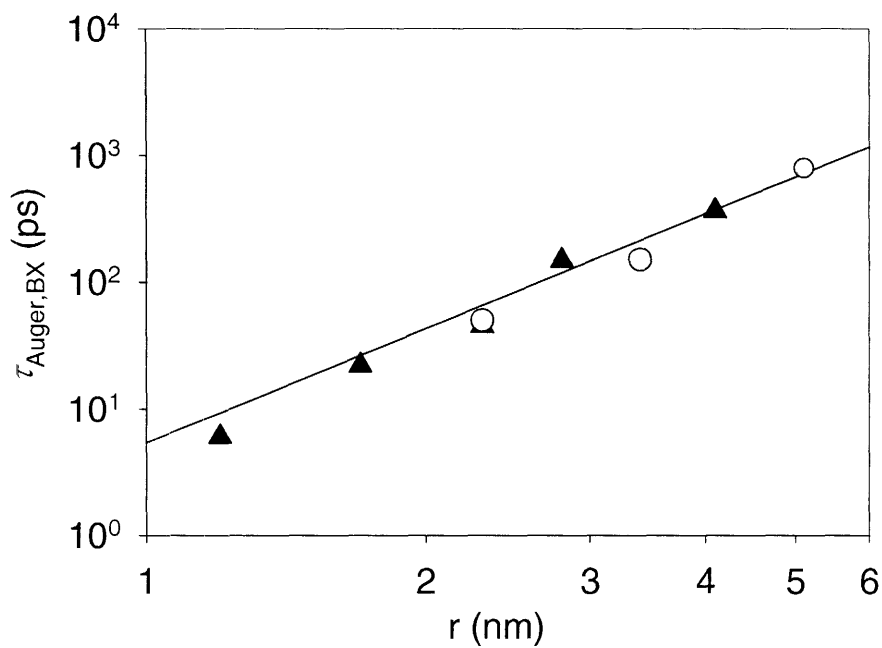


Figure 4.6 Log-Log plot of decay times of the BX emission measured in this work (circles) and in reference 4 (triangles). The linear dependence on volume (r^3) is evident.

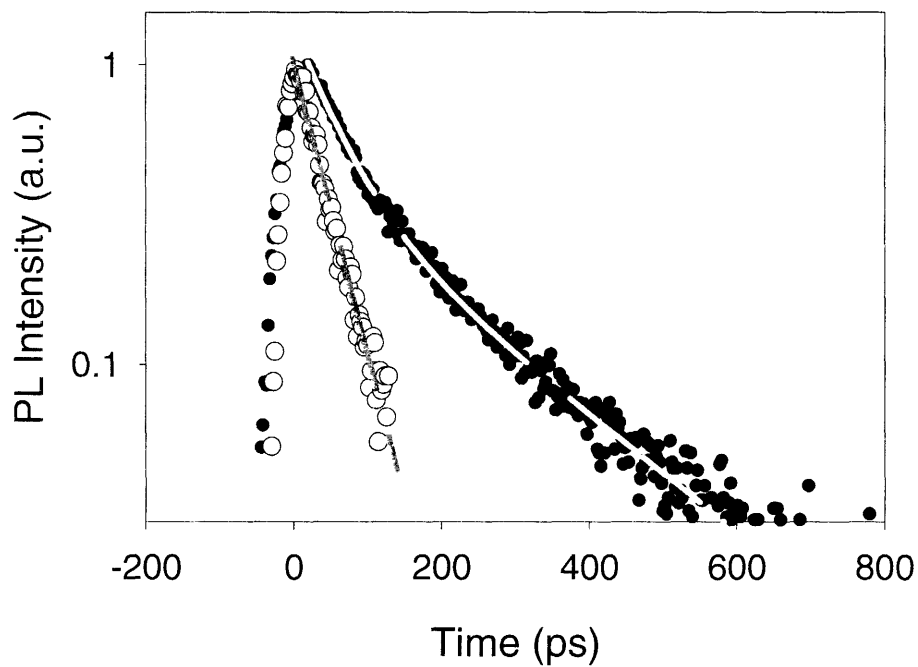


Figure 4.7 PL decay curves of the TX band for 3.4 nm (open circles) and 5.1 nm (solid circles) radius NC samples with lifetimes of 50 ps and 230 ps respectively.

4.6 Quantum Yield of Multiexciton States

Figure 4.8 presents overlaid temporal profiles of both the TX and the band-edge emission bands from the 5.1 nm NC sample, excited at both low and high excitation intensity. The data taken at low power were rescaled such that the band-edge intensity at 4 ns matched for low and high power. By comparing the integrated area of the pure BX decay component to the area of the complete, pure X decay (low-power), we can estimate the QY of the BX (Q_2) relative to that of the X (Q_1) (see chapter 8 for detailed discussion of this technique). To compare QY values we have to take into account the initial excitation probability for one, two and three excitons (p_n^o , $n = 0,1,2,3\dots$), as well as the luminescence bandwidth ($\Delta\lambda$) of each state over which the photons are distributed. A simple equation relates these parameters through the total counts registered for X, BX and TX emission:

$$\frac{A_{BX,TX}}{A_X} \frac{\Delta\lambda_{BX,TX}}{\Delta\lambda_X} = \frac{BX,TX \text{ counts}}{X \text{ counts}} = \frac{Q_{2,3} \times p_{\geq 2,3}^o}{Q_1 \times p_{\geq 1}^o}$$

Solving for the relative QY of the BX we obtain, $q_2 = Q_2/Q_1 = 0.11$. An analogous calculation for the TX yields $q_3 = Q_3/Q_1 = 0.05$. Taken with the single exciton QY of about 0.75 (measured by standard methods, described in chapter 8, using a SPEX fluorometer) and the measured decay rates of the BX and TX, these relative QYs lead to radiative decay times of 8.4 ns and 6.8 ns for the BX and TX respectively.

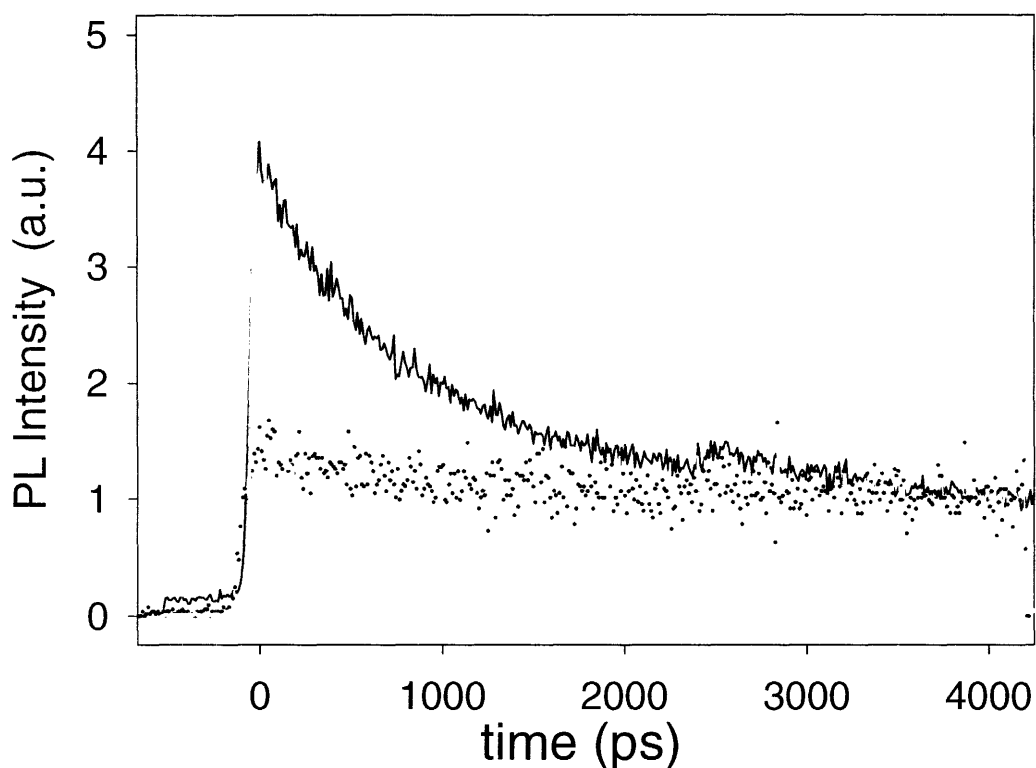


Figure 4.8 PL decays extracted from band-edge and TX regions of transient spectra, 1.87eV-1.92eV and 2.02eV-2.09eV, respectively, at low ($2 \mu\text{J}/\text{cm}^2$) and high ($240 \mu\text{J}/\text{cm}^2$) fluence using 5.1nm NCs. Data are rescaled so that low and high intensity band-edge decays match at 4.2ns.

4.7 Multiexciton Emission from CdSe Nanocrystals at Low Temperature

At the end of section 4.4 we discussed the ambiguity surrounding the reason that TX emission can even be observed at all. Two cases were mentioned. In the first case, the crystal field splitting of the heavy and light holes is less than the confinement energy for holes at the valence band edge meaning that the lowest state available to the TX's hole should be an S state that is forbidden to recombine with the 1P electron of the TX. The second case is the reverse of the first which leads to allowed radiative recombination of the TX. If the first case is true then either some kind of relaxation of the selection rules or thermal population of excited hole states would be required in order to have TX

emission. Precluding relaxation of the selection rules, low temperatures studies should show no TX emission if the first case is true. In this section we show the contrary – TX emission indeed can be observed at cryogenic temperatures (4.3K) from samples of very large CdSe nanocrystals whose hole confinement energy is less than the crystal field splitting energy. These studies provide further insight into the nature of the TX transition.

In figure 4.9 we present a sequence of emission spectra from a film of large NCs at 4.3 K that were taken using 200ps gates on using an ultrafast, gated CCD camera at various post excitation delays. The first three or four transient spectra show a clear blue-

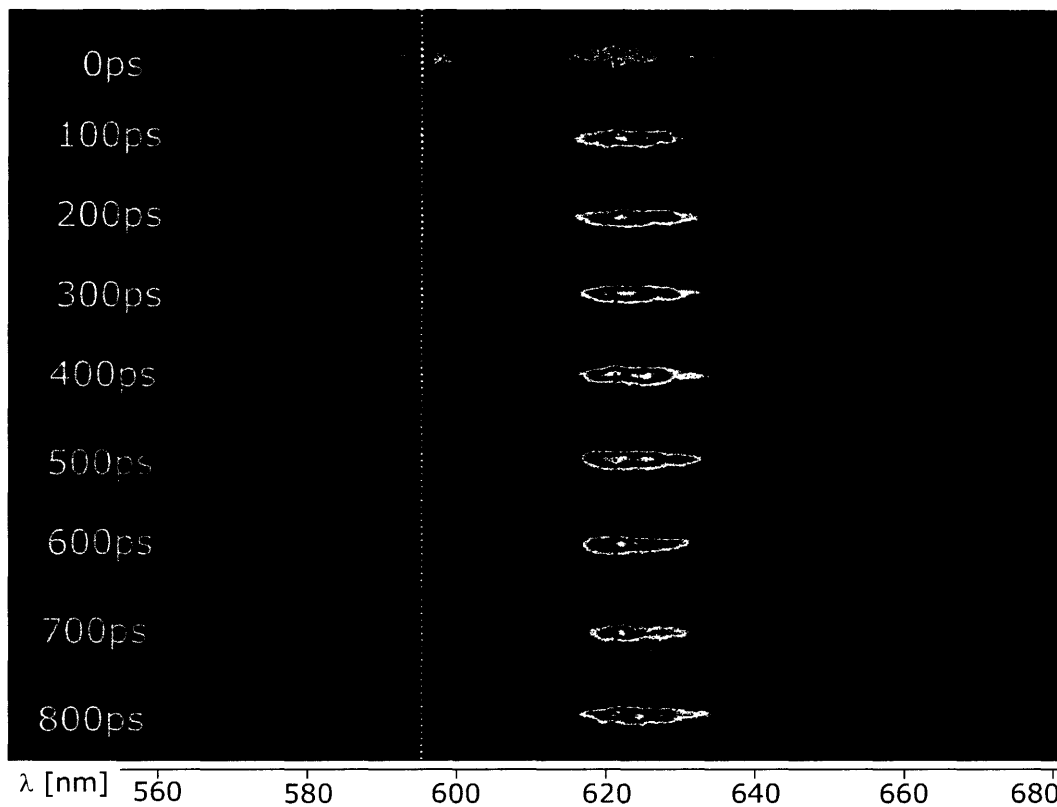


Figure 4.9 Sequential frames of nanocrystal PL spectra taken using an ultrafast gated CCD camera with 200ps gates. 400nm excitation laser pulses were focused onto the sample by a microscope objective and excited the sample with an average power of 182 μW ($115\mu\text{J}/\text{cm}^2$). Each pulse generated about 4 excitons per NC per pulse on average.

shifted emission band from that likely originates from TX emission. By integrating the spatial dimension of the spectra shown in figure 4.9 and then stacking the spectra at progressively longer delay times along the y axis of a color-coded 3D plot, the temporal evolution of the spectrum can be represented on a single plot. The data in such a plot are analogous to streak camera data as in figure 4.1(a). Two plots of this kind are shown in figure 4.10. One was taken from an ensemble film at room temperature and the other at 4.3K.

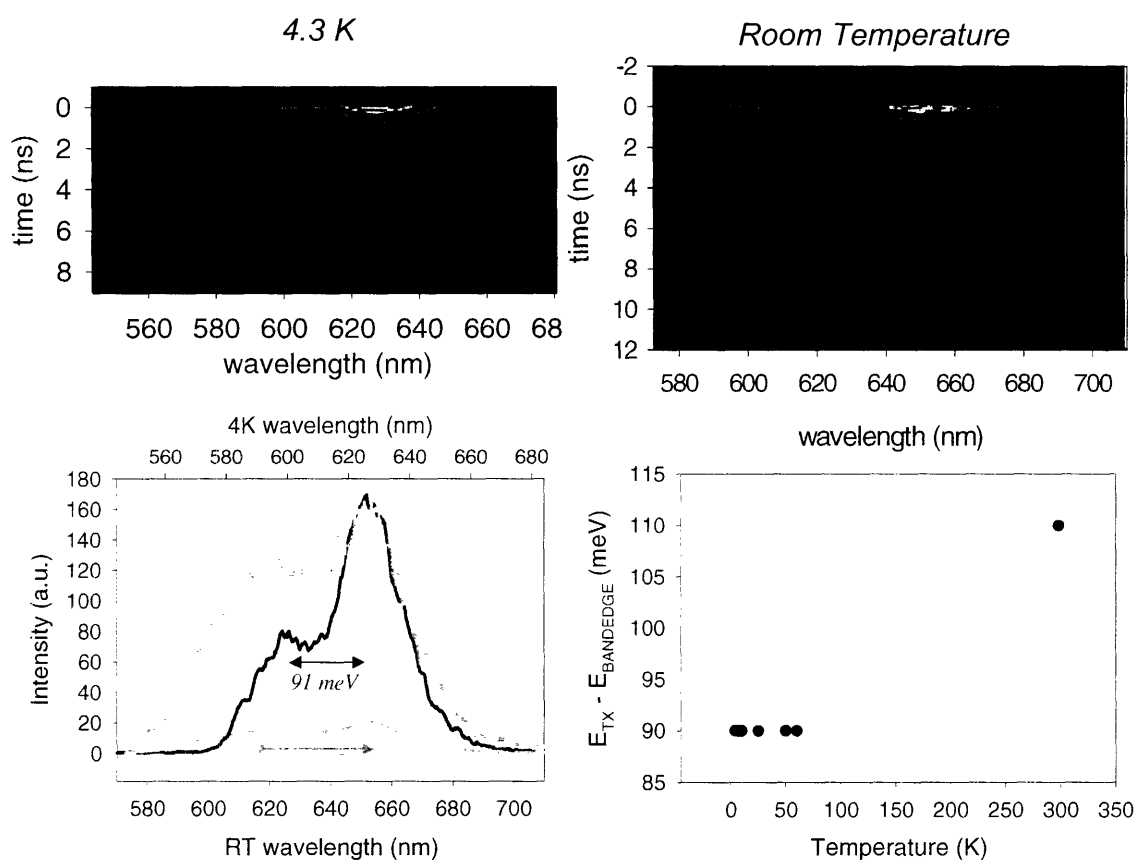


Figure 4.10 *Top*: Transient spectra of CdSe nanocrystal polymer films at room temperature and at liquid helium temperatures (4.3K) with high intensity pulsed excitation ($180\mu\text{W}$ mean power; $115\mu\text{J}/\text{cm}^2$ pulse fluence). *Bottom left*: Comparison of multiexciton features in transient spectra at room temperature (gray) and 4.3K (black). The dashed gray line is the actual intensity of room temperature transient spectrum, whereas the solid gray line is the room temperature spectrum after rescaling for comparison. *Bottom right*: plot of splitting of triexciton band energy splitting at various temperatures. The ~ 20 meV difference in splitting between room temperature and 4.3K can be accounted for by kT .

Comparing the low temperature spectrum to the room temperature spectrum we note, first, that the emission bands appear narrower at low temperature. The same phenomenon is well known for the band edge emission of CdSe NCs, and it results from a narrowing of the *single* NC line width to approximately 1nm FWHM. Of course the ensemble linewidths remains much broader than 1nm because of the imperfect size distribution of the sample.

Of greater interest is the energy splitting between the TX and the band edge. Room temperature streak camera measurements of the same sample of NCs in hexane solution showed $\Delta \sim 120\text{meV}$ as discussed earlier. The room temperature splitting in figure 4.8 is similar, $\Delta = 111\text{meV}$. However, at 4.3K the splitting is reduced to only 91 meV.

One possible reason for the smaller splitting between the TX and the band edge emission at low temperatures as well as the narrowing is the existence of a ladder of fine structure states for the TX, analogous to those for the single exciton. At room temperature the TX thermally populates a ladder of fine-structure states, but at low temperatures it is frozen into the lowest energy TX fine structure state. Rigorous calculation of these states is beyond the scope of this study, however, it is interesting to speculate on whether the lowest of these is optically active. For this we needed to compare the room temperature lifetime and quantum yield of the TX to values at low temperature.

By integrating over a spectral range of data in 3D plots like figure 4.8 we obtain the decay behavior of the luminescence in that given spectral range. Figure 4.11 shows this decay behavior for the TX band as a function of temperature, where the decays have

been rescaled so that their maximum intensity values are equivalent at $t=0$. Using the same raw data we also generated the PL decay of band edge luminescence (BX+X) at the same temperatures, which are shown in figure 4.11.

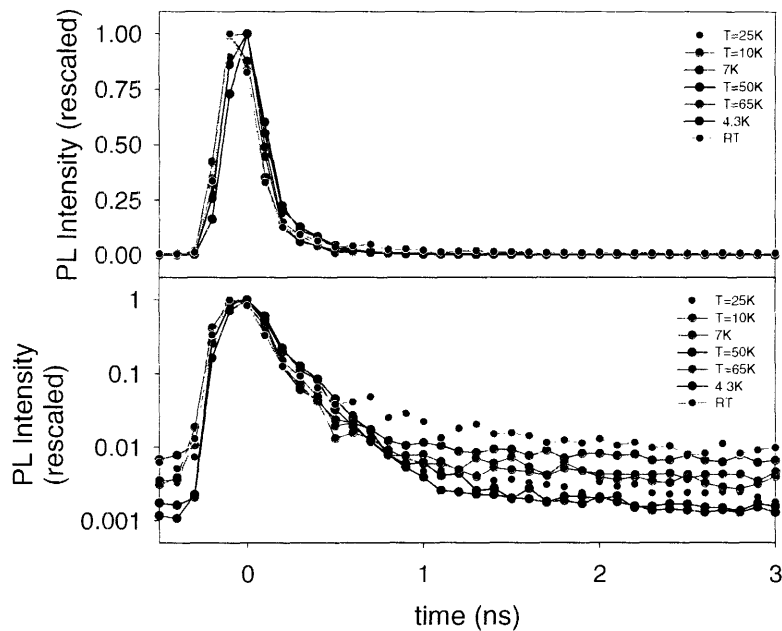


Figure 4.11 Decay of TX emission from 5.1 nm radius CdSe/ZnS nanocrystals at various temperatures. These experiments were performed with $180 \mu\text{W}$ excitation power ($115 \mu\text{J}/\text{cm}^2$, $1 \mu\text{m}$ radius spot size).

The decays shown in figures 4.11 and 4.12 were obtained from films of NCs that were pumped with $180 \mu\text{W}$ in a confocal geometry leading to an excitation pulse fluence of $115 \mu\text{J}/\text{cm}^2$. This excitation fluence generates on average N excitons in a given NC per pulse, so we know that we are in the multiexciton generation regime. This is confirmed by power dependent studies at low temperature, shown below.

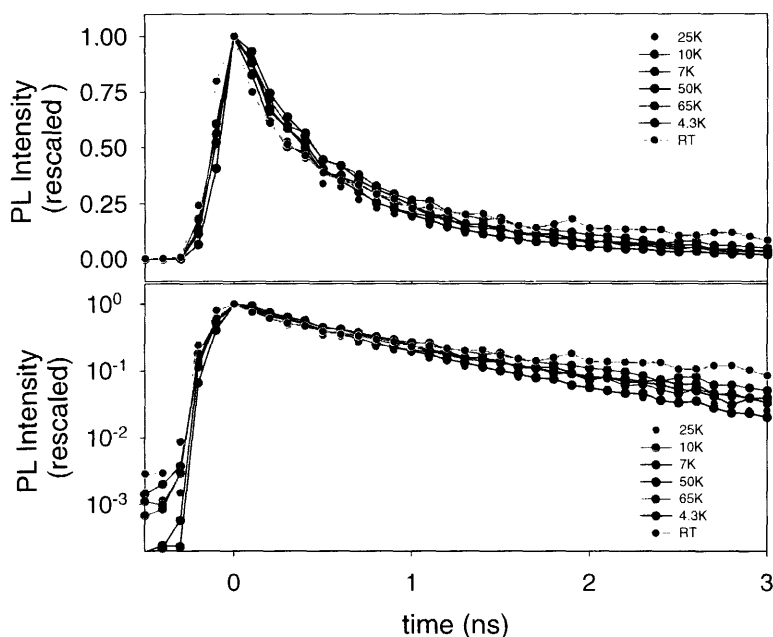


Figure 4.12 Decay of BX emission from 5.1nm radius CdSe/ZnS nanocrystals at various temperatures. These experiments were performed with $180 \mu\text{W}$ excitation power ($115 \mu\text{J}/\text{cm}^2$, $1 \mu\text{m}$ radius spot size).

Variation of the temperature between room temperature and 4.3K appears to have little influence on the decay rate of the TX or BX emission. The most likely reason for this is that Auger recombination, known to play the most important role in multiexciton relaxation at RT, still provides the most efficient relaxation pathway for multiexcitons at low temperature. This is not surprising because one would not expect the Coulombic coupling of carriers – the basis for Auger recombination – in a semiconductor to have a strong temperature dependence, especially in confined systems like these nanocrystals.

This means that the dominant non-radiative rate for multiexciton relaxation is approximately temperature independent. As a result, any change in quantum yield of a multiexciton will reflect a change in the radiative decay rate of that multiexcitonic transition. At low temperatures excitons occupy only the lowest levels of the fine

structure. A change (or lack thereof) in the radiative decay rate gives us insight into whether the lowest energy state of the TX fine structure is optically inactive (or active).

Previously, at room temperature, we judged the quantum yield of multiexciton states by comparison to the emission intensity of the single exciton in the same experiment. Since the QY of the single exciton is not constant as a function of temperature¹⁹, we did not reference the QY of the multiexciton emission to the single exciton QY and cannot obtain absolute values for the multiexciton QY. However, the TX emission intensity grew significantly as the temperature was reduced, indicating that the TX quantum yield increased. These observations are shown in figure 4.13.

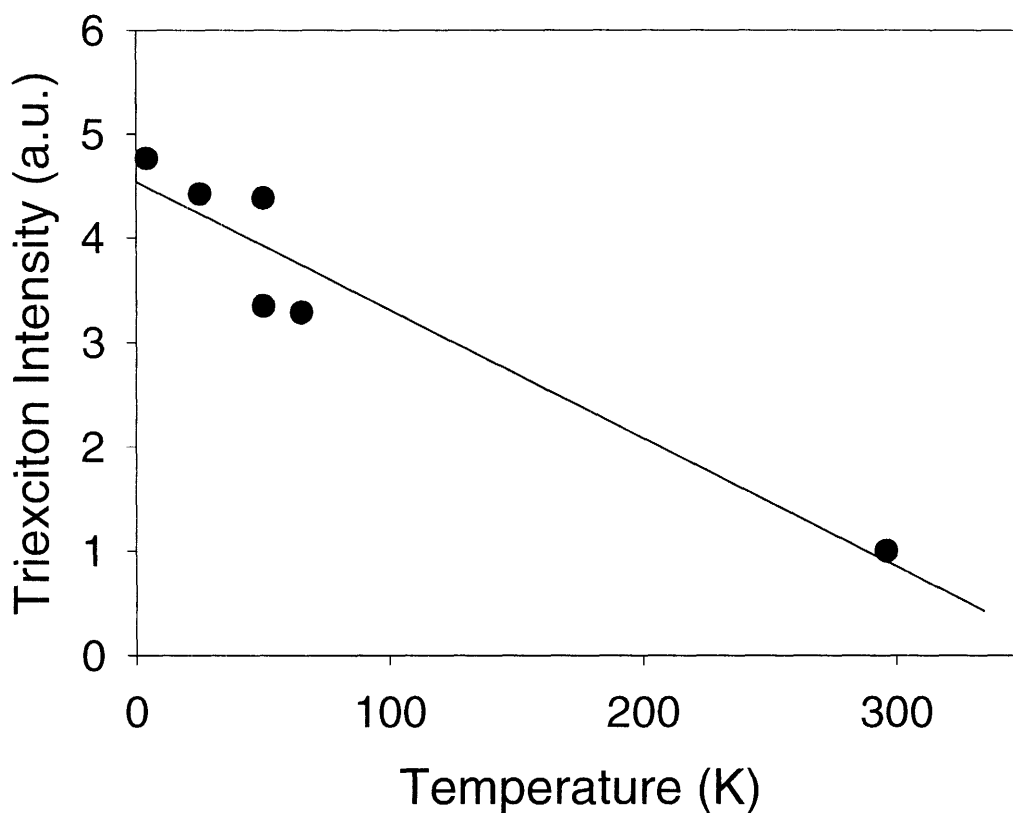


Figure 4.13 Temperature dependence of TX emission intensity at constant pump intensity. Integrated TX emission counts are normalized against the value at room temperature. The line is a linear fit to guide the eye.

If we ignore non-homogenous change of the quantum yield (described in chapter 8), then the increased quantum yield of the TX must be associated with an increase of its radiative rate, since the non-radiative rate was found to be temperature independent. This increase of TX radiative rate strongly suggests that the lowest energy state of the TX fine structure is optically active.

Lastly we studied the power dependence of the BX and TX emission at low temperature. Figure 4.14 shows the evolution of the TX luminescence decay as the average PL pump power is varied from $1\mu\text{W}$ to $180\mu\text{W}$ ($0.6\mu\text{J}/\text{cm}^2 - 115\mu\text{J}/\text{cm}^2$). The

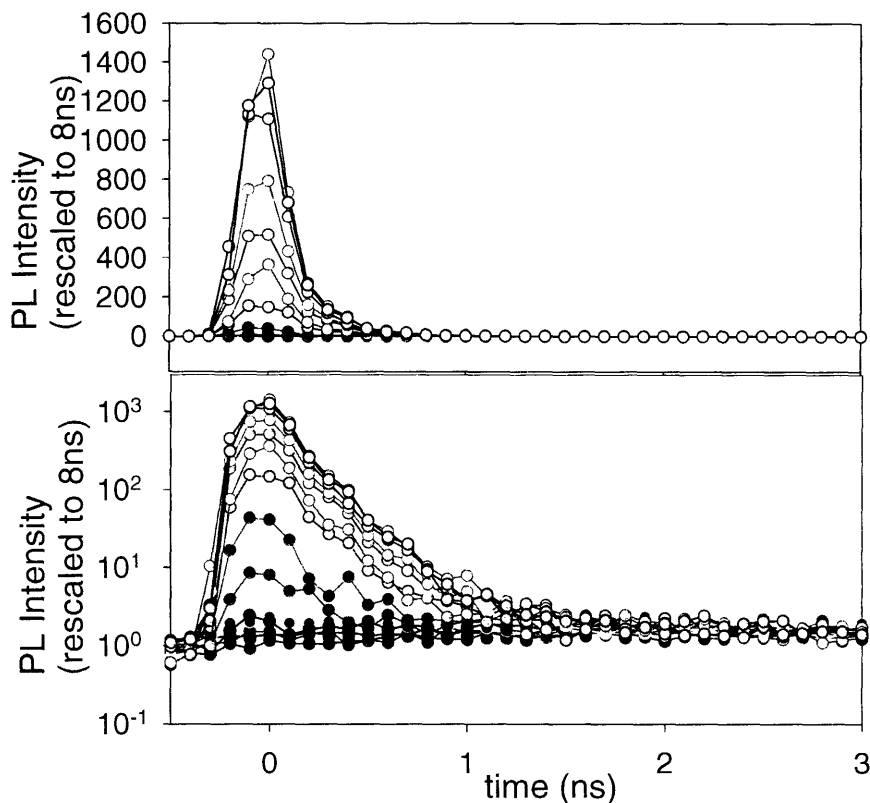


Figure 4.14 Power dependence of the luminescence decay of TX emission from 5.1nm radius CdSe/ZnS NCs at 4.3 K as a function of excitation power. The top plot shows the results on a linear scale. The bottom plot shows the data on a log-scale plot. Powers: $1\mu\text{W}$, $2\mu\text{W}$, $4\mu\text{W}$, $8\mu\text{W}$, $12\mu\text{W}$ (pink line, black dot), $30\mu\text{W}$, $60\mu\text{W}$, $80\mu\text{W}$, $100\mu\text{W}$, $120\mu\text{W}$, $140\mu\text{W}$, $160\mu\text{W}$ (pink line, gray dot), $180\mu\text{W}$ (dark green line, gray dot), $180\mu\text{W}$ (dark blue line, gray dot).

integrated emission intensity of the TX and of the BX could be obtained from decays like those in figure 4.14 by rescaling the curves so that their emission intensities match at long times (3 ns in the case of the TX decay, 8 ns in the case of the BX decays). The intensity of TX and BX emission as a function of pump power is summarized in figure 4.15.

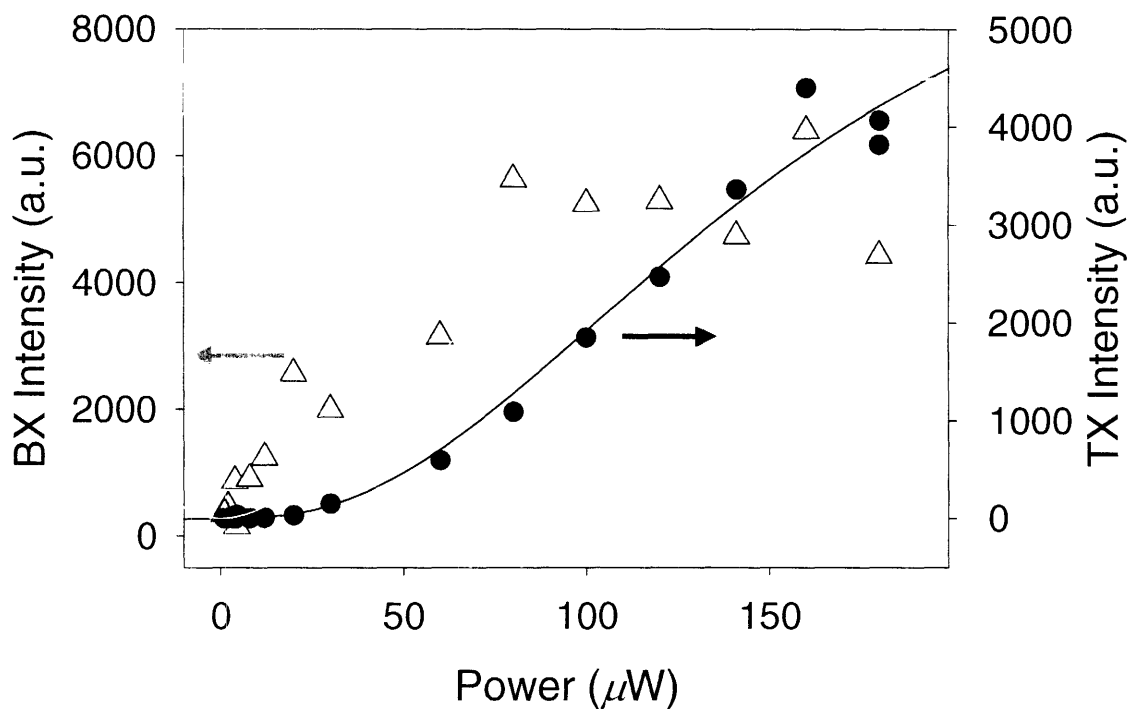


Figure 4.15 Power dependence of BX and TX emission from 5.1 nm radius CdSe/ZnS nanocrystals at 4.3 K. The power range covers average exciton generation values of $\bar{n} = 0$ to ~ 4 excitons per NC per pulse.

4.7 Conclusions

We have observed multiexciton photoluminescence from semiconductor NCs. Our studies of the power dependence and energy splittings of transient photoluminescence strongly imply that the high-energy multiexciton band results from three $e-h$ pair TX emission involving the 1P electron state of the nanocrystal. Our battery of experiments at room temperature allowed us to extract fundamental values like

radiative lifetime and quantum yield of the multiexciton emission. Low temperature experiments provided new insight into the nature of the states involved in these transitions, suggesting that the TX emission occurs through an optically allowed transition at the bottom of a ladder of fine structure energy levels comprising the $1P_{3/2}$ - $1P_e$ transition.

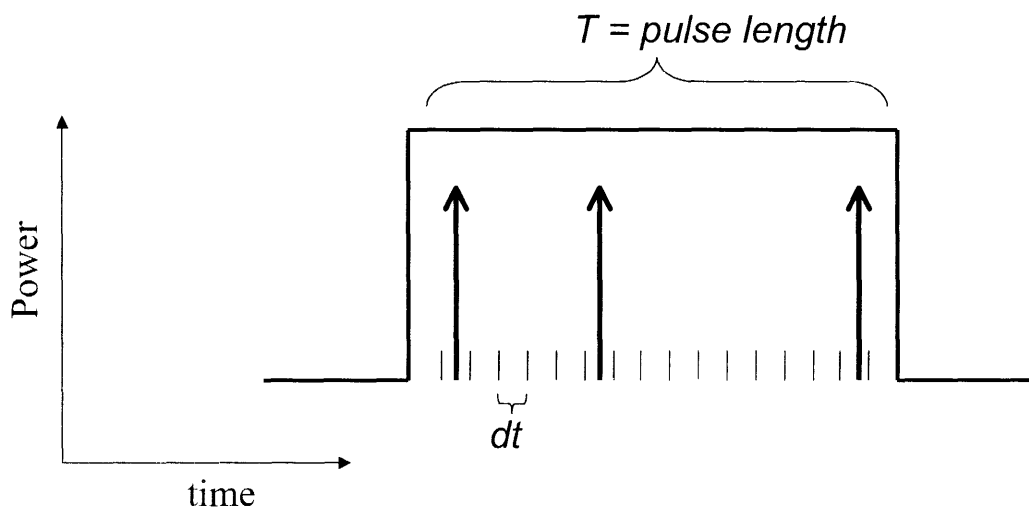
The results presented in this chapter are of fundamental scientific interest for the understanding of nanocrystal electronic structure. They are also useful for applications like studies of NC doped titania films with distributed feedback (DFB) gratings in our group which revealed simultaneous ASE and lasing from both the BX and TX transitions²⁰. Moreover, the relatively high QY and long lifetime of multiexciton emission from large NCs found in these studies suggest the possibility of studying multiexciton emission at the single NC level. We address this effort in the next chapter.

4.8: Addendum: Poisson Statistics for Probability of Multiexciton Generation

For pulsed experiments the power dependence of n -exciton state generation is derived from the probability that a single excitation pulse generates the n excitons in a single nanocrystal. We justify the use of a Poisson distribution to estimate this probability on the basis of the following arguments.

Our pump laser is tuned to a non-resonant transition in the nanocrystal (400nm – ~1 eV above the conduction band edge, depending on the NC sample), and the pump pulse lasts for about 150fs to 200fs. Because of the very high density of states at this non-resonant transition, and because the decay of hot-carriers to the band edge is known to be very efficient (<1ps)²¹⁻²³, it is reasonable to assume that each separate absorption

event within the excitation pulse length occurs independently of one another – there should be no bleaching of this transition, even within the pulse duration. If the various absorption events by a single nanocrystal occur independently of one another, then the total number of absorption events that occur during a given time period (e.g. length of the pulse) is governed by the Poisson distribution²⁴ as described in the caption of figure 4.14 below. We note that these assumptions are invoked with extensive precedent in the literature^{4, 25}.



We approximate the excitation pulse as a square function of width T . Within the pulse, the single NC is excited at a constant average rate of $\phi_a = I_{peak} \sigma$, where σ and I_{peak} are the cross-section and peak laser intensity respectively. Therefore the average number of excitations during the pulse is $\langle n \rangle = \phi_a * T$. If we divide the pulse into a sufficient number (N) of time bins of width, $dt = T/N$, then the stochastic probability that an excitation event (represented by “up arrows”) occurs in an interval is $p = \langle n \rangle / N$. The probability of finding $\langle n \rangle$ independent excitation events in the N intervals follows the binomial distribution. The Poisson distribution emerges from the binomial distribution in the limit that $dt \rightarrow 0$. This explanation is adapted from Saleh and Teich.

4.9 References

- ¹ E. Moreau, I. Robert, L. Manin, et al., Physical Review Letters **87**, 183601 (2001).
- ² O. Benson, C. Santori, M. Pelton, et al., Physical Review Letters **84**, 2513 (2000).
- ³ G. Chen, N. H. Bonadeo, D. G. Steel, et al., Science **289**, 1906 (2000).

- 4 V. I. Klimov, A. A. Mikhailovsky, D. W. McBranch, et al., *Science* **287**, 1011
(2000).
- 5 V. A. Kharchenko and M. Rosen, *Journal of Luminescence* **70**, 158 (1996).
- 6 J. M. Caruge, Y. Chan, V. Sundar, et al., *Physical Review B* **70**, 085316 (2004).
- 7 M. Achermann, J. A. Hollingsworth, and V. I. Klimov, *Physical Review B* **68**,
245302 (2003).
- 8 B. R. Fisher, H. J. Eisler, N. E. Stott, et al., *Journal of Physical Chemistry B* **108**,
143 (2004).
- 9 M. A. Hines, Guyot-Sionnest, P., *Journal of Physical Chemistry* **100**, 468 (1996).
- 10 B. O. Dabbousi, J. Rodriguez-Viejo, F. V. Mikulec, et al., *Journal of Physical
Chemistry B* **101**, 9463 (1997).
- 11 Z. A. Peng and X. G. Peng, *Journal of the American Chemical Society* **124**, 3343
(2002).
- 12 M. Kuno, J. K. Lee, B. O. Dabbousi, et al., *Journal of Chemical Physics* **106**,
9869 (1997).
- 13 D. J. Norris and M. G. Bawendi, *Physical Review B* **53**, 16338 (1996).
- 14 T. Vossmeier, L. Katsikas, M. Giersig, et al., *Journal of Physical Chemistry* **98**,
7665 (1994).
- 15 Y. P. Varshni, *Physica* **34**, 149 (1967).
- 16 P. Guyot-Sionnest and M. A. Hines, *Applied Physics Letters* **72**, 686 (1997).
- 17 C. A. Leatherdale, W. K. Woo, F. V. Mikulec, et al., *Journal of Physical
Chemistry B* **106**, 7619 (2002).
- 18 K. H. Hellwege, *Landolt-Bornstein Numerical Data and Functional Relationships
in Science and Technology* (Springer-Verlag, Berlin, 1982).
- 19 G. W. Walker, V. Sundar, C. M. Rudzinski, et al., *Applied Physics Letters* **83**,
3555 (2003).
- 20 Y. T. Chan, J.-M. Caruge, P. Snee, et al., *Applied Physics Letters* **85**, 2451
(2004).
- 21 P. Guyot-Sionnest, M. Shim, C. Matranga, et al., *Physical Review B* **60**, R2181
(1999).
- 22 V. I. Klimov, D. W. McBranch, C. A. Leatherdale, et al., *Physical Review B* **60**,
13740 (1999).
- 23 V. I. Klimov, A. A. Mikhailovsky, D. W. McBranch, et al., *Physical Review B*
61, 13349 (2000).
- 24 B. E. A. Saleh and M. C. Teich, in *Fundamentals of Photonics* (Wiley-
Interscience, p. 385.
- 25 V. I. Klimov, *Journal of Physical Chemistry B* **104**, 6112 (2000).

Chapter 5: Multiexciton Emission from Single CdSe Nanocrystals

- 5.1 Introduction
- 5.2 Methods
- 5.3 Multiexciton Emission in Single Nanocrystal Emission Spectra
- 5.4 Multiexciton Emission in Single Nanocrystal Lifetimes
- 5.5 Quantum Yield of Multiexciton Emission from Power Dependence
- 5.6 Blinking in Multiexciton Emission
- 5.7 Conclusions
- 5.8 References

5.1 Introduction

The results of the last chapter demonstrating multiexciton emission of significant quantum yield (QY) from nanocrystals (NCs) suggest that single molecule spectroscopy experiments on multiexciton emission might also be possible. In the field of epitaxially grown Stranski-Krastanow quantum dots (QDs), spectroscopic studies of multiexciton emission at the single QD level is already commonplace. Recent low temperature studies of multiexciton-exciton splitting¹, multiexciton lifetimes^{2, 3} and fine structure⁴, coherent control of multiexcitons⁵ and non-classical light emission via multiexciton channels^{6, 7} are only a few examples. It is an ongoing challenge and of great interest to perform these same kind of experiments on single *nanocrystals*.

In this chapter we investigate the multiexciton transitions of CdSe at the single nanocrystal level. The primary challenge here is to distinguish the multiexciton emission from the regular single exciton band (X) edge emission of a single NC. In chapter 4 relatively large QY and lifetimes values were measured for the biexciton (BX) and triexciton (TX) in large (5.1nm) NCs, implying that multiexciton emission should be detectable from single NCs. Here we succeed in temporally and spectrally resolve this emission in single NC experiments. We observe a correlation of the multiexciton

emission to the single NC fluorescence intermittency. We also arrive at quantum yield values for the BX and TX by fitting our single NC lifetime data to the behavior of a simple four level system (4LS). These values agreed with QY values of the BX and TX obtained by ensemble measurement of the same samples as chapter 4.

5.2 Methods

For single NC experiments presented in this chapter, we selected the 5.1nm radius nanocrystal sample from Quantum Dot Corporation (QDC, Cat. No.1002-1), that was studied in chapter 4. We focused on this sample because it had a very high quantum yield for both its single-exciton band-edge emission (~70%) and its BX and TX emission (estimated to be about 7% and 3% respectively). We prepared single NC samples in a manner very similar to chapter three. A very dilute solution of the NCs in a toluene plus poly(methyl methacrylate) mixture was spin-coated onto a coverglass to produce a low-density field of single NCs ($<0.1 \mu\text{m}^{-2}$) in a polymer matrix. Single NCs were excited using one of two pulsed lasers: (a.) the 400nm pulsed output of a frequency-doubled Ti:Sapphire oscillator ($\tau_{\text{pulse}} < 500\text{fs}$, 4.715 MHz repetition rate); (b.) 414nm output of a pulsed laser diode (Picoquant GmbH, $\tau_{\text{pulse}} < 100\text{ps}$, 5 MHz repetition rate). A high NA objective (100x/1.4) was used for both excitation and collection of PL on a home built piezo scanning confocal microscope. The high NA oil immersion objective allowed us to achieve smaller spot sizes and hence even higher excitation fluences than were possible for the intra-cryostat experiments in chapter 4. For instance, the 400nm excitation light could be focused with the 1.4NA objective to a spot size of $<200\text{nm}$ HWHM (radius). A Timeharp200 (Picoquant GmbH) was used to measure lifetimes of single NCs by time

correlated single photon counting (TCSPC). Transient spectra of single NCs were obtained by sending the light collected from a single NC through a spectrograph (Triax320, 300mm^{-1} , 550nm =blaze) whose output was detected using an ultra-fast, gated charge-coupled device (CCD, LaVision GmbH). In each of these experiments the entire luminescence spectrum was collected, and all measurements were at RT.

5.3 Multiexciton Emission in Single Nanocrystal Emission Spectra

Transient spectra at zero and 5 ns post-excitation delays from a *single* NC are shown in figure 5.1. The zero-delay spectrum with a 1000ps gate integrates over the lifetime of the TX, revealing the blue-shifted TX emission from the single NC, which is

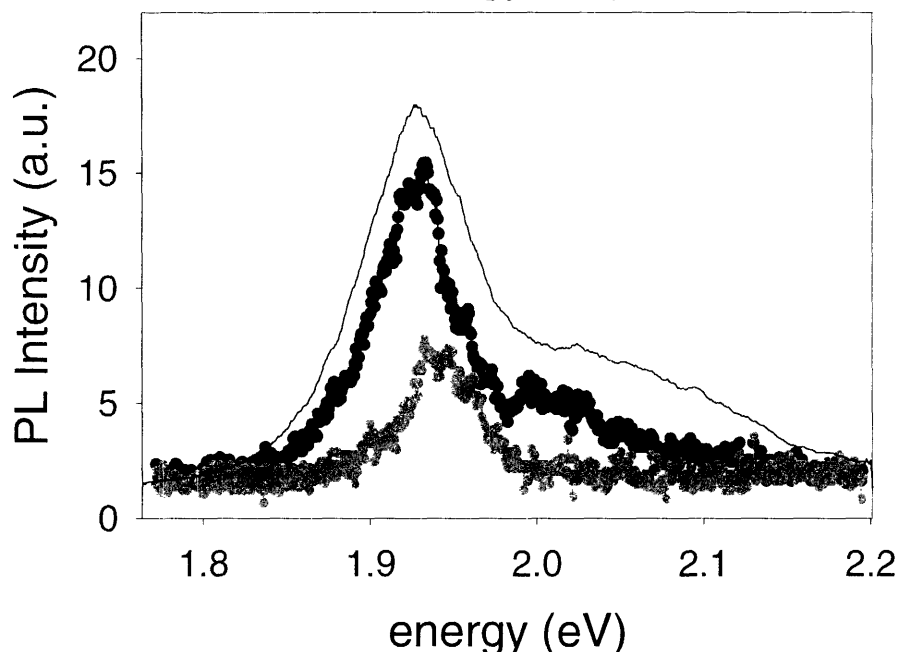


Figure 5.1 Transient spectra (1000ps gate) from a *single* NC ($280\mu\text{J}/\text{cm}^2$) at zero (black) and 5ns (gray) delay. The sample's ensemble transient spectrum (solid line) is superimposed (1000ps integrated, 10meV shift for comparison).

in qualitative agreement with the transient spectrum of the solution (black line). In contrast, the single NC spectrum obtained after a 5 ns delay (gray line) shows no blue-shifted TX band, because it has completely decayed. We note that the single NC spectrum at 5 ns delay does not coincide with the main peak at zero delay because of spectral diffusion, which is well documented in single NCs^{8,9}. Spectra like figure 5.1 could be repeatably obtained from many different NCs as long as the NC did not blink off or spectrally shift too much before sufficient averaging could be completed (usually 10-30 seconds).

5.4 Multiexciton Emission in Single NC Lifetimes

BX and TX emission was evident in lifetime measurements of these single NCs as well. Figure 5.2(a) shows the emission intensity of a single NC under progressively higher intensity, pulsed excitation. The lifetime was measured for the duration of excitation at each intensity. Selected lifetime curves (shown in figure 5.2(b)), obtained during periods of high and low intensity excitation of the intensity trace, show a two component decay when the excitation intensity is high and just a single component exponential decay when the excitation intensity is low.

We observe from figure 5.2 that the fast component is a reversible effect of increasing the excitation pulse energy – after raising the excitation power high enough to induce the fast component, single component decays can be recovered by lowering the power again. This is important to note because it indicates that the fast component is not

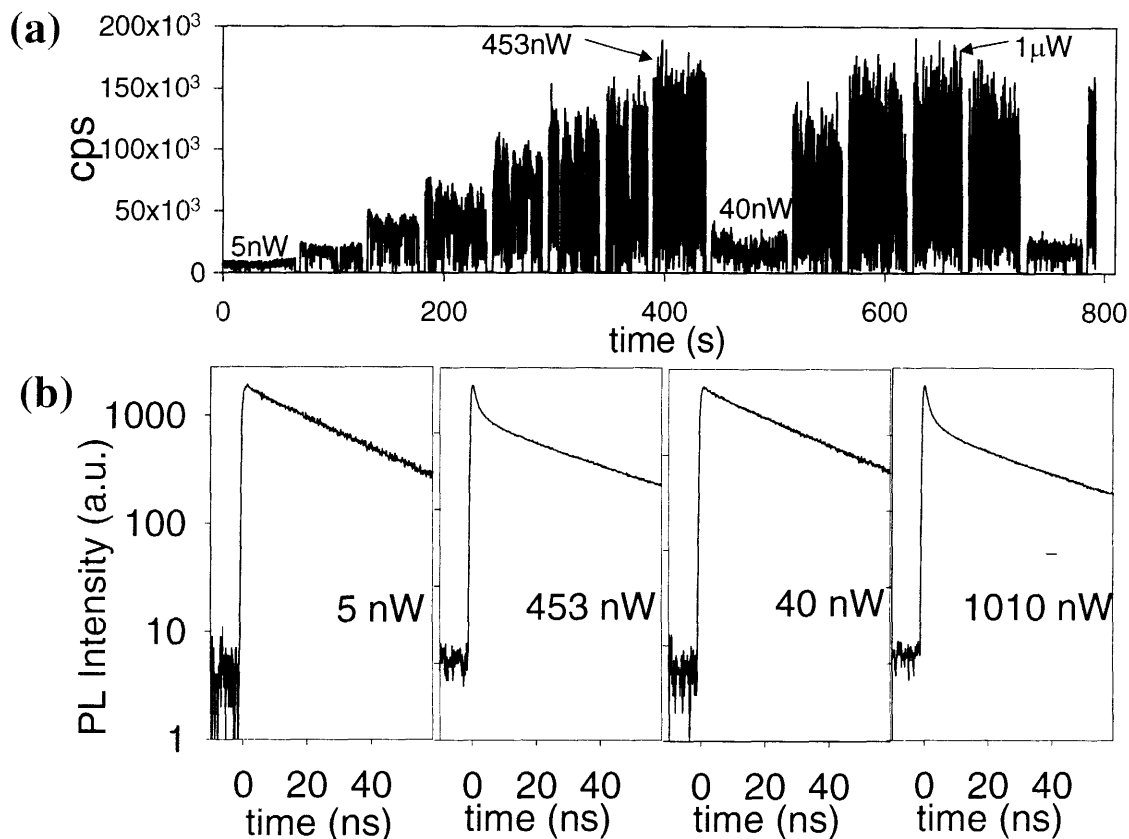


Figure 5.2 Emission intensity and PL decay of a single nanocrystal at various excitation powers ranging from 5 nW to 1 mW (1.4 to $280 \mu\text{J}/\text{cm}^2$). (a.) intensity trajectory of the single nanocrystal as it is illuminated at various intensities (b.) PL decays obtained by TCSCP corresponding to various excitation intensities indicated in (a).

caused by some kind of irreversible photo-induced damage of the nanocrystal (e.g. photochemical modification of the surface to introduce trap states that open a fast decay pathway).

Having discounted the possibility that the fast component of the decay resulted from nanocrystal damage, we did an experiment to show that the instrument limited fast component of the decay truly originated from nanocrystal PL and not from scattered laser excitation that may have reached the detector (which would also lead to a power-dependent, fast decay component).

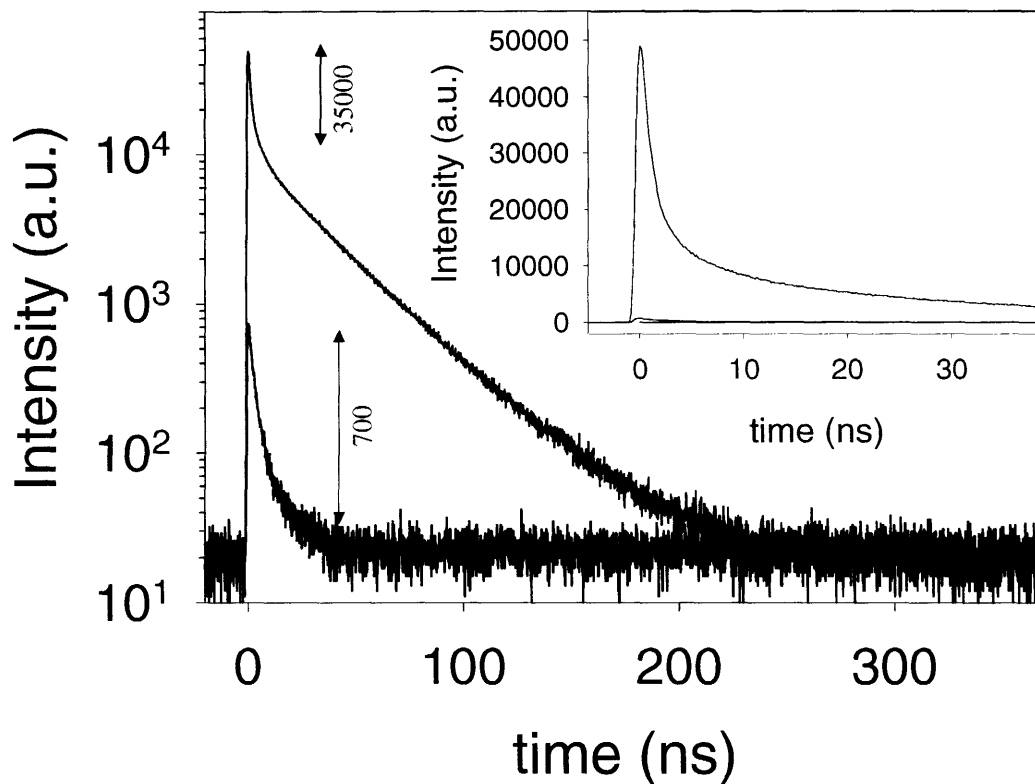


Figure 5.3 PL decay from a single nanocrystal under high excitation intensity compared to the decay of scattered excitation light obtained using the same illumination intensity. The intensity of the fast decay component is too large to be explained by the small number of counts obtained in the decay of scattered excitation light.

In Figure 5.3 the decay of a single nanocrystal under 1825nW (~ 0.4 to 0.5 mJ/cm², $\bar{n} > 10$) pulsed excitation is compared to the TCSPC decay of only scattered excitation obtained by illuminating a region of the sample completely devoid of NCs with 2000nW of excitation intensity. It is clear that the number of counts obtained from the scatter of excitation (at an even higher power) is of two orders of magnitude lower intensity than the fast component intensity of the PL decay from the NC. This result provides strong evidence that the two-component, power dependent decay that we have observed truly originates from the PL of NCs.

To analyze the precise excitation intensity dependence of the PL decays recorded from a single NC, we rescaled each decay to its intensity at $t=0$ and superimposed the decays in a single plot, shown in figure 5.4. Each decay curve was fit to a bi-exponential function. It is clear from these decay curves that the slow component of all decays has the same decay constant ($1/\Gamma_1 = 29\text{ns} \pm 1\text{ns}$). This decay rate matches the measurements observed in chapter 3 and corresponds to band-edge emission from the single exciton state of the NC. As the excitation intensity increases the fast decay component becomes more prominent. The fast component was found to have an

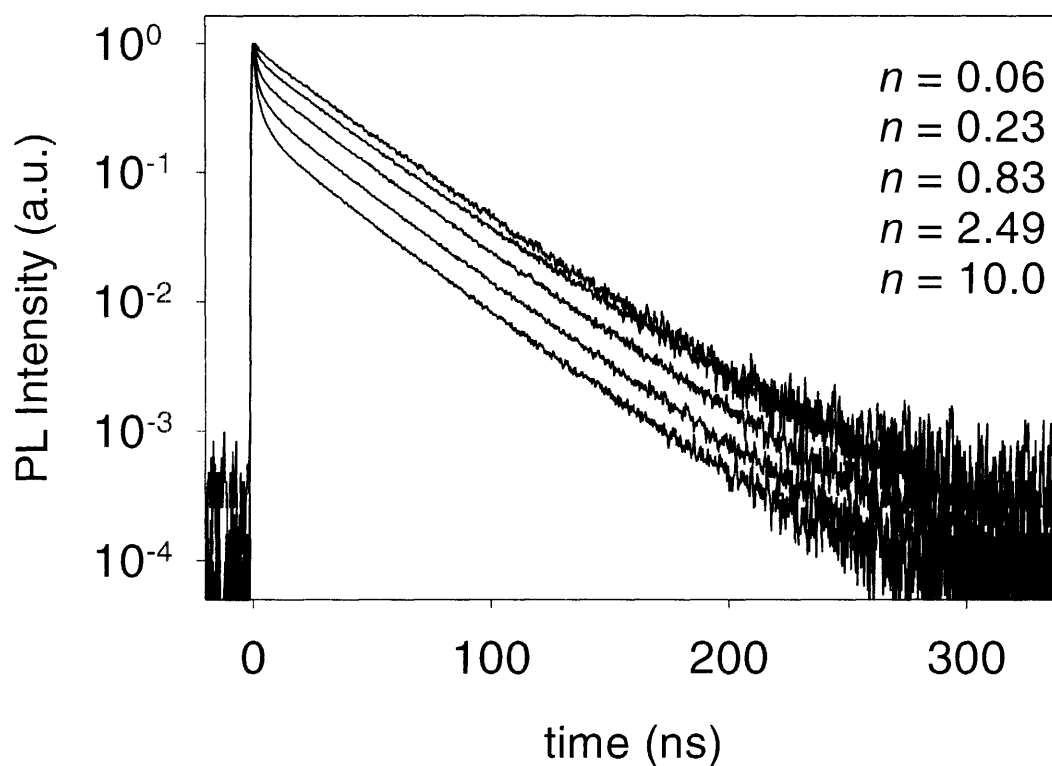


Figure 5.4 Excitation intensity dependence of PL decay from a single NC. Excitation intensity is denoted by n , the average number of excitons generated in the NC per excitation pulse.

instrument-limited decay constant (~ 1 ns). Since the detected luminescence in these experiments was spectrally integrated, the fast component originates from both BX and TX emission.

5.5 Quantum Yield of Multiexciton Emission from Power Dependence

The explicit intensity dependence of the fast decay component in figure 5.4 can be expressed as the ratio of fast and slow weighting parameters obtained from bi-exponential fits of numerous lifetime curves from the same NC. These data are plotted in figure 5.5. To fit the data in figure 5.5 we assumed a 4LS as illustrated by the inset of figure 5.5.

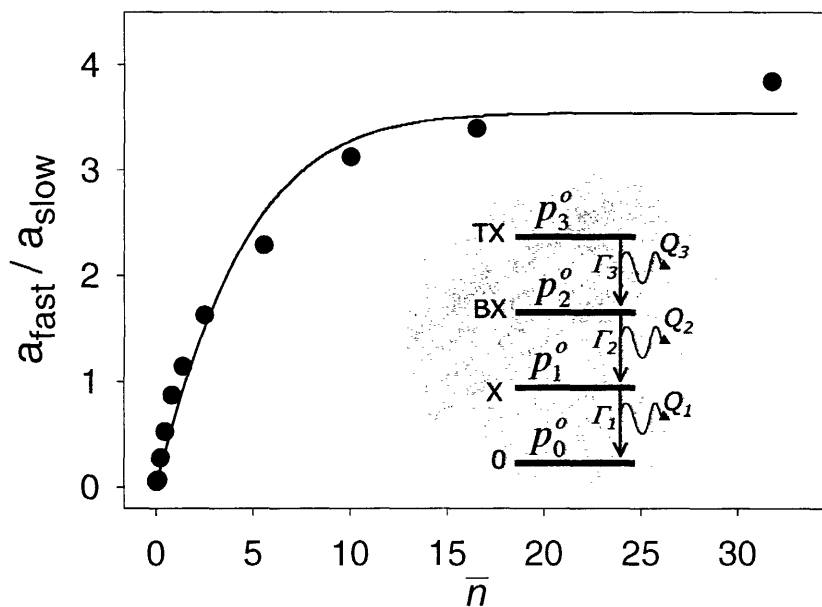


Figure 5.5 Relative strength of fast decay component as a function of n , the average number of excitons generated in the NC per excitation pulse ($\bar{n} \sim 1$ exciton per NC per pulse). *Inset:* illustration of the 4LS described by equation 5.1 that is used to model multiexciton emission after pulsed excitation.

The time evolution of the occupation probabilities ($p_i(t)$) of a 4LS after pulsed excitation is given by ($\tau_{\text{pulse}} \ll 1/\Gamma_i$):

$$\begin{aligned}
\frac{dp_3(t)}{dt} &= -\Gamma_3 p_3(t) \\
\frac{dp_2(t)}{dt} &= \Gamma_3 p_3(t) - \Gamma_2 p_2(t) \\
\frac{dp_1(t)}{dt} &= \Gamma_2 p_2(t) - \Gamma_1 p_1(t)
\end{aligned} \tag{5.1}$$

The initial conditions, p_i'' , are given by the Poisson distributed probability of exciting $i = 0, 1, 2$, or greater than 2 excitons, given an *average* number of excitons generated per pulse, \bar{n} . which is equivalent to the number of excitation photons in a given laser pulse multiplied by the cross-section of the NC^{10, 11}. Solutions of equations 5.1 give the time dependence of the total PL, which is the sum of three exponential decays.

$$\begin{aligned}
PL(t) &= \sum_{i=1}^3 Q_i \Gamma_i p_i(t) \\
&= p_3'' \left(Q_3 \Gamma_3 + Q_2 \Gamma_2 \frac{\Gamma_3}{\Gamma_2 - \Gamma_3} + Q_1 \Gamma_1 \frac{\Gamma_2 \Gamma_3}{(\Gamma_2 - \Gamma_3)(\Gamma_1 - \Gamma_3)} \right) e^{-\Gamma_3 t} \\
&\quad + \left(Q_2 \Gamma_2 \left(p_2'' - p_3'' \frac{\Gamma_3}{\Gamma_2 - \Gamma_3} \right) + Q_1 \Gamma_1 \left(p_2'' \frac{\Gamma_2}{\Gamma_1 - \Gamma_2} - p_3'' \frac{\Gamma_2 \Gamma_3}{(\Gamma_2 - \Gamma_3)(\Gamma_1 - \Gamma_3)} \right) \right) e^{-\Gamma_2 t} \\
&\quad + Q_1 \Gamma_1 \left(p_1'' - p_2'' \frac{\Gamma_2}{\Gamma_1 - \Gamma_2} - p_3'' \left(\frac{\Gamma_2 \Gamma_3}{\Gamma_2 - \Gamma_3} \right) \left(\frac{1}{(\Gamma_1 - \Gamma_3)} - \frac{1}{(\Gamma_1 - \Gamma_2)} \right) \right) e^{-\Gamma_1 t}
\end{aligned} \tag{5.2}$$

Since the instrument response of our TCSPC measurements was slower than the first two exponentials of equation 5.2, these fast terms are combined into a single response-limited component. This yields a *two-component* total PL decay: $PL(t) = a_{fast} e^{-\Gamma_{fast} t} + a_{slow} e^{-\Gamma_{slow} t}$ which leads to an expression for the intensity dependence of the data in figure 5.5,

$$\frac{a_{fast}}{a_{slow}} = \frac{q_3 \eta_3 p_3'' + (q_2 \eta_2 - 1) p_2''}{p_1'' + p_2'' + p_3''} \tag{5.3}$$

where $\eta_i = \Gamma_i / \Gamma_1$ and relative multiexciton quantum yields, are defined as in chapter 4: $q_2 = Q_2 / Q_1$ and $q_3 = Q_3 / Q_1$. We fixed the relaxation rates to values measured for this sample in chapter 4 ($\Gamma_1 = 1/29$ ns, $\Gamma_2 = 1/790$ ps, $\Gamma_3 = 1/230$ ps) and fit equation 3 to the

experimental data of figure 5.5, varying only q_2 , q_3 , and a scaling factor. The best-fit result gives $q_2=0.14$ and $q_3=0.04$, which is in good agreement with the values $q_2=0.11$ and $q_3=0.05$ that were obtained in chapter 4 from streak camera decays of the same sample of NCs. These values imply radiative lifetimes of 8.4ns and 6.8ns for the BX and TX respectively.

5.6 Blinking and Multiexciton Emission in Single Nanocrystals

Fluorescence intermittency or blinking¹²⁻¹⁵, is a ubiquitous phenomenon in single NC fluorescence and was observed in all of our experiences in this chapter, despite the large multiexciton QY and lifetimes and relatively slow Auger relaxation of this NC sample. A typical example of the blinking behavior that we observed from our samples is shown in figure 5.6 where the power dependence of the blinking is explicitly shown. This shortening of on and off times at high power illumination is well known¹⁵. However, we know from the PL decays (figures 5.2 and 5.3) and spectra (figure 5.1) of these NCs that the low-power blinking trajectory of figure 5.6 arises from pure exciton emission, whereas the fast, high-power blinking arises from exciton plus multiexciton emission. Combining these results, we can make the noteworthy observation that the rate of blinking is clearly correlated to the generation of multiexcitons. This fits the idea that blinking is in part driven by the generation of biexcitons, which recombine by an Auger process leaving the NC in a charged state^{12, 16}.

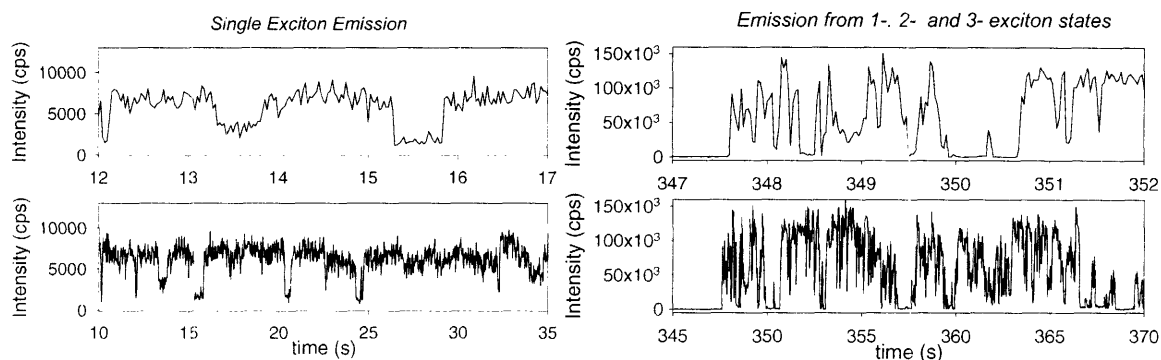


Figure 5.6 Comparison of blinking associated with pure single-exciton emission versus multiexciton emission.

Further experiments indicated that the multiexciton emission itself may exhibit intermittency just like as the band edge single exciton emission. Since the TX is spectrally resolved from the band edge emission, we used a narrow bandpass filter (2.016eV-2.046eV) to selectively detect only TX emission (see figure 4.1(d) transient triexciton band). A detailed analysis of the signal detected after transmission through this bandpass filter showed that the signal was between 50% and 80% pure triexciton emission from a single nanocrystal. The intensity trajectory of this nearly pure TX emission, shown in figure 5.7, clearly exhibits blinking just as the band edge emission blinks. Moreover, simultaneous acquisition of band-edge emission and triexciton emission reveals that the blinking events are highly correlated – when the band edge emission blinks off, so does the triexciton emission. A detailed analysis of these observations is given in Appendix 2.

Blinking of triexciton emission is surprising because Auger relaxation, which is supposed to be responsible for the off-state of charged NCs¹² is known to be relatively slow in this sample, as the BX and TX both have appreciative QYs. If we refuse to abandon our current understanding of blinking – that the off state is non-emissive

because of efficient Auger relaxation involving the free carrier of a charged NC – then the blinking of the TX emission suggests that the Auger quenching of charged NCs is much more efficient than Auger relaxation in neutral nanocrystals, which have an equal number of excited electrons and holes (e.g. neutral BX and TX). Such a conclusion is surprising and not easily explained.

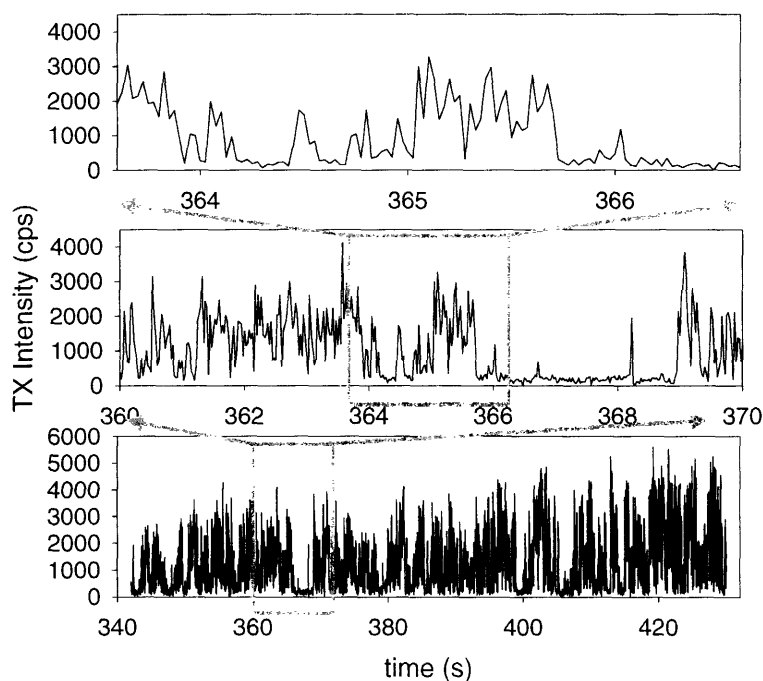


Figure 5.7 Fluorescence intermittency is observed from purely TX emission of a single NC by using a narrow band-pass filter to allow only photons with energy between 2.015eV (615nm) and 2.045eV (606nm) to reach the detector. The time resolution of this intensity trajectory is 25ms.

5.7 Conclusions

In this chapter we have presented measurements that explicitly show photoluminescence from radiative relaxation of multiexciton states of single CdSe nanocrystals. Transient spectra of single NC emission, obtained using a gated, intensified CCD camera, revealed a blue-shifted emission band that matches the TX emission band previously identified in ensemble transient spectra. A power dependent fast component

in the PL decay of single NCs was also observed and was found to originate from multiexciton emission. Fitting the power dependence to a 4LS yielded quantum yield values for the multiexciton that matched previous estimates well.

Whereas the spectroscopy of multiexciton states in single *quantum dots* is already commonplace, there are no previous reports of multiexciton emission detected from single *nanocrystals* because of the dominant role that Auger relaxation plays in the quenching of multiexciton states in small nanocrystals. The results presented in this chapter are significant because they demonstrate the possibility of investigating multiexcitonic states of nanocrystals at the single particle level when large enough nanocrystals are used. This opens a new area of spectroscopy for single nanocrystals, as many of the multiexciton experiments that have been carried out on single quantum dots, should also be possible with single nanocrystals. Our observation of blinking in the multiexciton emission already shows one interesting result of spectroscopy of multiexciton emission. Further work on multiexciton emission from single NCs might now address some of the experiments already carried out on single *quantum dots*¹⁻⁷. One such possibility is the potential use of multiexciton emission for non-classical photon pair generation. This application is investigated in the next chapter.

5.7 Reference

- ¹ I. A. Akimov, A. Hundt, T. Flissikowski, et al., Applied Physics Letters **81**, 4730 (2002).
- ² G. Bacher, R. Weigand, J. Seufert, et al., Physical Review Letters **83**, 4417 (1999).
- ³ G. Bacher, R. Weigand, J. Seufert, et al., Physica Status Solidi B-Basic Research **221**, 25 (2000).
- ⁴ V. D. Kulakovskii, G. Bacher, R. Weigand, et al., Physical Review Letters **82**, 1780 (1999).

- 5 T. Flissikowski, A. Betke, I. A. Akimov, et al., *Physical Review Letters* **92**,
227401 (2004).
- 6 C. Santori, D. Fattal, M. Pelton, et al., *Physical Review B* **66**, 045308 (2002).
- 7 S. M. Ulrich, S. Strauf, P. Michler, et al., *Applied Physics Letters* **83**, 1848
(2003).
- 8 S. A. Empedocles and M. G. Bawendi, *Journal of Physical Chemistry B* **103**,
1826 (1999).
- 9 S. A. Empedocles, R. G. Neuhauser, K. T. Shimizu, et al., *Advanced Materials*
11, 1243 (1999).
- 10 V. I. Klimov, A. A. Mikhailovsky, D. W. McBranch, et al., *Science* **287**, 1011
(2000).
- 11 J. M. Caruge, Y. Chan, V. Sundar, et al., *Physical Review B* **70**, 085316 (2004).
- 12 A. L. Efros, *Physical Review Letters* **78**, 1110 (1997).
- 13 S. A. Empedocles, in *Chemistry* (Massachusetts Institute of Technology,
Cambridge, 1999), p. 204.
- 14 M. Kuno, D. P. Fromm, H. F. Hafmann, et al., *Journal of Chemical Physics* **115**,
1028 (2001).
- 15 K. T. Shimizu, R. G. Neuhauser, C. A. Leatherdale, et al., *Physical Review B* **63**,
205316 (2001).
- 16 A. L. Efros, in *Archives* (Naval Research Laboratory, 2002).

Chapter 6: Non-classical Light Generation by Single CdSe Nanocrystals

- 6.1 Introduction
- 6.2 Methods
- 6.3 Antibunching and Triggered Single Photons
- 6.4 Quantum Cascaded Emission from Multiexciton States
- 6.5 Modeling Single Photon Correlation Measurements
- 6.6 Ordered Emission of Photons via Radiative Quantum Cascades
- 6.7 Photon Pair Generation Using Nanorods
- 6.8 Conclusion
- 6.9 Addendum: Summary of Results for Various Single Nanocrystal Samples
- 6.10 References

6.1 Introduction

Sources of non-classical light and ordered multiphoton emission offer a fascinating example of the quantum nature of light and have received attention because of their potential uses, among others, quantum cryptography^{1,2}. The first sources of non-classical radiation were isolated atoms^{3,4}, ions⁵, or molecules⁶. However single semiconductor quantum dots (QDs) have recently proven capable of providing highly efficient sources of sub-Poissonian or antibunched light^{7,8}, triggered single photons⁹, correlated photon pairs¹⁰⁻¹³, and even three stage radiative quantum cascades¹⁴. Single QDs have even enabled the generation of entangled photon pairs¹⁵. The QDs used in these previous experiments were fabricated using Stranski-Krastanow growth or similar self-assembly methods in highly controlled vacuum conditions, and have typically been InAs or InP QDs^{14,16}.

Semiconductor nanocrystals (NCs) may offer a convenient, inexpensive alternative to QDs as a solid-state source of non-classical radiation. Because NCs are smaller and more spherically symmetric with greater quantum confinement, they may even offer advantages over QDs for certain applications. For instance, whereas QDs

must be cooled to liquid helium temperatures to get atomic-like band-edge states, NCs exhibit atomic-like band-edge states at room temperature. On the other hand, whereas QDs have successfully been used to generate n -photon states with $n \geq 2$, the dominance of Auger relaxation for multiexciton states has precluded the use of NCs for this purpose. Our observation of multiexciton emission from single NCs, discussed in the chapter 4, opens the door to explore the potential of single NCs for non-classical light generation.

In this chapter we first present single photon correlation experiments showing antibunching from single NCs. We then show photon correlation measurements of single NC emission under pulsed excitation. We find that at high powers, multiexciton emission can lead to photon pair or triplet emission via a radiative quantum cascade. Finally we analyze the temporal characteristics of this emission and find the photons emitted from the multiexciton states to be well ordered. These experiments were carried out on many samples of NCs including rod-shaped nanocrystals.

6.2 Methods

We used high quantum yield (30%-80%) CdSe(CdZnS) core(shell) NCs of various sizes (2.5nm - 5nm, core radius) synthesized in our laboratory or obtained from Quantum Dot Corp. (QDC), (Cat. No.1002-1). Rod shaped, one-dimensional nanocrystals (nanorods, NRs) of aspect ratio 5:1 were synthesized in our lab using procedures adapted from a previously reported direct one-pot synthesis¹⁷ with *n*-tetradecylphosphonic acid and cadmium oxide (99.99%). These were overcoated using procedures analogous to those used for the spherical nanocrystals¹⁸. Experimental results presented in this chapter were obtained primarily from the nearly spherical QDC sample (radius 5.1nm, 655nm PL band, 75% quantum yield), although similar results were

obtained from all large spherical samples ($\sim 5\text{nm}$ radius). The results of all the various samples investigated, including smaller spherical NCs are tabulated in the addendum at the end of the chapter (section 6.9).

Single NC samples were prepared as described in chapter 5 by spin coating a dilute solution of NCs with PMMA in toluene onto a coverglass to produce a low-density field of single NCs in a thin polymer film. The single NCs were studied using a home built microscope with confocal excitation and collection using a 1.4NA oil immersion objective as in chapter 5. To excite the single NCs we used either CW laser light from the 514nm line of an Argon ion laser or pulsed laser light from the second harmonic generation of a pulse-picked Ti-sapphire oscillator (4.775 MHz, 400nm, 150fs). PL from

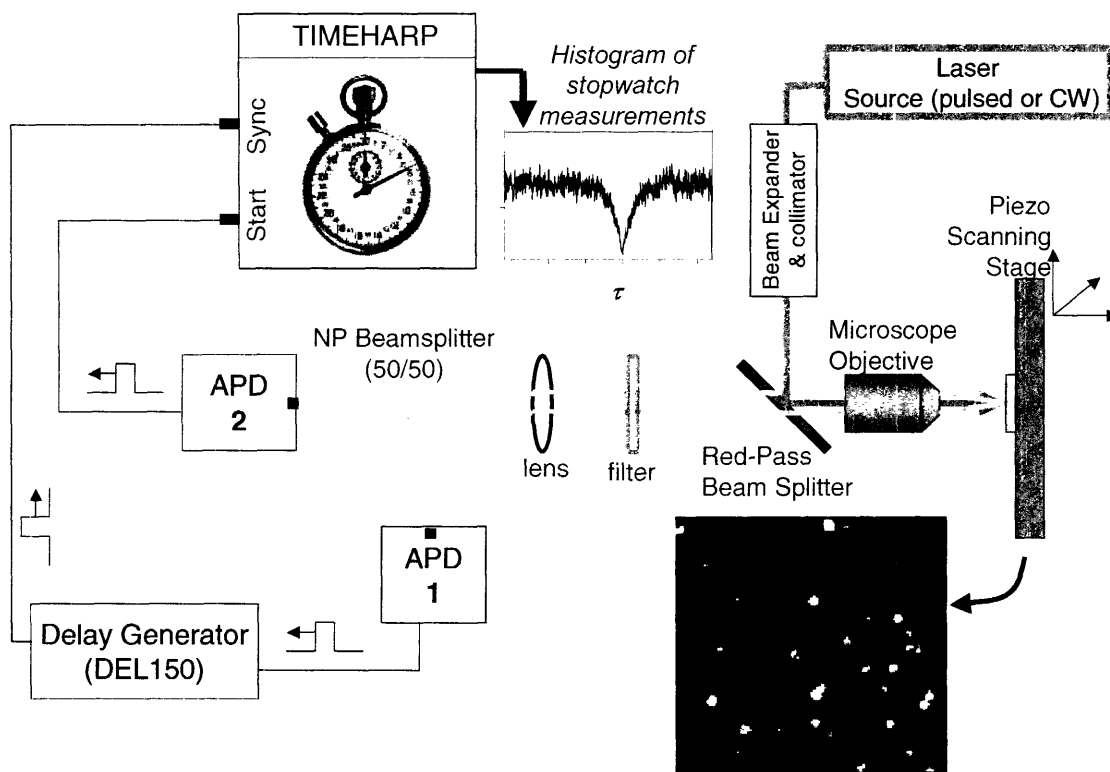


Figure 6.1 Hanbury-Brown and Twiss setup with homebuilt confocal microscope for single photon correlation measurements.

single NCs was sent to a pair of single photon detectors arranged in the Hanbury-Brown and Twiss (HBT) geometry as shown in figure 6.1 (50/50 non-polarizing beamsplitter). A Timeharp200 (Picoquant GmbH) was used to perform correlated the detection events from the APDs, which yielded $h(\tau)$ the histogram of single-photon coincidence events. All single NC measurements were at RT.

The cabling used in these experiments for correlation of single photon detection events is shown explicitly in figure 6.1. TTL pulses corresponding to single photon detection events were passed through the DEL150 delay card for two reasons. First, the TTL pulse generated by the APD was about +3V, whereas the sync input of the timeharp200 requires a negative voltage TTL signal input. The DEL150 is capable of efficiently reversing the polarity of the trigger pulse. Second, the DEL150 provides a delay time for the signal. This allows us to set the propagation time from APD to Timeharp such that it differs by about 300ns for the two APDs. This difference in propagation (Δt_{21}) time allows us to measure both negative and positive time differences between detection events ($\tau = t_{apd2} - t_{apd1}$), even though the Timeharp only measures positive time differences between sync and start inputs ($t_{timeharp} = t_{sync} - t_{start}$). Therefore: $\tau = t_{timeharp} + \Delta t_{21}$. By setting the cabling such that $\Delta t_{21} < 0$, we can measure $\tau < 0$.

6.3 Antibunching and Single Photon Emission from Single CdSe Nanocrystals

Our first experiments confirmed that NCs can indeed act as single quantum emitters even at room temperature. Figure 6.2 presents room temperature HBT measurements of a single NC that is excited by a low-intensity CW laser. Antibunching of the single NC emission is observed as reported previously^{19,20}. In the HBT experiment, an individual photon cannot be divided by the beamsplitter and so it must go

to one detector or another. When the photon is detected by the APD a trigger signal is sent to the Timeharp which is used as a stopwatch to measure the time difference between a single photon hitting APD #1 and another hitting APD #2 (or vice versa for $\tau < 0$). The histogram of these time values results in the curve given in figure 6.2.

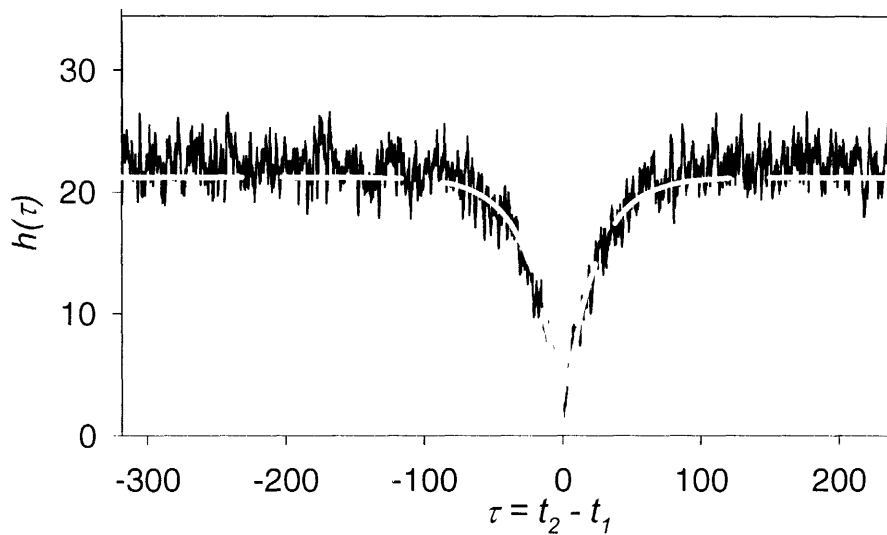


Figure 6.2 $h(\tau)$ for a single NC under CW excitation (60 W/cm^2). $h(\tau=0)/h(\infty) < 0.05$; an exponential fit with a time constant of 23 ns (gray) gives $h(0)/h(\infty) = 0.025$.

If it were the case that the timing between individual photons were Poisson distributed (this would be true for coherent light from a well stabilized CW laser) then the $h(\tau)$ would be constant for all τ . It would be equally likely to have two sequential photons separated by any period of time (for $\tau < 1/\text{cps}$). However, the emission from a single NC under low-intensity CW excitation is seen here to result in a curve that dips to zero at $\tau = 0$. This antibunching results from light whose photon distribution is sub-Poissonian (i.e. its Mandel Q factor is < 0)²¹, meaning that the photons are spaced out from one another as illustrated in figure 6.3. A detailed description of $h(\tau)$, which is

proportional to the second order intensity correlation function, $g^{(2)}(\tau)$, is available elsewhere²².

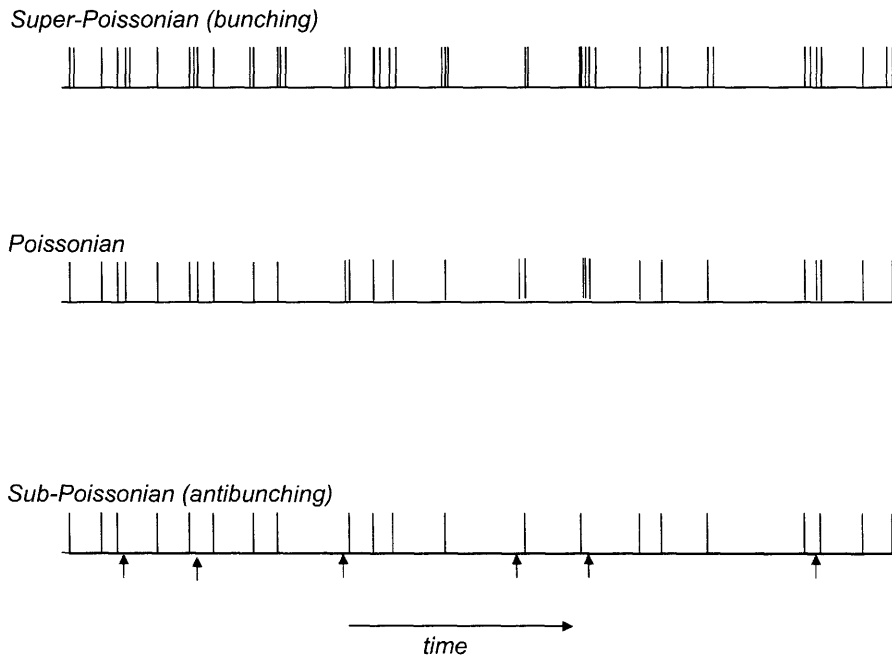


Figure 6.3 Illustration of different photon distributions. Red arrows are examples of photons that are missing in antibunched light, compared to the regular Poissonian distributed light.

Photon coincidence events are suppressed near $\tau=0$ in the emission of a single NC (figure 6.2) because emission of a single photon projects the NC from the single exciton state to the ground state. This means that the NC must wait to be re-excited before it can emit a second photon to complete a coincidence event – it is impossible to recover two photons simultaneously from a NC with a single exciton. This provides strong evidence that the photon sources probed were truly single NCs. Moreover, antibunching of the photons shows that single NCs behave as single quantum emitters even at room temperature.

When the HBT measurement is carried out over larger values of τ , we found that $h(\tau)$ rolls over and begins to decrease again, as reported previously¹⁹. This is shown in

figure 6.4. The reason that $h(t)$ decays at large τ is simple to explain: $h(\tau)$ does not represent the probability that a photon is detected at time τ after the first photon, rather, $h(\tau)$ represents the probability that *the next* photon is detected at time τ after the first photon. Since at long times it becomes less and less likely that no other photon has been detected in the meantime, $h(\tau)$ decreases. The rate of decrease is proportional to the emission intensity of the NC^{19, 22}.

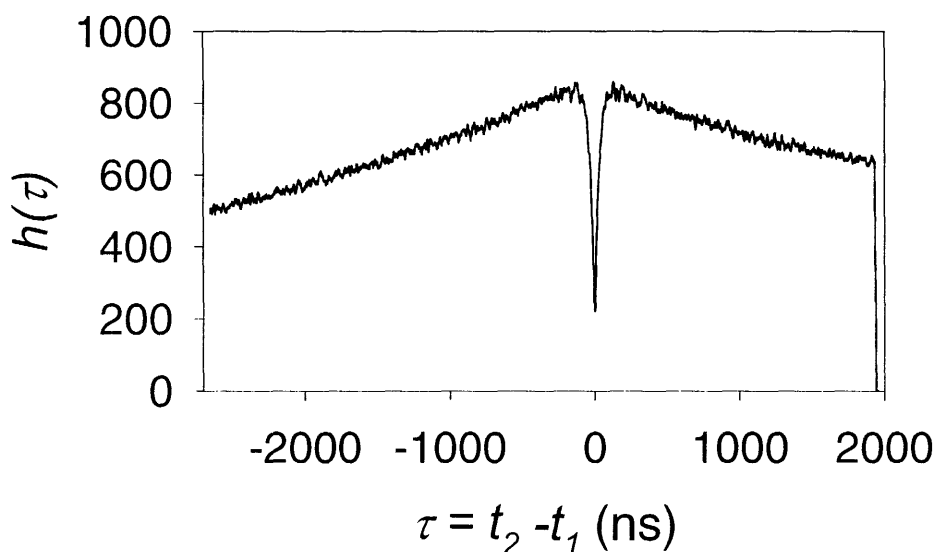


Figure 6.4 HBT measurement of a single NC over long time range showing the decay of both antibunching at small τ and the decay of $h(\tau)$ at large $|\tau|$. Antibunching at $\tau=0$ does not reach zero counts because of insufficient time resolution at this broad time range.

In the introduction we discussed the interest in generating single photons on demand and realizing the so-called photon gun. So far we have demonstrated that single NCs with one exciton behave as single quantum emitters at room-temperature, however their emission of single photons is unpredictable. One way to impose a trigger on the emission time of the single photons from the NC is to trigger the excitation of the NC

using a pulsed laser source. In figure 6.5 we show the results of HBT measurements of single NC emission when it is pumped by a pulsed laser. We see that $h(\tau)$ consists of a series of peaks corresponding to high probability time differences between photon emission. The absence of a peak at $\tau = 0$ indicates that there are never more than one photon emitted from the single NC after excitation by a laser pulse. This result confirms previous reports²³.

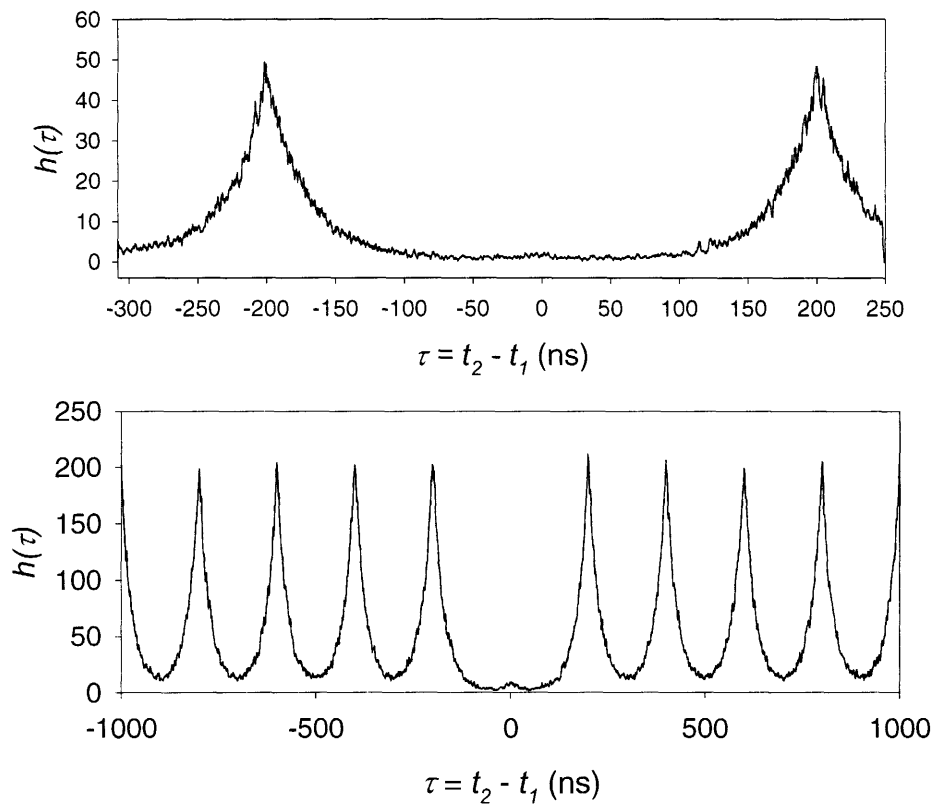


Figure 6.5 Single photon emission at room temperature from a single nanocrystal under pulsed excitation (5 MHz repetition rate). The top and bottom figures show the same measurement taken on different nanocrystals and using different time ranges: 550ns (top) and 2000ns (bottom). In both cases no coincidence events are observed for $\tau=0$ because the single nanocrystal only emits a single photon per excitation pulse.

We know from figure 6.5 that no more than one photon is emitted by the NC per excitation pulse. To minimize the probability that zero photons are emitted after a given excitation pulse we wish to maximize the probability that an exciton is generated in the

NC. This is done by raising the excitation power. However, raising the power causes there to be significant probability that multiexcitons will be generated as well. In the case of small NCs the Auger rate efficiently quenches these multiexcitons so no more than one photon can be emitted per excitation pulse. However, as was shown in the previous two chapters, large NCs can have appreciable radiative quantum yield (QY) values for their multiexciton states. This means that for large NCs, the excitation power should be kept low enough to minimize multiexciton generation, in order to prevent emission of more than one photon per NC.

6.4 Quantum Cascaded Emission from Multiexciton States

In the last section we demonstrated and discussed the behavior of single NCs as quantum emitters and their use in generating triggered single photons. For some applications and fundamental interest it would also be desirable to generate multiple photons for each excitation pulse impinging on a single NC^{2, 21}. For smaller NCs Auger recombination has efficiently quenched multiexcitonic states, preventing emission of more than one photon from a single NC after an excitation pulse²³. However, our demonstration of multiexciton emission from single NCs in chapter 5 implies that we should be able to observe multiphoton emission in HBT measurements of large NCs.

In figure 6.6, using the sample of large NCs (5.1nm radius), we show that it is indeed possible to generate triggered multiphoton emission from single NCs.

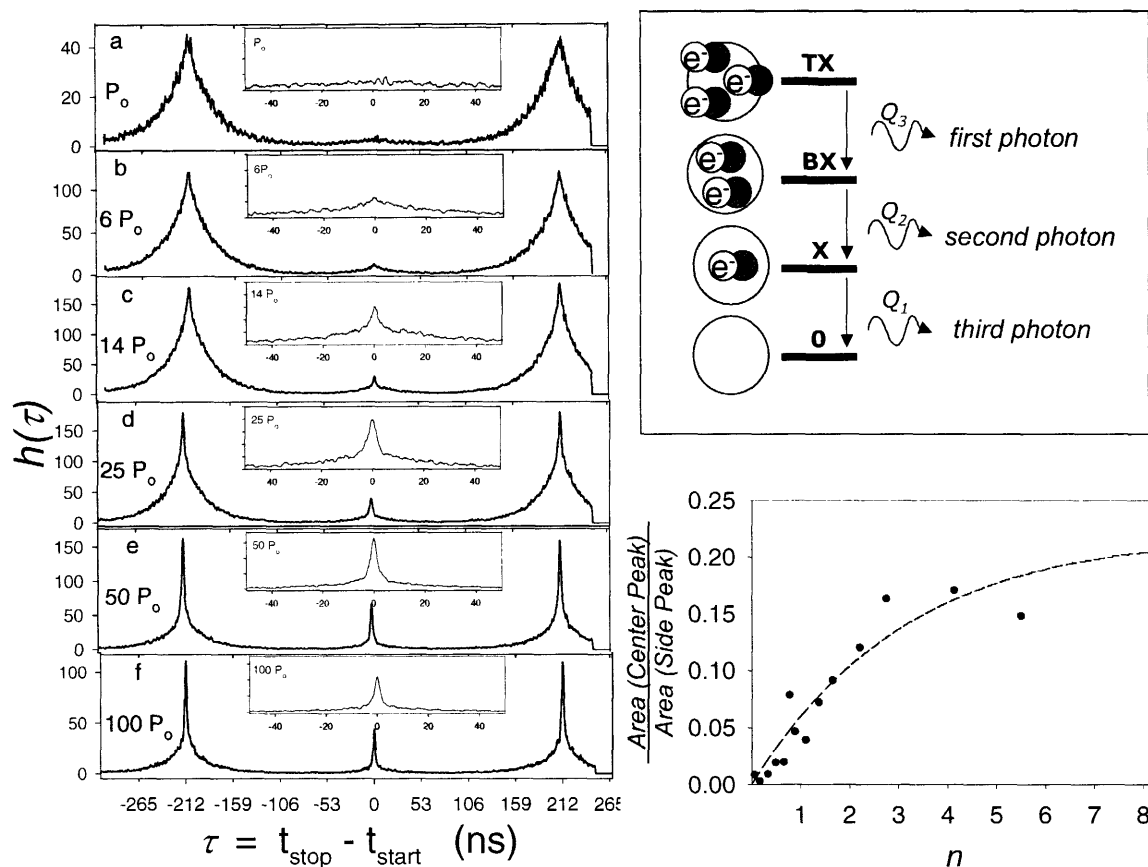


Figure 6.6 (a)-(f) single photon correlation of emission from a *single* NC under increasing excitation intensities. (g) Ratio of center to side peak area versus excitation intensity (solid circles) along with the predicted ratio (dashed line) calculated using a simple 4LS. **Illustration:** Graphical description of the radiative quantum cascade from multiexciton states that lead to multiphoton emission from a single NC.

At low excitation intensities (figure 6.6(a)), less than one exciton is generated in the NC per pulse on average. Therefore the single photon correlation is missing the peak at $\tau=0$ just as in figure 6.5 – no more than one photon was emitted from the NC per excitation pulse. As the excitation intensity is raised, however (figures 6.6(b)–6.6(f), *same* NC), a symmetric center peak appears in $h(\tau)$, indicating that multiple photons are emitted from the single NC after excitation by a single laser pulse. Multiple photons originate from emission out of the single exciton (X) plus the biexciton (BX) and/or triexciton (TX) states of the single NC, which can be accessed only by using higher intensity excitation pulses. The intensity dependence of the multiphoton emission was

quantified in figure 6.6(g) (dots) by the ratio of the areas of the center and side peaks in $h(\tau)$ from the same single NC, taken at various excitation intensities. The ratio of areas was used as a normalization to account for differences in collection time, coincidence rate, etc. that would affect raw peak areas integrated directly from the un-normalized $h(\tau)$.

We investigated the possibility that the center peak observed in figure 6.6 originated from the emission of multiple NCs lying next to one another in the focal region of the microscope.

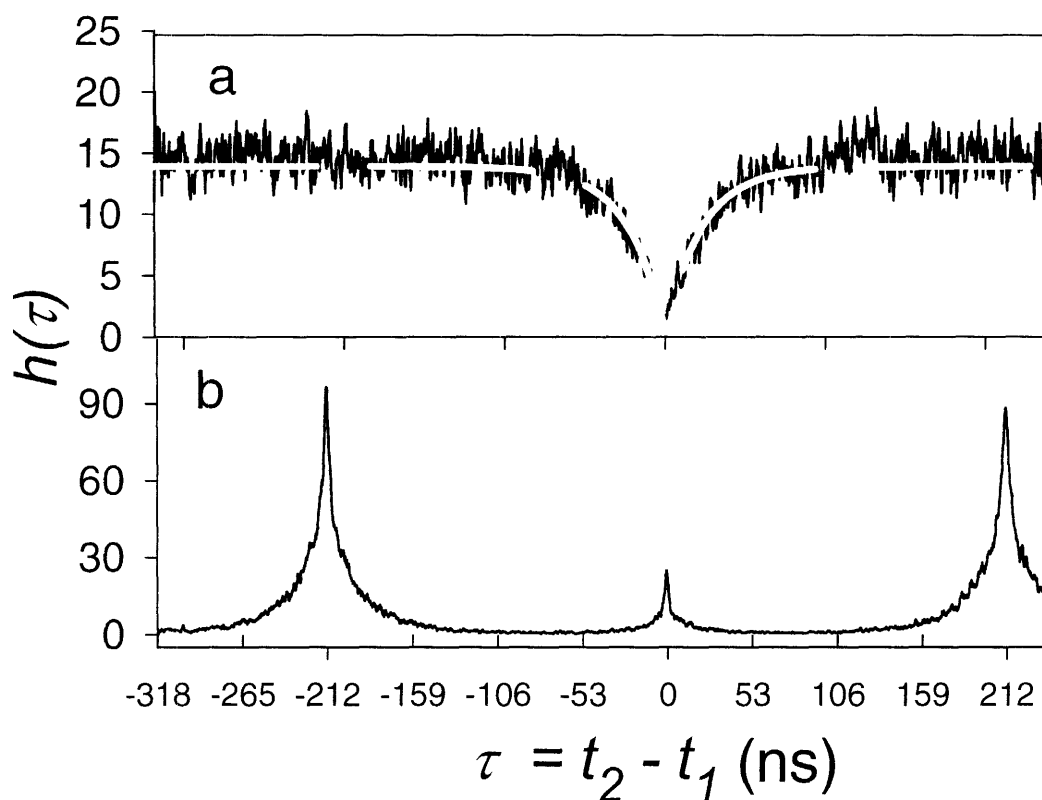


Figure 6.7 Single photon correlation of the emission from the same NC, first under low intensity CW excitation (top), then under higher intensity pulsed excitation (bottom).

In order to verify that the supposed multiphoton emission originated from a *single* NC (and not a pair of NCs) we performed HBT measurements using CW excitation followed by pulsed excitation measurements as shown in figure 6.7. The clean antibunching

observed in figure 6.7 assures us that a single NC is probed. Single photon correlation of the emission from that same NC, this time under pulsed excitation, still results in a center peak at $\tau = 0$, the signature of multiphoton emission.

6.6 Modeling Single Photon Correlation Measurements

Using solutions of the 4LS given in chapter 5 we modeled $h(\tau)$ at different excitation intensities in order to understand the results of figure 6.6. Temporal profiles, $R_i(t)$, of emission from each of the multiexciton states were calculated by multiplying the solutions of equation 5.1 [$p_i(t)$] by the corresponding radiative relaxation rates ($k_i = Q_i \Gamma_i$). The second order correlation function was then calculated for each type of photon coincidence event (e.g. X&BX or X&X, etc.),

$$g_{i,j}^{(2)}(\tau) = \frac{\langle R_i(t) R_j(t + \tau) \rangle}{\langle R_i(t) \rangle \langle R_j(t + \tau) \rangle} - 1 \quad (6.1)$$

where angled brackets indicate time averaging, and $i,j = (1,2,3)$ indicate (X, BX, TX). Finally, the total correlation function measured, $g^{(2)}(\tau)$, was obtained by a weighted average,

$$g_{total}^{(2)}(\tau) = \frac{\sum_{i,j=1}^3 \langle R_i \rangle \langle R_j \rangle g_{i,j}^{(2)}(\tau)}{\langle R_1 + R_2 + R_3 \rangle^2} \quad (6.2)$$

Equations 3 and 4, along with the previously determined decay and quantum yield parameters for this sample ($1/\Gamma_1=29\text{ns}$, $1/\Gamma_2=790\text{ps}$, $1/\Gamma_3=230\text{ps}$, $q_2=0.11$, $q_3=0.4$), allowed modeling of the excitation intensity dependence of the center v. side peak area ratio in figure 6.6(g). The result (dashed line) is superimposed with good agreement on the actual data.

In figure 6.8 the predicted $g^{(2)}(\tau)$ is plotted for the same excitation intensities used in the experiments of figure 6.6 ($g^{(2)}(\tau)$ is rescaled to match $n(\tau)$ at each intensity). We note that a blinking induced reduction of mean Q_I , experimentally observed at high

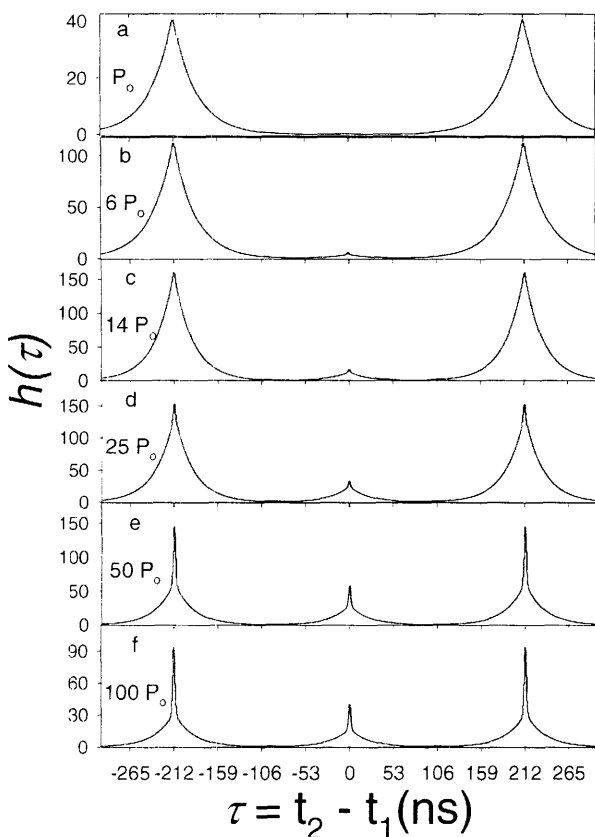


Figure 6.8 4LS model prediction for $h(\tau)$ from a single NC at various excitation intensities.

excitation intensities, was taken into account in modeling the curves at high intensity*.

Given the simplicity of the model, the predicted plots for $g^{(2)}(\tau)$ show a strong similarity to those obtained experimentally.

* The time-averaged emission intensity of the single exciton as measured in the intensity trajectory was seen to decrease during actual experiments. At high excitation intensities the on-intensity of NC emission no longer kept up with increases of excitation power, and the on-times decreased dramatically. To account for this, the parameter Q_I in the 4LS model – a time-averaged measure of single exciton emission – was lowered by $\sim 1/2$.

6.6 Ordered Emission of Photons via Radiative Quantum Cascades

In order to investigate the nature of the multiphoton emission observed in section 6.4, we carried out asymmetric HBT measurements. Figure 6.8 demonstrates that the single NC generates single photons for the X, BX and TX with a definite order. A narrow band pass filter (2.015–2.045 eV) in front of the start detector restricts TX photons to the start detector only, while a long pass filter (1.97 eV cutoff) in front of the stop detector restricts BX and X photons to the stop detector only. In this experimental

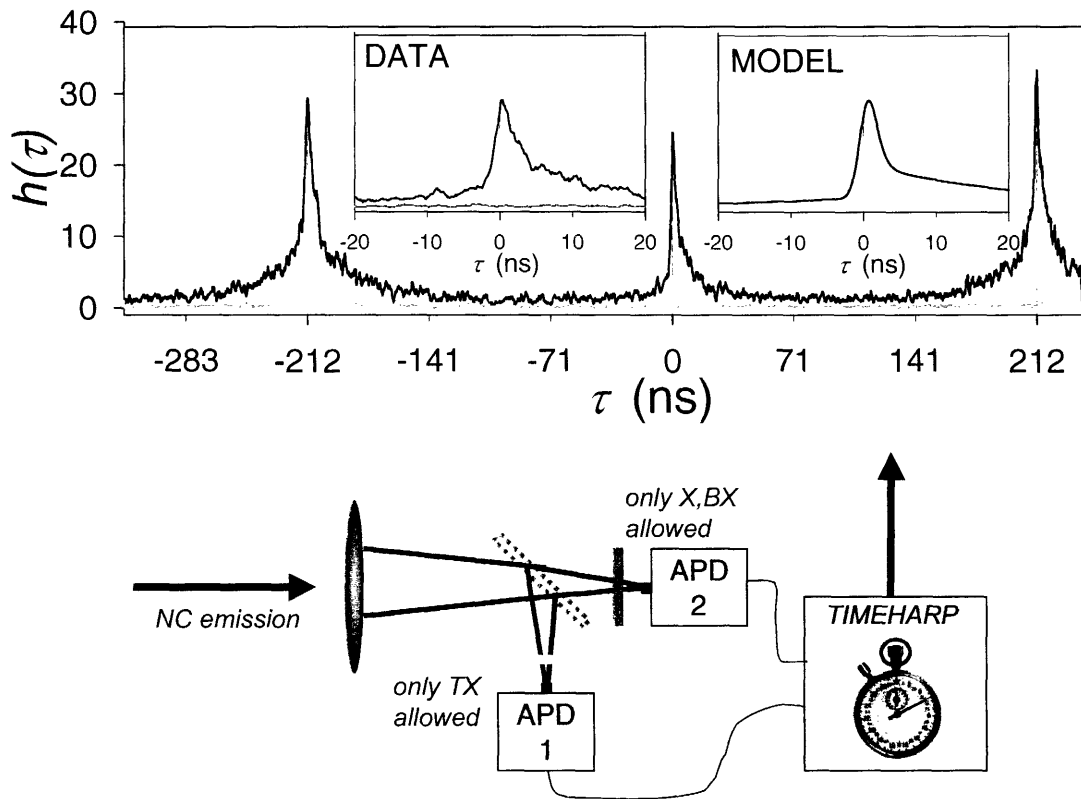


Figure 6.9 *Top*: Black: $h(\tau)$ for asymmetric HBT experiment at high excitation fluence ($120 \mu\text{J}/\text{cm}^2$; $\bar{n} \sim 4.5$ exciton per NC per pulse). Gray: $h(\tau)$ at low excitation fluence ($<20 \mu\text{J}/\text{cm}^2$) using same setup. *Left inset*: close up of $h(\tau)$. *Right Inset*: $h(\tau)$ predicted by the 4LS model for a single NC under high intensity excitation. Vertical cursors: laser rep. rate. Ordered multiphoton emission from a radiative quantum cascade is indicated by the asymmetric center peak of $h(\tau)$. *Bottom*: schematic of asymmetric HBT setup used in this experiment.

configuration practically no coincidence events are observed at low intensity, because the TX is not generated. At high excitation intensity, however, an *asymmetric* center peak is

obtained. The asymmetry is observed because TX photons necessarily precede BX and X photons — the photon emission is ordered. The asymmetric peak agrees with the simple 4LS model, as shown in the right inset of figure 6.9.

6.7 Photon Pair Generation Using Nanorods

Because of the known strong dependence of multiexciton lifetime (and QY) on nanocrystal volume²⁴, it is expected that one-dimensional rod-shaped nanocrystals, nanorods (NRs), of CdSe should show even stronger generation of multiphoton emission.

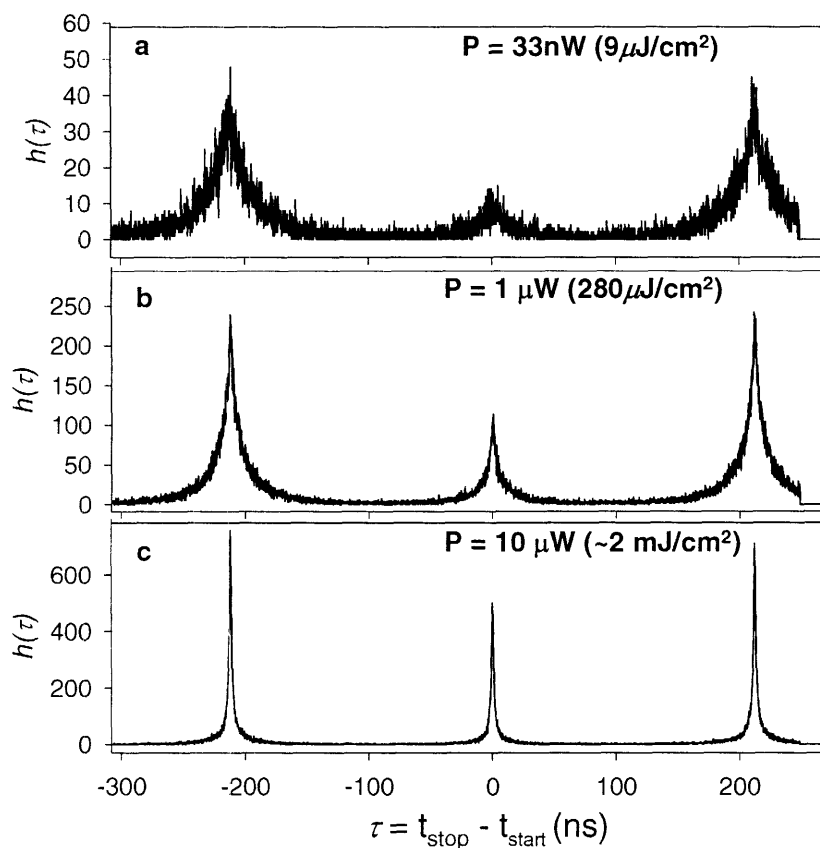


Figure 6.10 $h(\tau)$ for a single nanorod under pulsed excitation at various excitation intensities. The two arms of the HBT setup are identical so the peaks are symmetric.

Indeed, longer Auger lifetimes have been reported for nanorods²⁵. Figure 6.9 shows $h(\tau)$ measured from a single NR at three progressively higher excitation intensities using a symmetric HBT setup. Even at excitation intensities that would be low for a spherical

NC (figure 6.10(a)), a center peak is observed for two main reasons. First, the NR is physically larger and has a correspondingly larger absorptive cross-section than the NC, leading to more efficient multiexciton generation. Second, the larger volume of the NR leads to a slower Auger recombination²⁵ and consequently higher QY of multiexciton fluorescence. At higher excitation intensities, shown in figures 6(b) and 6(c), the multiphoton generation and emission dominates coincidence events, resulting in sharp peaks at $\tau=0$. Since nanocrystals of all shapes, sizes and materials can be synthesized, these data show that the non-classical light generation properties of the NC can be tailored.

6.8 Conclusions

The observation of multiexciton emission leading to non-classical photon pair generation by single spherical and rod-shaped NCs is an interesting development because unavoidable Auger quenching has been thought to preclude these materials as a viable source of n -photon states. These results show that the strength of Auger quenching, tuned by the volume of the NC, can actually be used to tailor the NC for single photon or photon pair production. Should single photons be desired, smaller NCs with efficient Auger relaxation allow the NC to be pumped hard, guaranteeing generation of at least one exciton per pump pulse. Any multiexcitons will be quenched leading to one and only one photon emitted per trigger pulse²³. If on the other hand, multiple photons per trigger pulse are desired, a NC with larger volume can be chosen which will have a significant QY for the multiexciton states leading to photon pair (or triplet, etc.) emission for each pump pulse. We note that the development of rod-shaped NCs allows researchers to tune

the Auger rate of the NC by changing the volume, without varying the radius of the rod and altering the band-edge energy of emission.

The rate of single photon or photon-pair generation is also of interest. If we are interested in photon pairs consisting of a photon from the BX and a photon from the X then the average rate (f_{pair}) of pair generation, using a 10MHz pump laser, would be approximately: $f_{pair(BX+X)} = f_{pump} Q_1 Q_2 P_{>2}^o \approx 500kHz$. This rate may be competitive with pair generation rates of current methods such as parametric down-conversion, however, at this time the extremely fast dephasing time²⁶⁻²⁸ of excitons in NCs still precludes any coherence or entanglement between the constituent photons of n -photon states generated by the NCs.

The long-term photostability as well as the well-known blinking phenomenon of NCs²⁹⁻³¹ also remain barriers to the practical implementation of these materials for generation of n -photon states. The samples investigated in this work still exhibited blinking and often bleached after many minutes of high intensity excitation. Nonetheless, given that we can now observe multiexciton emission from single NCs – a previously disregarded possibility because of Auger quenching – we are optimistic that continued development of these materials and studies of the blinking phenomenon can circumvent this problem making NCs a practical, inexpensive source of n -photon states at room temperature.

6.9 Addendum: Summary of Results for Various Single NC Samples

The data presented in this chapter represent primarily data collected from just a few samples. However, numerous others were studied. NCs with large volumes generally showed appreciable multiexciton emission, while smaller NCs exhibited very little. A qualitative description of results across a spectrum of samples is given in the table below.

Sample	r (nm)	λ (emission, nm)	MX evidence in HBT experiment?	MX evidence in Ensemble Transient Spectrum
A	5.1	655	Yes, Strong	Yes, Strong
B	2.6	605	very weak, rarely seen	Weak
C	5	653	Yes, Strong	Yes, Strong
D	3.4	630	NA	moderate
E	2.8	610	very weak, seen only once	weak
F	3.8	637	Strong	moderately strong
G	~8	670	NA	weak
H	2.8	610	NA	weak to moderate

Sample A is the sample whose data are presented in this chapter.

6.10 References

- 1 G. Brassard, N. Lutkenhaus, T. Mor, et al., *Physical Review Letters* **85**, 1330 (2000).
- 2 N. Gisin, G. Ribordy, W. Tittle, et al., *Reviews of Modern Physics* **74**, 145 (2002).
- 3 H. J. Kimble, M. Dagenais, and L. Mandel, *Physical Review Letters* **39**, 691 (1977).
- 4 R. Short and L. Mandel, *Physical Review Letters* **51**, 384 (1983).
- 5 F. Diedrich and H. Walther, *Physical Review Letters* **58**, 203 (1987).
- 6 T. Basche, W. E. Moerner, M. Orrit, et al., *Physical Review Letters* **69**, 1516 (1992).
- 7 C. Becher, A. Kiraz, P. Michler, et al., *Physical Review B* **63**, 121312 (2001).
- 8 V. Zwiller, H. Blom, P. Jonsson, et al., *Applied Physics Letters* **78**, 2476 (2001).
- 9 C. Santori, M. Pelton, G. Solomon, et al., *Physical Review Letters* **86**, 1502 (2001).
- 10 A. Kiraz, S. Falth, C. Becher, et al., *Physical Review B* **65**, 161303 (2002).
- 11 E. Moreau, I. Robert, L. Manin, et al., *Physical Review Letters* **87**, 183601 (2001).
- 12 C. Santori, D. Fattal, M. Pelton, et al., *Physical Review B* **66**, 045308 (2002).
- 13 S. M. Ulrich, S. Strauf, P. Michler, et al., *Applied Physics Letters* **83**, 1848 (2003).
- 14 J. Persson, T. Aichele, V. Zwiller, et al., *Physical Review B* **69**, 233314 (2004).
- 15 D. Fattal, K. Inoue, J. Vuckovic, et al., *Physical Review Letters* **92**, 037903 (2004).
- 16 V. Zwiller, T. Aichele, W. Seifert, et al., *Applied Physics Letters* **82**, 1509 (2003).
- 17 Z. A. Peng and X. A. Peng, *Journal of the American Chemical Society* **124**, 3343 (2002 Supplemental Information).
- 18 B. O. Dabbousi, J. Rodriguez-Viejo, F. V. Mikulec, et al., *Journal of Physical Chemistry B* **101**, 9463 (1997).

- ¹⁹ B. Lounis, H. A. Bechtel, D. Gerion, et al., *Chemical Physics Letters* **329**, 399 (2000).
- ²⁰ P. Michler, A. Imamoglu, M. D. Mason, et al., *Nature* **406**, 968 (2000).
- ²¹ M. Kolobov, *Reviews of Modern Physics* **71**, 1539 (1999).
- ²² M. Orrit, *Single Molecules* **3**, 255 (2002).
- ²³ X. Brokmann, E. Giacobino, M. Dahan, et al., *Applied Physics Letters* **85**, 712 (2004).
- ²⁴ V. I. Klimov, A. A. Mikhailovsky, D. W. McBranch, et al., *Science* **287**, 1011 (2000).
- ²⁵ H. Htoon, J. Hollingsworth, R. Dickerson, et al., *Physical Review Letters* **91**, 227401 (2003).
- ²⁶ R. W. Schoenlein, D. M. Mittleman, J. J. Shiang, et al., *Physical Review Letters* **70**, 1014 (1993).
- ²⁷ D. M. Mittleman, R. W. Schoenlein, J. J. Shiang, et al., *Physical Review B* **49**, 14435 (1994).
- ²⁸ M. R. Salvador, M. A. Hines, and G. D. Scholes, *Journal of Chemical Physics* **118**, 9380 (2003).
- ²⁹ S. A. Empedocles, R. G. Neuhauser, K. T. Shimizu, et al., *Advanced Materials* **11**, 1243 (1999).
- ³⁰ B. R. Fisher, H. J. Eisler, N. E. Stott, et al., *Journal of Physical Chemistry B* **108**, 143 (2004).
- ³¹ K. T. Shimizu, R. G. Neuhauser, C. A. Leatherdale, et al., *Physical Review B* **63**, 205316 (2001).

Chapter 7: Resolution of Biexciton Emission from CdSe Nanocrystals

- 7.1 Introduction
- 7.2 Detection of Biexciton Emission: Signal Intensity
- 7.3 Detection of Biexciton Emission: Spectral Resolution
- 7.4 Methods
- 7.5 Biexciton Emission in single NC Fluorescence
- 7.6 Biexciton Emission in FLN Spectra
- 7.7 Conclusions
- 7.8 References

7.1 Introduction

One of the most important overall results of this thesis is the observation of multiexciton emission in various ensemble and single nanocrystal (NC) experiments. Although experiments in previous chapters succeeded in spectrally resolving the triexciton (TX) emission, biexciton (BX) emission overlapped the single exciton (X) emission at the band edge and was not spectrally resolved. The reason is that both the first and second excitons occupy the same electronic level in the nanocrystal ($1S_c$), save for a slight perturbation of the BX energy, which originates from a Coulombic interaction between the two excitons. This BX Coulomb energy is much less than the band-edge emission bandwidth at room temperature, so the BX cannot be spectrally resolved from the X easily.

Spectral resolution of the BX is an important goal in the study of CdSe nanocrystals because it would allow experiments to study the behavior of biexcitons independently of single excitons. This has already been possible for a long time in semiconductor quantum dots, which are related to nanocrystals. One study, for instance, measured the relative intensity and lifetime for BX and X emission, simultaneously from

a single CdSe quantum dot¹. In this experiment a BX-X splitting of 18.5meV was reported and the lifetimes of the two states were found to be very similar. In another experiment spectral resolution of BX emission from a single quantum dot allowed the study of the polarization of BX emission relative to that of the single exciton². Indeed a plethora of single quantum dot studies of multiexciton emission testify to the understanding of nanocrystal physics that stands to be gained through spectrally resolving the BX³⁻⁵. Besides interest in the fundamental spectroscopy of nanocrystals, direct study of the BX is also of practical interest since the BX plays a critical role in applications and phenomena of nanocrystals such as lasing and blinking. Nanocrystal-titania composite lasers use stimulated emission of the BX for gain^{6,7}, and the on-off blinking phenomenon of single nanocrystals is thought to be driven in part by generation of the BX state⁸⁻¹¹.

Although we did not spectrally resolve the BX in our previous experiments, time resolved studies of the band-edge luminescence decay from single nanocrystals and solutions of nanocrystals allowed us to derive important parameters, including quantum yield (QY) values. Motivated by higher than expected values of the BX quantum yield (Q_2) for very large nanocrystals ($Q_2/Q_1 \equiv q_2 \sim 0.1$ for 5.1nm radius NCs, chapter 4,5), we seek in this chapter to lay the foundation for fundamental studies of the BX by spectrally resolving its emission. Our primary goals are, first, to investigate the possibility of spectral resolution and second to achieve it. Subsequent studies may then exploit the resolution of BX emission to understand physics such as BX polarization or the size dependence of the Coulomb binding energy in nanocrystals.

7.2 Detection of Biexciton Emission – Signal Intensity

Realizing that ultrafast, non-radiative Auger relaxation of multiexcitonic states in nanocrystals can potentially disable our ability to detect multiexciton emission of nanocrystals, we first investigated the expected emission intensity of the BX state of a single nanocrystal. We modeled this assuming either pulsed or CW excitation. In the case of pulsed excitation, the four level system (4LS) used in chapters 4, 5 and 6 is appropriate. The experiments presented in this chapter used CW excitation so we present a modification of the 4LS for CW excitation. Figure 7.1 illustrates the model of dynamics between different multiexcitonic states for a NC under CW excitation.

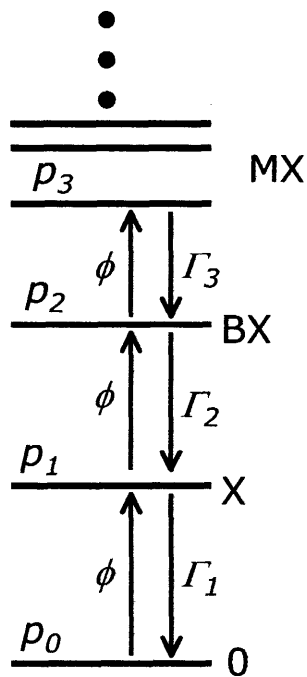


Figure 7.1 Illustration of four level model used to calculate expected emission intensities for CW experiments

New excitons are generated in the NC at a steady rate, ϕ , which is the product of P , the excitation power and α , which was defined in chapter 4 as the ratio of the absorptive

cross section (σ) and the illumination spot size (A_{focus}) divided by the energy per excitation photon:

$$\alpha = \frac{\lambda_{excitation}}{hc} \frac{\sigma}{A_{focus}} \quad (7.1)$$

Relaxation of multiexciton states is given by the lifetimes of the states, which were measured for numerous samples of nanocrystals earlier. The kinetic equations describing the model shown in figure 7.1 are:

$$\begin{aligned} \frac{dp_0(t)}{dt} &= \Gamma_1 p_1(t) - \phi p_0(t) \\ \frac{dp_1(t)}{dt} &= \phi p_0(t) + \Gamma_2 p_2(t) - (\phi + \Gamma_1) p_1(t) \\ \frac{dp_2(t)}{dt} &= \phi p_1(t) + \Gamma_3 p_3(t) - (\phi + \Gamma_2) p_2(t) \\ \frac{dp_3(t)}{dt} &= \phi p_2(t) - \Gamma_3 p_3(t) \end{aligned} \quad (7.2)$$

where $p_i(t)$ denotes the probability of the nanocrystal having i excitons. We are interested in the intensity of emission from the i -exciton state, which is given at time, t , by the product of $p_i(t)$ and the radiative decay rate from that state. Since we are focusing on CW experiments we can make the steady-state approximation when solving equations 7.2 – $dp_i(t)/dt = 0$ for all i – so the solutions have no time dependence. This assumption along with the restriction that probabilities sum to unity leads to the solutions:

$$\begin{aligned}
p_0 &= \left(1 + \frac{\phi}{\Gamma_1} + \frac{\phi^3}{\Gamma_1\Gamma_2\Gamma_3} + \frac{\phi^2}{\Gamma_1\Gamma_2} \right)^{-1} \\
p_1 &= \left(\frac{\Gamma_1}{\phi} + 1 + \frac{\phi^2}{\Gamma_2\Gamma_3} + \frac{\phi}{\Gamma_2} \right)^{-1} \\
p_2 &= \left(\frac{\Gamma_1\Gamma_2}{\phi^2} + \frac{\Gamma_2}{\phi} + 1 + \frac{\phi}{\Gamma_3} \right)^{-1} \\
p_3 &= \left(\frac{\Gamma_1\Gamma_2\Gamma_3}{\phi^3} + \frac{\Gamma_1\Gamma_2}{\phi^2} + \frac{\Gamma_3}{\phi} + 1 \right)^{-1}
\end{aligned} \tag{7.3}$$

The power dependence of these solutions is contained in the parameter ϕ . Using reasonable parameters, we can calculate these probabilities as a function of average excitation power at 514nm. This is shown in figure 7.2. In this modeling, we chose parameters obtained from a sample of nanocrystals studied earlier that had strong multiexciton emission (Quantum Dot Corp., 5.1nm radius). The decay rates, Γ_1 , Γ_2 , Γ_3 were 1/29ns, 1/790ps, and 1/230ps respectively, and the cross section at 514nm was calculated to be $4.5 \times 10^{-15} \text{cm}^2$ using previously reported methods¹².

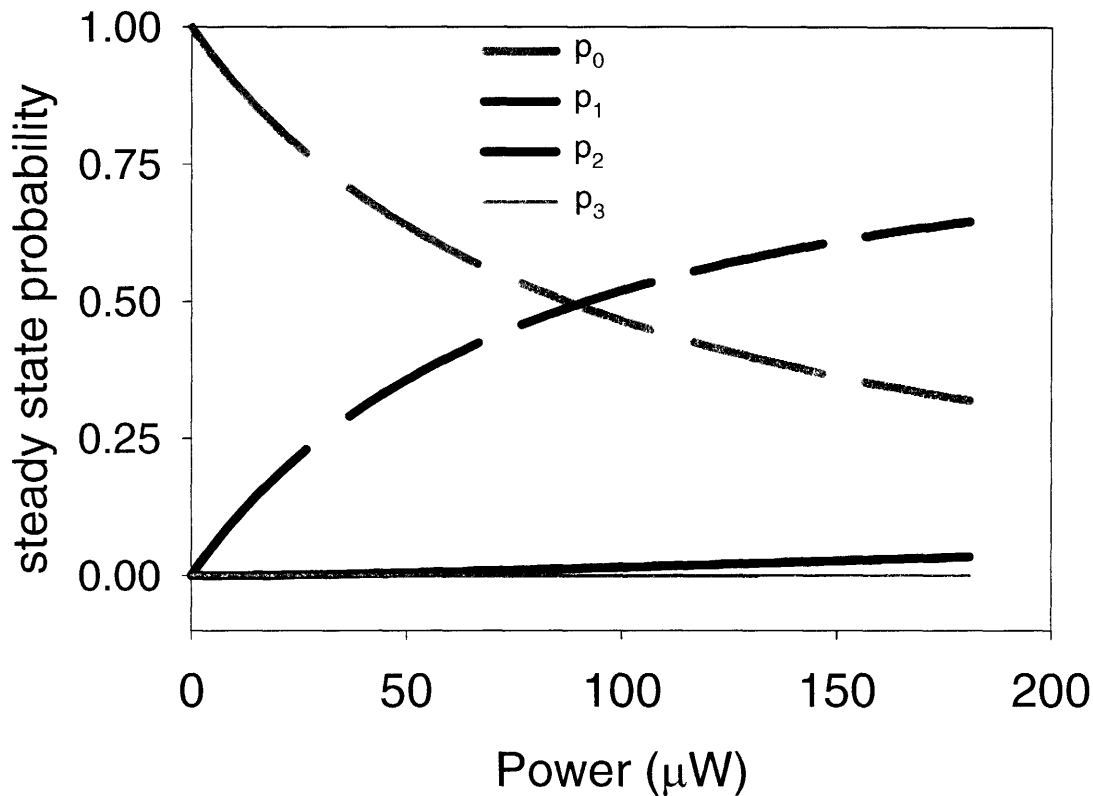


Figure 7.2 Calculated occupation probabilities of the four different levels of the model system in the steady state over a range of continuous illumination powers. A cross section of $4.5 \times 10^{-15} \text{cm}^2$ at 514nm and spot size of $1 \mu\text{m}$ radius is used for this calculation.

Figure 7.2 covers a range of excitation power that extends significantly higher than the range typically used for confocal microscopy, yet generation of the BX state is still very weak compared to the single exciton. However these powers are easily accessible to the experiment so significant BX generation capacity is available. To calculate actual emission intensities, we multiplied the results, p_i , by the radiative emission rate, $\Gamma_i Q_i$ for each state i . Q_1 was assumed to be 0.75 as measured in chapter 4 for the 5.1nm nanocrystal sample, and Q_2 and Q_3 were obtained using the relative quantum yield values, $Q_2/Q_1 \equiv q_2 = 0.1$ and $Q_3/Q_1 \equiv q_3 = 0.04$ that were obtained for the same sample in chapter 4. This calculation of BX and X emission intensities is shown in figure 7.3.

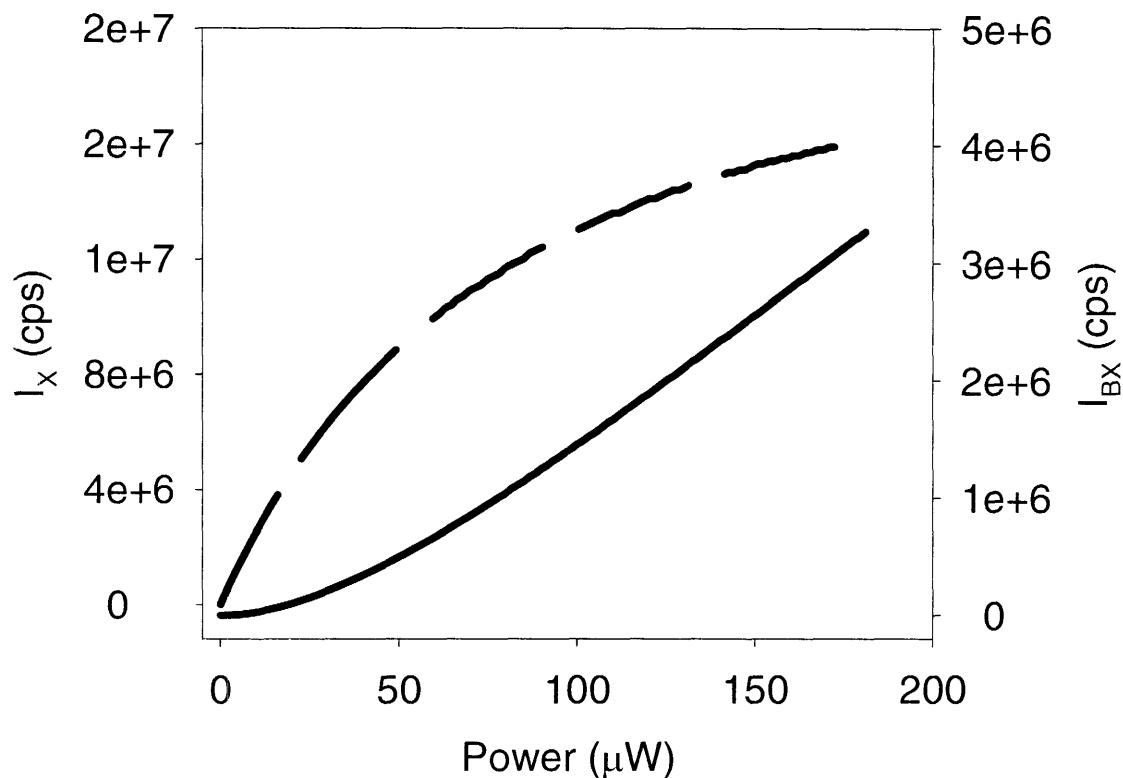


Figure 7.3 Calculated intensity of BX and single exciton emission as a function of excitation power. These emission intensities are based on the occupation probabilities shown in figure 7.2 with $q_2 = 0.1$ and decay times of 29ns and 790ps for the X and BX respectively. For a spot size of $1\mu\text{m}$ radius the intensity of $200\mu\text{W}$ is 6300 W/cm^2 .

At low excitation powers single exciton emission varies linearly with power and BX emission varies quadratically. However at higher intensity excitation, the single exciton emission saturates and BX emission intensity varies linearly with power. A simpler power dependence is obtained for the ratio of the emission intensities of the BX and single exciton, which is shown in figure 7.4. The linear increase of I_{BX}/I_X indicates that at a sufficiently high power the BX emission should be strong compared to X emission, but the slope of this line is proportional to q_2 . Therefore we chose a sample with very high BX quantum yield for our experiments.

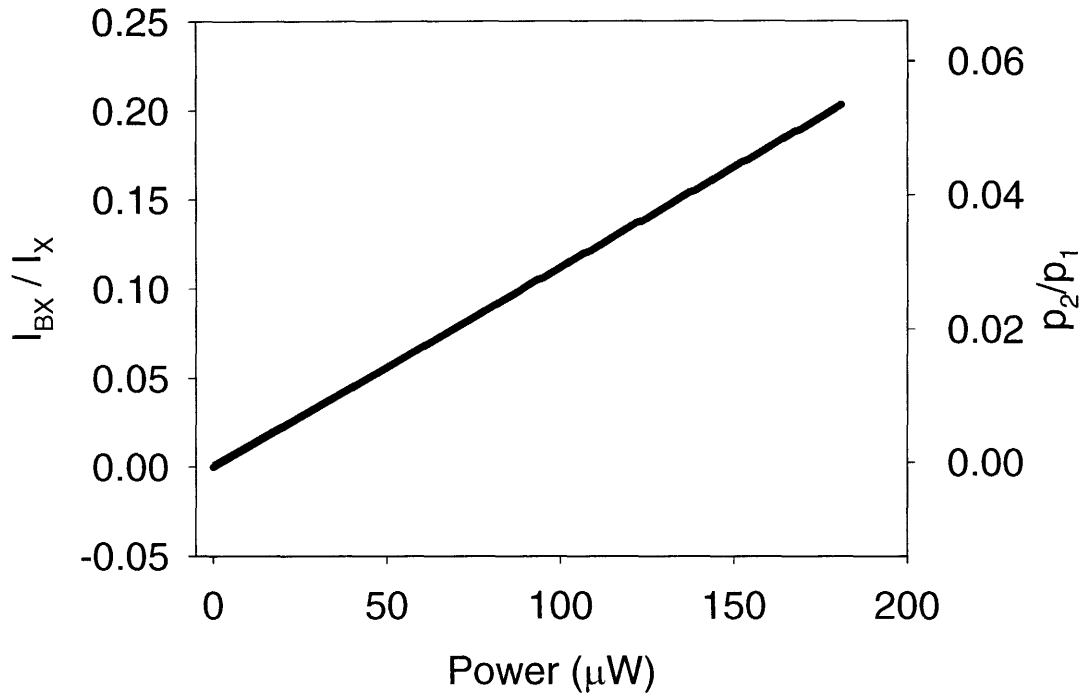


Figure 7.4 Ratio between BX and X occupation probabilities and emission intensities as a function of excitation power for a $1\mu\text{m}$ spot size and $4.5 \times 10^{-15} \text{ cm}^2$ cross-section at 514nm.

7.3 Detection of Biexciton Emission: Spectral Resolution

In the last section a simple model helped us determine that the intensity of BX emission ought to be large enough to be significant compared to single exciton emission if the excitation intensity is high enough. The second fundamental requirement we must meet is spectral resolution of the BX. We now address how large of a splitting should be expected between the BX and the X.

When two excitons are present in a semiconductor a Coulomb force between them causes the energy of the 2-exciton state (BX) to be relaxed slightly so that the energy released by whichever exciton relaxes first is slightly red-shifted. In *bulk* CdSe this BX binding energy – the Coulombic attraction between two excitons – is rather small:

$\sim 1.2\text{meV}$ ¹³. However, because of quantum confinement the distance between two excitons in a NC is forced to be small, and the Coulombic interaction is consequently larger. This means that the BX binding energy ought to be larger for nanocrystals. Previous work on self assembled CdSe and CdS quantum dots indicates that this is the case with 20-30meV splitting between the BX and X energies reported¹⁴⁻¹⁷. Theoretical work also predicted enhanced BX binding energies for CdSe nanocrystals¹⁸. Furthermore, in chapter 4 we presented transient spectra of solutions of nanocrystals that showed multiexciton emission. In that case the band edge emission was observed to blue shift slightly at between zero and one nanosecond. This shift was attributed to the decay of the BX (whose emission should be red-shifted from the single exciton) during the first nanosecond. For the 2.3nm nanocrystals shown in figure 4.1(c), the shift was approximately 30meV, which is much larger than the bulk value. For the experiments we propose in this chapter we want to use much larger nanocrystals because they have slower Auger rates and higher multiexciton quantum yields. One previous work reported the BX binding energy for a size series of smaller CdSe nanocrystals (up to 3.4nm)¹⁹ using indirect methods. These results, derived from the slight blue-shift during the first 100ps of the band edge transient emission spectrum of ensembles, are shown in figure 7.5. By extending the trend they observed to 5.1nm – the size of NCs to be used in this chapter – a BX binding energy of 10meV is obtained.

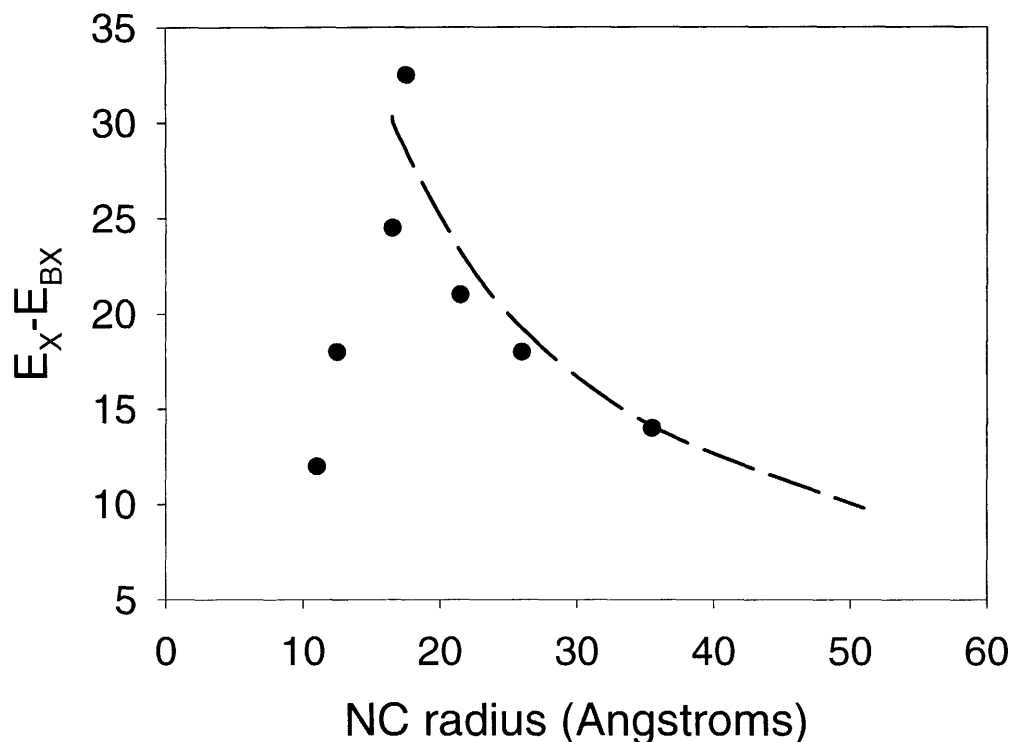


Figure 7.5 Biexciton-Exciton splitting energies of CdSe NCs obtained by fluorescence up-conversion using ensemble solution samples¹⁹.

7.4 Methods

Since the binding energy of the BX is so much smaller than the bandwidth of room temperature band-edge luminescence our experiments must narrow the non-homogenous broadening of the nanocrystal luminescence. The two major sources of nonhomogenous broadening of nanocrystal emission are high temperature (i.e. room temperature) and polydispersity of sizes in the sample. Carrying out experiments at liquid helium temperatures addresses temperature driven broadening. To narrow the distribution of sizes interrogated in the experiments, two methods are used in this chapter: fluorescence line narrowing (FLN) and single NC spectroscopy. FLN experiments use an excitation wavelength that is nearly resonant with the emission so that only the largest

(i.e. lowest energy) nanocrystals of an ensemble are excited²⁰. In practice this means that the excitation laser wavelength is tuned to the red edge of the full (non-resonantly excited) band-edge PL spectrum. Using this technique on NCs, linewidths of just a few meV, can be achieved. Single nanocrystal spectroscopy, obviously, is the ultimate limit of narrowing the size distribution as only a single nanocrystal is interrogated. This technique results in line widths that can be less than 1 meV, but has the well known drawback of spectral diffusion, whereby the emission spectrum of the nanocrystal spontaneously shifts its emission energy up and down over the course time^{21, 22}.

The sample of nanocrystals used in these experiments is the same high multiexciton quantum yield sample used in previous chapters – 5.1 nm radius CdSe/ZnS core/shell nanocrystals obtained from Quantum Dot Corporation. Sample preparation for single nanocrystal experiments was the same as in previous chapters (3,5,6) except for two differences. First, in order to get the best thermal contact between the nanocrystals and the substrate no polymer matrix was used for spin coating. Second, only single crystal quartz substrates were used (~0.2 mm thick) to insure that good thermal conductivity between the nanocrystals and cold finger is maintained. Samples for FLN were prepared on single crystal quartz substrates as well. However, these thin film samples used a polymer matrix to obtain high spatial densities of nanocrystals without bringing the individual nanocrystals into contact with one another (necessary to prevent interdot Förster energy transfer which occurs in close-packed films^{23, 24}). Poly-(lauryl methacrylate) (PLMA) was chosen for these films because it minimized phase segregation between the nanocrystals and the polymer matrix, which was observed for high densities of nanocrystals in PMMA.

In figure 7.6 the basic setup of the confocal microscope, which is used for both FLN and single nanocrystal experiments, is shown. Since the sample is contained inside of a cryostat for low temperature experiments, galvo-mirrors are used to scan images of the sample, and a lower NA (0.7) objective is used to accommodate the longer working distance (same objective as low temperature experiments of chapter 4). The collected light is split between the APD (for imaging the NCs) and the spectrograph/CCD (to

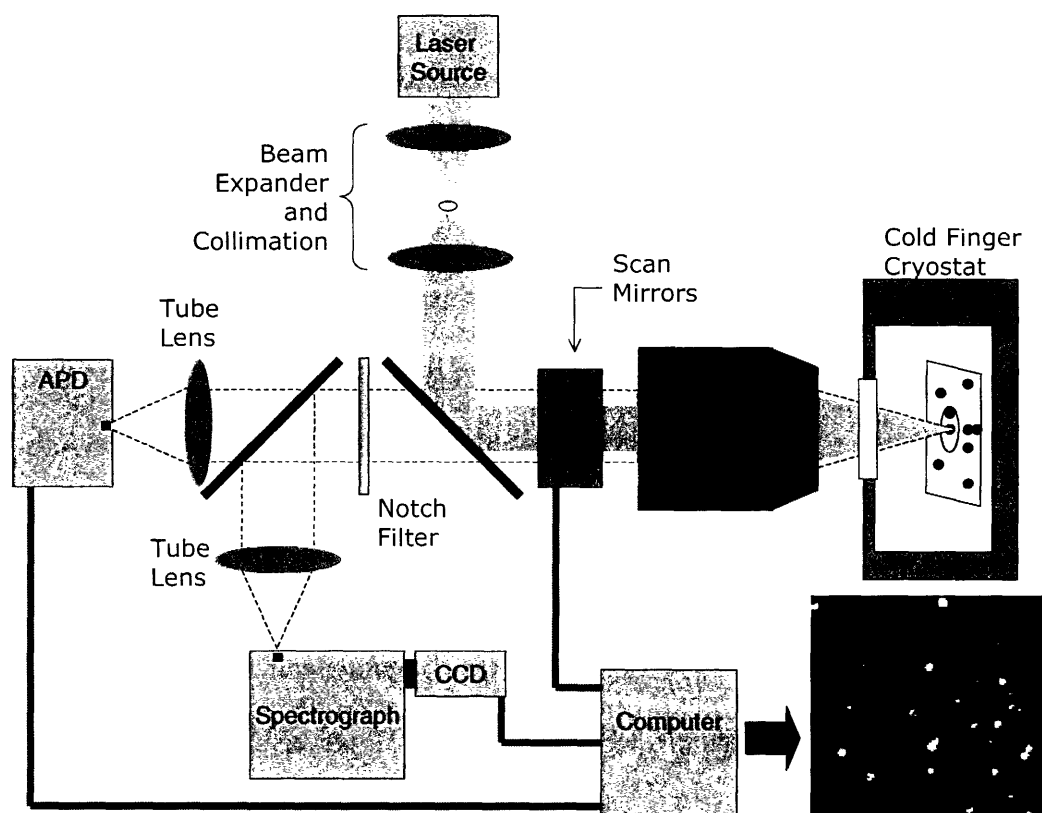


Figure 7.6 Confocal microscope setup used for FLN and single nanocrystal experiments in this chapter.

obtain the spectrum of light collected at a given point in the sample). Since non-resonant excitation (Argon Ion Laser, 514nm CW) was used for single nanocrystal experiments, a dichroic red-pass beamsplitter was used to couple the excitation and detection arms. In FLN experiments, however, a polarizing beam splitter (PBS) was used for this purpose. The PBS was advantageous for FLN because the reflected excitation is polarized and a

majority of it is reflected out of the collection path, whereas fluorescence emission from the nanocrystal ensembles is non-polarized and is evenly split by the PBS. This maximized the fluorescence relative to reflected or scattered excitation light in the collection arm of the microscope, which is necessary in FLN since spectral filters (e.g. band-pass filters) generally cannot distinguish excitation light from fluorescence under resonant excitation conditions.

It was mentioned earlier that one disadvantage of spectroscopy on single nanocrystals is the phenomenon of spectral diffusion. Since spectral diffusion tends to become more rapid at higher excitation intensities, we expected it would be difficult to carry out a study of excitation intensity dependence of the spectrum. As the power is increased spectral diffusion will usually cause it to quickly shift red and blue, potentially within the CCD exposure that measures the spectrum. Therefore we constructed a simple method of synchronizing CCD measurements of the emission spectrum with live measurement of the excitation intensity. This allowed us to quickly vary the excitation intensity over large ranges within a few seconds with the intensity corresponding to each spectrum automatically recorded. The chance of obtaining an intensity dependence of the spectrum, free of large spectral diffusion, is dramatically improved by this simple technique, which is illustrated in figure 7.6.

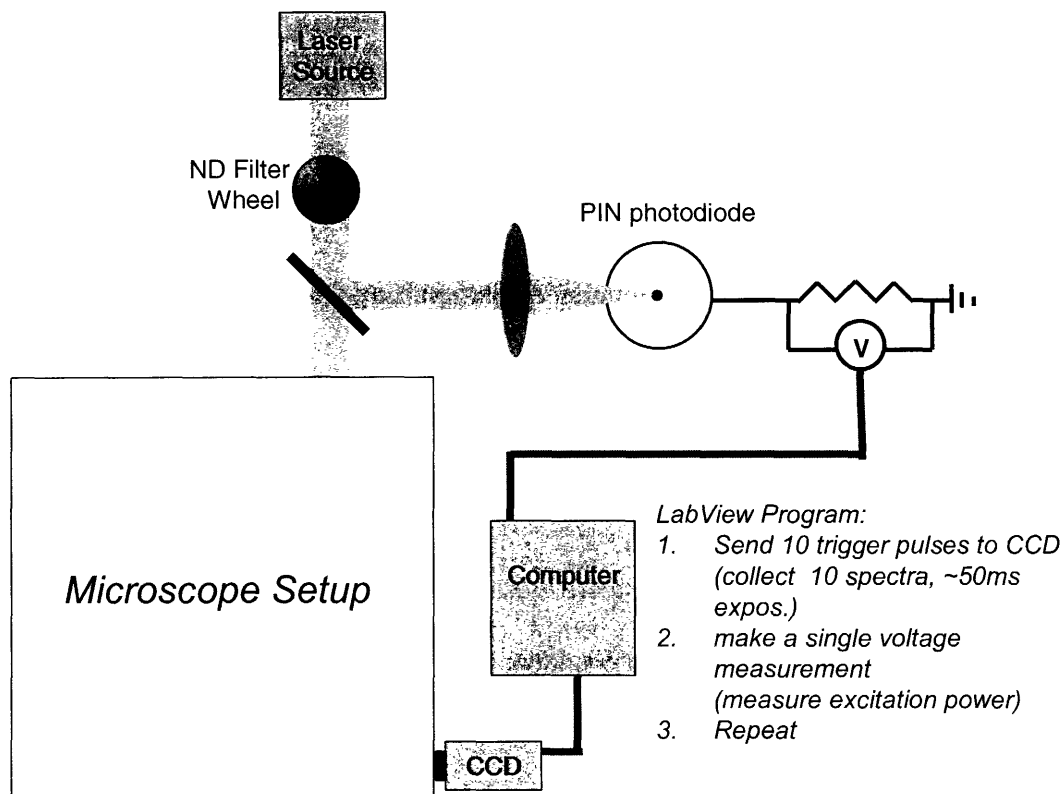


Figure 7.7 Live measurement of excitation power synchronized to collection of spectra on CCD.

7.5 Biexciton Emission in Single Nanocrystal Fluorescence

A typical image of single nanocrystal fluorescence using 514nm CW excitation is shown in figure 7.7. To obtain good images here we used significantly higher excitation power ($>1\mu\text{W}$) than was used for the room temperature (RT) experiments of chapters 5 and 6 ($<1\mu\text{W}$). Higher power was necessary for intra-cryostat imaging, first, because some fraction of the light is reflected by the cryostat window, and second, because a lower NA objective (and consequently larger spot size) was necessary in these experiments to obtain a long enough working distance to work inside the cryostat – here we used a 0.7NA objective, whereas RT experiments used a 1.4NA objective.

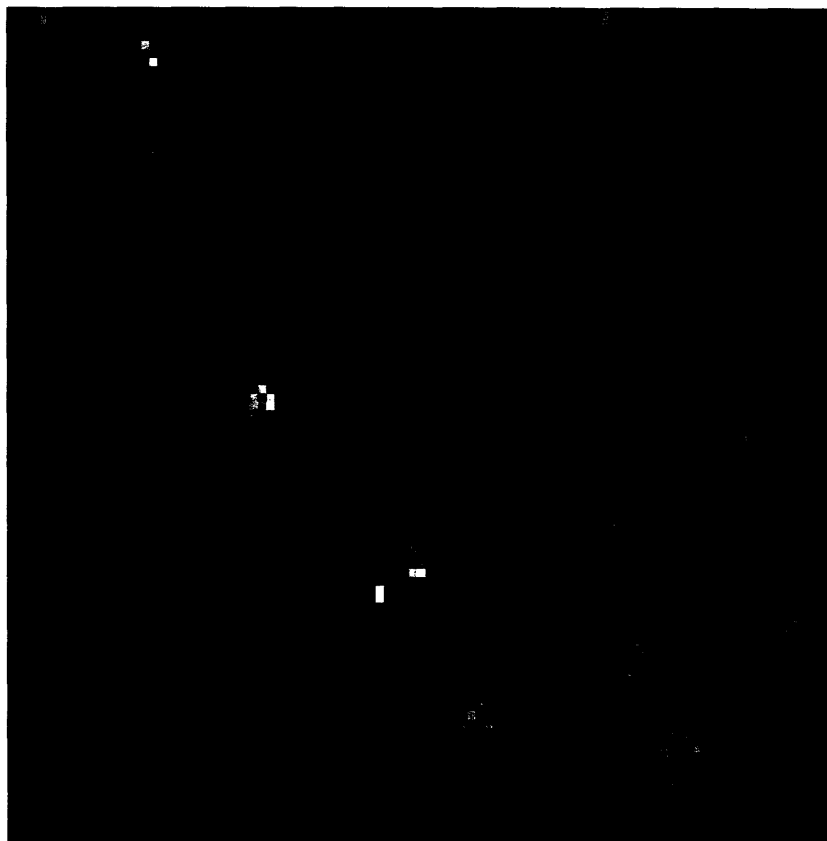


Figure 7.8 Confocal scanned fluorescence image of single nanocrystal at 4.3K. The dimensions of the image are approximately $7\mu\text{m} \times 7\mu\text{m}$.

Focusing the microscope onto a single nanocrystal chosen from an image like 7.8 yielded a typical single nanocrystal spectrum at low temperature, which is shown in figure 7.9.

This low temperature, spectrum of a single NC matches the results of previous work well^{21, 25}, showing a main emission peak with red shifted phonon replica of the first. The main peak is referred to as the zero phonon line (ZPL) and the phonon replica is the one-phonon line (OPL). Second and third phonon lines are visible as well. The spacing between the ZPL and OPL peaks of the single NC spectrum is about 25meV which matches the LO phonon frequency of 210cm^{-1} reported previously for CdSe nanocrystals of this size²⁰. This spacing confirms the identity of these peaks.

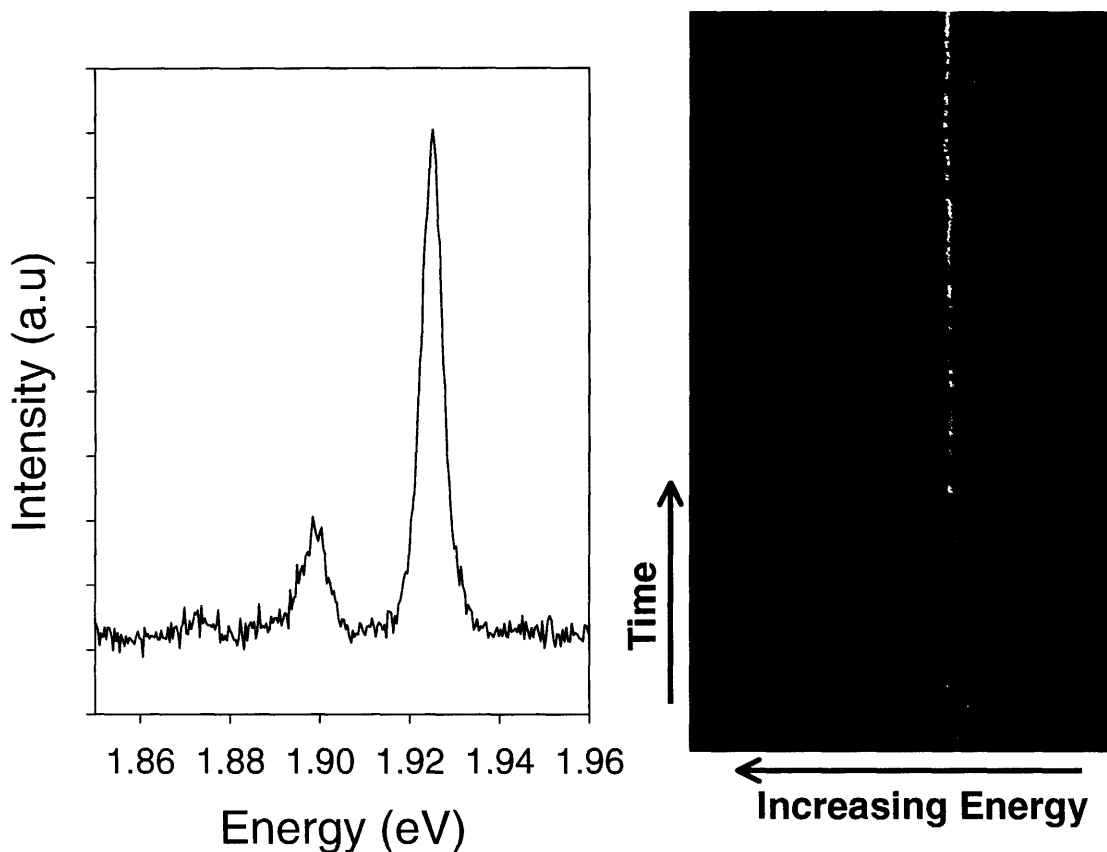


Figure 7.9 *Left:* Spectrum of a single nanocrystal at low temperature with one and two phonon lines (OPL, 2PL) visible in a progression to the red from the zero phonon line. The spacing of the phonon progression is 25meV. *Right:* time trace of spectrum from a single nanocrystal over a period of 50 seconds. Spectral diffusion causes the spectrum to shift red and blue.

A time trace of the emission spectrum of a single nanocrystal, shown on the right side of figure 7.9 shows the degree to which spectral diffusion can dominate the spectrum of a single nanocrystal. Although spectral diffusion is practically ubiquitous in measurements of single NC spectra, nanocrystals can occasionally withstand high intensity excitation for a brief period before making spectral diffusion shifts. By quickly varying and measuring the excitation power for each spectrum acquired (as described in the methods), we were able obtain power dependencies of single NC spectra that were mostly free of spectral diffusion. One example is shown in figure 7.10

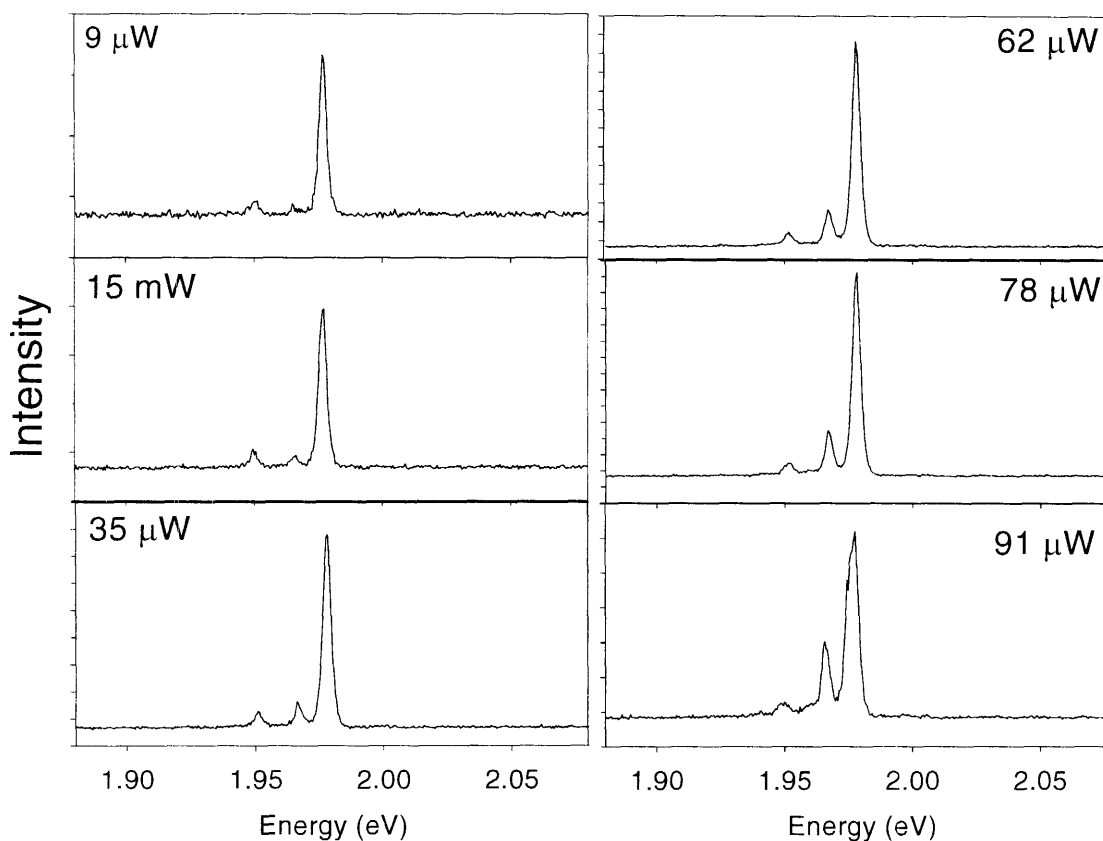


Figure 7.10 Emission spectra at 4.3K from a single, 5.1nm radius CdSe/ZnS nanocrystal at various CW excitation powers ($\sim 280 \text{ W/cm}^2$ to $\sim 2900 \text{ W/cm}^2$).

In this figure, the ZPL and OPL are both present at low excitation power, but as the power is increased a third peak emerges that is slightly red shifted from the ZPL. The spacing between this peak and the ZPL is 11 meV, which is very close to the expectation of 14meV for samples of this size, based on previous studies¹⁹.

The power dependence of the intensity of this new peak in the single NC spectrum supports the notion that it originates from BX emission. We calculated the total emission intensity (using the integrated area) of each of the three peaks in the single NC spectra at each power. Because of blinking and other fluctuations, the intensity of the

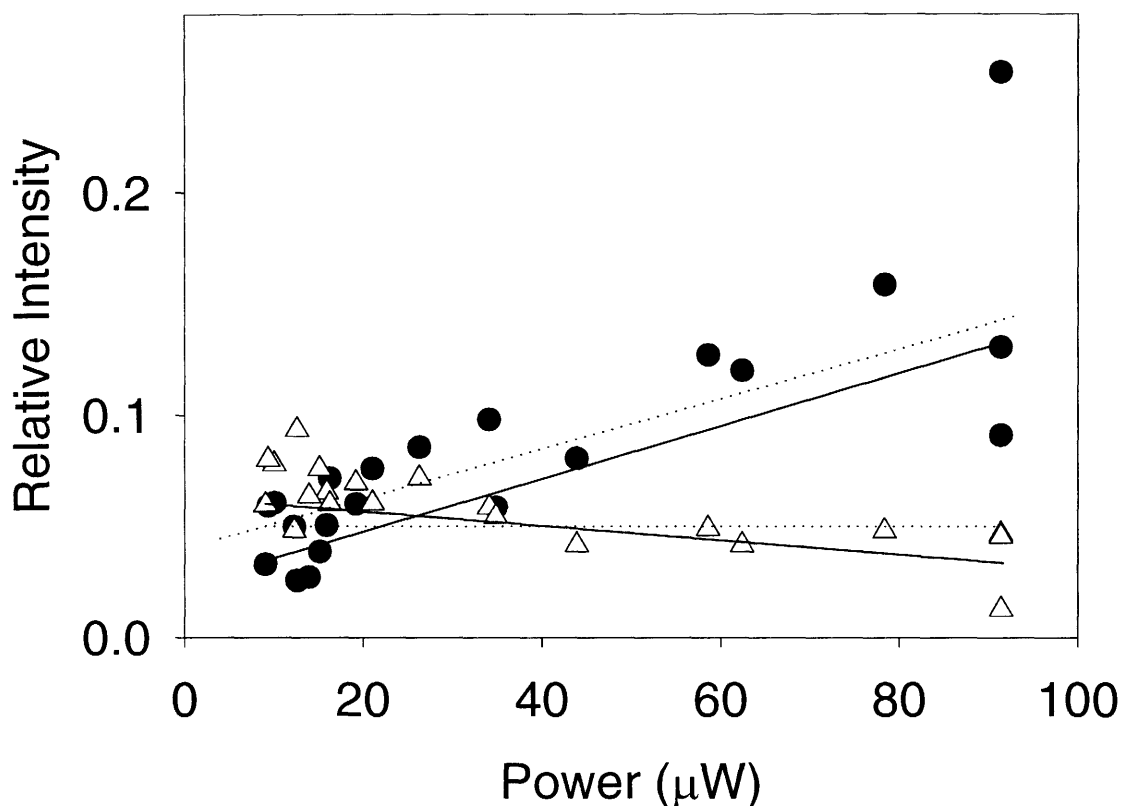


Figure 7.11 Excitation power dependence of BX (•) and OPL (Δ) intensities relative to the ZPL intensity. Solid lines indicate linear fits of the experimental data. Dotted lines represent the predicted power dependence, based on calculations in section 7.2 using a $4.5 \times 10^{-15} \text{ cm}^2$ cross-section at 514nm and a spot size of $1 \mu\text{m}$ radius.

new peak and the OPL were referenced to the intensity of the ZPL by taking the ratio of the two. The power dependence of the intensity of these peaks, relative to the ZPL peak is shown in figure 7.10, along with results of fitting to a linear power dependence (solid lines).

As expected the ratio of OPL intensity to ZPL intensity shows no power dependence, since both peaks arise from the same single exciton transition. The relative intensity of the new peak compared to the ZPL clearly increases with excitation power, and a fit to a linear polynomial gives a positive slope of $0.0012 \mu\text{W}^{-1}$. Recall from section 7.2 that a linear, positive slope is expected for the power dependence of the ratio

of BX and single exciton emission intensity. Using the equation that describes this power dependence,

$$\frac{I_{BX}}{I_X} = \frac{\alpha Q_2}{\Gamma_1 Q_1} P \quad (7.1)$$

we can back out the absorptive cross-section that corresponds to the measured slope in figure 7.11 (solid line; assume the same single exciton and multiexciton relaxation rates, Γ_i , and quantum yields, Q_i , measured for this 5.1nm sample in chapters 4 and 5). For an excitation focus spot size of $1\mu\text{m}$ radius, the measured slope of $0.0012\ \mu\text{W}^{-1}$ corresponds to a cross section of $5 \times 10^{-15}\ \text{cm}^2$. This result is in almost perfect agreement with the cross section for this sample derived using previously reported methods ($4.5 \times 10^{-15}\ \text{cm}^2$ at 514nm)¹². Conversely, the expected power dependence of the BX, calculated using a cross section of $4.5 \times 10^{-15}\ \text{cm}^2$, agrees with the data very well (dotted line in figure 7.11). This agreement between model and data, along with the new peak's energy splitting from the ZPL gives us confidence that the new peak arises from BX recombination.

7.6 Biexciton Emission in FLN Spectra

The results of the last section show that it is possible to spectrally resolve the BX from the X in the steady state emission spectrum of a nanocrystal. The major drawback of that experiment, however, is that the spectrum of most single nanocrystals is so unstable under high excitation intensities that the BX can only be studied for a brief period, sometimes only a few seconds. FLN experiments offer the possibility of obtaining more stable spectra for two reasons. First, an ensemble of nanocrystals is studied so that blinking and other single NC phenomena are minimized by ensemble averaging. Second, only the subset of nanocrystals with the *lowest energy* band gaps are

interrogated at any given moment. For instance, if a subset of nanocrystals have a spectral shift to the blue, they will no longer be excited, and the emission spectrum will not change.

Our first FLN results are shown in figure 7.12. These FLN spectra were obtained at 4.3K from the sample of 5.1nm nanocrystals on the SPEX fluorometer using low excitation intensity at various wavelengths ranging from 400nm (3.1eV) to 645nm (1.925eV). The first spectrum at the bottom of 7.12(a) is the full emission spectrum (non-resonant excitation). Progressively lower energy excitation is used in each subsequent FLN spectrum above it. As the excitation energy is decreased features

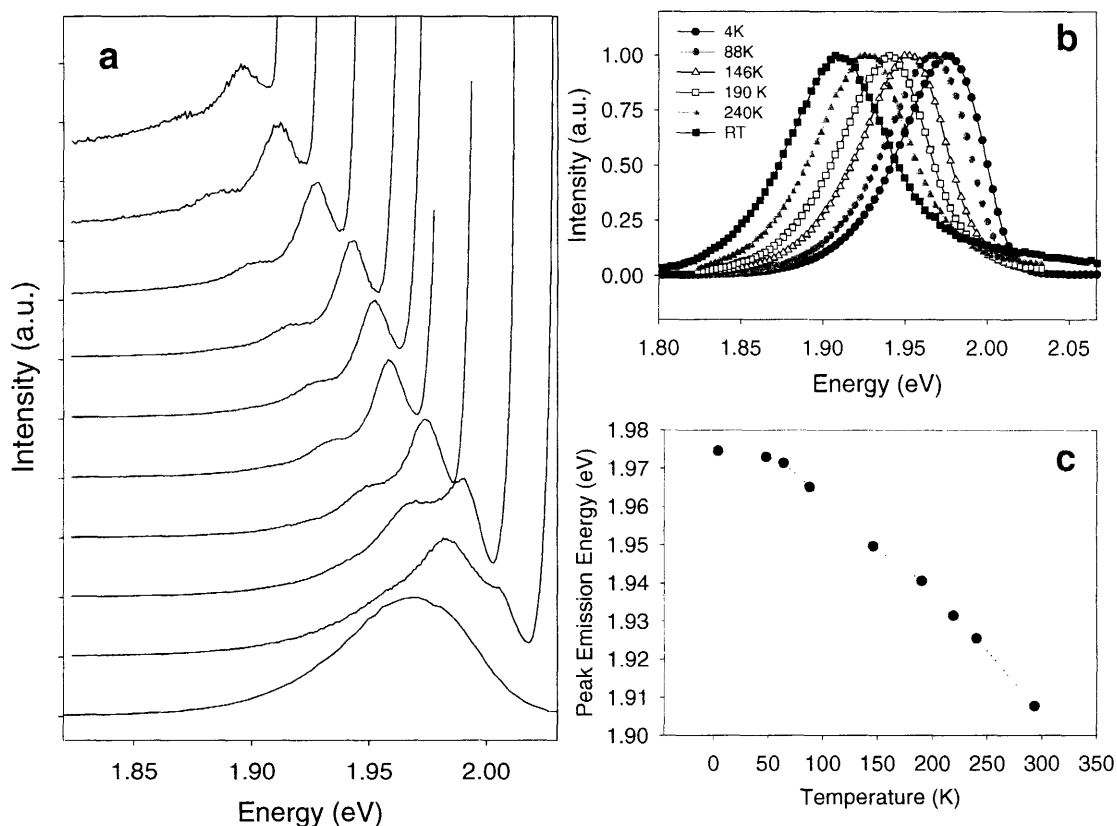


Figure 7.12 (a.) FLN spectra of nanocrystals at low temperature using SPEX fluorometer with excitation at the following wavelengths, beginning with the bottom spectrum: 400nm, 610nm, 615nm, 620nm, 625nm, 627nm, 630nm, 635nm, 640nm, 645nm. **(b.)** Full luminescence spectra (using non-resonant excitation) of the same sample at various temperatures. **(c.)** energy of the full luminescence versus temperature.

become evident in the spectra. The main peak seen in most of these spectra is the OPL. Further to the red is a weak shoulder that is the second LO phonon replica, denoted the 2PL. We know that the main peak is the OPL because it is located about 25meV from both the 2PL and the excitation energy. 25meV is the LO phonon energy for these nanocrystals²⁰, and their expected resonant stokes shift is ~1meV so the main peak cannot be the ZPL. The ZPL remains unresolved from the excitation in these FLN spectra because the overall spectral resolution of the experiment was only about 1nm (~10meV).

The very small resonant stokes shift of these 5.1nm nanocrystals presented a major obstacle for doing this FLN experiment using a confocal microscope where scattered excitation light is efficiently captured by the objective and must be optically discriminated from the fluorescence. The small stokes shift of <1meV makes ordinary methods of discriminating emission fluorescence from reflected excitation light (e.g. bandpass filters and dichroic beam splitters) practically useless. Dark field microscopy was considered for rejecting the reflected light, but we lacked a dark field objective of sufficient NA for this experiment. Similarly, grazing angle excitation was tried, but reflection and scattering of excitation off of the rough polymer film was found to be still too great, so fluorescence emission was dominated by excitation light. The best method found for this CW experiment was to use a holographic notch filter (NF) centered at 633nm. Fortuitously, excitation near 633nm (1.959 eV) is on the red edge of the non-resonant band-edge emission spectrum, as shown in figure 7.11(b). Furthermore, the precise wavelength of the edge of the NF rejection band can be precisely tuned by changing the angle between it and the light passing through it. With careful alignment we were able to use excitation wavelengths up to 635nm (1.953 eV) to obtain low-

temperature (4.3K) FLN spectra that resolved the ZPL in emission from the 5.1nm sample of CdSe nanocrystals. Figure 7.12 shows an example of an FLN spectrum obtained at 4.3K, using a confocal microscope setup and tuned notch filter for rejection of the scattered excitation light from the dye laser. The sample was excited with low power ($1.7\mu\text{W}$; 60 W/cm^2) in this spectrum.

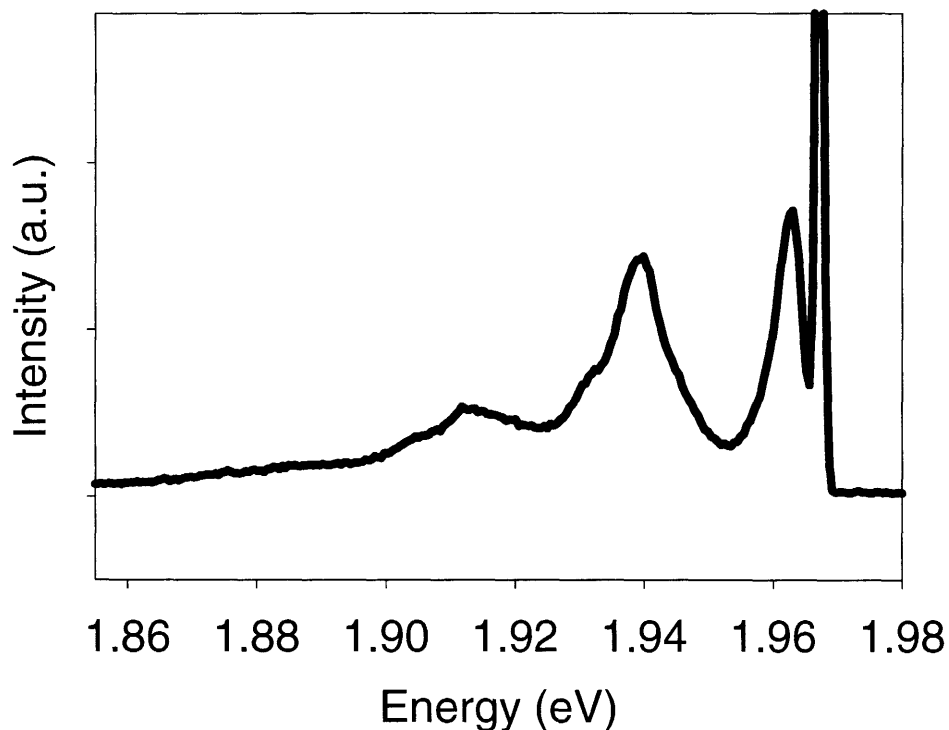


Figure 7.13 Low Power FLN spectrum of the ensemble NCs at 4.3K. The sharp peak at the highest energy (on right) is the scatter of the illumination laser. The first peak to the red of this is the ZPL at 1.965eV followed by the OPL and the 2PL at 1.94eV and 1.915eV respectively. The ZPL is artificially weak and red-shifted because its blue edge in this spectrum is defined by the notch filter used in the experiment.

We note that the ZPL is only partially resolved in the FLN spectrum of 7.12. Its apparent peak position is red-shifted from its actual position because its blue edge is defined by the transmission spectrum of the NF. The OPL and 2PL are also both prominent in this spectrum with a spacing of 25meV as expected.

Raising the excitation power to $>30\mu\text{W}$ ($\sim 1000\text{W}/\text{cm}^2$) yielded the spectrum shown in figure 7.13 where a new peak appears between the ZPL and the OPL. The spectral shift between the ZPL and this new, power dependent peak was obtained by measuring the spacing of the new peak and the OPL, and then subtracting it from the known ZPL-OPL spacing of 25 meV. A spacing of about 12meV is observed, indicating that the new peak probably originates from BX emission.

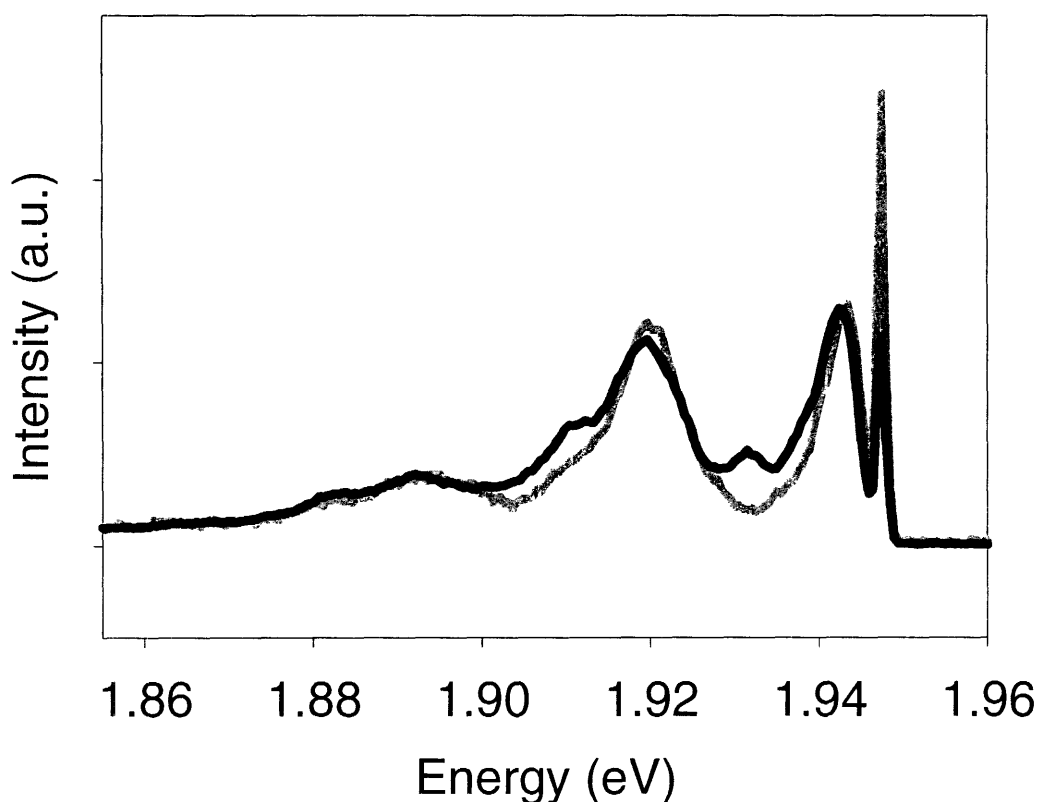


Figure 7.14 Comparison of low (gray) and high (black) excitation intensity FLN spectra obtained from an ensemble of 5.1 nm NCs at 4.3K. The features of the low power spectrum are described in the caption to figure 7.13. The high power spectrum exhibits new features, in particular a 12 meV red-shifted peak (relative to the ZPL), which we assign to BX emission.

Furthermore, a phonon progression is apparent with shoulders appearing on the OPL and 2PL in the high power FLN spectrum. The phonon progression of single exciton emission comes from the band edge fine structure of CdSe nanocrystals. An offset but replicated

progression in the BX emission is an indication that the presence of multiple carriers does not greatly perturb the energy levels of the band-edge fine structure.

7.7 Conclusions

In this chapter we have explored the possibility of directly resolving BX and single exciton emission peaks from one another in the band edge emission of CdSe nanocrystals. We first calculated the expected BX emission signal relative to that of the single exciton and found it to be appreciable for nanocrystals with sufficiently high BX quantum yield. Using a sample of large nanocrystals with high BX quantum yield we performed two kinds of experiments, both at low temperature, to narrow the band edge emission enough to resolve the expected energy splitting between the BX and X. Low temperature emission spectra from a single nanocrystal showed a sharp new peak 11 meV to the red of the ZPL when the power was increased. The power dependence of this new peak agreed well with a simple model for the power dependence of BX emission. We also showed that FLN techniques can also be used to resolve the BX emission. In these experiments the ZPL, OPL and 2PL were resolved at low temperature by exciting the sample with a dye laser on the red edge of the sample's full luminescence. The FLN spectrum at high CW excitation intensity showed an excitation intensity dependent peak that was red shifted 12 meV from the ZPL and likely originates from BX emission.

The next step to take in these investigations is to develop more robust measurement techniques. For instance, time-gated FLN spectra using a pulsed excitation source would be a great step for two reasons. First, pulsed excitation should be much more efficient at generating BXs in the nanocrystals. Second, time-gated spectra offer a

better method of rejecting reflected excitation and may circumvent the need for a notch filter. This would allow the experiment to be performed at any excitation energy (not just those matching the notch filter) so that the size dependencies of BX emission can be investigated. Improvements in single nanocrystal experiments would also be useful, particularly, the ability to perform measurements quickly while a nanocrystal is stable at a given energy. Single nanocrystal experiments would be well suited to investigate polarization properties of the BX emission relative to the polarization of single exciton emission as well.

7.8 References

- 1 G. Bacher, R. Weigand, J. Seufert, et al., *Physica Status Solidi B-Basic Research* **221**, 25 (2000).
- 2 C. Santori, D. Fattal, M. Pelton, et al., *Physical Review B* **66**, 045308 (2002).
- 3 V. Zwiller, P. Jonsson, H. Blom, et al., *Physical Review A* **66** (2002).
- 4 I. A. Akimov, A. Hundt, T. Flissikowski, et al., *Physica E - Low-Dimensional Systems and Nanostructures* **17**, 31 (2003).
- 5 R. Weigand, G. Bacher, V. D. Kulakovskii, et al., *Physica E* **7**, 350 (2000).
- 6 H. J. Eisler, V. C. Sundar, M. G. Bawendi, et al., *Applied Physics Letters* **80**, 4614 (2002).
- 7 V. I. Klimov, A. A. Mikhailovsky, S. Xu, et al., *Science* **290**, 314 (2000).
- 8 A. L. Efros, *Physical Review Letters* **78**, 1110 (1997).
- 9 K. T. Shimizu, R. G. Neuhauser, C. A. Leatherdale, et al., *Physical Review B* **63**, 205316 (2001).
- 10 I. Chung and M. G. Bawendi, *Physical Review B* **70**, 165304 (2004).
- 11 A. L. Efros, in *Archives* (Naval Research Laboratory, 2002).
- 12 C. A. Leatherdale, W. K. Woo, F. V. Mikulec, et al., *Journal of Physical Chemistry B* **106**, 7619 (2002).
- 13 K. H. Hellwege, *Landolt-Bornstein Numerical Data and Functional Relationships in Science and Technology* (Springer-Verlag, Berlin, 1982).
- 14 V. D. Kulakovskii, G. Bacher, R. Weigand, et al., *Physical Review Letters* **82**, 1780 (1999).
- 15 V. Turck, S. Rodt, R. Heitz, et al., *Physica Status Solidi (b)* **224**, 217 (2001).
- 16 U. Woggon, K. hild, F. Gindele, et al., *Physical Review B* **61**, 12632 (2000).
- 17 G. Bacher, R. Weigand, J. Seufert, et al., *Physical Review Letters* **83**, 4417 (1999).

- ¹⁸ K. I. Kang, A. D. Kepner, S. V. Gaponenko, et al., *Physical Review B* **48**, 15449 (1993).
- ¹⁹ M. Achermann, J. A. Hollingsworth, and V. I. Klimov, *Physical Review B* **68**, 245302 (2003).
- ²⁰ D. J. Norris, in *Chemistry* (Massachusetts Institute of Technology, Cambridge, 1995), p. 158.
- ²¹ S. A. Empedocles, in *Chemistry* (Massachusetts Institute of Technology, Cambridge, 1999), p. 204.
- ²² S. A. Empedocles, R. G. Neuhauser, K. T. Shimizu, et al., *Advanced Materials* **11**, 1243 (1999).
- ²³ C. R. Kagan, C. B. Murray, M. Nirmal, et al., *Physical Review Letters* **76**, 1517 (1996).
- ²⁴ C. R. Kagan, C. B. Murray, and M. G. Bawendi, *Physical Review B* **54**, 8633 (1996).
- ²⁵ S. A. Empedocles and M. G. Bawendi, *Accounts of Chemical Research* **32**, 389 (1999).

Chapter 8: Lifetime and Quantum Yield of Nanocrystals

- 8.1 Introduction
- 8.2 General Relationship Between Quantum Yield and Lifetime
- 8.3 Methods
- 8.4 Quenching Experiments
- 8.5 Discussion
- 8.6 Temperature Dependent Quantum Yield of TiO₂-Nanocrystal Composites Films
- 8.7 Conclusions
- 8.8 References

8.1 Introduction

Measurement of the quantum yield (QY) of photoluminescent compounds is an essential tool for the optical characterization of both basic materials and their device applications. Throughout this thesis we have used the fundamental relationship between quantum yield (QY) and lifetime to draw conclusions about the QY of the photoluminescence observed. Compared to conventional measurement techniques, lifetime measurements are a very practical method for judging QY because they do not require absolute measurements of light intensity and can be obtained from very weakly emitting samples. However, conclusions from the results of these measurements must be drawn carefully.

In this chapter we discuss this approach to characterizing changes in QY using the lifetime, and show how it must be adapted for the multi-exponential PL decays observed from nanocrystals. Furthermore, we demonstrate a clear limitation on the reliability of using the lifetime to judge QY in nanocrystals. We find that the lifetime is useful for judging so-called *homogenous* changes in lifetime, where all of the nanocrystals of the ensemble behave similarly and exhibit approximately the same

lifetime. However, the integrated area of the PL decay fails to account for *inhomogenous* variation of the QY, whereby a sub-population of the nanocrystals are rendered completely quenched by an ultrafast, unresolved non-radiative decay.

8.2 General Relationship Between Quantum Yield and Lifetime

The relationship between QY and lifetime is one of the most basic concepts in fluorescence spectroscopy. Most standard approaches to the topic treat the luminescence efficiency as a competition between the rates of radiative relaxation and all other (non-radiative) decay paths. In this way the QY is given by,

$$QY = \frac{k_r}{k_r + \sum_{all} k_{nr}} \quad (8.1)$$

where k_r denotes the rate of *radiative* relaxation, and k_{nr} denotes the rate of *non-radiative* relaxation. Since the lifetime of the excited state of a molecule is defined as the inverse of the sum of all relaxation rates (i.e. the denominator of equation 1), we find that the QY is linearly related to the lifetime of the excited state through the radiative decay rate,

$$QY = \tau \cdot k_r \quad (8.2)$$

so a longer lifetime corresponds to a higher QY, if the radiative decay rate remains constant. Conversely, if a faster lifetime and higher QY are observed, then we know that the radiative rate, k_r , has increased.

A more physical approach to the definition of QY produces the same results. Fundamentally the QY is defined as the probability that an excited molecule will emit a photon. Statistically, this probability is approximated by the number of photons emitted

by a molecule (or ensemble) divided by the number of excitation photons that are absorbed,

$$QY = \frac{N_f}{N_a} = \frac{\bar{I}_f / \eta}{\bar{I}_x \sigma} \quad (8.3)$$

where N_f and N_a are the total number of photons emitted and absorbed in a given experiment, I_f and I_x are the average detected intensities of fluorescence and excitation during a real experiment, and η and σ are the detection efficiency and the absorptive cross section respectively. The conventional measurement of QY¹ is based on equation 8.3, but in practice I_x and η are difficult to determine with sufficient accuracy. Therefore one usually compares I_f of a the unknown to I_f of a standardized reference sample whose QY is known.

$$QY_{unk} = QY_{ref} \frac{\bar{I}_{f,unk} \sigma_{ref}}{\bar{I}_{f,ref} \sigma_{unk}} f_{geometrical} \quad (8.4)$$

where the ratio of cross-sections ($\sigma_{ref}/\sigma_{unk}$ - easily measured accurately) accounts for any difference absorption between reference and unknown, and the geometrical factor, $f_{geometrical}$, accounts for differences in refractive index of the solvents used for unknown and reference samples, which can significantly alter the relative collection efficiency^{1,2}.

If we consider that the total integrated area beneath the PL decay curve is proportional to N_f , we can see that equation 8.3 leads to equation 8.1 for samples with exponential PL decay dynamics. This is demonstrated by first writing the definition of the absolute area, A , beneath the un-normalized PL decay, $I_f(t)$, and equating it to the total number of photons emitted times the collection efficiency,

$$A \equiv \int_0^{\infty} I_f(t) dt = \eta N_f = \eta N_a QY \quad (8.5)$$

The last equality of 8.5 is derived by substitution of 8.3, and shows that A is proportional to the QY. We note that the intensity at time zero, $I(0)$ is equal to the radiative rate times the population in the excited state at time zero, which is N_a .

$$I_f(0) = \eta N_a k_r \quad (8.6)$$

Combining 8.5 and 8.6 reveals that A_N , the area beneath a PL decay that is rescaled to unity at time zero is directly equal to the QY divided by k_r .

$$A_N \equiv \frac{A}{I_f(0)} = \frac{QY}{k_r} \quad (8.7)$$

If normalized PL usually decays exponentially, $I_f(t)/I_f(0) = \exp(-t/\tau)$, the normalized area is just equal to the time constant,

$$A_N = \int_0^{\infty} \exp(-t/\tau) dt = \tau \quad (8.8)$$

Combining this result with 8.7 recovers the original description of the QY, which was given in equation 8.1.

Although equation 8.1 is often presented as a definition of QY, the foregoing simple derivation shows it is actually a special case of the fundamental definition, equation 8.3, for the case of luminescent samples that exhibit single exponential decay dynamics. This distinction is very important in the case of NCs because their PL decay is in general multiexponential, as discussed in previous chapters and elsewhere^{3,4}. As a result, when using PL decays to monitor QY in samples of NCs we discard equation 8.2 and instead use,

$$QY = A_N \cdot k_r \quad (8.9)$$

Since we do not measure k_r independently, we can use 8.9 only to monitor changes in QY of samples. For instance the ratio of QY values before and after a chemical or physical treatment of some kind is given simply by the ratio of the normalized areas.

$$\frac{QY}{QY_0} = \frac{A_N}{A_{N,0}} \quad (8.10)$$

This equation is the basis for the analysis described in this chapter.

8.3 Methods

QY Measurements: Absolute QY measurements of dilute solution samples were carried out by the conventional dilute solution dye-referenced method², using a SPEX Fluorolog spectrophotometer to collect the steady state PL emission spectrum. After correction for wavelength dependent spectrometer and PMT sensitivity, emission spectra were integrated over visible wavelengths to determine the total steady state PL intensity. To determine the QY of the unknown sample, its spectrally integrated steady state PL intensity was compared to that from a reference dye solution, taking into account differences in absorbance and solution refractive index² as in equation 8.4. Both reference and unknown samples were excited at the same wavelength in order to avoid wavelength dependent variations in the excitation intensity.

Lifetime Measurements: We used a homebuilt, wide-field fluorescence microscope coupled to a spectrometer and time-gated MCP intensified CCD camera (LaVision GmbH, Imager QE) as discussed in Chapter 2 to measure fluorescence decay from all samples. The excitation light was coupled into the microscope collection axis using a dichroic filter. A 0.7 NA Nikon objective (finite) was used both to focus the laser excitation and to collect the sample fluorescence. The laser excitation source was either a

frequency doubled, pulse-picked Ti:Sapphire laser operated in picosecond mode (400nm, 4.75 MHz, 1.5 ps FWHM, Coherent MIRA900) or a diode laser (414nm 5 MHz, 90 ps FWHM, PicoQuant GmbH, LDH400). The total instrument response time was limited to 200 ps by the CCD image intensifier microchannel plate. Room-temperature solution samples were held in FUV cuvettes. Measurements of NC-titania films were carried out in an evacuated cold finger cryostat at temperatures ranging from 77K to room temperature. The sample film was held in a rigorously fixed geometry to eliminate any variation of excitation intensity and collection efficiency from measurement to measurement.

Samples: Fluorescent solution samples used for calibration of relative normalized lifetime area versus relative QY were tri-octylphosphine oxide (TOPO) capped colloidal CdSe/ZnS-core/shell nanocrystals (NC) dispersed in hexane to approximately 0.1 optical density in a 1 cm FUV cuvette. CdSe NCs overcoated with ZnS were synthesized according the methods of Murray et al.⁵⁻⁷ and had core radii of approximately 2.7nm (sample 1, 605nm at the first absorption feature), or 2.3nm (sample 2, 570nm absorption feature). Reference solutions for conventional QY measurements were Rhodamine 640 diluted in methanol with an optical density of 0.1 at the excitation wavelength (QY=100%,⁸).

Comparison of relative QY to relative normalized lifetime area was carried out by progressively quenching the luminescence of NC/hexane solutions with known NC quenchers – either pyridine for sample 1 or p-thiocresol (p-TC) for sample 2 – and then measuring the QY and normalized PL decay trace each time an aliquot of quencher was added. QY and lifetime measurements for each sample were completed within minutes

of one another to minimize any possible temporal variation of QY. The *relative* QY (A_N) of each sample is then expressed as a fraction of the QY (A_N) obtained in the control measurement that used no quencher.

NC-titania films used in the study of inhomogeneous versus homogenous degradation of QY were fabricated according to published methods⁹.

8.4 Quenching Experiments

We sought to validate equation 8.10 for use on nanocrystal samples by performing quenching experiments on solutions of NCs. Figure 8.1 shows the typical response of PL decay curves for NC-hexane solutions to progressive addition of pyridine.

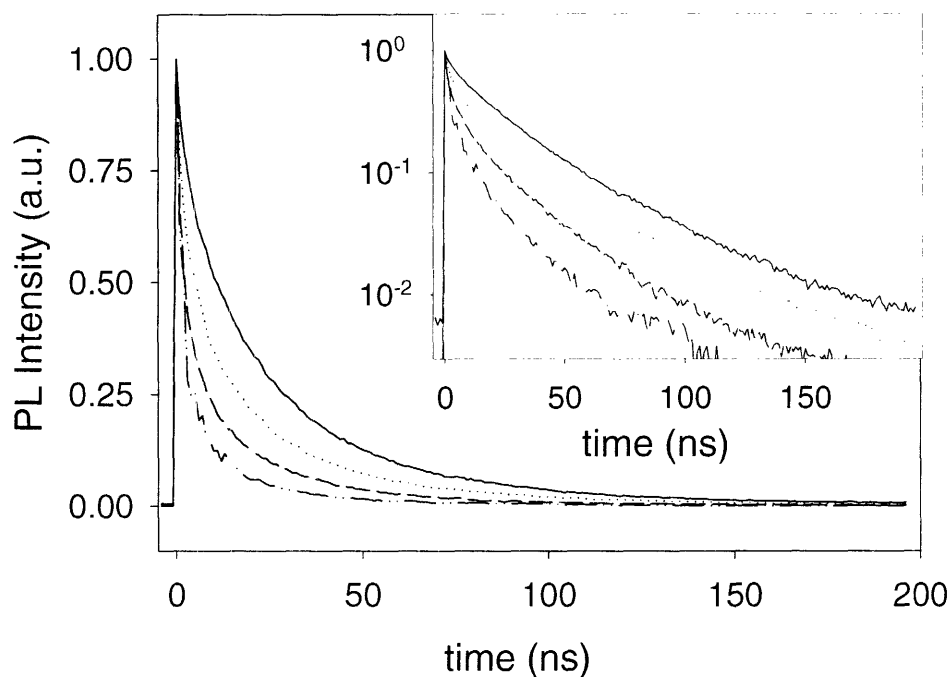


Figure 8.1 Room temperature PL decay traces (normalized at $t=0$) for QD solution samples treated with progressively greater amounts of pyridine. The normalized integrated area of the PL traces decreases with continuing addition of pyridine. The decrease in area beneath the normalized PL decay curve mirrors the sample's decrease in QY. **Inset:** log-scale plots of same PL decays.

The lifetime curves are normalized against the maximum measured value of the curve, I_{max} . The longest lifetime curve is from the control sample of CdSe/ZnS NCs, which containing no pyridine (2 mL NC-hexane, 0.1 optical density at first absorption feature). The next three curves are from the same NC sample with 40, 60, and 80 μL of pyridine added, respectively. Typically QY quenching covered a range of approximately QY=30-35% in control samples, down to about QY=10%. No measurable change in the absorption spectra of the sample was observed as pyridine was added.

Although previous studies¹⁰⁻¹² showed a faster non-radiative decay from pyridine, those studies looked at *bare* NCs (not overcoated) that gave pyridine direct access to the NC core, whereas our nanocrystals were overcoated with ZnS. Also, in our experiment there was no complete cap exchange to pyridine; instead pyridine was added to diluted growth solution that contained extra capping molecules (tri-octyl phosphine [TOP], and trioctylphosphine oxide [TOPO]), which could compete with the pyridine for binding to the nanocrystal surface.

Figure 8.2 shows the results of plotting relative QY measurements against the corresponding relative normalized lifetime area measurements for many different samples. A linear relationship is obtained between relative QY (Q_i/Q_0) and relative normalized lifetime area ($A_{N,i}/A_{N,0}$), with a slope of 0.85. Error bars were derived from two or three independent, sequential measurements of QY.

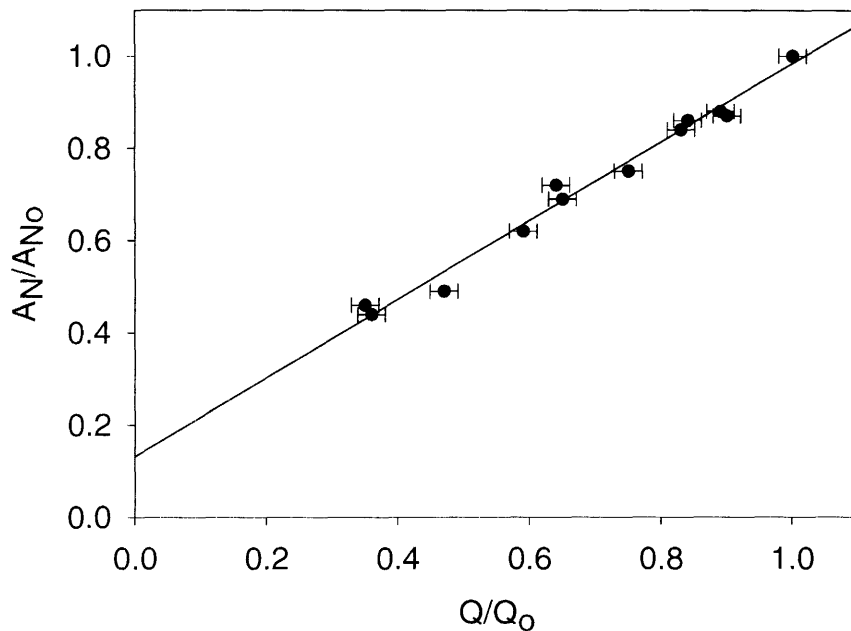


Figure 8.2 Comparison of the relative change in the normalized lifetime area versus the relative change in QY for a number of pyridine quenched samples. A linear fit gives a slope of 0.85 and an intercept of 0.13.

Although the slope is not perfectly unity, these results seem to support the use equation 8.10 to monitor the QY of NCs. However, when we performed analogous experiments on other nanocrystals using different quenching techniques, we found that 8.10 did not hold nearly as well. For instance in figure 8.3 we show the results of quenching with p-TC instead of pyridine. Here the relationship between integrated area and QY is weak, resulting in a slope of only 0.24 for a linear fit. Instead of a faster PL decay, the reduction of QY in the presence of p-TC resulted in a weaker overall signal intensity in the PL decay, while the decay rate

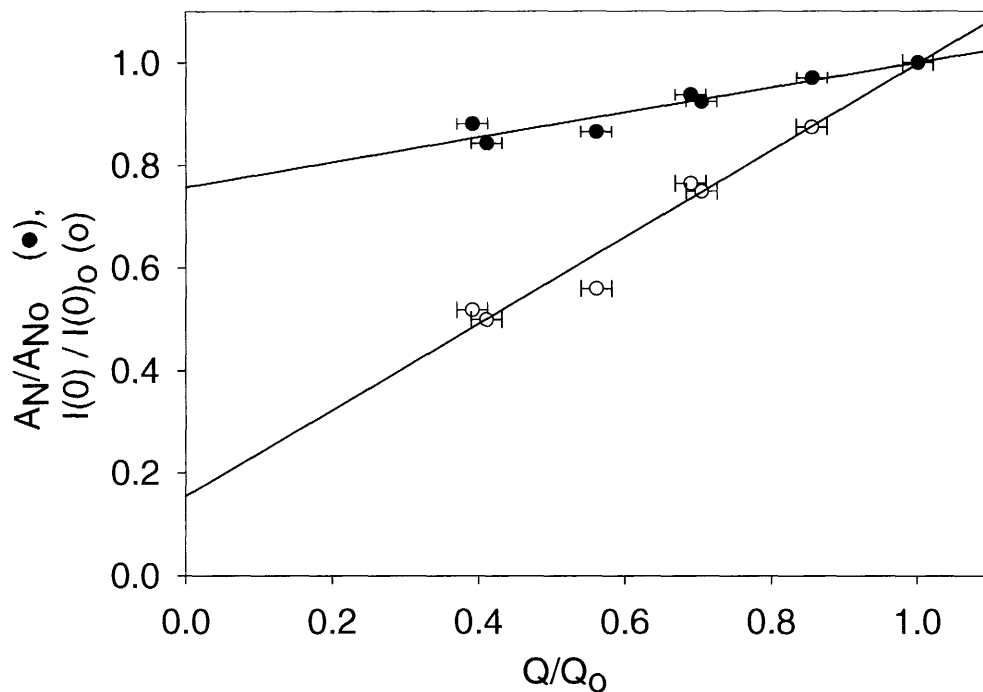


Figure 8.3 Comparison of the relative change in A_N (\bullet) versus the relative change in QY for samples treated with p-TC. A linear fit yields a slope of 0.24. The symbols (\circ) represent the relative change in absolute peak ($t=0$) intensity, I_{max} , for the lifetime curves of the same samples. A fit to the open circles gives a slope of 0.84 and intercept of 0.15.

remained approximately the same. Since the decay rate did not change very much, the “shape” of the decay curve was constant and A_N did not change much with QY. The initial intensity, I_{max} , however, did vary significantly with QY.

In other experiments, treatment of solution samples with other chemicals also produced PL decays whose normalized areas did not reflect actual changes in QY. For instance, when octylamine was added to samples of bare NCs in hexane solution, the QY was observed to increase, while the lifetime sped up leading to a *smaller* area beneath the normalized PL decay.

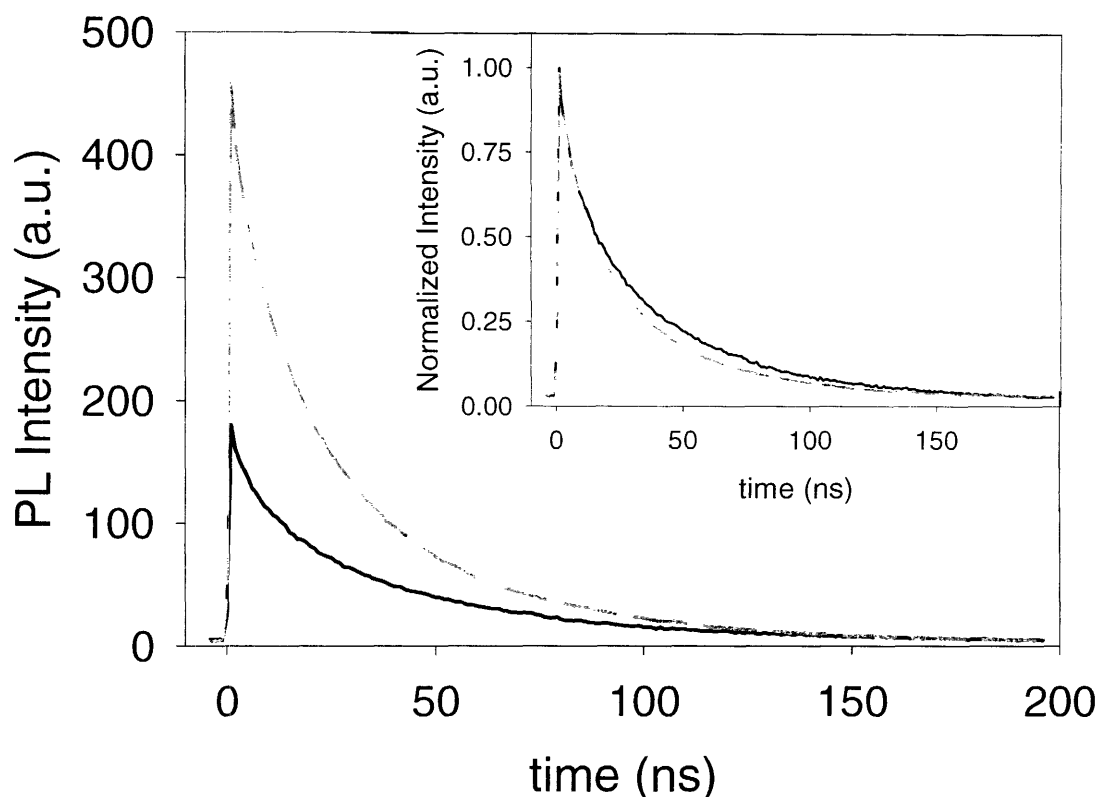


Figure 8.4 Main: Absolute PL decay of a solution of nanocrystals in hexane before (black, solid) and after (gray, dashed) addition of octylamine. The optical setups of both measurements were nearly identical, so the absolute intensities represent actual change in QY of the sample. *Inset:* the sample decays are shown, after normalizing the peak intensity values to unity. The amine treated sample has a slightly faster lifetime.

8.5 Discussion

The foregoing results highlight two critical restrictions on using A_N to judge changes in QY. The first and simplest restriction to explain is that the radiative rate should not change in order for the results to be accurate. If the radiative rate is different between two samples, then k_r does not cancel between equations 8.9 and 8.10, so equation 8.10 is not valid on its own. This can explain the simultaneous *increase* in QY and *decrease* in lifetime (and A_N) observed in figure 8.4. Clearly the use of A_N for monitoring QY must be limited to variations in QY that result from change of the non-radiative rate.

The second critical requirement for using equation 8.10 to monitor QY is that all temporal dynamics of the PL decay must be resolved by the experiment in order to accurately calculate A_N . The derivations discussed in section 8.2 assume that $I_f(t)$ is known with arbitrary precision, but in reality, we measure $I(t)$ which is a convolution of $I_f(t)$ with the experimental instrument response function. Convolution does not affect the value of the total absolute lifetime area, A , because integration over all time counts all photons, regardless of the time delay at which each was detected. However, the finite instrument response is critical to the absolute PL intensity peak value at time zero, I_{max} .

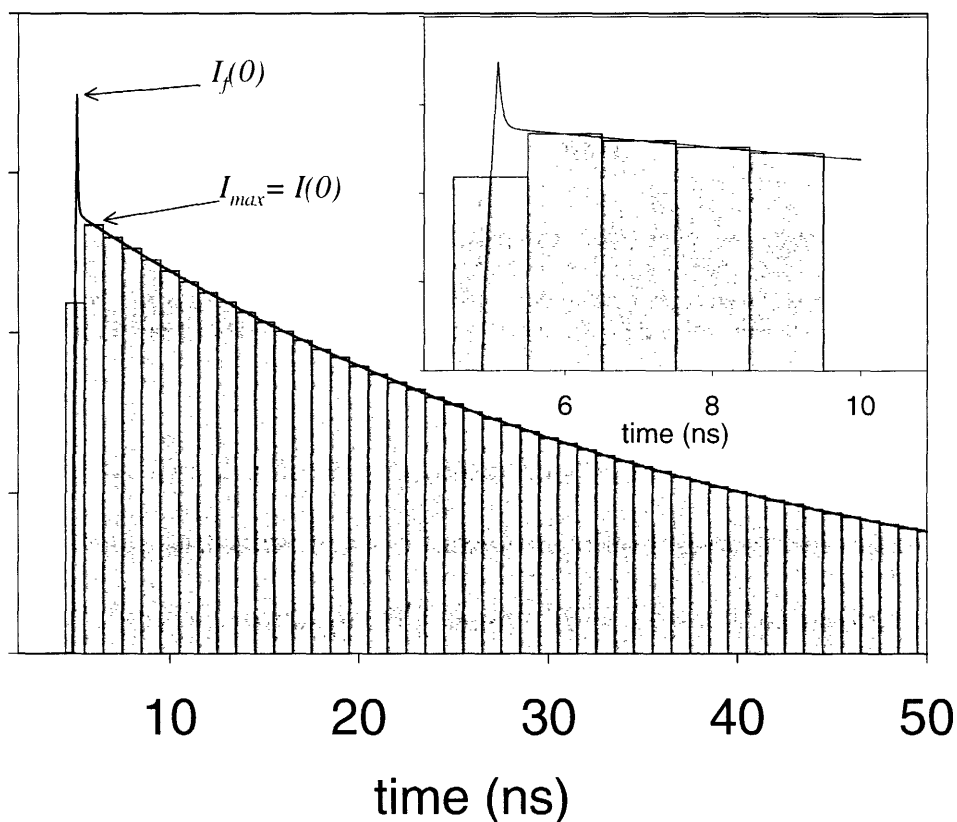


Figure 8.5 Illustration of the way that convolution of a slow instrument response can cause fast dynamics of a PL decay to be lost. The important point is that, although the total integrated area of the boxes approximates the actual integrated area quite accurately, the peak intensity measured by the experiment with imperfect time resolution (boxes), is much lower different than the actual peak intensity (line).

If the time resolution of the experiment is not sufficient to capture the dynamics, then I_{max} is measured completely inaccurately, as can be seen in figure 8.5.

Since A_N depends on I_{max} for normalization, I_{max} must be measured accurately to get an accurate measure of A_N . In the example of figure 8.5 poor time resolution would cause the measured I_{max} to be too small, and A_N would be overestimated. Accordingly, accurate QY estimation by equation 8.10 demands that changes in QY arise exclusively through processes whose rates can be resolved by the lifetime instrumentation. Any contributions of non-radiative pathways to QY quenching that are faster than the instrument response are lost through normalization.

This subtlety is the reason that the method worked in the pyridine quenching experiment, but not for the p-TC quenching experiment. The effect of pyridine on the excited state relaxation was resolved on a nanosecond time scale as shown in figure 8.1. p-TC on the other hand introduces deep, static hole traps, which leave the NCs charged. Band-edge exciton relaxation of charged NCs is thought to be dominated by non-radiative Auger recombination processes that occur on timescales less than 100 ps and are faster than our system's resolution^{12, 13}. This violates the assumption that changes in relaxation rates be resolved by the lifetime measurement, and thus make the method insensitive to QY changes induced this way.

From another perspective, p-TC causes an *inhomogeneous* decrease in QY – at any given time a subset of NCs in the ensemble are rendered completely non-luminescent or “off” by the p-TC induced charging, while the remaining NCs in the ensemble are unaffected (i.e. uncharged) by the p-TC. In terms of figure 8.5 the fast component of the PL decay is corresponds to the population of “off” NCs, which have ultrafast non-

radiative decays. The slow component comes from the remaining population of uncharged nanocrystals, which exhibit PL decay rates of the native sample. Hence the “shape” of the rescaled PL decay (and the ratio $A_{N,i}/A_{N,0}$) is mostly unaffected by *inhomogenous* variation of the ensemble QY. This is why the slope (\bullet) is so flat in figure 8.3. On the other hand, the measured value of I_{max} was found to vary much more accurately with the QY in 8.3 indicating that the important dynamics affecting QY all occurred within the first time-resolved data point.

8.6 Temperature Dependent Quantum Yield of TiO₂-Nanocrystal Composites Films

By making the distinction between inhomogenous and homogenous variation of the QY we gain insight into some important processes that affect the QY of nanocrystals.

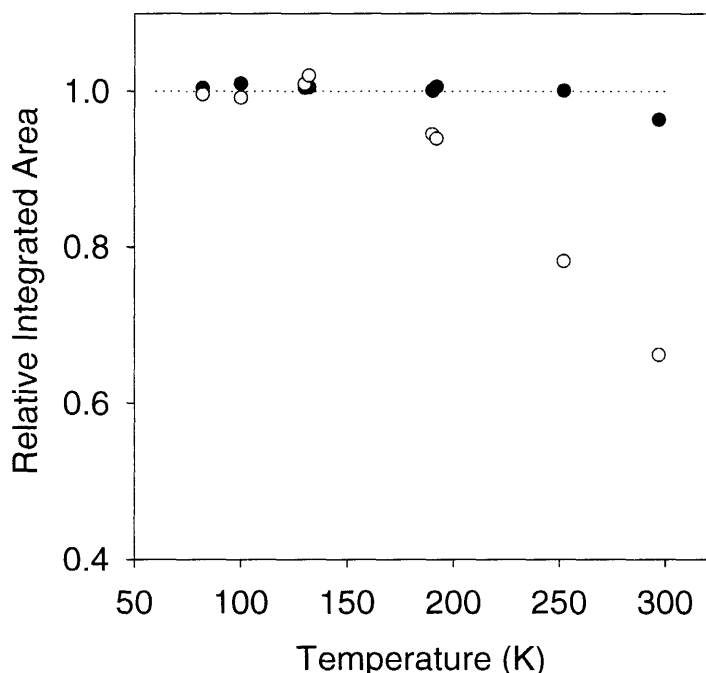


Figure 8.6 The temperature dependence of the integrated area beneath normalized (\bullet) versus absolute (o) lifetime curves are shown. The normalized lifetime area is virtually independent of temperature. The relative areas beneath *absolute* lifetime curves, on the other hand, show a clear temperature dependence above a threshold temperature of $\sim 130\text{K}$ as the QY decreased from its value at lower temperatures.

The QY of nanocrystals is known to vary significantly with temperature¹⁴, but the exact nature of this variation was not well understood. In figure 8.6 we plot ratios of the normalized and absolute lifetime areas of NCs in a TiO₂ film relative to their values at 77K.

The absorptive cross-section for non-resonant excitation should not vary significantly with temperature. Therefore, by carefully maintaining the same excitation power, optical focus etc., the ratio of the *absolute* lifetime areas against a control measurement is a good representation of the relative QY at a given temperature. We see that although the absolute area ratio (i.e. QY ratio) decreases at higher temperatures (as expected¹⁴), the ratio of the normalized areas does not change. This is a clear indication that the variation of the QY with temperature is inhomogenous – the QY decreases as the temperature increases because an increasing population of NCs are non-luminescent. This suggests that the temperature dependence of the ensemble QY could be driven by the blinking of individual nanocrystals which is known to be highly temperature dependent¹⁵⁻¹⁷ – at higher temperatures there is a higher probability that a given NC is “off”, so the population of “off” nanocrystals at a given time would be higher. Recent results that suggest the room temperature QY of a single NC in the “on” state is unity^{3, 18}. If this is true then there is no other way that the QY of an ensemble of NCs could increase as the temperature is lowered, other than for there to be a change in the populations of “on” and “off” nanocrystals. Our observation of inhomogenous changes in the QY of these nanocrystal-titania composites fits this hypothesis.

8.7 Conclusions

The purpose of this chapter has been to discuss the method by which one can use the PL decay of fluorescent solutions to monitor its QY and to show how it applies to the case of fluorescent nanocrystals in solution. Because NCs in general do not exhibit single exponential decays, we derived an equation (8.10), which can be used to monitor changes in QY simply through changes in the integrated area of a PL decay that is normalized to unity at time zero.

Our quenching experiments involving various chemicals demonstrated the limitations of using this method, particularly for nanocrystals. First, the radiative decay rate must be assumed to remain constant. Second, in order for the method to work accurately, any change in QY must be caused by a change in the PL decay that can be resolved in time by the instrumentation. The terms “homogenous” and “inhomogenous” categorize variations of the QY that meet or do not meet this second requirement. Homogenous variation of the QY means that all members of the ensemble exhibit the same PL decay dynamics, whereas inhomogenous variation implies that two or more sub-populations of NCs exhibit significantly different PL decay rates, with one sub-population’s decay being completely unresolved, causing equation 8.10 to fail. We took advantage of this caveat to gain new insight into the nature of temperature dependent changes in QY. Since changes in the A_N did not account for actual temperature induced variation of the QY, we concluded that the variations were inhomogenous and therefore possibly related to blinking of single NCs.

By understanding clearly the conditions that cause 8.10 to fail, we know more clearly when it is applicable and when it is not. We also have a method by which to gain

insight into the nature of changes in QY. The relationship between QY and integrated lifetime area is a useful technique for NCs, and it has been applied in a number of analyses in this thesis.

8.8 References

- 1 J. N. Demas, Crosby, G.A., *Journal of Physical Chemistry* **75**, 991 (1971).
- 2 J. J. Hermans, Levinson, S., *Journal of the Optical Society of America* **41**, 460.
- 3 B. R. Fisher, H. J. Eisler, N. E. Stott, et al., *Journal of Physical Chemistry B* **108**, 143 (2004).
- 4 M. G. Bawendi, P. J. Carroll, W. L. Wilson, et al., *Journal of Chemical Physics* **96**, 946 (1991).
- 5 C. B. Murray, et al., *Journal of the American Chemical Society* **115**, 8706 (1993).
- 6 B. O. Dabbousi, J. Rodriguez-Viejo, F. V. Mikulec, et al., *Journal of Physical Chemistry B* **101**, 9463 (1997).
- 7 M. A. Hines, Guyot-Sionnest, P., *Journal of Physical Chemistry* **100**, 468 (1996).
- 8 P. C. Beaumont, Johnson, D.G., Parsons, B.J., *Journal of the Chemical Society, Faraday Transactions* **89**, 4185 (1993).
- 9 V. Sundar, Eisler, H.J., Bawendi, M.G., *Advanced Materials* **14**, 739 (2002).
- 10 P. Guyot-Sionnest, *Physical Review B* **60**, R2181 (1999).
- 11 M. Shim, Guyot-Sionnest, P., *Journal of Physical Chemistry B* **104**, 1494 (2000).
- 12 V. I. Klimov, *Journal of Physical Chemistry B* **104**, 6112 (2000).
- 13 P. Roussignol, *Journal of the Optical Society of America* **4**, 5 (1987).
- 14 G. W. Walker, V. Sundar, C. M. Rudzinski, et al., *Applied Physics Letters* **83**, 3555 (2003).
- 15 M. Kuno, D. P. Fromm, H. F. Hafmann, et al., *Journal of Chemical Physics* **115**, 1028 (2001).
- 16 K. T. Shimizu, R. G. Neuhauser, C. A. Leatherdale, et al., *Physical Review B* **63**, 205316 (2001).
- 17 S. A. Empedocles, in *Chemistry* (Massachusetts Institute of Technology, Cambridge, 1999), p. 204.
- 18 X. Brokmann, L. Coolen, M. Dahan, et al., *Physical Review Letters* **93**, 107403 (2004).

Chapter 9: Fluorescence Correlation Spectroscopy of CdSe Nanocrystals

- 9.1 Introduction
- 9.2 Theory of FCS
- 9.3 Methods: Software Autocorrelation
- 9.4 Methods: Optical Setup and Hardware
- 9.5 Preliminary FCS measurements
- 9.6 Measurement of R_H of CdSe Nanocrystals in Aqueous Solution
- 9.7 FCS of Nanocrystals in High Viscosity Aqueous Solutions
- 9.8 Conclusions
- 9.9 References

9.1 Introduction

Previous chapters have focused nearly exclusively on using fluorescence spectroscopy to understand the physics of excited electrons in the core of nanocrystals. The experiments in this chapter, in contrast, aim to use the fluorescence from the nanocrystals as a handle for understanding their *chemical* behavior in a solution environment. Fluorescence correlation spectroscopy is a well-developed method for the study of molecules in solution environments. FCS relies on the statistical analysis of equilibrium fluctuations to measure kinetic properties of a chemical system. The technique has been applied to the study of translational diffusion and rotational diffusion¹⁻³, and chemical reactions⁴. Other applications of the technique have studied photophysical dynamics including triplet state^{5,6} kinetics or photobleaching kinetics⁷. FCS has emerged as a truly powerful technique for the study of molecular dynamics and interactions in solution. Despite this, only a few studies have used FCS to study colloidal nanocrystals in solution⁸.

Our primary motivation for developing FCS in this chapter is the study of nanocrystal diffusion in a solution environment in order to determine their hydrodynamic radius (R_H). The hydrodynamic radius describes the effective size of the particle in solution, reflecting both the physical dimension of a particle and its interaction with the solvent molecules surrounding it. For instance, a strong interaction with the solvent can lead to a tightly bound “first solvent shell” which increases the particle’s effective size in solution. For this reason mere TEM measurements are not sufficient to measure this property.

Our interest in the hydrodynamic radius of nanocrystals was motivated by their recent *in vivo* use for sentinel lymph node mapping (SLM). The goal of SLM is to locate the nearest lymph node to a point of interest, usually a malignant tumor. Whether a sentinel lymph node contains malignant cells is a strong indicator of whether the tumor has metastasized. Nanocrystals are well suited to SLM because their size is small enough for uptake into the lymph system, but large enough to become localized inside the lymph node and hence to mark its location. A robust measurement of hydrodynamic radius is necessary to achieve this. Other methods for determining diffusion coefficients and particle size like diffractive light scattering (DLS) do not produce robust measurements at the very small sizes of interest here (<20nm). Although DLS is highly similar to FCS, it relies on elastically scattered light for its signal, the intensity of which scales as R^6/λ^4 ⁹.¹⁰ Therefore any dust particles or other agglomerates easily dominate the scattering of small nanocrystals, making the technique highly sensitive to dust or agglomerated particles. Because FCS does not suffer this shortcoming, we explored its use for the analysis of our nanocrystals.

The basic idea behind FCS measurements is illustrated in figure 9.1. Dashed lines and an oval represent the beam-path of excitation light and the spatial extent of the confocal point-spread function (PSF) respectively. This PSF is the product of the functions that describe the spatial distribution of excitation probability and of detection efficiency. Particles in solution randomly diffuse in and out of the PSF causing the number of molecules detected, and hence the intensity of the fluorescence signal, to fluctuate as a function of time. These fluctuations are illustrated using actual data at the bottom of figure 9.1.

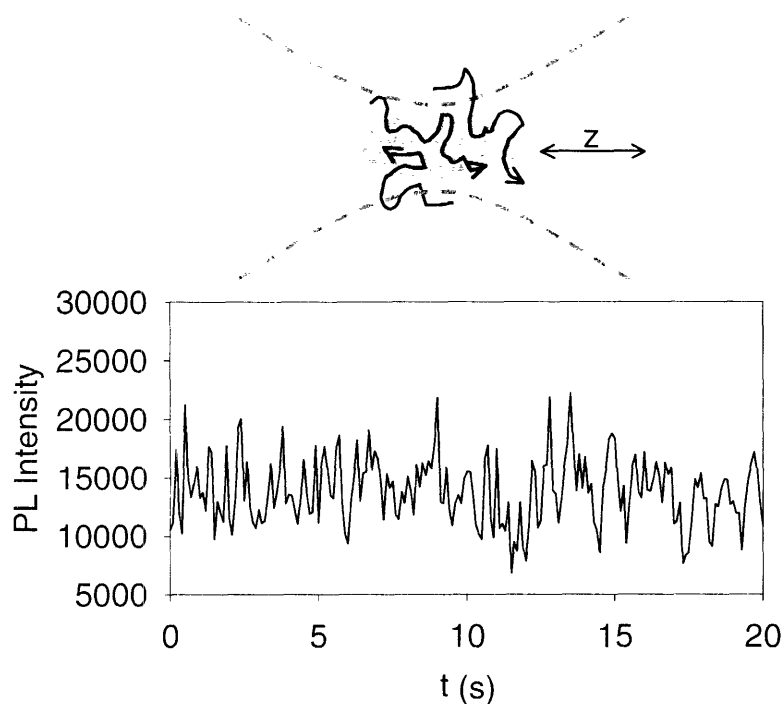


Figure 9.1 *Top:* cartoon of the diffusional trajectories of three molecules into and out of the optical focal volume (PSF, gray ellipsoid). *Bottom:* Intensity trajectory taken from an FCS experiment. The intensity fluctuates with large amplitude as the number of fluorescent particles occupying the focal volume varies.

Shot noise cannot account for the fluctuations of this intensity trajectory. The standard deviation of the fluctuations in 9.1 is 2940 counts per second (cps), whereas shot noise for this mean signal intensity would only be 120cps. Measurement of the autocorrelation of the signal intensity reveals the relaxation dynamics of the fluctuations.

These dynamics may arise not only from diffusion of the particles into and out of the PSF, but also through other chemical fluctuations such as chemical reactions and particle binding, or molecular rotation to name a few. The inventors of FCS, for instance, used the technique to study the kinetics of a biologically relevant binding reaction between a dye, ethidium bromide (EtBr) and DNA molecules⁴. The quantum yield of EtBr is known to increase 20x when intercalated inside DNA. Hence the fluctuation of fluorescence intensity reflected the binding of EtBr in addition to the diffusion of fluorescent particles in and out of the PSF. Unfortunately the technique used in these early experiments required high concentrations of particles, had low sensitivity and were cumbersome to implement. The basic problem of early experiments was that experimentally measurable fluctuations occur only for very small sample volumes. Although excitation lasers can be focused well in the radial dimension, it took the depth sectioning ability (see chapter 2) of confocal microscopy to confine the PSF along the z-axis enough to make FCS widely practical¹¹. The development of two-photon microscopy (2PM) has improved the technique further¹². With 2PM a 3D confined sample volume is achieved even without a pinhole in the collection path, since the excitation PSF is naturally confined in all 3 dimensions. In the FCS experiments of this chapter, two-photon excitation is the method of choice.

9.2 Theory of FCS

FCS uses the fluctuation of fluorescence intensity to represent fluctuations of an open system near equilibrium. We are interested in the fluctuation of the concentration of component j at a point in space and time:

$$\delta C_j(r,t) = C_j(r,t) - \langle C_j \rangle \quad (9.1)$$

In its most general form, translational fluctuations of molecules as well as fluctuations from chemical equilibrium are described by the general diffusion equation,

$$\frac{\partial \delta C_j(r,t)}{\partial t} = D_j \nabla^2 \delta C_j(r,t) + \sum_{k=1}^m K_{jk} \delta C_k(r,t) \quad (9.2)$$

Here the D_j is the diffusion constant of species j and K_{jk} are the chemical rate constants from species j to species k . We connect the local concentration fluctuations to observable fluorescence intensity fluctuations by assuming that the number of fluorescence photons collected is proportional to both the intensity of the excitation light and the concentration at each position, r . Therefore the number of photons emitted as a function of time, $n(t)$, is given by,

$$n(t) = \Delta t \int d^3 r I(r) \sum_{j=1}^m Q_j C_j(r,t) \quad (9.3)$$

Where Q_j is the product of the absorption cross-section and the fluorescence quantum yield of component j . The fluctuation in photon number $\delta n(t)$ can be obtained simply by replacing $C_j(r,t)$ with $\delta C_j(r,t)$ in equation 9.3.

FCS experiments measure the autocorrelation of the intensity fluctuations, which is the time average of the products of the intensity fluctuations:

$$G(t) = \frac{\langle \delta n(t+t') \delta n(t') \rangle}{\langle \delta n(t+t') \rangle \langle \delta n(t') \rangle} = \frac{\langle n(t) n(0) \rangle}{\langle n(0) \rangle^2} - 1 \quad (9.4)$$

The angled brackets indicate time averaging, and ergodicity is assumed to equate the two expressions. Substitution of $\delta n(t)$ into 9.4 yields a complicated expression for $G(t)$ which

is a convolution of the correlation function of concentration fluctuations with the excitation intensity profile $I(r)$.

$$G(t) = \frac{(\Delta t)^2}{\langle n \rangle^2} \iint d^3 \bar{r} d^3 \bar{r}' I(\bar{r}) I(\bar{r}') \sum_{j,k} Q_j Q_k \langle \delta C_j(\bar{r}, 0) \delta C_k(\bar{r}', t) \rangle \quad (9.5)$$

Fluctuations in the concentration are given by the solutions of equation 9.2. These solutions are obtained by Fourier transform of equation 1. Details of these solutions for the general case of an arbitrary excitation profile and an arbitrary number of interacting species can be found elsewhere^{3, 13}. In this chapter we are interested in the specific case of a single species component in the system – uniformly fluorescent nanocrystals in solution. Therefore the second term on the right hand side of 9.2 is ignored and the solutions, obtained by Fourier transform, have the well-known form,

$$\delta C(\vec{q}, t) = \delta C(\vec{q}, 0) \exp(-Dq^2 t) \quad (9.6)$$

where q is the Fourier variable, and D is the diffusion coefficient of interest to us.

The form of the illumination profile is assumed in this work to be Gaussian in all three directions, and radially symmetric about the z axis,

$$I(\vec{r}) = I_o \exp\left(-\frac{2(x^2 + y^2)}{w_{xy}^2} - \frac{2z^2}{w_z^2}\right) \quad (9.7)$$

The three dimensional Gaussian (3DG) assumption is actually a weak assumption for many optical setups¹². However, it is the only way of obtaining a closed form solution for $G(t)$ to which experimental data can be fitted. As a result, except for a few notable exceptions¹², most implementations of FCS use the 3DG assumption. To obtain a closed form for $G(t)$ we take the Fourier transform of 9.7 and plug it along with $\delta C(q, t)$ back into the Fourier transform of 9.5:

$$G(t) = \frac{(2\pi)^{-3/2}}{Q^2 \langle C \rangle^2} \int d^3 \vec{q} Q^2 \langle C \rangle \exp\left(-\frac{w_x^2}{4}(q_x^2 + q_y^2) - \frac{w_z^2}{4}q_z^2 - Dt(q_x^2 + q_y^2 + q_z^2)\right) \quad (9.8)$$

which simplifies to,

$$G(t) = \frac{1}{\langle C \rangle V} \left(1 + \frac{t}{\tau_D}\right)^{-1} \left(1 + \frac{t}{\tau'_D}\right)^{-1/2} \quad (9.9)$$

where V is the focal volume ($^{4/3}\pi w_x w_y^2 w_z^2$), $\tau_D = w_{xy}^2/4D$ and $\tau'_D = w_z^2/4D$. The right hand side of equation 9.9 has a good physical description. Each direction of translational diffusion contributes a factor of $(1 + t/\tau_D(k))^{-1/2}$ to $G(t)$, where $\tau_D(k)$ approximates the time necessary for the particle to traverse the focal volume in the direction k . Since the 3DG illumination profile assumes a PSF that is symmetric about the z -axis, $\tau_D(x) = \tau_D(y) = \tau_D$. These combine to make the first term, $(1 + t/\tau_D)^{-1}$, while diffusion in the z direction contributes $(1 + t/\tau'_D)^{-1/2}$ which has a different value, since the focal volume is longer in the z direction.

In addition to this interpretation of 9.8, one can see that the smaller the mean number of particles occupying the probe volume, $\langle n \rangle = \langle C \rangle V$, the larger the amplitude, $G(0)$, of the correlation function. If the probe volume, V , is independently known, the amplitude of $G(t)$ provides a method of directly measuring the concentration of a solution.

After obtaining the diffusion time constant τ_D by fitting the $G(t)$ decay, the diffusion coefficient for the species can be obtained,

$$D = \frac{1}{p} \frac{w_{xy}^2}{4\tau_d} \quad (9.9)$$

The hydrodynamic radius can be calculated from D using the Stokes-Einstein equation as well,

$$R_H = \frac{kT}{6\pi \eta D} \quad (9.10)$$

The parameter p in equation 9.9 accounts for the type of excitation used – one or two photon. If two photon excitation is used the illumination profile must be squared to account for the two photons used in every excitation event. The result is that p takes a value of 2 whereas it has a value of unity for single photon excitation¹².

In order to extract D from equation 9.9 the focal volume parameter w_{xy} is required. Although one can theoretically calculate w_{xy} and w_z from the optical properties of the microscope [26], we found it unreliable in practice. Moreover, we mentioned earlier that the 3DG approximation is imperfect so these parameters only represent an approximation of the actual illumination profile anyway. Therefore, FCS measurements are usually calibrated against a set of samples with known R_H and concentration to yield effective values for the focal volume, $V=V_{eff}$ and w_{xy} . The basis for calibration of R_H is given by combining equations 9.9 and 9.10,

$$R_H = \left(\frac{kT}{6\pi \eta} \frac{4p}{w_{xy}^2} \right) \tau_D \quad (9.11)$$

and the basis for calibration of concentration is derived from equation 9.8,

$$\langle C \rangle = V^{-1} G(0)^{-1} \quad (9.12)$$

It is worth briefly noting the potential use of FCS to measure the absolute absorptive cross section for nanocrystalline materials. This value has been obtained for CdSe using other methods¹⁴, but that experiment is tedious and impractical to perform on

a large scale for many new nanocrystalline materials. It is possible, though, using FCS to directly measure an unknown concentration of nanocrystals in a solution after calibrating $G(t)$ according to 9.12. The concentration, along with a UV/VIS absorption spectrum, which gives the optical density at all wavelengths, allows the cross-section of an individual nanocrystal to be calculated using Beers law.

9.3 Methods: Software Autocorrelation

Two options are available for the measurement of $G(t)$. The first, most experimentally straightforward option is to use a commercially available hardware correlator that is capable of directly generating $G(t)$ over many orders of magnitude of time from either a digital or analog signal intensity input. In our experiments this was not available so a second option was used, namely to simply acquire the fluorescence intensity signal continuously using finely spaced time intervals. Using software $G(t)$ can then be numerically calculated from the recorded intensity trajectory, $n(t)$. The equation used to correlate the discretely sampled $n(t)$ is obtained by first substituting $\delta n(t) = n(t) - \langle n \rangle$ into equation 9.4, and then writing out the time averaging explicitly:

$$G(t) = \frac{\langle n(t'+t)n(t') \rangle}{\langle n(t'+t) \rangle \langle n(t') \rangle} - 1 = \frac{\frac{1}{N-j} \sum_{i=0}^{N-j} n_{i+j} n_i}{\frac{1}{N-j} \sum_{i=0}^{N-j} n_{i+j} \times \frac{1}{N} \sum_{i=0}^N n_i} - 1 \quad (9.13)$$

where $t_c = j \times \Delta t$ and N is the total number of samples comprising the intensity trajectory.

Although the right hand side of equation 9.13 gives a simple prescription for the calculation of $G(t)$, the calculation is more challenging in practice. For instance, in our case we acquired $n(t)$ using the Timeharp200, which was capable of registering the

absolute arrival time of every single photon with 100ns resolution. The photon detection rate was kept well below 10^6 cps so single photons were not missed on account of the detection speed. By reading out the absolute arrival time, t_p , of each photon, p , and counting how many photons occur within a specified time interval (or 'bin'), Δt , the trajectory of photon intensity, $n(t)$ could be recovered. The example data shown in Figure 9.1 were generated in this way using $\Delta t = 1$ second. The value of Δt can be set arbitrarily small, but since the error on t_p is 100ns it is useless to set Δt smaller than 100ns. Nonetheless, a very small Δt is desirable, since it defines the smallest correlation time, t , of the function $G(t)$ that we aim to numerically calculate.

The reason that $G(t)$ is not simple to calculate from $n(t)$ in practice originates in the sheer scale of the problem. We would like to set Δt to a value of about $1\mu\text{s}$, while the total length of $n(t)$ is at least on the order of seconds, usually 10 to 100 seconds. This results in about 10^7 time intervals (or data points) for a typical $n(t)$. If one were to write a simple numerical code to calculate the value of $G(t)$ for all t between $1\mu\text{s}$ and 1s using equation 9.13 as it is written (e.g. using two nested for loops, the outer one through all j , the inner one over all i), the program would have to hold two arrays, one for $G(t)$ and one for $n(t)$, each with 1 to 10 million elements. At least 32 bit (4 byte) precision would be required for each element, so the array sizes would be on the order of $4 \times 10^7 = 40$ MB. Although this is within the physical RAM capacity of modern computers, it requires significant manipulation of memory resources and most simple C compilers tried by us did not allow such large arrays. Furthermore, these memory considerations do not even mention the problem that $10^7 \times 10^6$ iterations of the outer loop are necessary which also

takes much longer than is desired – one would like to generate $G(t)$ quickly (i.e. within a few seconds) after each FCS collection run.

The solution to this problem lies in recognizing that in order to see dynamics over so many orders of magnitude in time, we will always visualize the data on a logarithmic plot. This means that at small t , the time interval should be short with a high sample rate, whereas slower sample rates and larger time intervals can be used at large t . By using logarithmically spaced t the number of data points in $G(t)$ can be reduced from millions to a couple hundred. Furthermore, by using an intelligent algorithm we can avoid having

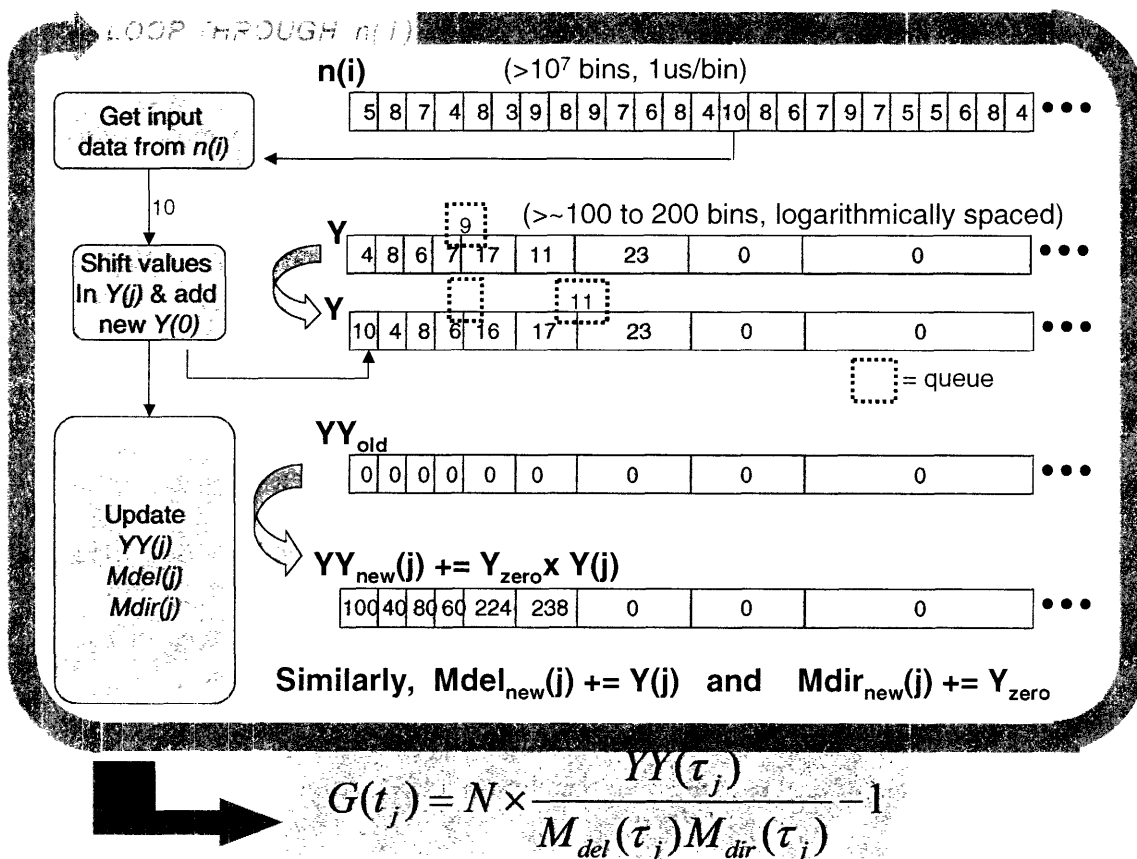


Figure 9.2 Illustration of the software algorithm used to quickly calculate $G(t)$ on a logarithmic time scale without having to store $n(i)$ in running memory. At each turn of the loop an intensity value is read in from the file containing $n(i)$ which is used to update $Y(j)$ whose corresponding times are logarithmically spaced. Then three other log-spaced data structures are updated based on the current $Y(j)$. After repeating the loop for every value read in from $n(i)$, the correlation function can be calculated simply according to equation 9.11.

to store the entire $n(t)$ data vector in running memory during the calculation. Instead, for each value of $n(t)$ that is read off, the couple hundred $G(t)$ data points are updated and the process is repeated without storing the entire $n(t)$ trajectory in RAM at any time. This approach mimics the algorithm used in a well-known correlator hardware design¹⁵ and is illustrated in figure 9.2.

The main data structures that are held in memory, Y , YY , M_{del} and M_{dir} are all logarithmically spaced and sized in time, covering $t_j = 0$ to T_j^{max} . The spacing and size of the time intervals are set by the logarithmic base and the parameter Npg – the number of bins per group. For instance if the base is 2 and Npg is 4, then the values of t_j will be the following multiples of the smallest time interval (Δt): 1, 2, 3, 4; 6, 8, 10, 12; 16, 20, 24, 28; 36, 44, 52, 60; 76, 92, 108, 124; ... T_j^{max} . Therefore, as shown in figure 9.2, $Y(j)$ essentially holds the most recent $n(i)$, but with logarithmic spacing and binning. Each element of $YY(j)$ is updated at each turn of the loop by multiplying the j^{th} element of Y by its 0^{th} element and then adding the product to the previous $YY(j)$ value. In this way a running sum of the product of intensities separated by time t_j is kept. (Note that here t_j is given by a logarithmic spacing, so $t_j \neq j\Delta t$). An analogous procedure is executed for M_{del} and M_{dir} , such that these vectors hold the running sums of the $Y(j)$ and $Y(0)$ respectively. After reading in each individual data point from the entire linearly spaced $n(t)$, and updating Y , YY , M_{del} and M_{dir} at each turn, $G(t)$ can be calculated simply for each (logarithmically spaced) t_j .

$$G(t_j) = \frac{YY(t_j)}{M_{del}(t_j)M_{dir}(t_j)} \quad (9.11)$$

It is worth noting that because the size of each logarithmically spaced interval is not uniform, updating Y is not as simple as incrementing the value of each interval. Instead,

at the edge of each “group” of like-sized intervals, a queue is kept. This queue is used for updating $Y(j)$ when each new data point from $n(i)$ is added. For example, assume for example that $Y(j)$ is logarithmically spaced using base=2 (this can be generalized simply to higher base values), then the first interval in a group accounts for twice as much time as that of the preceding interval, which belongs to the previous group. If the queue adjoining these groups is empty (and all previous queues are filled), then the queue in question is filled by the value in the last interval of the previous group. If, on the other hand, the queue contains a value (and all previous queues are filled), then that queue’s

		loop 1	loop 2	loop3	loop 4	loop 5	loop 6	loop 7	loop 8	loop 9	loop 10	loop 11
Corr.Time for bin (sec)	Binsize (s)	Y (initial)	newY = 6	newY = 7	newY = 8	newY = 9	newY = 10	newY = 11	newY = 12	newY = 13	newY = 14	newY = 15
0	0.000001	0	6	7	8	9	10	11	12	13	14	15
0.000001	0.000001	1	0	6	7	8	9	10	11	12	13	14
0.000002	0.000001	2	1	0	6	7	8	9	10	11	12	13
0.000003	0.000001	3	2	1	0	6	7	8	9	10	11	12
0.000004	0.000001	4	3	2	1	0	6	7	8	9	10	11
0.000005	0.000001	5	4	3	2	1	0	6	7	8	9	10
0.000006	0.000001	6	5	4	3	2	1	0	6	7	8	9
0.000007	0.000001	7	6	5	4	3	2	1	0	6	7	8
0.000008	0.000002	8	8	13	13	9	9	5	5	1	1	13
0.00001	0.000002	9	9	8	8	13	13	9	9	5	5	1
0.000012	0.000002	10	10	9	9	8	8	13	13	9	9	5
0.000014	0.000002	11	11	10	10	9	9	8	8	13	13	9
0.000016	0.000004	12	12	12	12	21	21	21	21	17	17	17
0.00002	0.000004	13	13	13	13	12	12	12	12	21	21	21
0.000024	0.000004	14	14	14	14	13	13	13	13	12	12	12
0.000028	0.000004	15	15	15	15	14	14	14	14	13	13	13
0.000032	0.000008	16	16	16	16	16	16	16	16	29	29	29
0.00004	0.000008	17	17	17	17	17	17	17	17	16	16	16
0.000048	0.000008	18	18	18	18	18	18	18	18	17	17	17
0.000056	0.000008	19	19	19	19	19	19	19	19	18	18	18

Figure 9.3 Actual test data for the use of “queues” to accurately increment values in $Y(j)$ each time a new data point is read from $n(i)$ and added to the beginning of $Y(j)$. Each column shows $Y(j)$ at a subsequent loop iteration and each row corresponds to a different value of j . The base of the logarithmic time spacing is 2. The first interval group was arbitrarily chosen to have twice as many intervals as the rest of the groups.

value is added to the value in the last interval of the previous group to make the value that is shifted into the first interval of the next group. Finally if any previous queues are empty, they must be filled first, before action occurs on the queue in question.

The effect of the foregoing is to keep track of all photons as they are re-binned with logarithmic spacing in $Y(j)$, so that their complete contribution to the correlation is accounted for. An example of the use of queues is shown in figure 9.3. In this example each column represents Y at a subsequent iteration, while each row represents an interval, j . The base used is 2 with $Npg = 4$. *Note:* the first group of intervals is chosen to have 2 x Npg intervals in our program, while all subsequent groups have Npg intervals.

9.4 Methods: Optical Setup and Hardware

The previous section described in detail the method used to quickly calculate $G(t)$ on a logarithmic scale using $n(t)$ acquired using the Timeharp200 photon counting hardware. Here we discuss how the fluorescence itself was collected. Two-photon excitation was used to excite the NCs, and the optical setup for these experiments is shown in figure 9.4. The setup is completely analogous to those used in previous chapters with the exception that 150fs pulses of 800nm wavelength laser light (Ti:Sapphire oscillator at 76 MHz) are used for excitation instead of the 400nm or 514nm wavelength light used in other chapters. This means that the dichroic chosen for these experiments reflects red wavelengths but passes shorter wavelengths (Chroma, Q720DCSX). We used either a 1.25NA oil-immersion or a 1.2 NA water immersion objective with infinity correction to focus the excitation into the sample and to collect the

fluorescence. As discussed in chapter 2, the use of two-photon excitation limits the region of excitation to a very small volume at the focus of the objective.

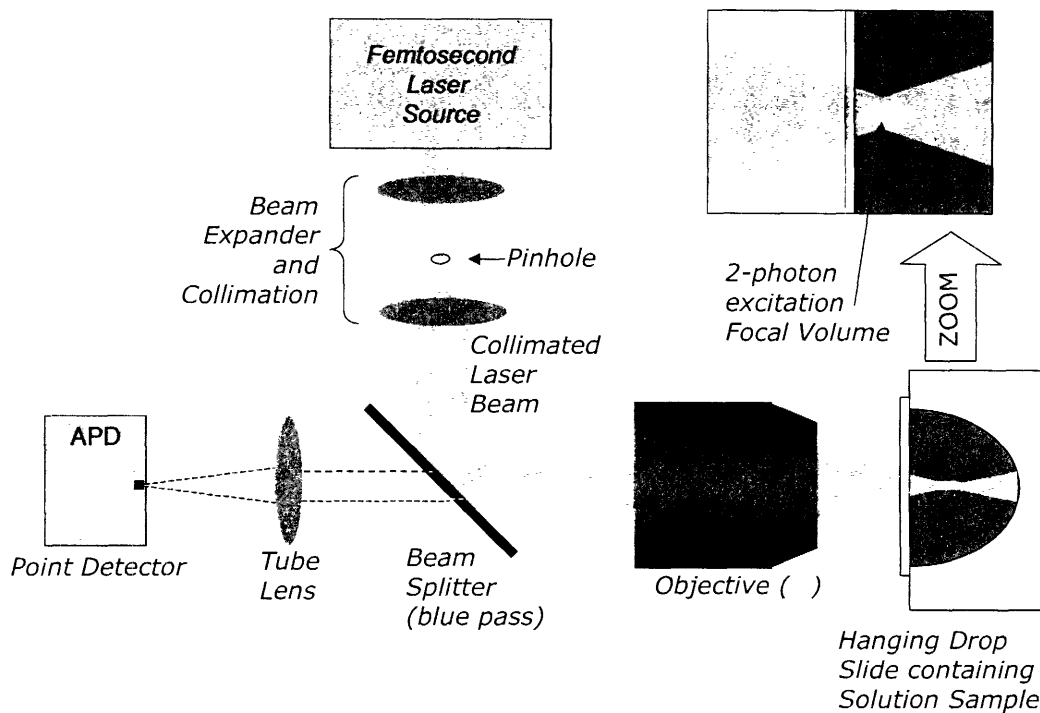


Figure 9.4 Optical Setup Used for FCS measurements with two-photon excitation in a confocal geometry. Collimated, pulsed laser light (gray) is focused by a high NA objective in the bulk solution creating only a small volume of two-photon excitation (white). The fluorescence from this small volume is collected and focused to a single point detector.

In theory the PSF of two-photon excitation with 800nm light is approximately an ellipsoid with a transverse radius of 205nm and axial radius of 635nm[26]. Fluorescence is not generated anywhere else in the solution, so no pinhole is required to tighten the axial dimension of the collection PSF – the excitation PSF is already tight. This advantage of 2PM for FCS experiments allows greater detection sensitivity without compromising the small size of the focal volume. To be sure that the fluorescence that we observed originated from two-photon excitation we measured the fluorescence intensity

as a function of power. If the fluorescence intensity increased quadratically with power, we could be sure that it was driven by two-photon excitation.

Only a single detector was used for acquisition of $n(t)$. Other implementations of FCS use a beam splitter to send the fluorescence to two different detectors and then calculate $G(t)$ by the cross-correlation of the intensity trajectories collected by the two detectors¹³. The reason for two detectors is that detectors have a dark period after detection of a photon that usually lasts about 200ns, causing $G(t)$ to be artificially strong at these times. Since our experiments did not sample sub microsecond timescales a single detector was sufficient.

All samples used in these experiments were in the solution phase and were contained in a hanging drop slide, which was covered by a standard amorphous quartz coverglass (No. 1.5). For calibration of the FCS experiment aqueous solutions of fluorescent microspheres of known size were used. These were obtained from Duke Scientific and had the following hydrodynamic radii: $R_H = 14\text{nm}$, 22nm , 28.5nm , 35.5nm , 43.5nm . After calibrating the measurement numerous samples of nanocrystals in both aqueous and organic (e.g. hexane or toluene) solution were investigated.

To study the effect of different water-solubilization techniques on the R_H of the nanocrystals in solution, we prepared two different aqueous samples from the same batch of nanocrystals (core radius = 2.2nm , based on band-edge absorption of 570nm). Sample A was water solubilized using an oligomeric phosphine cap^{16, 17}, whereas sample B was water solubilized using a phospholipid micelle technique¹⁸.

To study the effect of solvent viscosity on $G(t)$ for nanocrystals, we added small, measured amounts of glycerol to the aqueous solutions of nanocrystal. By varying the

volume fraction of glycerol present in the aqueous solutions of nanocrystals the solvent viscosity could be tuned over a large range.

9.5 Preliminary FCS Measurements

Before undertaking the studies of specific samples nanocrystals we performed control experiments to investigate the behavior of FCS measurements when specific parameters are varied, namely the axial focal depth, and the excitation power. We found that the curve, $G(t)$, varied widely for different depths of focus in the solution sample. This is shown in figure 9.5 where $G(t)$, obtained from aqueous solutions of fluorescent microspheres ($22\text{nm} = R_{II}$) using the oil immersion objective, is shown at focal depths ranging from about $1\mu\text{m}$ to $100\mu\text{m}$.

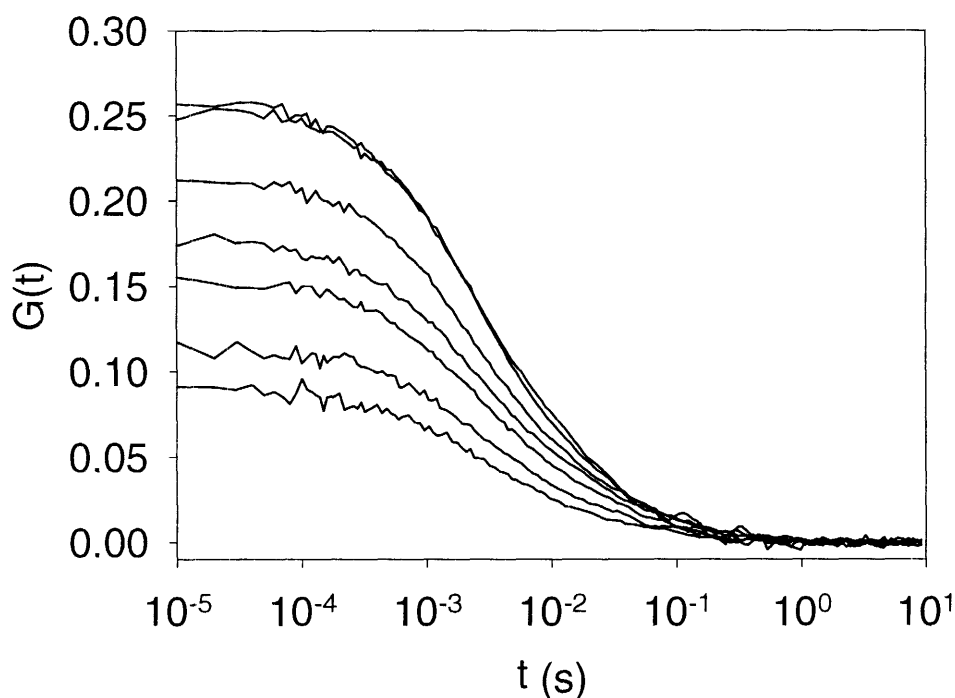


Figure 9.5 FCS measurements on fluorescent polymer microspheres in aqueous solution using an oil immersion objective. Each measurement was taken at a different focal depth over a range of $100\mu\text{m}$. The amplitude of the measurements was highly dependent on the focal position, but the time constant of the decay remained constant.

The dependence of $G(t)$, as well as the mean fluorescence intensity, $\langle I \rangle$, on focal depth is shown explicitly in figure 9.6. The highest amplitude of $G(t)$ is obtained near the edge of the sample. As the focus is moved deeper into the solution, $G(t)$ decreases asymptotically toward zero. On the other hand, as the PSF is pulled back out of the solution across the coverglass interface, $G(t)$ drops quickly. Note that the peak of the average intensity occurs at a deeper focus than the peak of $G(t)$. The reason is likely that at $z=0$, the PSF is approximately cut in half by the coverglass interface so the probe volume is smaller and fewer nanocrystals on average occupy the focal volume – recall that $G(t)$ is inversely proportional to $\langle n \rangle$.

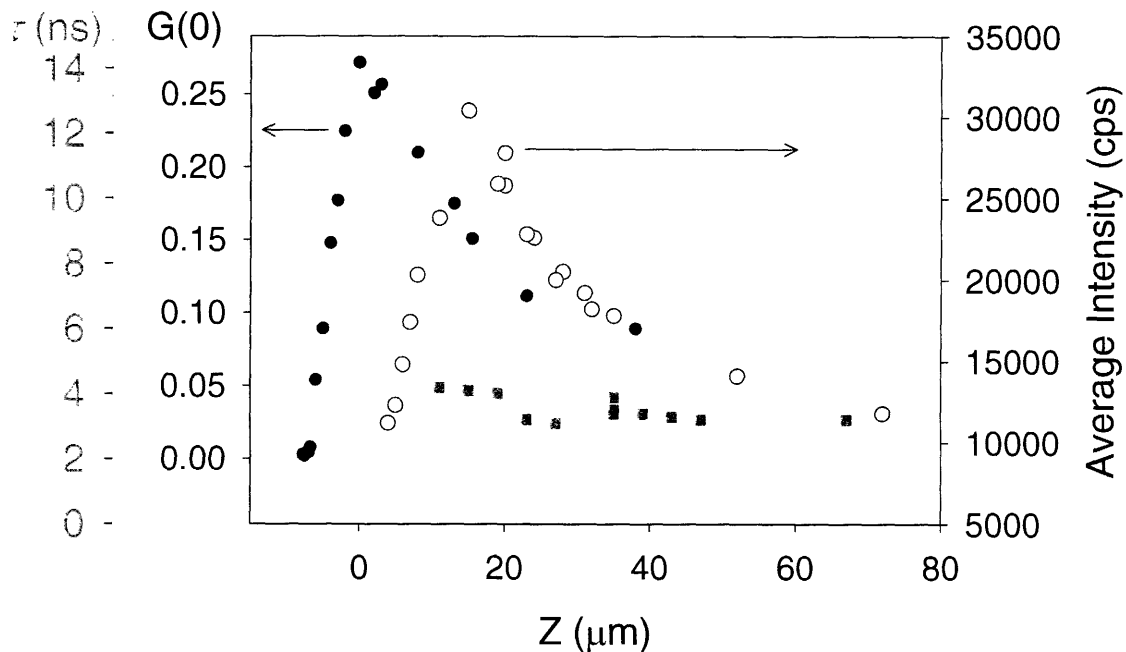


Figure 9.6 Summary of focal depth dependence of $G(t)$ (●), average fluorescence intensity ($\langle n \rangle$, ○), and the time constant of the decay of $G(t)$ (■). These data were obtained from two-photon FCS measurements of aqueous microspheres using an oil immersion objective.

The average intensity, on the other hand, peaks when the full excitation PSF is within the solution, and it decays thereafter as the focus is pushed deeper in the sample. Most importantly for these measurements, however, the time constant of the decay remains the same for all of these measurements (gray squares). The time-constants shown in this graph are the $t_{1/2}$ values, where $G(t_{1/2}) = 1/2 G(0)$. The use of $t_{1/2}$ instead of fitted τ_D is discussed in section 9.6. For now suffice it to say that $t_{1/2} \sim \tau_D$.

The reason for the strong variation of $G(\theta)$ with focal depth is improper index matching of the immersion oil ($n_{oil}=1.51$) with the sample solution ($n_{H_2O}=1.32$). This is effect has been described previously in references on confocal microscopy¹⁹ described and illustrated in figure 9.7. The simple diagram here allows us to geometrically derive a relationship between the relative position of the objective to the sample, s and the actual depth of focus, z :

$$\delta z = \Delta s \frac{\tan\left(\sin^{-1}\left(\frac{NA}{n_1}\right)\right)}{\tan\left(\sin^{-1}\left(\frac{NA}{n_3}\right)\right)} \quad (9.11)$$

One can see that if $n_1 \neq n_3$ then incremental changes of focal depth, Δs , are magnified in the objectives PSF. The end effect is that the PSF is elongated over its theoretical value when n_1 and n_3 are mismatched, and moreover, the size of the PSF can vary as a function of focal depth. This leads to variability in $G(\theta)$ as the focal volume varies at different focal depths.

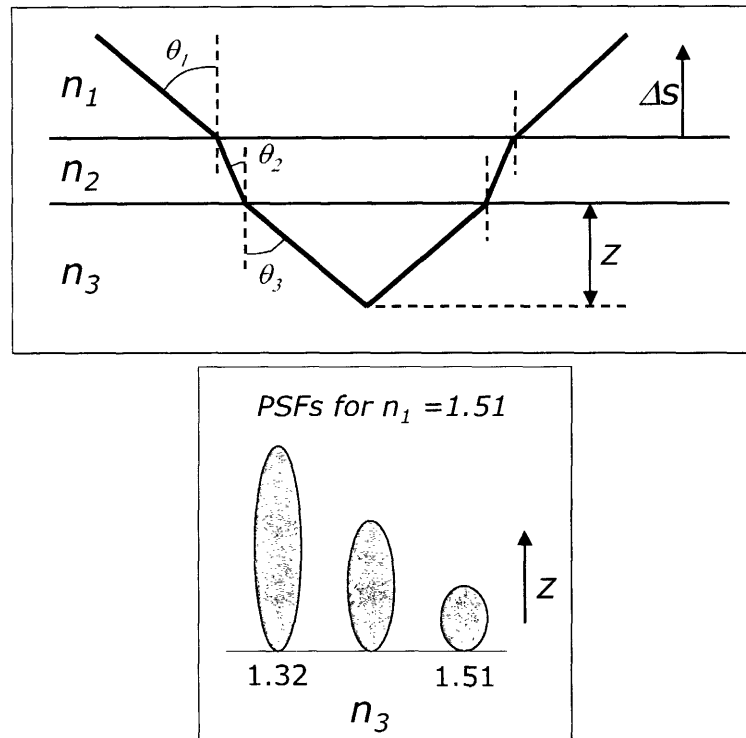


Figure 9.7 Illustration of the effect that mismatched of the refractive indices of the solution and the objective immersion fluid. The PSF becomes elongated, and the shape of the PSF changes with different focal depths. This effect causes the variation of $G(0)$ with focal depth that is observed. These figures were adapted from other work¹⁹.

On the other hand, if n_1 were to match the index of the solution, n_3 , then the ratio of tangent functions in equation 9.11 cancels to unity, $\Delta s = \delta z$, and the variation of $G(0)$ with focal depth should be reduced. We observed this in side-by-side comparison of oil ($n_1 = 1.51$) and water ($n_1 = 1.32$) immersion objectives on aqueous samples ($n_3 = 1.32$).

Besides the strong dependence of $G(t)$ on focal depth, we also found that it was highly dependent on excitation power. In figure 9.8 a series of $G(t)$ is presented that were taken from the same sample at the same focal depth but using various excitation powers. The value of $G(0)$ at higher excitation powers was less than $G(0)$ at lower powers. The reason for the decrease of $G(0)$ above a critical power level is the excitation saturation of

nanocrystals that are in the center of the focal volume. This effect has been observed previously for organic dye molecules under two photon excitation²⁰ and is illustrated in the inset of figure 9.8. At very high powers the probability of exciting a nanocrystal in the center of the focal volume approaches unity. This means that the fluorescence emission intensity from the center of the focal volume cannot grow commensurately with the edges as the power is raised further yet. The result is that the effective PSF starts to look like a top-hat and its effective size (the full width at half maximum, FWHM) is increased. The increased effective size of the PSF causes $G(l)$ to decrease.

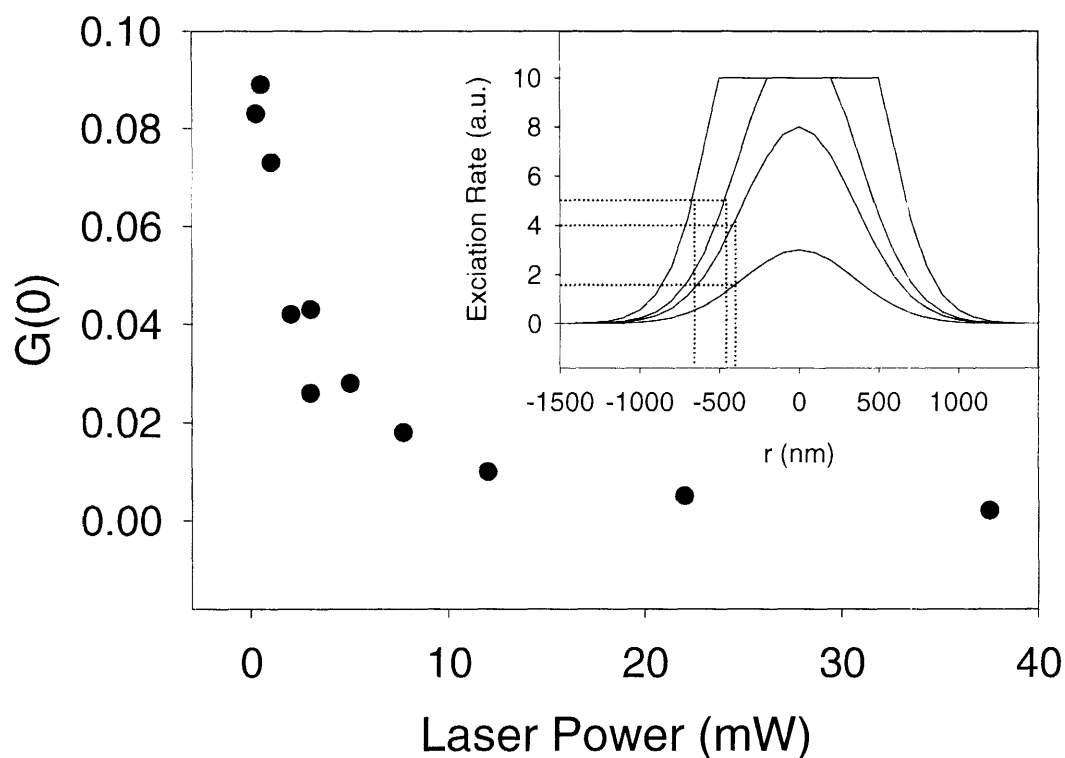


Figure 9.8 Power dependence of $G(l)$ at a constant focal depth. As the excitation power is increased, $G(l)$ decreases on account of an artificially expanded excitation volume. **Inset:** profile of the excitation rate of a chromophore as a function of position in solution. As power is increased the probability of excitation by a given pulse approaches unity and the excitation rate saturates causing the flattening of top of the excitation volume shown. This causes the effective volume to increase and $G(l)$ to decrease as a result.

The diffusion times measured in FCS can be affected by saturation of the nanocrystals as well. Therefore, FCS measurements in this chapter are carried out using as low an excitation power as possible.

The primary conclusions obtained in these experiments place guidelines on the manner in which FCS experiments should be executed. First, we found a strong sensitivity of $G(0)$ to focal depth when index matched immersion fluid is not used. Since exact focal depth cannot be easily reproduced from measurement to measurement, this instability precludes the dependable use of $G(0)$ as a parameter for robust measurement of solution properties like concentration, unless an index matched immersion fluid is used (e.g. a water immersion lens). Despite this instability, we did find the time constant ($t_{1/2}$) of the $G(t)$ decay to be very robust, even for objectives that are not index matched. In addition to these focusing issues, we also found, that the measurement of $G(t)$ can be easily ruined if the measurement is carried out with more than a few milliwatts of excitation power. With these caveats in mind we were able confidently make FCS measurements of CdSe nanocrystals in solution.

9.6 Measurement of R_H of CdSe Nanocrystals in Aqueous Solutions

FCS measurements of fluorescent polymer microspheres in aqueous solution are shown in figure 9.9. The hydrodynamic radii of the microsphere samples used in these measurements were known so these results could be used for calibration. The inset of figure 9.9 shows the linear relationship found between microsphere size and $t_{1/2}$, where, as earlier, $G(t_{1/2}) = 1/2G(0)$. We use $t_{1/2}$ to calibrate our measurements because fits to

equation 9.8 were unsatisfactory and produced time constants that were not easily reproduced in sequential measurements.

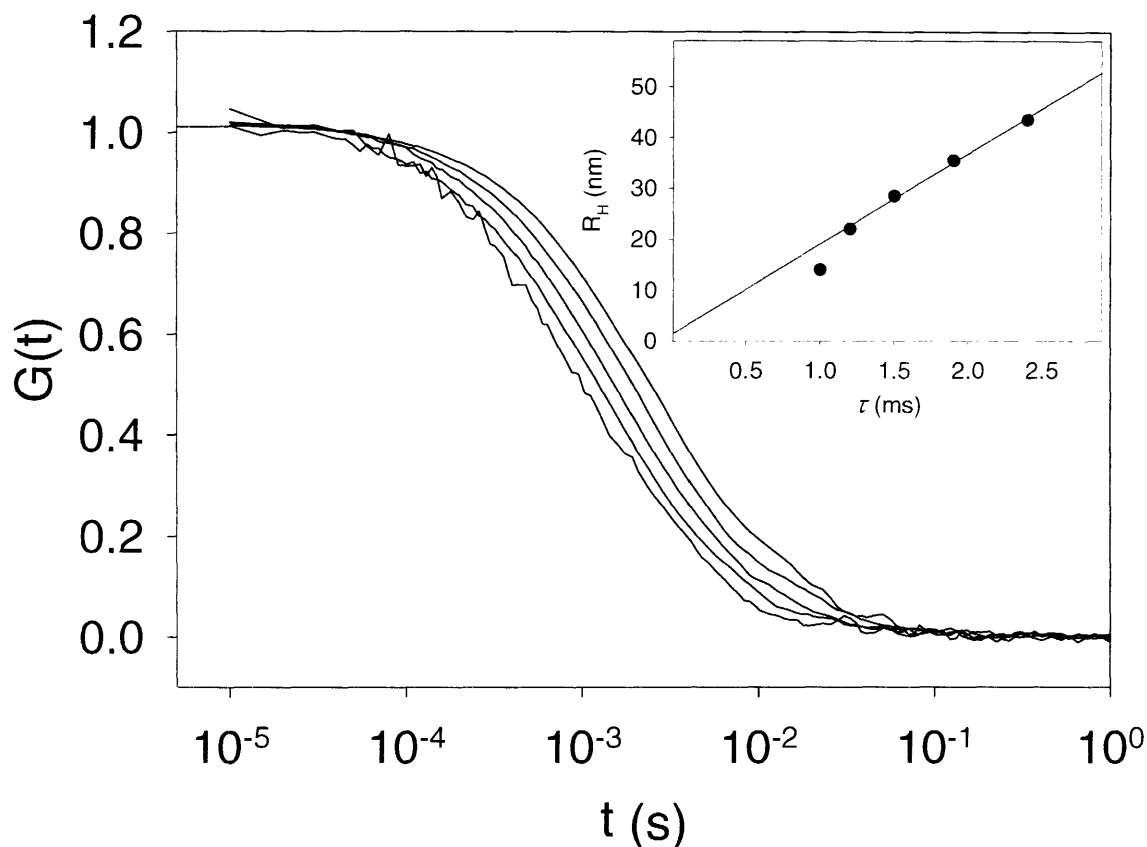


Figure 9.9 Normalized FCS curves for fluorescent polymer microspheres of five different sizes. **Inset:** calibration of the $t_{1/2}$ against known particle size (R_H) using the FCS curves shown in the main graph.

A simple polynomial fit to the R_H calibration data, shown in the inset of figure 9.9

yielded $R_H [nm] = 18.137 t_{1/2}[ms]$. Using the known viscosity of water, 0.89cP, and equations 9.8 and 9.9 we can back out the transverse dimension of the focal volume: $w_{xy} = 327nm$. The value of w_z was determined to be about $2\mu m$ by taking the first derivative of the average fluorescence intensity versus focal depth as the PSF is crosses from the sample holder into the solution, as in figure 9.6. From the values of w_z and w_{xy} we can calculate the volume of the ellipsoid: $4/3\pi w_{xy}^2 w_z = 0.8fL$. Although $G(0)$ was found to be a generally unreliable measurement, plotting $G(0)$ for the microsphere measurements

against the known concentrations, in this case, yielded a good linear relationship, shown in figure 9.10. The slope of a linear fit to the $G(0)$ versus concentration data was 0.6 indicating the effective focal volume was 0.6fL according to equation 9.11. This result matches reasonably well with the focal volume of 0.8fL that was derived using independently measured w_{xy} and w_z .

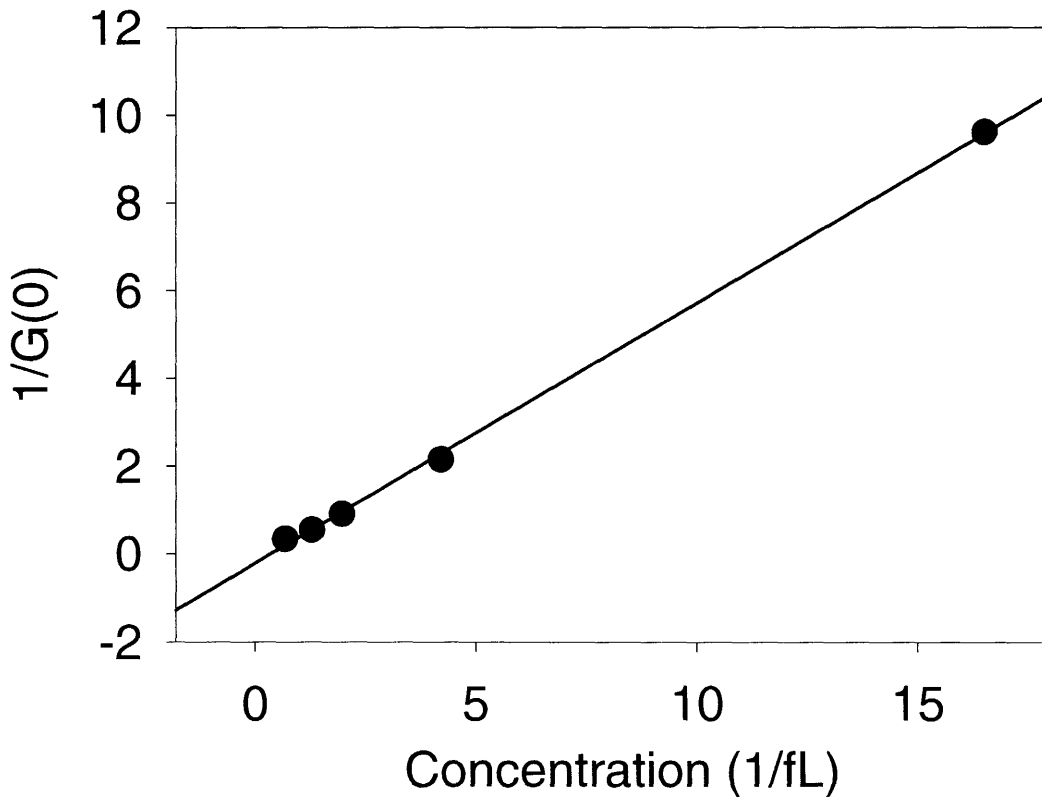


Figure 9.10 Calibration of $G(0)$ from figure 9.9 against known concentration of polymer microspheres in solution. A focal volume of about 0.6 fL was derived from this calibration.

We note that the self consistency of these parameters affirms our use of $t_{1/2}$ to characterize the diffusion driven decay of $G(t)$. Since w_{xy} is so much smaller than w_z the term $(1 + t/\tau_D)^{-1}$ decays much more quickly than the term for $(1 + t/\tau_D^z)^{-1}$. In this limit the z -axis contribution can be neglected and $G(t) \sim G(0)(1 + t/\tau_D)^{-1}$. In this approximation $t_{1/2} = \tau_D$.

To investigate the effects of different ligands on the hydrodynamic radius of nanocrystals in aqueous solution we carried out numerous measurements of two different sample solutions each containing nanocrystals from the same synthetic batch, but water solubilized using different methods. Sample A was made water-soluble using phospholipid micelles¹⁸, whereas sample B was made hydrophilic using oligomeric phosphine ligands¹⁶. In figure 9.11 we show the overlaid results of numerous measurements of sample A. One set of measurements employed an oil objective, while

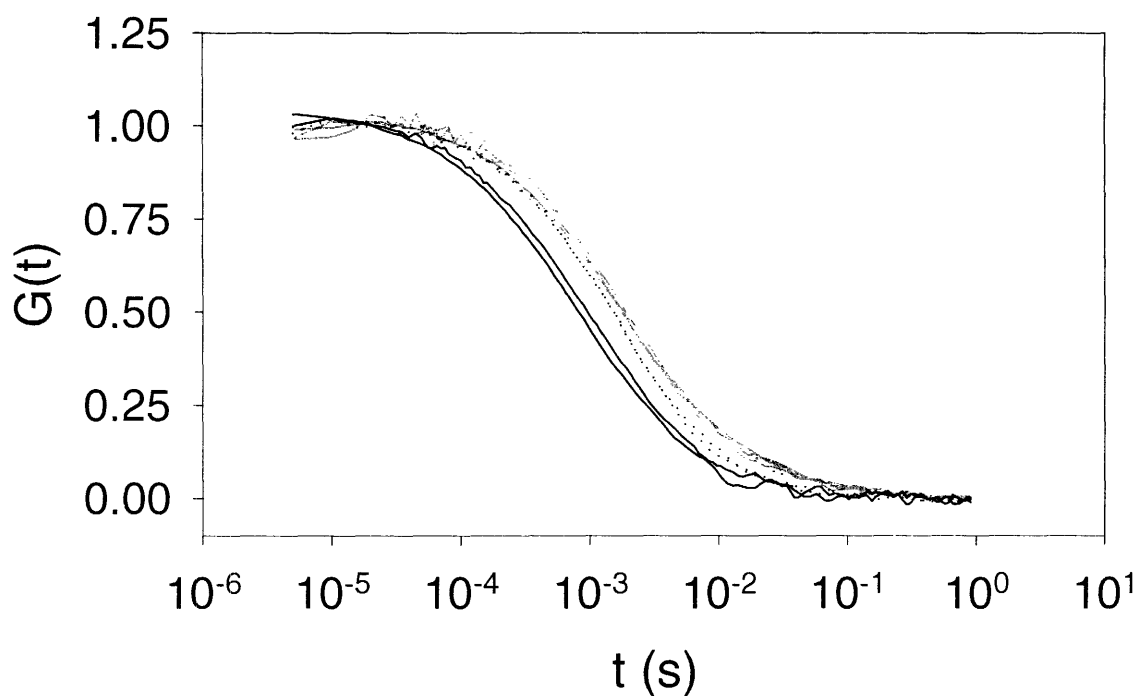


Figure 9.11 FCS curves for nanocrystal sample A. Repeated measurements using a water immersion objective are shown in gray, while measurements using an oil immersion objective are shown in black. The difference in the decay times for measurements is accounted for by separate calibration of the oil and water immersion lenses. After calibrating these decay times a hydrodynamic radius of 16nm is obtained for all of the measurements except two (dotted black lines).

another set employed a water immersion objective. Measurements with the lower NA water immersion objective had a longer time constant than measurements with the oil objective because of different sized PSFs, but for the most part repeated measurements with the same objective were robust yielding the same time constants. Using separate calibrations for FCS measurements employing water and oil immersion objectives we derived the hydrodynamic radius for all measurements, which was uniformly 16nm for measurements using either objective. These hydrodynamic radius results are summarized in figure 9.13.

Figure 9.12 shows the results of repeated FCS measurements of sample B, which was capped with the oligomeric phosphine ligand. Again numerous measurements

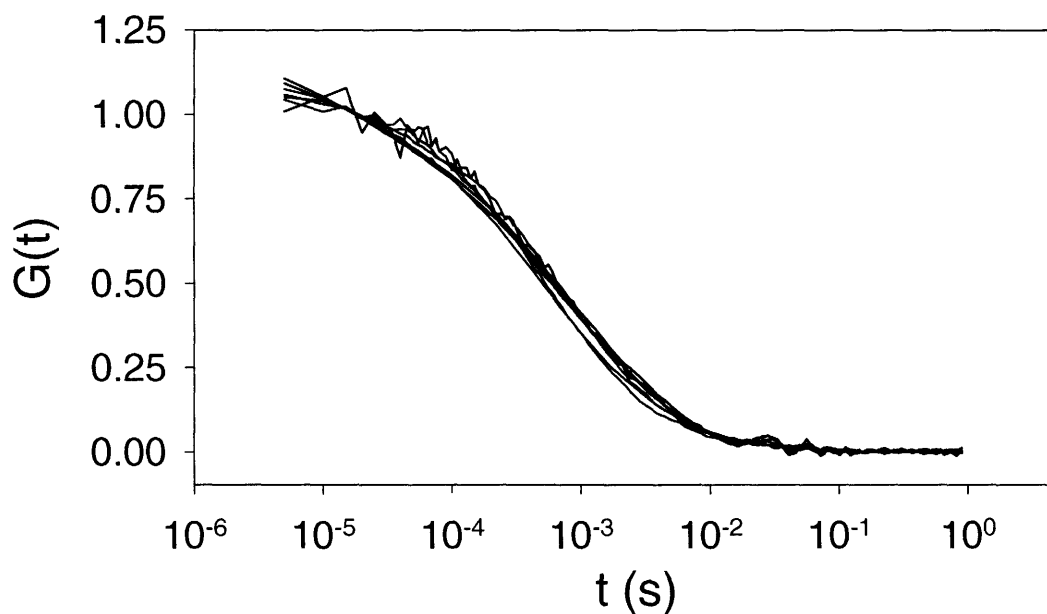


Figure 9.12 Repeated FCS measurements of the nanocrystal sample B, using the oil immersion lens. The decay times of these curves yields a hydrodynamic radius of 12nm.

yielded the practically identical $G(t)$ and the same time constant. These measurements were taken at the same time that the measurements of sample A were taken (using the oil immersion objective), so the same calibration was used. A hydrodynamic radius of 12nm was obtained for sample B.

A summary comparison of these measurements is shown in figure 9.13, along with overlaid plots of the $G(t)$ for samples A and B in the inset, illustrating the slower

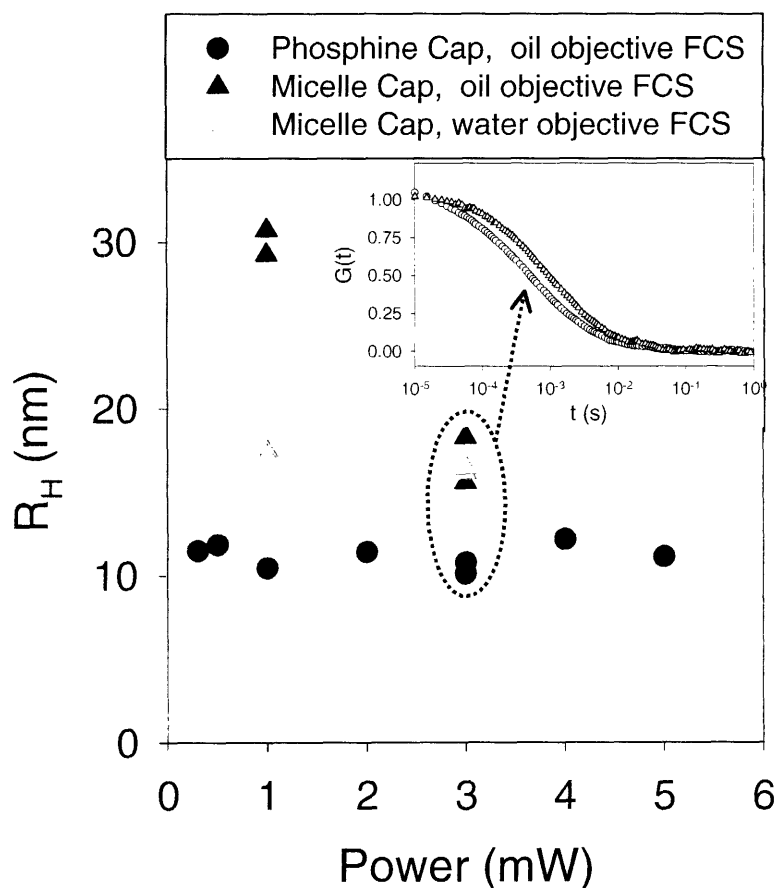


Figure 9.13 Summary of R_H obtained for all of the FCS measurements of nanocrystal sample A (triangles) and sample B (circles) at various excitation powers. Two outliers occurred for sample A because of agglomeration problems. **Inset:** overlaid plots of FCS measurements on samples A and B taken right after one another with the same calibration of the microscope. A slight difference in decay time of $G(t)$ is evident for the two samples of nanocrystals with different caps.

diffusion of the nanocrystals capped with the phospholipid micelle. These results demonstrate that different capping ligands can have a significant, measurable impact on the hydrodynamic radius of nanocrystal cores.

9.6 FCS of Nanocrystals in High Viscosity Aqueous Solutions

In the course of the foregoing measurements we noticed that the $G(t)$ of certain samples of nanocrystals occasionally exhibited a fast decay component at times shorter than the diffusion time. In order to investigate this inherent, non-diffusion driven decay, we slowed the diffusion time of nanocrystals by putting them in aqueous solutions with

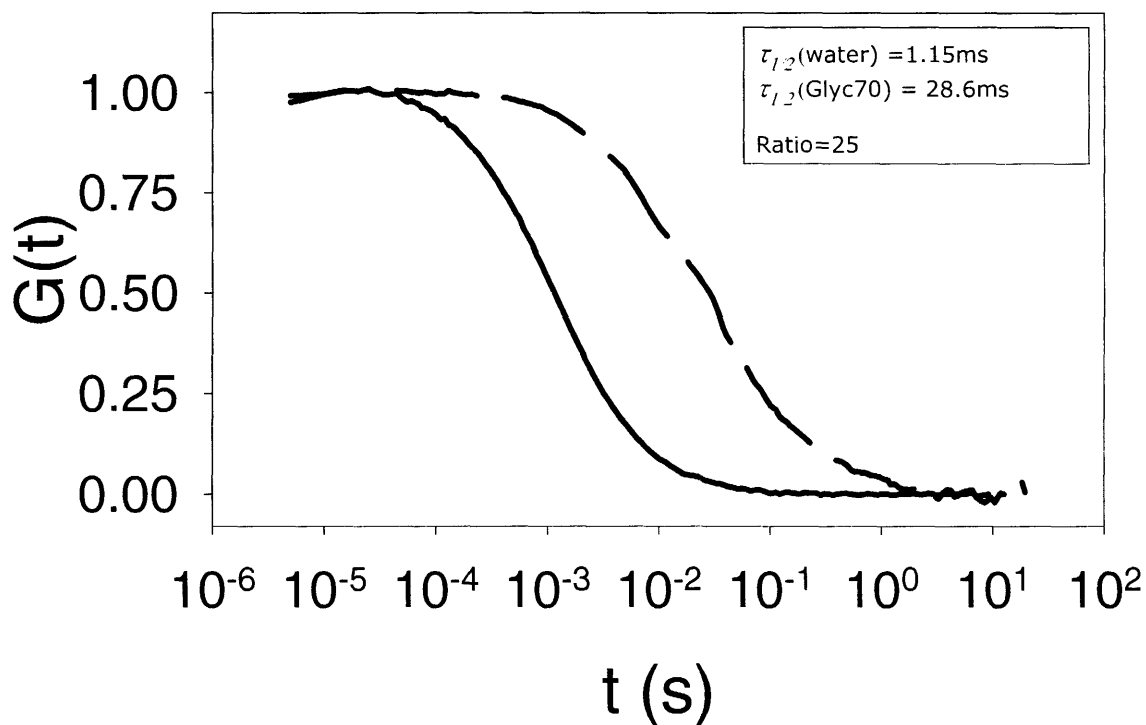


Figure 9.14 FCS measurements of the same fluorescent polymer microspheres in two different solvents. One solvent was pure water, the other was a mixture of glycerol in water (70% Glycerol v/v). The longer time constant of the decay for the 70% glycerol sample comes from a slower diffusion constant that arises from the higher viscosity of the solvent mixture.

high viscosity. According to equation 9.10, increasing the viscosity causes the diffusion constant to decrease, and the decrease in diffusion constant results in a longer diffusion time, as seen in equation 9.9. Figure 9.14 shows the slowing of diffusion using fluorescent polymer microspheres with $R_H = 22\text{nm}$ in solvents of different viscosity. The two FCS curves in figure 9.14 were measured using the same excitation power (1mW) and same microspheres. However, one sample was diluted in pure water, whereas the other was diluted in a solvent mixture of 70% v/v glycerol in water. The difference in time constants of the two curves $G(t)$ in figure 9.14 provides a direct measure of the difference in viscosity of the two solutions. The ratio of the time constants for the two FCS curves in 9.14 is 25. Therefore the 70% Glycerol solution is a 25x more viscous than pure water with a viscosity of about 22.3cP (water is 0.89cP).

Figure 9.15 compares the FCS curves for water-soluble nanocrystals dissolved in water-glycerol mixtures of the same proportion as the previous plot (0% and 70% v/v glycerol in water). The plot shows FCS curves measured using 1mW excitation power, and the plot on the bottom corresponds to 3mW excitation power. To aid comparison, the data from figure 9.14 is included in figure 9.15 (gray curves). Besides the faster time constants of the nanocrystals at each viscosity value (because the nanocrystals had smaller R_H than the microspheres), the FCS curves of the nanocrystals show obviously different dynamics at short timescales. This is especially clear for the higher viscosity curves. Although the time constant for relaxation due to diffusion fluctuations is about 10ms, $G(t)$ for the nanocrystals still shows a decay before this, in the time range of 10-100 μs . Furthermore, this fast FCS decay appears slightly different for the two different excitation powers shown in figure 9.15.

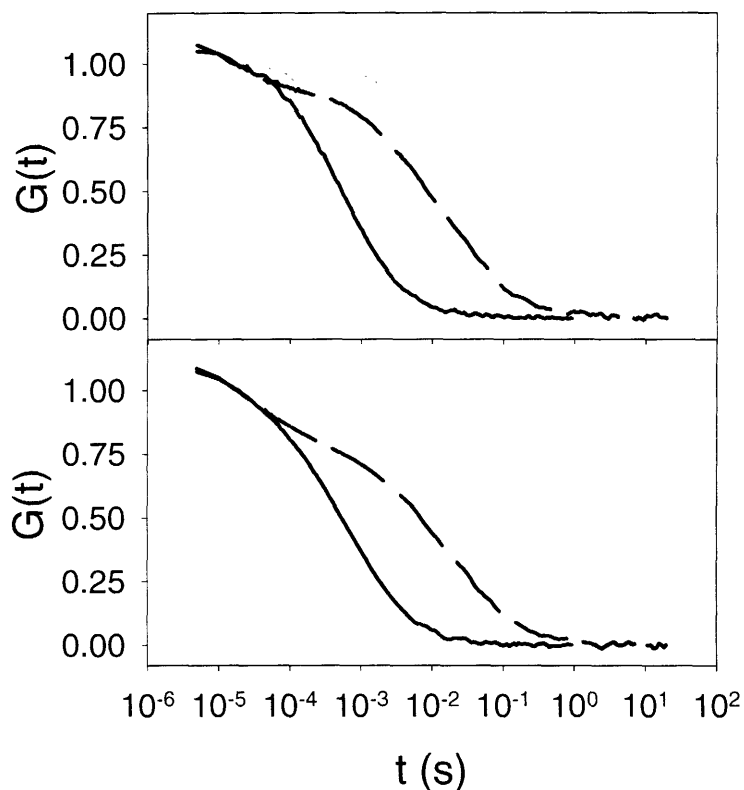


Figure 9.15 Effect of higher solvent viscosity on the FCS curve of nanocrystals for two different excitation powers (1mW top, 3mW bottom). Solid curves denote pure water solvent and broken lines denote 70% Glycerol v/v solvent. Black curves are for nanocrystals samples and gray curves are for fluorescent polymer microspheres.

In order to see the fast decay over a longer time scale we increased the viscosity of the glycerol water mixture further by raising the volume fraction to 90%. Overlaid FCS curves for three different viscosities are shown in figure 9.16 at two different excitation powers. The fast component of the decay of $G(t)$ is evident in all curves, but it has a slightly steeper slope at 3mW compared to 1mW excitation power.

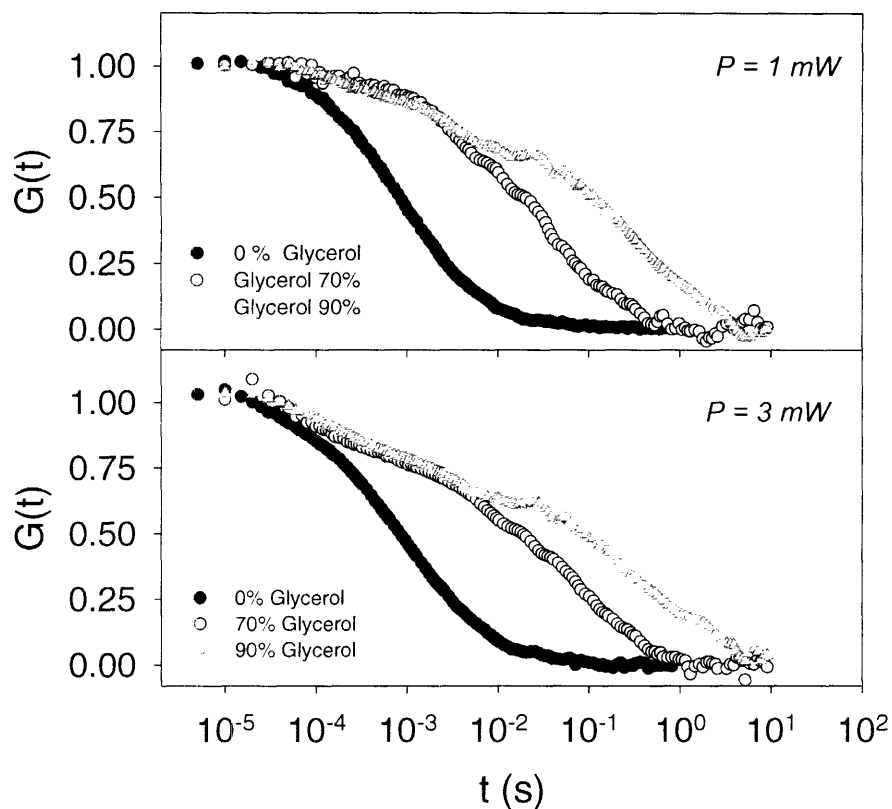


Figure 9.16 FCS curves of nanocrystals in three different solvents with different viscosities at different powers (top: 1mW, bottom: 3mW). The fast decay component changes slope at higher excitation power. Wiggles in the data at about 10^{-1} second are experimental artifacts that were obtained even in control runs with high concentration with $G(0)$ approaching zero.

The presence of a decay component in $G(t)$ before the diffusion based decay component means that the intensity signal of the group of nanocrystals in the focal volume fluctuates within their residence time in the focal volume (i.e. *before* they diffuse in and out of the focal volume). Some mechanism for this fluctuation other than diffusion must be present. To see more clearly the dependence of this fast fluctuation mechanism on power we plot $G(t)$ for the same sample of nanocrystals in the same 70%v/v glycerol/water mixture for three different excitation powers in figure 9.17.

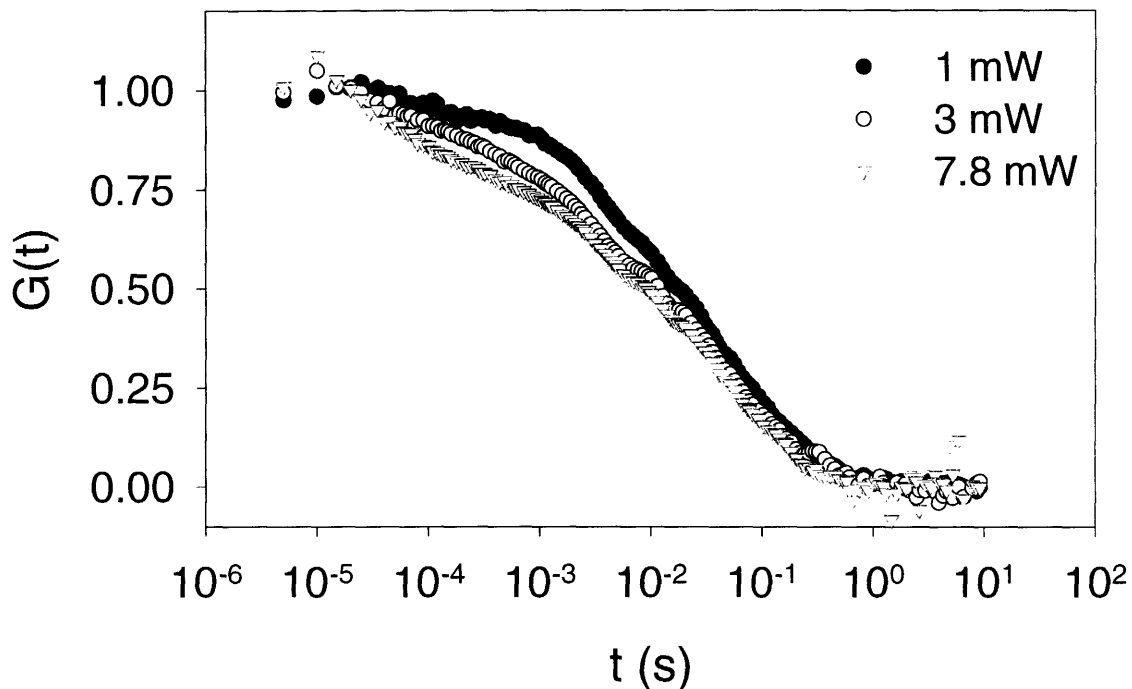


Figure 9.17 Explicit power dependence of the fast component in $G(t)$ for nanocrystals in a solvent of 70% glycerol v/v.

From these data it is clear that the fast timescale fluctuation decays more quickly when the excitation power is higher. This implies some kind of power dependence for the mechanism behind this fluorescence intensity fluctuation.

One possibility is that the fast time scale fluctuations observed here are connected to the well-known fluorescence intermittency phenomenon that is ubiquitous in single nanocrystal experiments^{21,22}. Nanocrystal blinking has been well studied and is known to have a very strong dependence on the excitation intensity. In general, at higher excitation intensities, nanocrystals appear to blink “faster.” Quantitatively speaking the cutoff of the power-law on-time probability distribution is shortened when the excitation power is increased^{23,24}. However the time scale of this cutoff time is nowhere near the

time scales we are examining here – the cutoff time is generally on the order of seconds to hundreds of seconds, depending on the excitation intensity²⁴, whereas we are looking at power dependent dynamics on the timescale of microseconds.

Nevertheless, even a simplistic consideration of the possible effect of blinking on FCS measurements of nanocrystals offers possible insight into our FCS data. If each individual nanocrystal that is probed by the FCS experiment is assumed to blink according to the power law shown in previous studies, then a modification of equation 9.8 is required. Appendix 3 explains in detail our approach to building blinking into the formalism of FCS. The end result is that the model function for the FCS correlation should be multiplied by the correlation function of blinking of a single nanocrystal.

$$G(t) \approx G_{\text{Diffusion}}(t) \times (1 + G_{\text{Blinking}}(t)) \quad (9.12)$$

where $G_{\text{diffusion}}(t)$ is just the single component diffusion-driven FCS correlation function derived earlier (with no consideration of blinking), and,

$$G_{\text{Blinking}}(t) \equiv \frac{\langle \delta b(0) \delta b(t) \rangle}{\langle b(0) \rangle \langle b(t) \rangle} = \frac{\langle b(0) b(t) \rangle}{\langle b(0) \rangle \langle b(t) \rangle} - 1 \quad (9.13)$$

Previous work²⁵ has shown that $G_{\text{blinking}}(t)$ is given by $A(1-B^{2-m})$ when the probability distributions of on and off times are given by power laws (the distributions are assumed to have maximum and minimum times so that averages can be defined). Figure 9.18 shows the shape of $G(t)$ on a plot with logarithmic time scale when this correlation function of single nanocrystal blinking is factored in according to equation 9.12. Here we chose a power law with exponent of $m=1.6$ and 1.8 in accordance with actual observations of nanocrystal blinking²⁴. These curves are qualitatively similar to the data collected for nanocrystals in high viscosity solvents – the curve decays significantly for

$t < \tau_{diffusion}$. This similarity suggesting that blinking could be an important driver of this system's fluctuations. Further studies of nanocrystal use in FCS experiments should address this intriguing question.

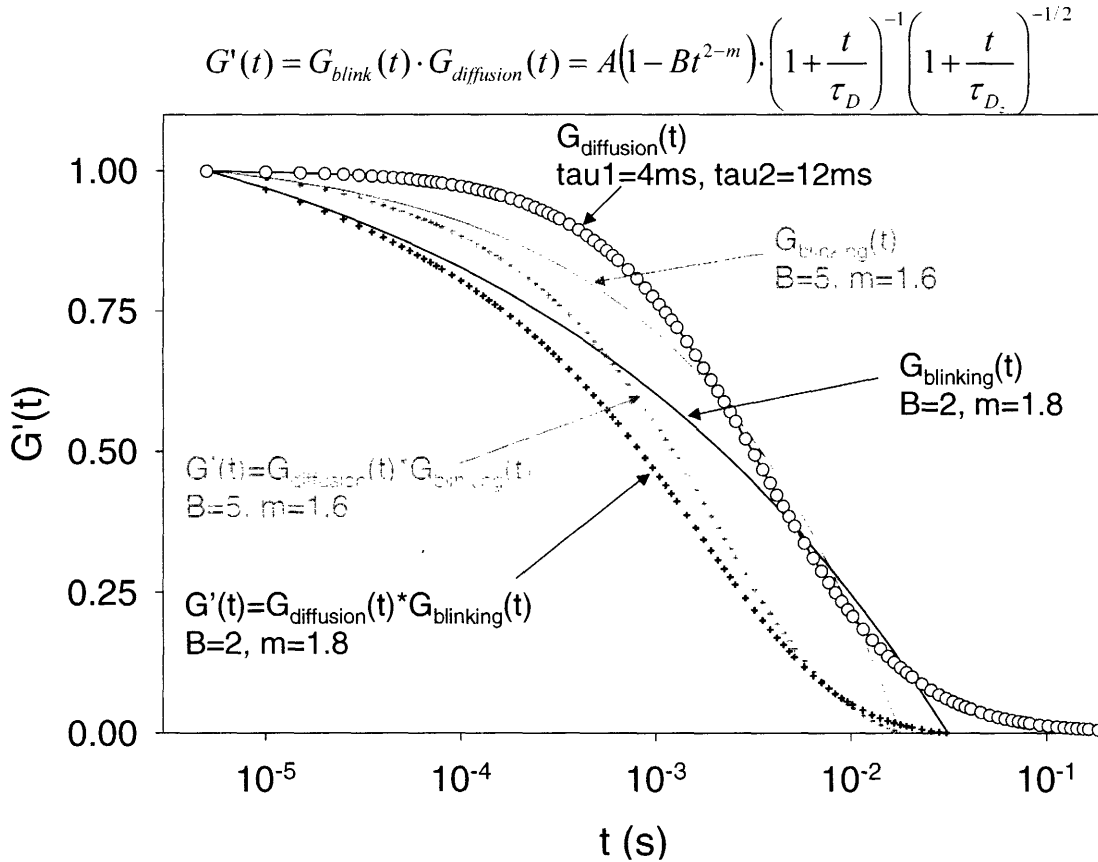


Figure 9.18 Hypothetical effect of power-law governed blinking on the FCS curve of nanocrystals. Correlation functions for power law blinking are plotted for two different decay parameters (black and gray lines), and the product of these blinking correlation functions with the regular diffusion driven $G(t)$ are plotted correspondingly (black and gray crosses). The regular diffusion driven $G(t)$ with no blinking applied is also plotted (circles).

9.8 Conclusions

This chapter has discussed the theory and the implementation of fluorescence correlation spectroscopy for the study of nanocrystals. We have described in detail the methods we developed to carry out FCS measurements in our lab, namely two-photon

microscopy and a novel software autocorrelation method. We have also shown the results of preliminary FCS measurements on nanocrystals. After describing some important caveats to the measurements, such as the importance of not saturating the nanocrystals as well as the dependence of $G(0)$ on focal depth, we measured the hydrodynamic radii of two similar samples of nanocrystals. Although the only difference between the two samples of nanocrystals was the ligand used to make them water soluble, FCS measurements were able to distinguish their hydrodynamic radii – the oligomeric phosphine ligated nanocrystals had $R_H = 12\text{nm}$, whereas the R_H of the phospholipid micelle solubilized nanocrystals was about 16nm. Other techniques for measuring R_H , such as DLS, are generally less reliable in this small size regime. Although our primary motivator for FCS experiments was the measurement of R_H for nanocrystals in solution, we discovered a second source of fluorescence intensity fluctuation in nanocrystals, at faster timescales than their diffusion fluctuations. This unforeseen source of fluorescence intensity fluctuations added new dynamics to FCS measurements on nanocrystals and we hypothesize that the fluctuations may be related to the blinking of single nanocrystals. Further study of this topic is warranted.

9.9 References

- 1 E. L. Elson and D. Magde, *Biopolymers* **13**, 1 (1974).
- 2 E. L. Elson and D. Magde, *Biopolymers* **13**, 29 (1974).
- 3 N. L. Thompson, in *Topics in Fluorescence Spectroscopy*, edited by J. R. Lakowicz (Plenum, New York, 1991), p. 337.
- 4 Magde, *Physical Review Letters* **29**, 705 (1972).
- 5 J. Widengren, U. Mets, and R. Rigler, *Journal of Physical Chemistry* **99**, 13368 (1995).
- 6 J. Widengren, R. Rigler, and U. Mets, *Journal of Fluorescence* **4**, 255 (1994).
- 7 J. Widengren and R. Rigler, *Bioimaging* **4**, 149 (1996).
- 8 D. R. Larson, W. R. Zipfel, R. M. Williams, et al., *Science* **300**, 1434 (2003).

- ⁹ M. C. Teich and B. E. A. Saleh, *Fundamentals of Photonics*, New York, Chichester, Brisbane, Toronto, Singapore, 1991).
- ¹⁰ P. N. Pusey and W. Megen, *Journal of Chemical Physics* **80**, 3513 (1984).
- ¹¹ R. Rigler, U. Mets, W. J., et al., *European Biophysics Journal with Biophysics Letters* **22**, 196 (1993).
- ¹² K. Berland, P. T. C. So, and E. Gratton, *Biophysical Journal* **68**, 694 (1995).
- ¹³ O. Krichevsky and G. Bonnet, *Reports on Progress in Physics* **65**, 251 (2002).
- ¹⁴ C. A. Leatherdale, W. K. Woo, F. V. Mikulec, et al., *Journal of Physical Chemistry B* **106**, 7619 (2002).
- ¹⁵ T. Wohland, R. Rigler, and H. Vogel, *Biophysical Journal* **80**, 2987 (2001).
- ¹⁶ S. Kim and M. G. Bawendi, *Journal of the American Chemical Society* **125**, 14652 (2003).
- ¹⁷ S.-W. Kim, S. Kim, J. B. Tracy, et al., *Journal of the American Chemical Society* **127**, 4556 (2005).
- ¹⁸ B. Dubertret, *Science* **298**, 1759.
- ¹⁹ T. D. Visser, J. L. Oud, and G. J. Brakenhoff, *Optik* **90**, 17 (1992).
- ²⁰ K. Berland and G. Shen, *Applied Optics* **42**, 5566 (2003).
- ²¹ M. Nirmal, B. O. Dabbousi, M. G. Bawendi, et al., *Nature* **383**, 802 (1996).
- ²² M. Kuno, D. P. Fromm, H. F. Hafmann, et al., *Journal of Chemical Physics* **112**, 3117 (2000).
- ²³ M. Kuno, D. P. Fromm, H. F. Hafmann, et al., *Journal of Chemical Physics* **115**, 1028 (2001).
- ²⁴ K. T. Shimizu, R. G. Neuhauser, C. A. Leatherdale, et al., *Physical Review B* **63**, 205316 (2001).
- ²⁵ R. Verberk, A. M. van Oijen, and M. Orrit, *Physical Review B* **66**, 233202 (2002).

$$[26] \quad w_{xy} = \frac{0.32\lambda}{NA\sqrt{m}}\sqrt{2} \quad w_z = \frac{0.532\lambda}{\sqrt{m}} \left(\frac{1}{n - \sqrt{n^2 - NA^2}} \right) \sqrt{2}$$

where $m = 1$ or 2 for single or two photon excitation respectively.

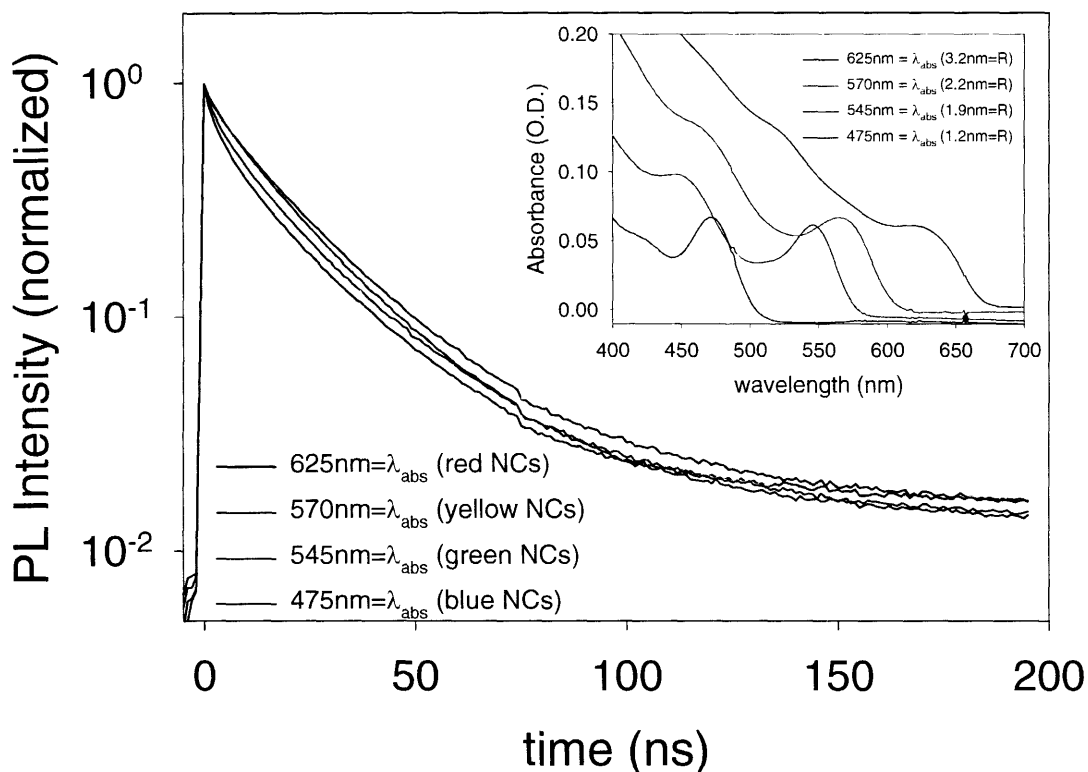
Appendix 1: Lifetime Measurements of Various Ensemble Nanocrystal Samples

- A1.1 Introduction
- A1.2 Size Dependence of CdSe Lifetimes
- A1.3 Shape Dependence of CdSe lifetimes – Nanorods
- A1.4 Lifetime of Type 2 Emission from CdTe/CdSe Nanocrystals
- A1.5 Effect of Amines on CdSe NC Lifetime and Quantum Yield
- A1.6 Effect of Overcoating on Nanocrystal Lifetimes
- A1.7 Lifetime of Closed Packed Films of Bare CdSe Nanocrystals
- A1.8 References

A1.1 Introduction

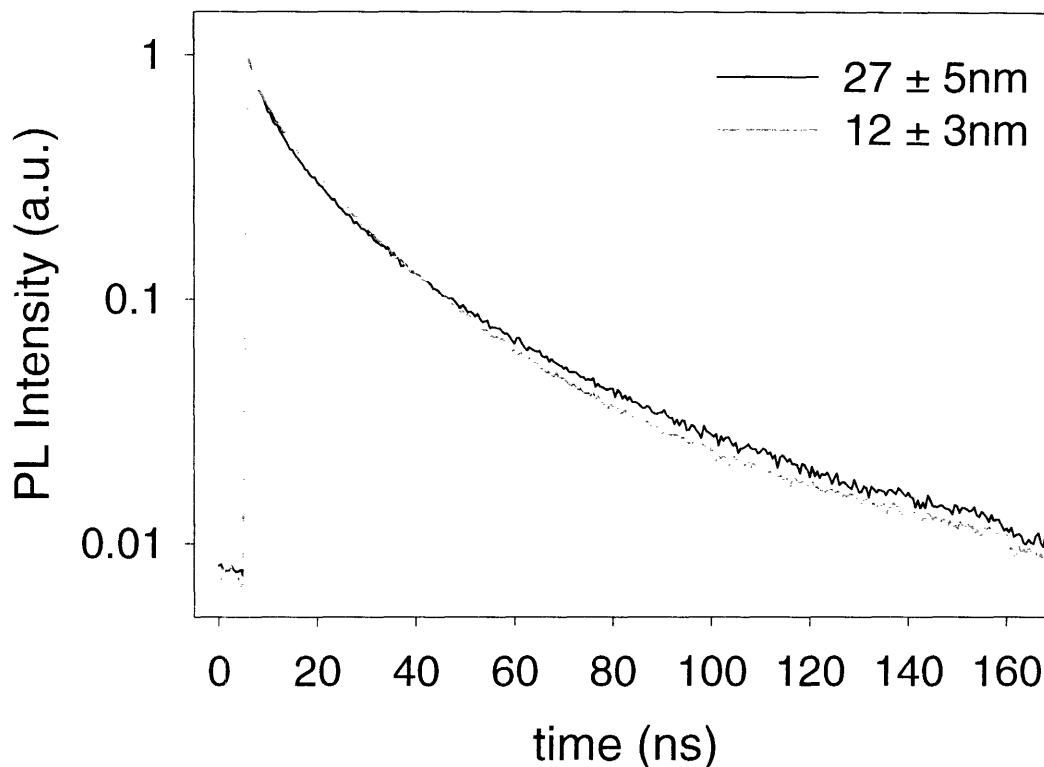
The results presented in this section serve to provide a summary of the general observations of lifetimes in a variety of samples studied over the course of research for this thesis. In general all of the measurements were obtained either using the Lavision gated intensified camera or by time correlated single photon counting carried out as described in previous chapters. Any significant modification to these procedures is described in the caption for each set of data along with the details of the sample that is studied in each measurement.

A1.2 Size dependence of CdSe Lifetimes

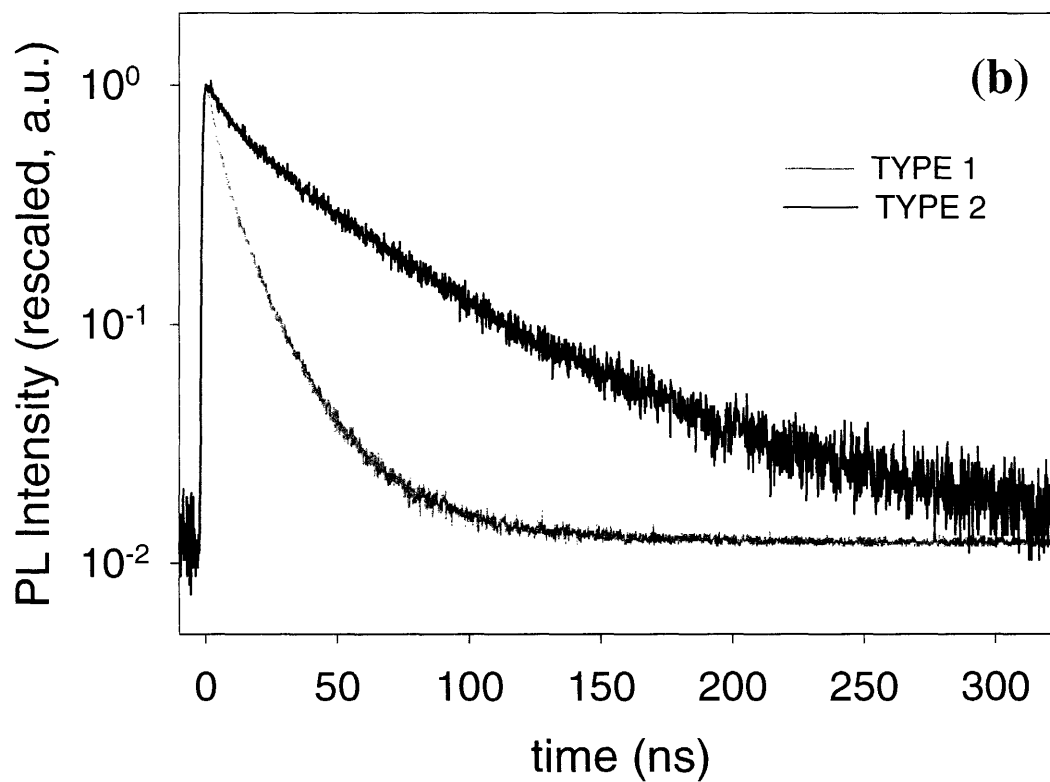
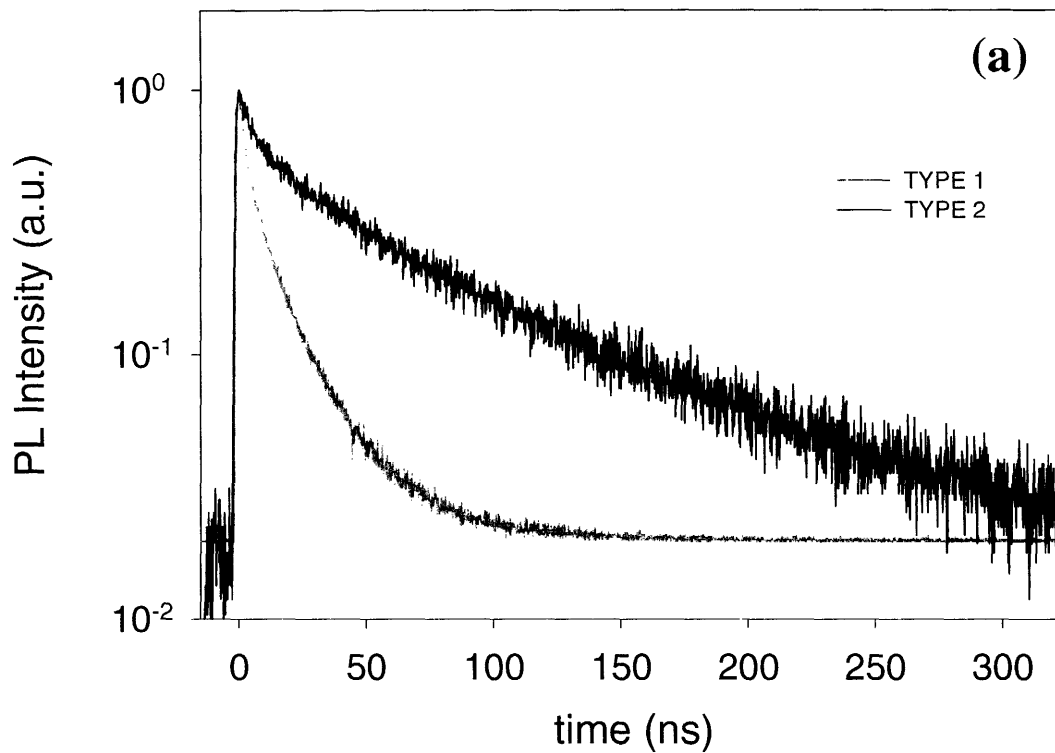


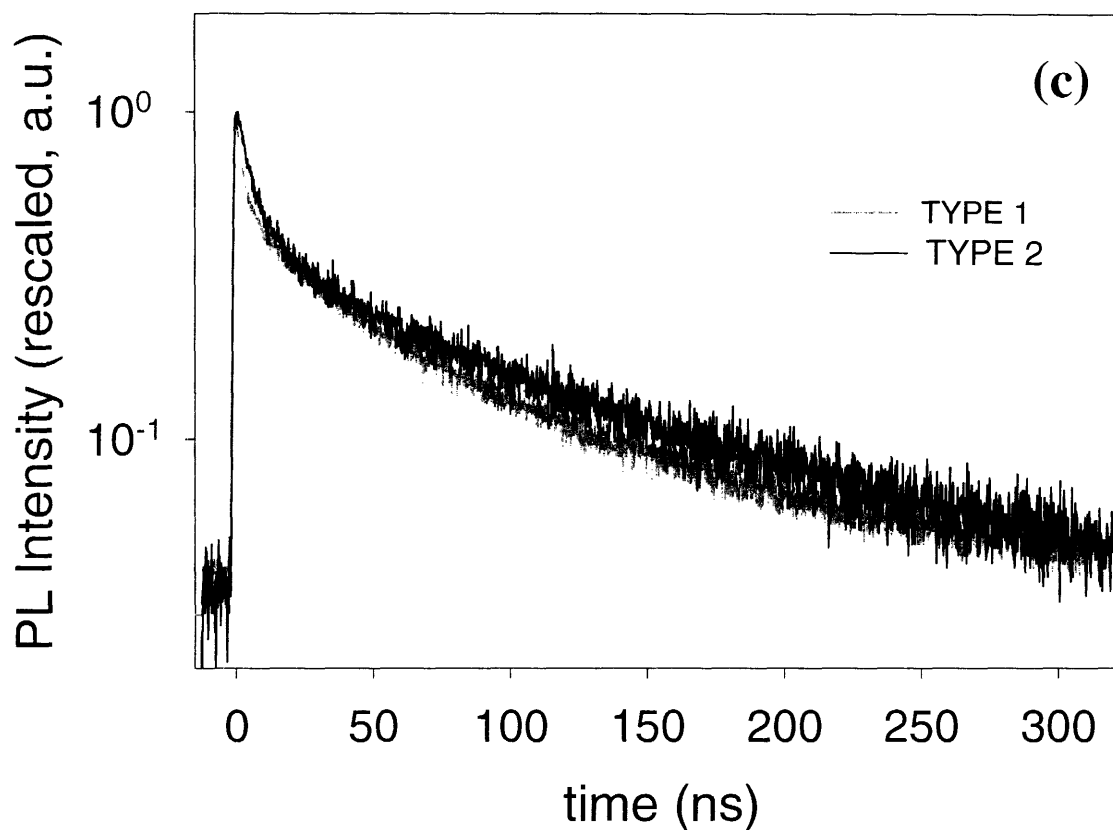
Here we show PL decays with peak intensity normalized to unity from four different solution (in hexane) samples of CdSe/ZnS nanocrystals of various sizes ranging from 1.2 to 3.2 nm (radius). The CdSe cores were prepared using the dimethyl cadmium synthesis¹ and were overcoated using diethyl zinc and $(\text{TMS})_2\text{S}$ ². A monotonic trend of decreasing $1/e$ lifetime is evident going from samples of small to samples of large nanocrystals. However, the difference is very small and could be attributed to small differences in quantum yield or differences in the stretch parameter (β) of the decays, among other possibilities. We conclude from data like these and the data of section 3.7 that the lifetime of CdSe nanocrystals is virtually independent of size.

A1.3 Shape dependence of CdSe Lifetimes – CdSe Nanorods



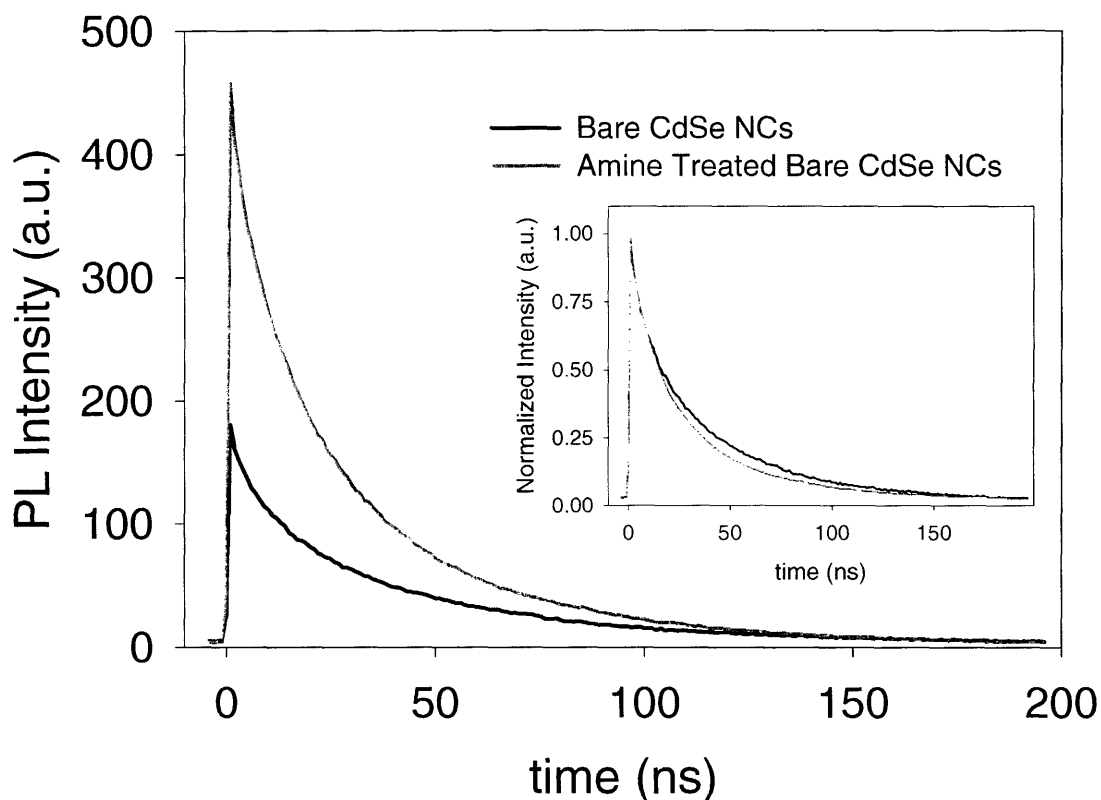
The PL decays presented in this figure are from two different samples of CdSe nanorods with the same radius, but different lengths (gray: 12 ± 3 nm, black: 27 ± 5 nm). The synthetic procedure used to prepare these samples was adapted from previous reports³ and these samples were overcoated with ZnS using established procedures². Compared to one another and compared to spherical nanocrystals of similar radius the lifetimes that we observe are very similar. Fitting of these PL decays to a stretched exponential decay yielded mean lifetimes of 14.1 ns and 14.5 ns for the long and short nanorods respectively. The two samples had slightly different stretch parameters, which accounts for the fact that the decays do not perfectly overlap one another. We conclude from these observations that the lifetime of CdSe nanorods is approximately the same as for nanocrystals and that the lifetime does not meaningfully vary as a function of rod length within the range of 10 to 30 nm.

A1.4 Lifetime of Type 2 Emission from CdTe/CdSe Nanocrystals



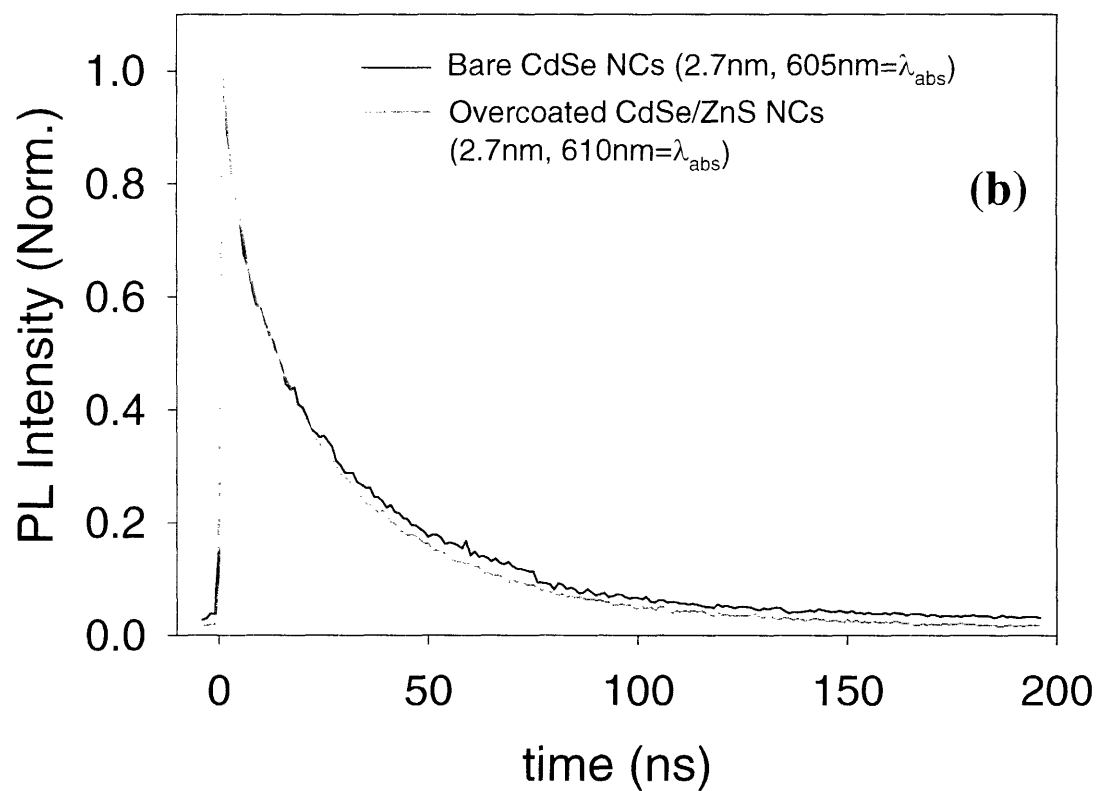
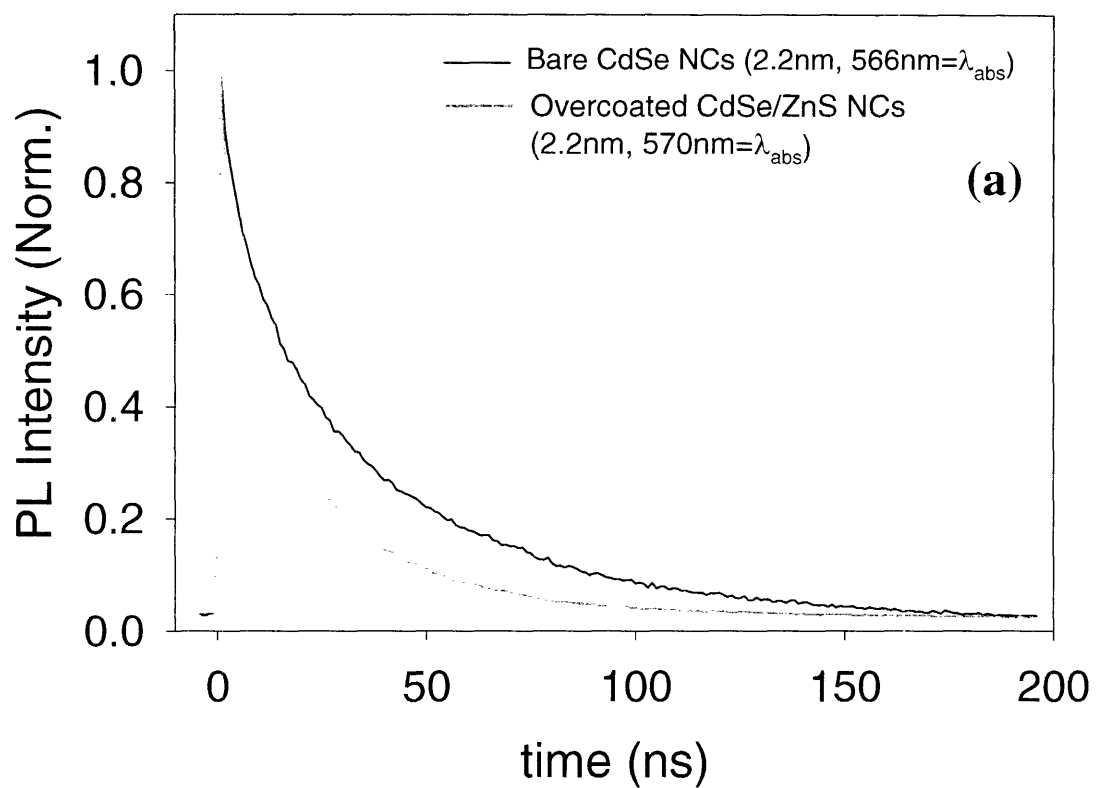
These data compare the lifetime of the two emission bands of CdTe/CdSe core-shell type-2 nanocrystals at room temperature (a), 77K (b) and 4.3K (c). Gray lines indicate emission originating from recombination of the electron-hole pair inside the core (type 1) while the black lines show the lifetime of emission originating from recombination of the electron-hole pair at the interface between the core and the shell (type 2). We expect the lifetime of the type 2 recombination to be very long because of poor overlap between photoexcited electrons and holes in type 2 structures (the hole resides in the core while the electron resides in the shell)⁴. The result is that the lifetime of type 2 recombination is dramatically longer than the lifetime of type 1 (core CdTe band-edge) recombination at room temperature and 77K. At liquid helium temperatures (4.3K) however, the lifetime of type 1 emission is known to become very long because the lowest excited state of the exciton within the core is an optically inactive “dark” exciton state^{5,6}. For this reason, at low temperatures the rate of *both* type 1 and type 2 radiative recombination is small, as seen in the low temperature PL decays.

A1.5 Effect of Amines on CdSe NC Lifetime and Quantum Yield



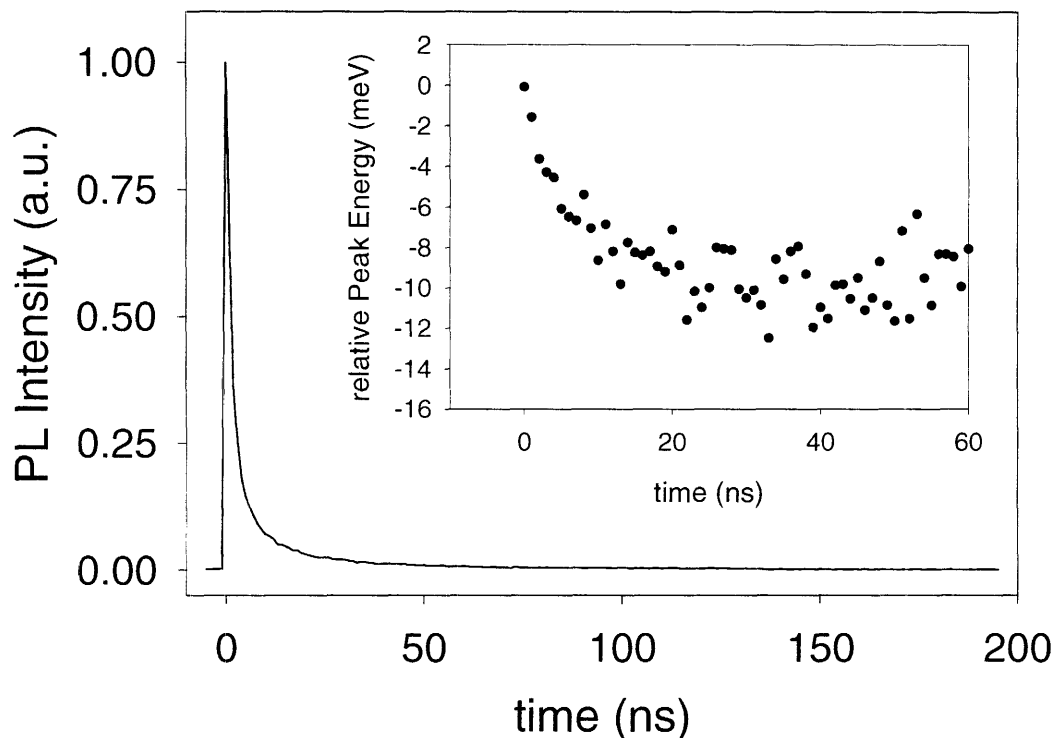
This figure demonstrates the effect on the PL decay of adding octylamine (5 μ L of 10% v/v octylamine in hexane) to a sample of bare CdSe nanocrystals suspended in 2mL of hexane. The nanocrystals were prepared using the dimethyl cadmium synthesis¹ and were capped only with trioctyl phosphine (TOP) and trioctylphosphine oxide (TOPO) in the control sample. The main plot compares the absolute intensity of PL following pulsed excitation for the native sample (black) and the sample with octylamine (gray). The inset shows the same data with their peak intensities rescaled to unity. The normalized lifetime is not much different with or without octylamine, however, from the absolute PL decays we can see that addition of octylamine clearly increased the quantum yield (since the integrated area of the absolute PL decay increased >2x). According to the arguments of chapter 8 we conclude that the octylamine increases the quantum yield “non-homogenously” by passivating ultrafast surface traps on the bare CdSe surface such that a sub-population of the nanocrystals that was effectively non-luminescent in the control sample becomes luminescent in the treated sample.

A1.6 Effect of Overcoating on Nanocrystal Lifetimes



Here we present the result of overcoating on the normalized lifetime for two different batches of CdSe nanocrystal cores, one synthesized by the dimethyl cadmium prep using no amines¹ (a) and the other synthesized with hexadecylamine present in the so-called Cd(acac) synthesis⁷ (b). Both were overcoated using the same method with diethyl zinc and (TMS)₂S precursors and only TOP as a solvent⁷. In the case of the dimethyl cadmium synthesized cores overcoating lengthened the lifetime significantly. This is consistent with the observed increase of quantum yield when the sample was overcoated. On the other hand, overcoating had little effect on the lifetime of the CdSe nanocrystals prepared using the Cd(acac) synthesis. This is consistent with general observations in our laboratory. Overcoating is generally not found to improve the native quantum yield (as measured in hexane suspension) of nanocrystals that were synthesized in the presence of amines, although the overcoating does confer a measure of stability to these aminated nanocrystals during further processing.

A1.7 Lifetime of Closed-Packed Films of Bare CdSe Nanocrystals



Here we show the lifetime of a close-packed thin film of bare CdSe nanocrystals (main plot) along with the time-evolution of the energy of the peak of the emission after pulsed excitation (inset). Clearly the lifetime is much shorter than the lifetime of nanocrystals observed in hexane solution. Förster energy transfer between adjacent nanocrystals in a close-packed film is responsible the reason for the shortened lifetime compared to solution phase nanocrystals^{8,9}. FRET involved energy transfer from a higher energy donor to a lower energy acceptor, so the excited state energy of smaller nanocrystals is transferred to larger nanocrystals resulting in the red-shift of the fluorescence band shown in the inset. Since energy is efficiently transferred among the nanocrystals in the film the excitons generated in the ensemble by a pulse sample all of the nanocrystals within some small range. Any nanocrystal that has a particularly fast lifetime (high non-radiative decay rate) will dominate the dynamics – this is why the lifetime is so much faster in the sample of close-packed nanocrystals. Inter-nanocrystal energy transfer allows excitons to quickly find the nanocrystals with the fastest lifetime and these fast lifetimes dictate the lifetime of the ensemble.

A1.8 References

- 1 C. B. Murray, et al., *Journal of the American Chemical Society* **115**, 8706 (1993).
- 2 B. O. Dabbousi, J. Rodriguez-Viejo, F. V. Mikulec, et al., *Journal of Physical Chemistry B* **101**, 9463 (1997).
- 3 Z. A. Peng and X. A. Peng, *Journal of the American Chemical Society* **124**, 3343 (2002 Supplemental Information).
- 4 S. Kim, B. R. Fisher, H. J. Eisler, et al., *Journal of the American Chemical Society* **125**, 29 August 2003 (2003).
- 5 M. Nirmal, D. J. Norris, M. Kuno, et al., *Physical Review Letters* **75**, 3728 (1995).
- 6 M. G. Bawendi, P. J. Carroll, W. L. Wilson, et al., *Journal of Chemical Physics* **96**, 946 (1991).
- 7 B. R. Fisher, H. J. Eisler, N. E. Stott, et al., *Journal of Physical Chemistry B* **108**, 143 (Supplemental Information 2004).
- 8 C. R. Kagan, C. B. Murray, M. Nirmal, et al., *Physical Review Letters* **76**, 1517 (1996).
- 9 C. R. Kagan, C. B. Murray, and M. G. Bawendi, *Physical Review B* **54**, 8633 (1996).

Appendix 2: Analysis of Triexciton Blinking

- A2.1 Introduction
- A2.2 Verification of Hanbury-Brown and Twiss Setup by Imaging
- A2.3 Verification of triexciton in single nanocrystal emission
- A2.4 Triexciton blinking is correlated to band-edge emission blinking
- A2.5 Use of a band-pass filter on channel 1 should result in 80% of its signal being from triexciton
- A2.6 Expected relative count rates match observations for the two channels
- A2.7 Lifetime data for a single nanocrystal shows 50% of channel 1 is triexciton emission
- A2.8 Power dependence of triexciton and biexciton emission from a single nanocrystal
- A2.9 Emission intensity of single nanocrystals in the “off” state

A2.1 Introduction

In chapter 5 we reported the observation that triexciton emission from a single nanocrystal appears to exhibit fluorescence intermittency identical in nature to the well-known intermittency of band edge emission from single nanocrystals (e.g. figure 5.7). We assigned the signal that we observed blinking in those experiments to triexciton emission from a single nanocrystal based on two pieces of evidence. First, the detector had a narrow band-pass filter that overlapped only with wavelengths in the triexciton emission band for that sample of nanocrystals. Second, the blinking trace in figure 5.7 was obtained simultaneously with the collection of single photon correlation measurements presented in chapter 6 (e.g. figure 6.9). Single photon correlation measurements exhibiting asymmetric peaks like figure 6.9 are a clear signature of triexciton emission.

Despite these compelling observations we lacked two important pieces of information, which we present in this appendix. First, it is important to know whether the blinking of the triexciton happens simultaneous to band-edge (i.e. single exciton emission) blinking. In other words are the blinking of the triexciton and band-edge emission correlated? The second question addresses the matter of whether triexciton emission really comprises the majority of the signal that we detect in blinking traces like the one shown in figure 5.8.

The experiments presented in this appendix all use a Hanbury-Brown and Twiss (HBT) setup as described in chapter 6 with one arm (channel 1) having a band-pass filter tuned to select the triexciton and the other with a long pass filter tuned to transmit only band-edge emission (channel 0). The same sample was used as in chapters 5 and 6 (Q-Dot Corporation, 655nm emission) and the excitation source was the 414nm pulsed laser diode from Picoquant (PDL800 driver, LDH400 laser head).

A2.2 Verification of Hanbury-Brown and Twiss Setup by Imaging

We first present evidence that both detectors were aligned to the same nanocrystal in the single photon cross-correlation measurements that we performed in this thesis. This is demonstrated by comparing two images of the same sample of nanocrystals, with one image obtained using one detector and the other image collected using the other detector.

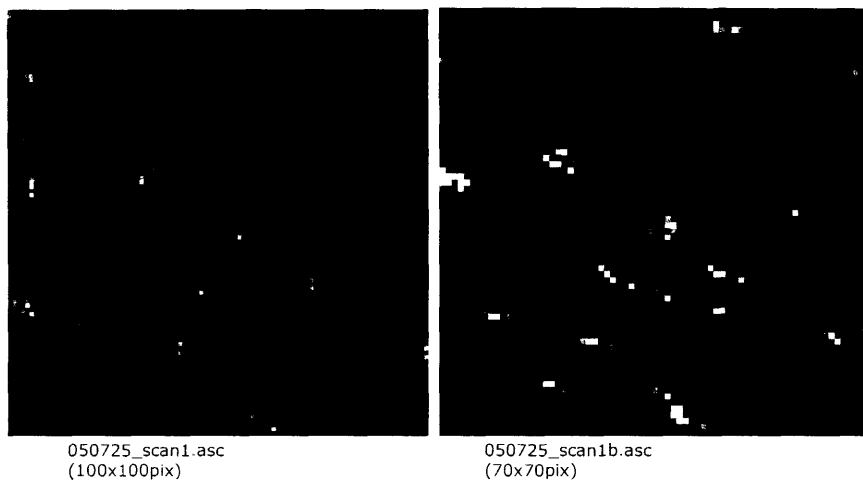


Figure A2.1: Image scans done using each of the APDs in their optimized positions. The similar positions of single nanocrystal locations indicates that the signal observed on each APD originates from the same location in the sample.

With this evidence we were confident that focusing the confocal microscope onto a particular single nanocrystal would direct its (and only its own) emission to each APD.

In figure A2.2 we show a confocal scanned image of single nanocrystals. The nanocrystal that is investigated in all of the subsequent experiments is circled.



Figure A2.2: Image scan used for subsequent data collection. The nanocrystal interrogated is indicated in the circle

A2.3 Verification of triexciton in single nanocrystal emission

The first experiment we present is a repeat of the single photon cross-correlation measurements done at the end of chapter 6, showing that triexciton emission is indeed observed in the emission of this single nanocrystal. Using appropriately selected band pass and long pass filters on either arm of the HBT setup we obtain an asymmetric center peak. This is a tell tale sign of ordered emission of single photons after excitation by a single laser pulse. Based on the spectral position of the filters used and the order of the photon detection we can confidently conclude that the coincidence counts that contribute to the asymmetric center peak always include the detection in channel 1 of a photon emitted from the triexciton state, i.e. a triexciton photon from the single nanocrystal. Note that the asymmetry of these peaks is reversed from the data presented in chapter 6 because we swapped which channels were used for triexciton and band-edge emission.

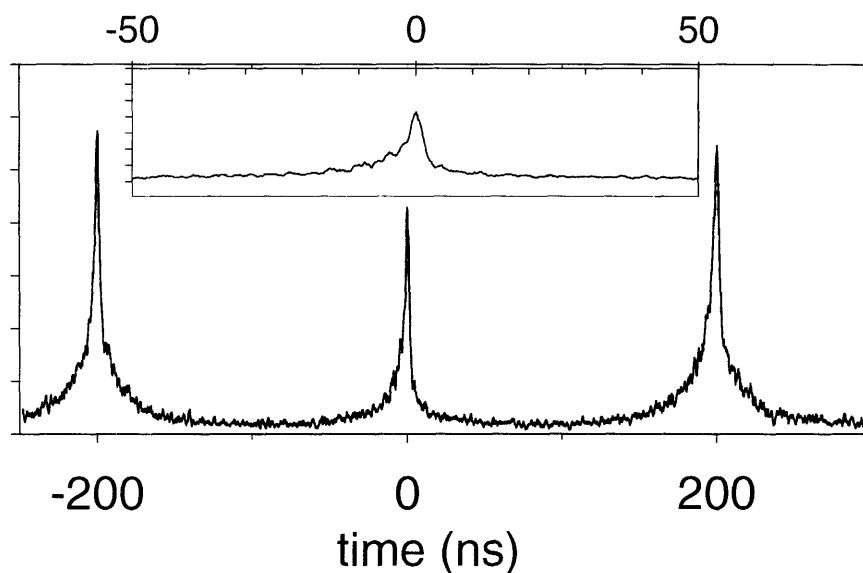


Figure A2.3: Single photon correlation plot – a histogram of coincidence counts collected by APDs in the HBT detection geometry. One arm of the setup (channel 0) had a long pass filter that passed photons with wavelength $>630\text{nm}$ whereas the other arm of the setup (channel 1) had a narrow bandpass filter that allowed only photons with wavelength between 606nm and 615nm to pass. For the sample under investigation this band pass overlaps with triexciton emission.

A2.4 Triexciton blinking of is correlated to band-edge emission blinking

At the same time that the single-photon cross-correlation measurement was performed (figure A2.3), the signal intensity on channel 0 (band-edge) and channel 1 (triexciton) were simultaneously recorded with 25ms time intervals. The results are shown in the following three figures.

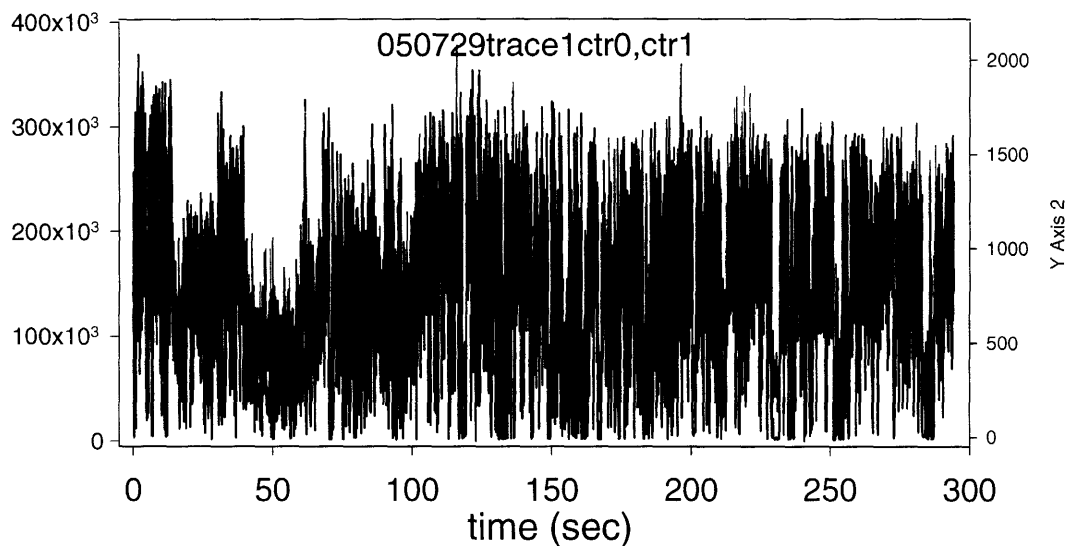


Figure A2.4a Simultaneously recorded blinking of the band edge (black) and the triexciton (green) channels. These data were taken during the recording of the correlation data in figure 3.

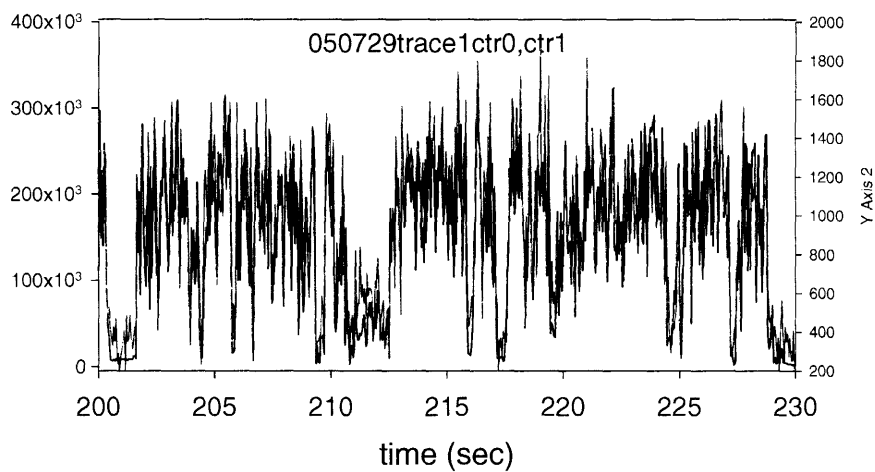


Figure A2.4b Zoom in of figure A2.4a. On this timescale the correlation of triexciton (green) and band edge (black) fluorescence is very clear – both signals blink on and off at the same time.

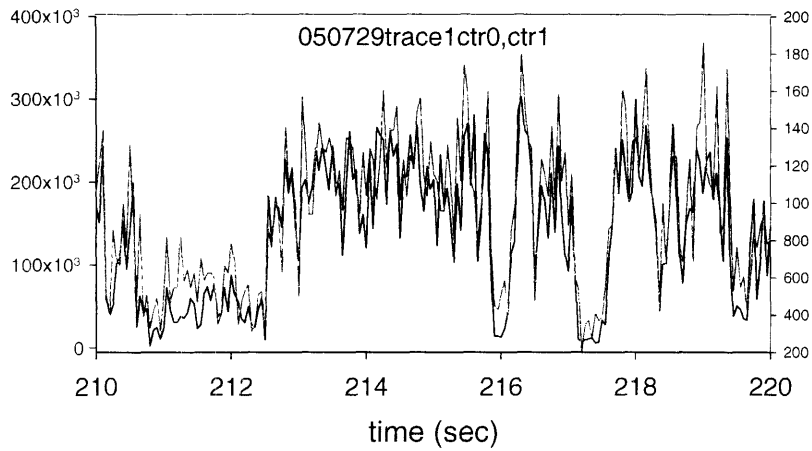


Figure A2.4c Zoom in of figure A2.4b.

From the foregoing three figures it is clear that the intensity trajectories of channel 0 and channel 1 are highly correlated, implying that the triexciton and band-edge blinking are correlated. To express the correlation in a different way, the intensity of the triexciton for each time interval was plotted against the intensity of the band-edge for each corresponding time interval. In other words an ordered pair (band-edge intensity, triexciton intensity) was plotted with a data point for every single time interval in the intensity trajectories. This is plotted in figure A2.4d

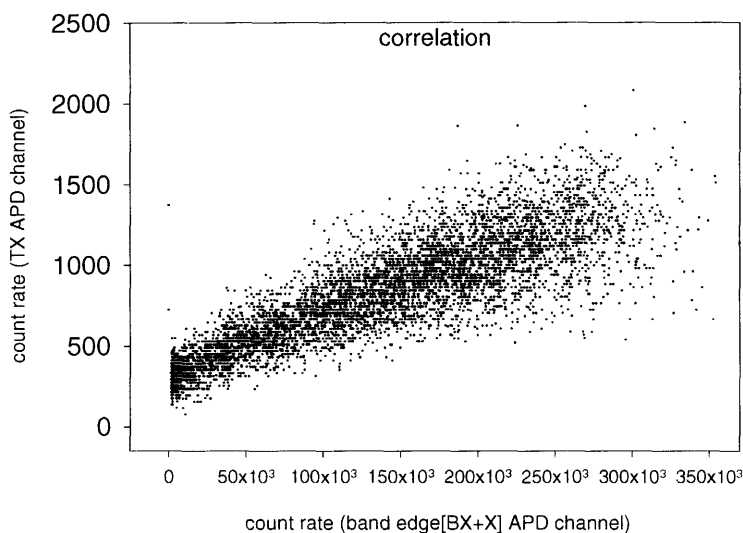


Figure A2.4d. Correlation of the intensity of each data point in the blinking trace of the band edge channel versus the triexciton channel. Each point on this scatter plot is an ordered pair: (channel 0 at time t , channel 1 at time t).

The extremely strong correlation of channel 0 and channel 1 is a highly intriguing result because it suggests that the same mechanism that turns a nanocrystal off and on can also drive the intermittency of the triexciton emission. However, it also calls into question whether channel 1 is really generated exclusively by triexciton emission – it is possible that this result is trivial and can be accounted for by leakage of band-edge emission into channel 1.

The asymmetric peak at zero τ in the single photon correlation (figure A2.3) established for certain that channel 1 has some amount of triexciton emission photons in it. If that were not the case then the center ($t=0$) peak could not be generated since there would be no coincidence events corresponding to a *single* excitation pulse (the peak at $\tau=0$ indicates detection of photon pairs emitted after a *single* excitation pulse). So the question is not *if* channel 1 contains triexciton emission, but rather *how much* of channel 1 is triexciton emission?

There are three ways to establish the relative contribution of triexciton emission to the signal in channel 1.

- a. Calculate the overlap integral of the triexciton emission with the bandpass filter used in channel 1. Compare this value to the corresponding value obtained using the band-edge emission spectrum.
- b. Calculate the expected count rate (e.g. on-time signal intensity) for channel 1 relative to channel 0, assuming that its signal is composed of only triexciton emission. Compare this expected ratio to the observed value.
- c. Measure the post-excitation lifetime of the signal on channel 1. If a significant component of band edge emission is present then the lifetime of the single exciton emission (which is much longer than multiexciton emission, $\sim 20\text{ns}$) should be present. If the lifetime is dominated by multiexciton emission, i.e. triexciton emission, then it should be effectively an instrument limited fast decay. (Our time-correlated single photon counting setup has an instrument response on the order of only $\sim 1\text{ns}$).
- d. Given the counting rates on channels 1 and 0 during the single photon correlation experiment, it should be possible to determine the rate of coincidence counts that contribute to the center peak, assuming a certain percentage of the channel 0 counts are from triexciton emission. Correspondingly, this “certain percentage” of the channel 0 emission that is from triexciton emission should be able to be backed out, given

the observed number of coincidence counts and the measured counting rates on channels 1 and 0.

In the following experiments we apply methods a, b and c to show that for most cases the majority of the signal detected by channel 1 from a single nanocrystal must originate from triexciton emission.

A2.5 Use of a band-pass filter on channel 1 should result in 80% of its signal being from triexciton

First we use the known emission spectrum of the triexciton and band edge (obtained by streak camera, see figure 4.1d) along with the transmission spectrum of the bandpass filter that was used to discriminate the light detected in channel 1 to calculate the expected contribution of the triexciton to channel 1.

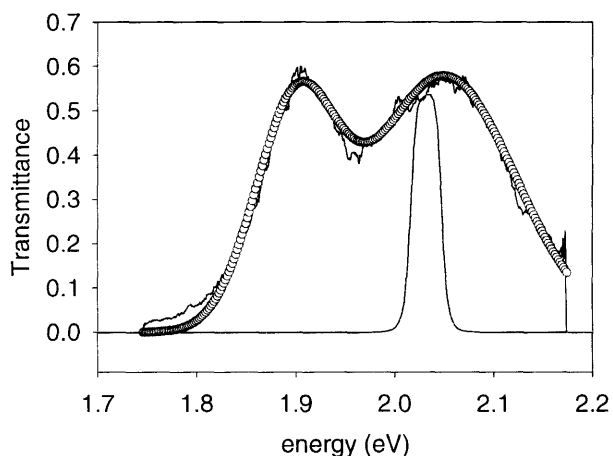


Figure A2.5: Transient spectrum of nanocrystal ensemble emission (showing triexciton and band-edge emission, black) along with a two-gaussian fit (red circles) of the spectral bands. Overlaid on the plot is the transmission of the bandpass filter (“L”) used in the experiment (blue).

The double gaussian fit to the triexciton and band-edge spectrum shown in figure A2.5

had the following parameters:

	x_0 (eV)	σ (eV)
band edge (biexciton + exciton)	1.899	0.04075
triexciton band	2.049	0.07295

The band pass filter used had the following parameters

	g_1 (eV)	g_2 (eV)
band pass filter	2.016	2.0462

To calculate the percent of triexciton (band-edge) signal transmitted through the bandpass filter, the following equations were used.

$$S_{totalband}(x_0, \sigma) = \int_{-x}^{x} \exp\left(-\frac{1}{2} \frac{(x-x_0)^2}{\sigma^2}\right) dx = \sigma \sqrt{2\pi} \quad (\text{A2.1})$$

$$S_{pass}(x_0, \sigma, g_1, g_2) = \int_{g_1}^{g_2} \exp\left(-\frac{1}{2} \frac{(x-x_0)^2}{\sigma^2}\right) dx = \sigma \sqrt{\frac{2}{\pi}} \left[\text{erf}\left(\frac{x_0 - g_1}{\sigma \sqrt{2}}\right) - \text{erf}\left(\frac{x_0 - g_2}{\sigma \sqrt{2}}\right) \right] \quad (\text{A2.2})$$

$$T[\%] = \frac{S_{pass}(x_0, \sigma, g_1, g_2)}{S_{totalband}(x_0, \sigma)} \times 100 \quad (\text{A2.3})$$

For the triexciton, T was calculated to be 10.1% and for band edge emission T was calculated to 0.12%. To get the actual relative contribution of triexciton emission, we also have to account for the number of triexciton photons in the signal incident on the filter. This is given by both the relative probability of generating triexcitons and the relative quantum yield. Since our experiments are at very high excitation flux, we assume that the probability of generating >3 excitons per laser pulse is about unity. From

previous work [Fisher et al] we know for this sample that the quantum yields of the exciton, biexciton and triexciton are approximately 70%, 7% and 3.5% respectively. This means that 4.3% ($=3.5/(70+7+3.5)$) of incident photons are triexciton, while the remaining 95.7 % are from the band edge. Combining this with T for the triexciton we obtain the following results:

$$\text{Channel 1 (triexciton contribution)} = 4.3\% \text{ incident} \times 10.1\% \text{ transmission} = 0.43473$$

$$\text{Channel 1 (band edge contribution)} = 95.7\% \text{ incident} \times 0.12\% \text{ transmission} = 0.11472$$

By this calculation about 4x as many triexciton photons as band edge photons, or 80% triexciton photons, are detected in channel 1.

A2.6 Expected relative count rates match observations for the two channels

We can also apply these results to justify the raw count rates observed on the two different channels. Whereas only 0.12% of the band edge spectrum is transmitted through to channel 1, a calculation using equations A2.1 – A2.3 for the long pass filter (1.984eV) indicates that about 96% of the band edge emission should pass to channel 0.

This results in:

$$\text{Channel 0 (band edge contribution)} = 95.7\% \text{ incident} \times 96.4\% \text{ transmission} = 92.255$$

$$\text{Ratio of Count rates on each channel} = \text{Channel 1 (TX + band edge)} / \text{Channel 0}$$

$$= (0.43473+0.11472) / 92.255$$

$$= 0.006$$

What is actually observed? As seen in figures A2.4- A2.4c channel 0 is generally between 200kcps and 300kcps, while channel 1 is generally around 1-3kcps. The ratio ranges from 0.003 to 0.15 but is usually around 0.005 – a very good match with the expected intensity based on the preceding arguments.

A2.7 Lifetime data for a single nanocrystal shows 50% of channel 1 is triexciton Emission

The next data that we present in support of the hypothesis that channel 0 is composed mostly of triexciton (or multiexciton) emission are lifetime measurements of the signal in channel 0 of the HBT setup. Figure A2.6 shows that, consistent with the triexciton hypothesis, the lifetime is composed mostly of a fast, instrument limited decay component. This experiment was performed at 1000nW, which is well into the multiexciton generation regime – the probability of generating greater than 3 excitons per excitation pulse asymptotically approaches unity at this power.

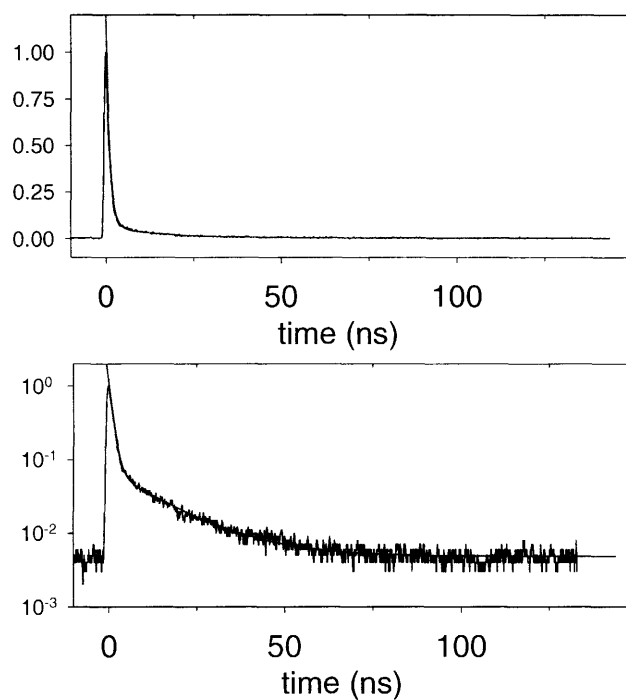
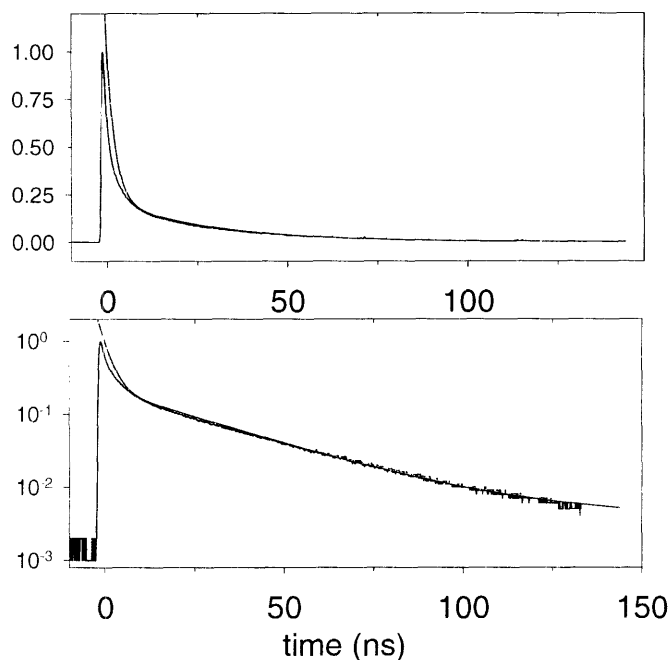


Figure A2.6: Lifetime of emission measured using time-correlated single photon counting of the TX channel for the same nanocrystal as data shown in figures 2 through 4d. Actual data is in black and results of a two-component exponential fit is shown in red. The weighting parameters of the components (normalized to unity) are: 0.9471784=fast; 0.058216=slow.

For contrast we performed the same lifetime measurement of a single nanocrystal under identical conditions using channel 0 which allows only band-edge emission. This is shown in figure A2.6b.



FigureA2.6b: Lifetime of emission measured using time-correlated single photon counting of the band-edge channel (biexciton plus single exciton) of a single nanocrystal. Actual data is in black and results of a two-component exponential fit is shown in red. The weighting parameters of the components (normalized to unity) are: 0.767101=fast; 0.232899=slow.

To derive a quantitative value for the percentage of signal that is attributable to triexciton emission we begin with the definitions of the signals that are measured. In channel 0 we expect zero contribution from the triexciton because the long pass filter cuts off the already weak (due to low quantum yield) emission of the triexciton. Therefore the lifetime will have the form,

$$y_0(t) = b_0 \cdot \exp(-t / \tau_2) + a_0 \cdot \exp(-t / \tau_1) \quad (\text{A2.4})$$

where b_0 and a_0 are weighting factors for the biexciton and exciton components respectively of the lifetime measured by channel 0. τ_1 and τ_2 are the exciton and biexciton lifetimes respectively. In channel 1 we have a narrow band pass filter that, in principle, transmits only photons whose wavelength coincides with the triexciton band. Because the quantum yield of the triexciton band is so very much smaller than that of the

band edge emission, however, we will consider the contribution of all three types of photons (triexciton, biexciton, and exciton) to the lifetime of this signal,

$$y_1(t) = c_1 \cdot \exp(-t / \tau_3) + b_1 \cdot \exp(-t / \tau_2) + a_1 \cdot \exp(-t / \tau_1) \quad (\text{A2.5})$$

Here c_1 , b_1 and a_1 are weighting factors for the triexciton, biexciton and exciton components respectively of the lifetime measured by channel 1. τ_3 is the lifetime of the triexciton. In these single nanocrystal time-correlated single photon counting experiments (TCSPC) and are not limited by instrument response, which is approximately 1ns. The lifetime of the single exciton is on the order of 20ns.

The results of the lifetime fits allow us to calculate relative signal strengths of the triexciton, biexciton and single exciton in either channel (i.e. relative number of photons of a given type collected in a given channel. The expressions for these are, for channel 0,

$$\begin{aligned} n_0(X) &= a_0 \cdot \tau_1 \\ n_0(BX) &= b_0 \cdot \tau_2 \end{aligned} \quad (\text{A2.6})$$

and for channel 1

$$\begin{aligned} n_1(X) &= a_1 \cdot \tau_1 \\ n_1(BX) &= b_1 \cdot \tau_2 \\ n_1(TX) &= c_1 \cdot \tau_3 \end{aligned} \quad (\text{A2.7})$$

The value we are interested in is the ratio between the number of photons detected in channel 1 that are from the triexciton band compared to the number that are from the band edge,

$$R_1(TX) \equiv \frac{n_1(TX)}{n_1(X) + n_1(BX)} \quad (\text{A2.8})$$

Unfortunately, since our instrument response time is not sufficient to resolve the biexciton and triexciton components we cannot directly obtain b_1 and c_1 from our fits

and simply calculate this value. Instead, our fits give us access to different but related values. In channel 0, by assumption only exciton or biexciton photons are detected and therefore the fast and slow components can be completely attributed to one or the other type of emission:

$$\begin{aligned} n_0(X) &= a_{slow,0} \cdot \tau_1 \\ n_0(BX) &= a_{fast,0} \cdot \tau_{IRF} \end{aligned} \quad (A2.9)$$

In channel 1 the fast component is assumed to be composed of both triexciton and biexciton photons, while the slow component is only exciton photons. This gives us the values:

$$\begin{aligned} n_1(X) &= a_{slow,1} \cdot \tau_1 \\ n_1(BX + TX) &= a_{fast,1} \cdot \tau_{IRF} \end{aligned} \quad (A2.10)$$

Note that in both equations we use the time constant of the instrument response, not the actual lifetime of the triexciton and biexciton to calculate the number of photons associated with these emission types. Using the results of the lifetime measurements on channels 0 and 1 (figures 5 and 5b) we can obtain measured values for the quantities in equations 6 and 7. To get to the desired quantity of equation 5 we define auxiliary quantities, the ratio of fast component photons to slow component photons in channel 1:

$$R_1(fast) \equiv \frac{a_{fast,1} \cdot \tau_{IRF}}{a_{slow,1} \cdot \tau_{slow}} = \frac{n_1(TX + BX)}{n_1(X)} = \frac{n_1(TX) + n_1(BX)}{n_1(X)} \quad (A2.11)$$

and the ratio of fast component photons to slow component photons in channel 0:

$$R_0(fast) \equiv \frac{a_{fast,0} \cdot \tau_{IRF}}{a_{slow,0} \cdot \tau_{slow}} = \frac{n_0(BX)}{n_0(X)} \quad (A2.12)$$

Because the spectra of the biexciton and exciton emission are identical at room temperature the ratio of the number of biexciton to exciton photons collected should be the same for either channel, that is,

$$\frac{n_1(BX)}{n_1(X)} = \frac{n_0(BX)}{n_0(X)} \equiv R_0(fast) \quad (A2.13)$$

This equality, along with some algebraic manipulation yields the desired result,

$$R_1(TX) = (R_1(fast) - R_0(fast)) \times \frac{1}{(1 + R_0(fast))} \quad (A2.14)$$

From our data and fitting we have the following results:

	$a_{fast} \times \tau_{IRF}$	$a_{slow} \times \tau_{slow}$	$R(fast)$	$R(TX)$	TX [%]
channel 0	0.798	6.567	0.12	0	0
channel 1	1.005	0.869	1.16	0.924	48%

We find that about half of the photons (48%) detected by channel 1 are from triexciton emission; there are 92 triexciton photons detected for every 100 band-edge photons detected.

Although this is lower than ideal, these results apply to only this particular single nanocrystal, which could be on the blue end of the size distribution meaning that the spectral filter used would not as effectively have blocked band edge from channel 1. Spectral analysis of the ensemble transient spectrum including previously measured quantum yields and lifetimes (performed in the next section) indicates that 80% of photons detected by channel 1 should originate from triexciton emission. A value of 80% is larger than the 48% given by the lifetime analysis and represents the average that

would be obtained if this single nanocrystal lifetime analysis were performed on a large number of single nanocrystals.

For the purpose of arguing that fluorescence intermittency is present in the triexciton exciton emission of a single nanocrystal it would be ideal that 100% of the emission observed in channel 1 be from the triexciton. Even though measurements on this particular nanocrystal resulted in half of the channel 1 signal coming from band edge emission, case for triexciton blinking is still very, very strong. If one were to cut the signal on channel 1 in half the signal would still be very clear and it would still very clearly follow the signal of channel 1.

Lastly, it is worth noting that about 10% of the band edge signal is from biexciton emission in this experiment. This means would result in a breakdown of the channel 1 signal in the following way: 48% = triexciton; 5.2% = biexciton; 46.8% = exciton – 53% of the signal is from multiexciton emission of some sort.

With two pieces of strong evidence that at least half and possibly up to 80% of the channel 1 emission originates from triexciton emission of a single nanocrystal we present more intensity trajectory data below. Using different time ranges, the signal intensity traces of both channel 0 and channel 1 are shown in figure A2.7. These were collected during the lifetime runs presented above. It is clear that the correlation of the two channels is strong, just as seen in the previous experiment.

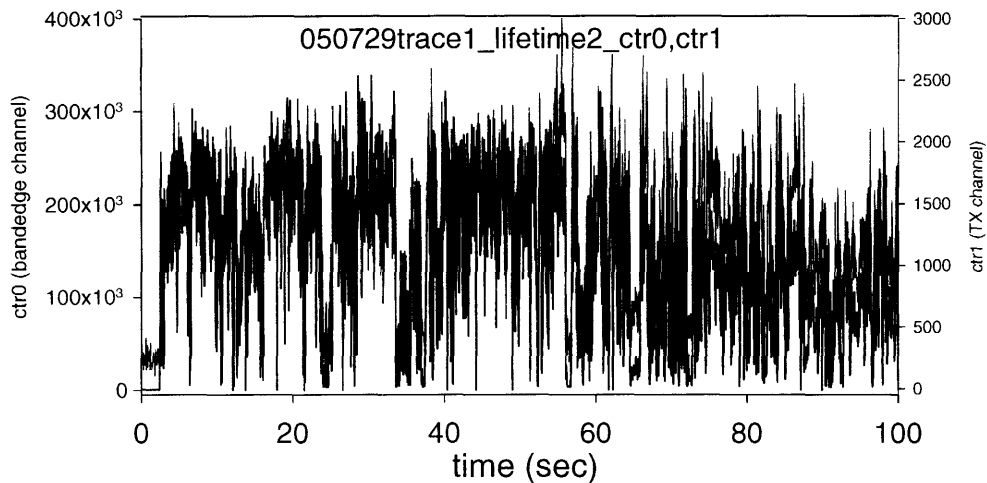


Figure A2.7 Simultaneously recorded blinking traces of the triexciton and band-edge channels collected during the lifetime measurements of figure A2.6.

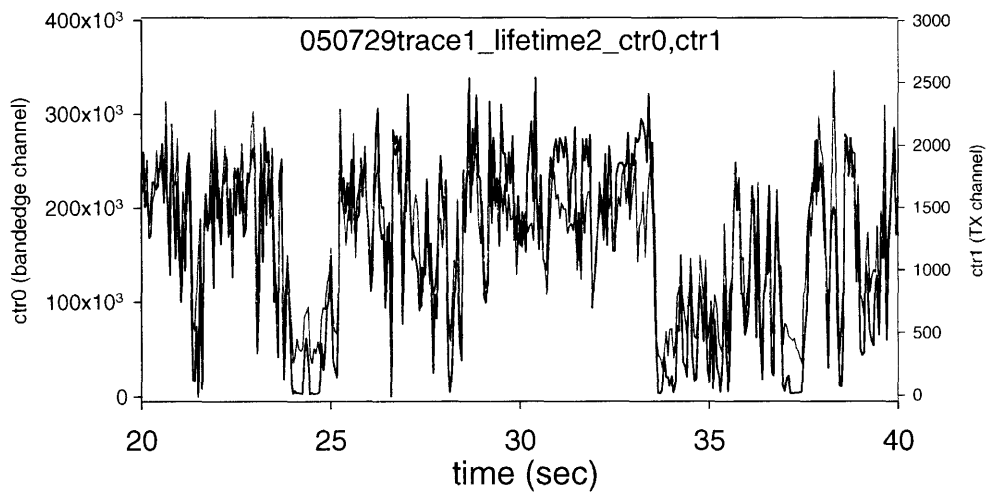


Figure A2.7b Zoom in of figure A2.7.

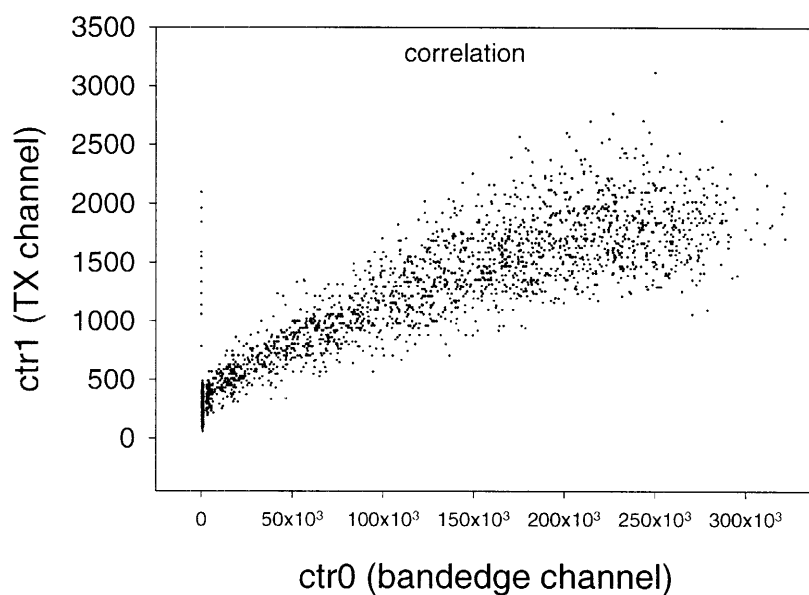


Figure A2.7c. Correlation of the intensity of each data point in the blinking trace of the band-edge channel versus the triexciton channel.

A2.8 Power dependence of triexciton and biexciton emission from a single nanocrystal

The preceding arguments (sections A2.5-A2.7) convincingly show that the signal on channel 1 not only contains some triexciton emission, but is actually composed mostly of triexciton emission. We solidify this point and further explore the triexciton emission by investigating the excitation power dependence of this triexciton emission.

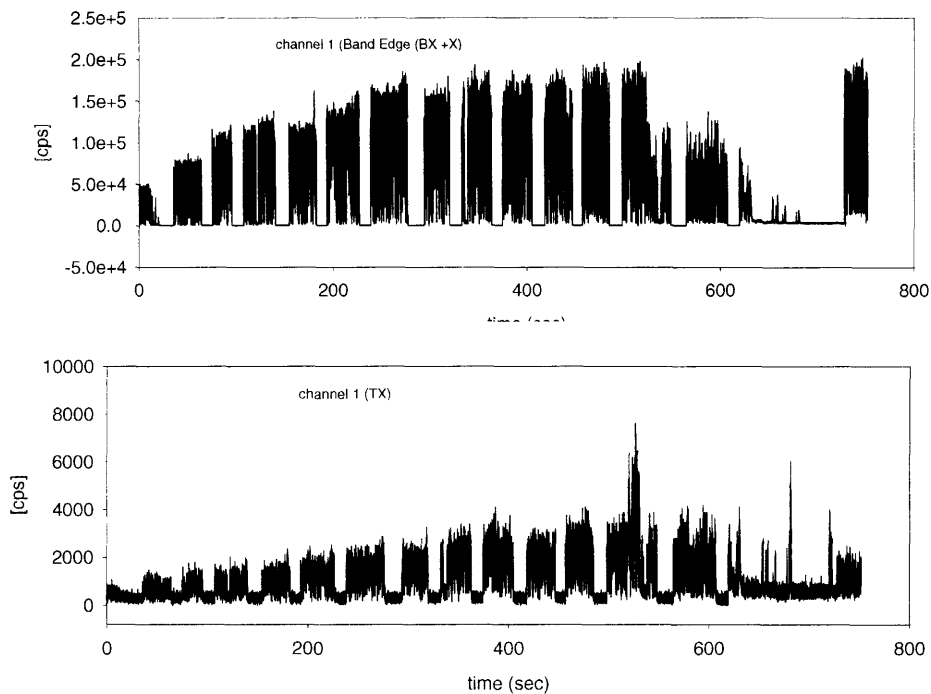


Figure A2.8 Intensity traces for channel 0 and channel 1 corresponding to the band edge emission and triexciton emission of a single nanocrystal respectively. In these plots, the power is increased in intervals as the time progresses. The beam is blocked while the power is changed which accounts for the gaps in the data.

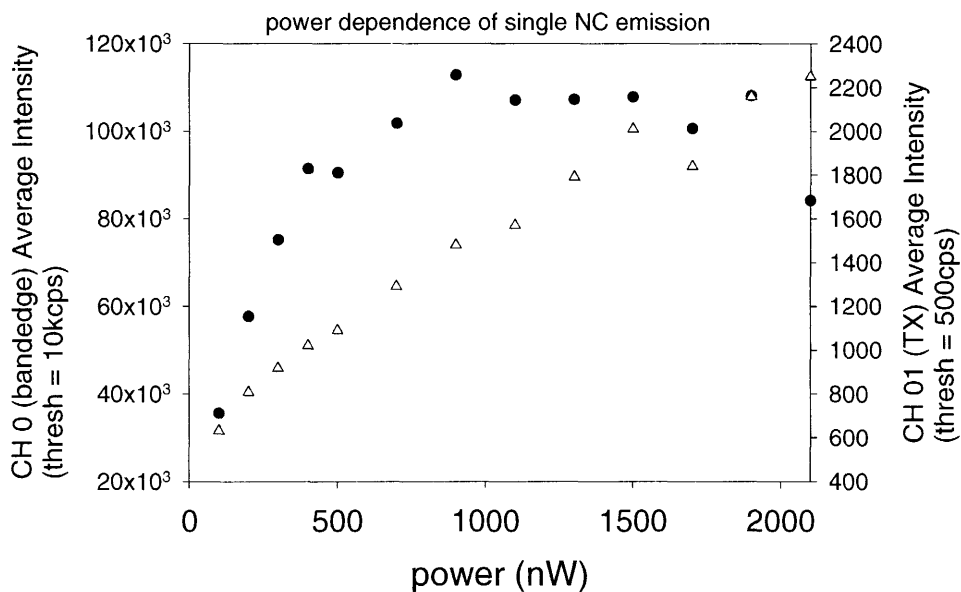


Figure A2.9 Power dependence of average intensity of channel 0 (circles) and channel 1 (triangles) where the average intensity is obtained by averaging over blinking the intensity of each data point in an intensity trace that corresponds to a particular excitation power.

The next two plots show every single data point intensity explicitly as a function of power. The first plot corresponds to data from channel 0 (band-edge) and the second for data corresponding to channel 1 (triexciton).

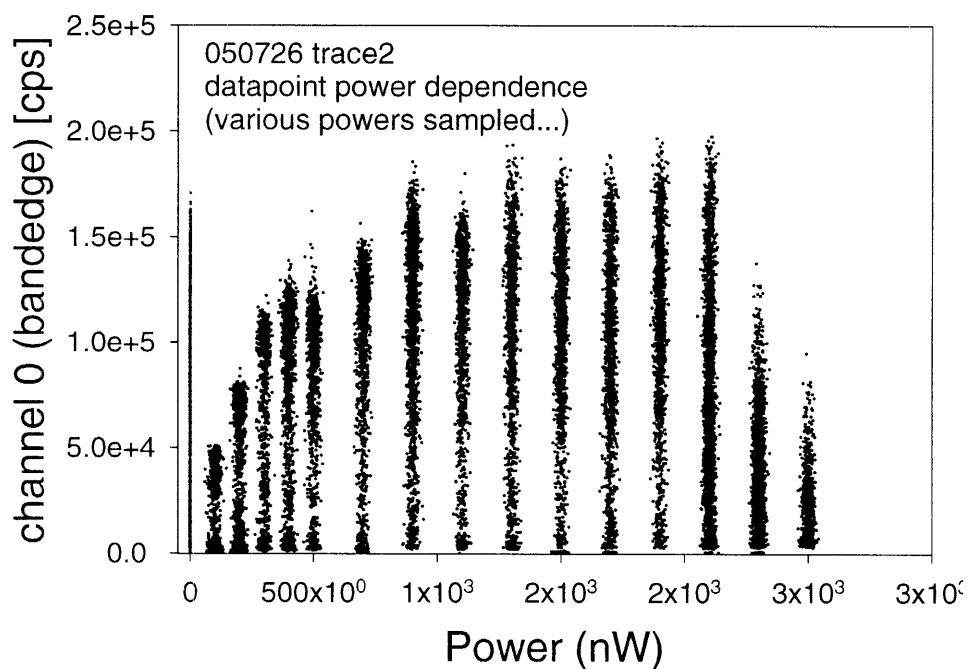


Figure A2.10a Power dependence of intensity of channel 0. In this plot every single data point of the intensity trajectory is plotted against the excitation power used. The density of data points at a given power indicate how much time the signal was at that intensity for that excitation power. Digital blinking of the emission is evident in the higher density of data points at the bottom and at the top of the columns of data points for each power.

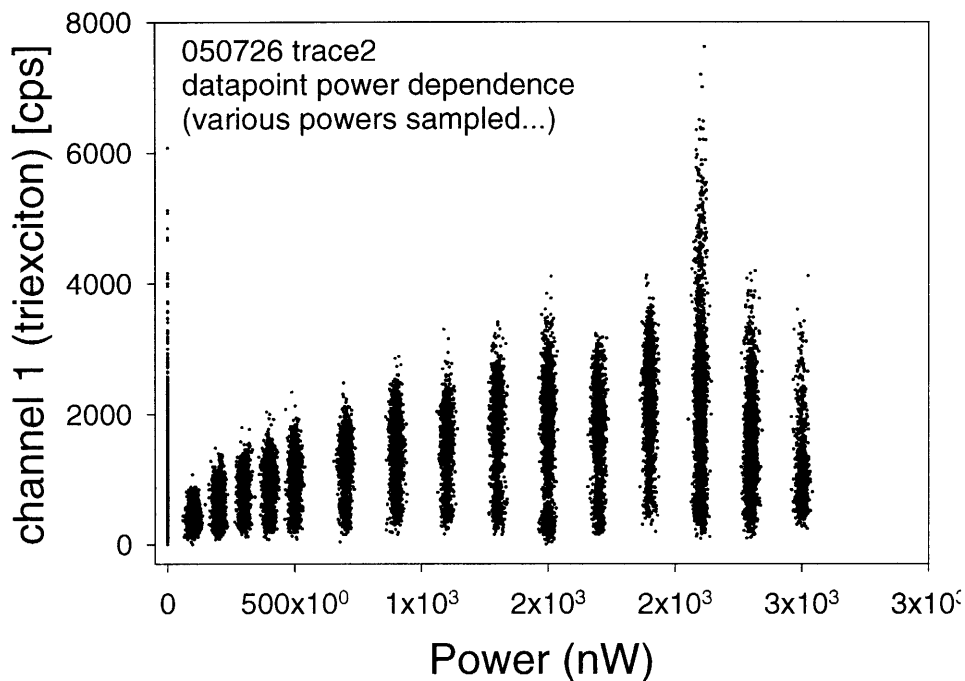


Figure A2.10b Same as A2.10a, but for the intensity of channel 1 (triexciton).

A2.9 Emission intensity of single nanocrystals in the “off” state

Our keen interest in the blinking of triexciton emission hinges on the following paradox. Off states in the currently accepted mechanism for blinking are supposed to be caused by highly efficient non-radiative Auger decay that occurs when the nanocrystal is singly charged. The very same non-radiative Auger decay mechanism is also supposed to be responsible for the low quantum yield of multiexciton states like the triexciton. Our previous work and this work showed that this Auger decay can be minimized enough to detect multiexciton emission by using very large nanocrystals. For instance, the fact that we can detect triexciton emission from single nanocrystals indicates that the multiexciton Auger decay rate is suppressed. If the current model of blinking is correct then the suppressed Auger decay rate should mean that “off” states of the nanocrystal should be “on.” Certainly it is surprising that the triexciton emission can blink “off” – why should

an additional carrier (charge) have a significant influence on the Auger rate when the triexciton already has 6 photoexcited carriers? We decided to investigate whether the “suppressed Auger” of this sample is evident in the “off-state emission” of the band-edge from the single nanocrystal (channel 0).

In the following we analyze the same data as the power dependence experiment (figure A2.8), but looked closely at the signal’s “off periods” during laser illumination and compared to the dark count baseline (no laser illumination). In figure A2.11 the non-illumination periods all correspond to about 500cps for the dark count rate. On the other hand, during illumination, the intensity when the dot is “off” is somewhat higher. However, it is hard to rule out the possibility of laser scatter contribution to this small intensity – especially given the power dependence of the observed “off intensity.” Yet, there were two independent bandpass filters in the beam path, which should have effectively blocked all of the scattered 414nm excitation light as was observed in chapter 5 (figure 5.3) where the setup was less rigorous about rejection of excitation scatter.

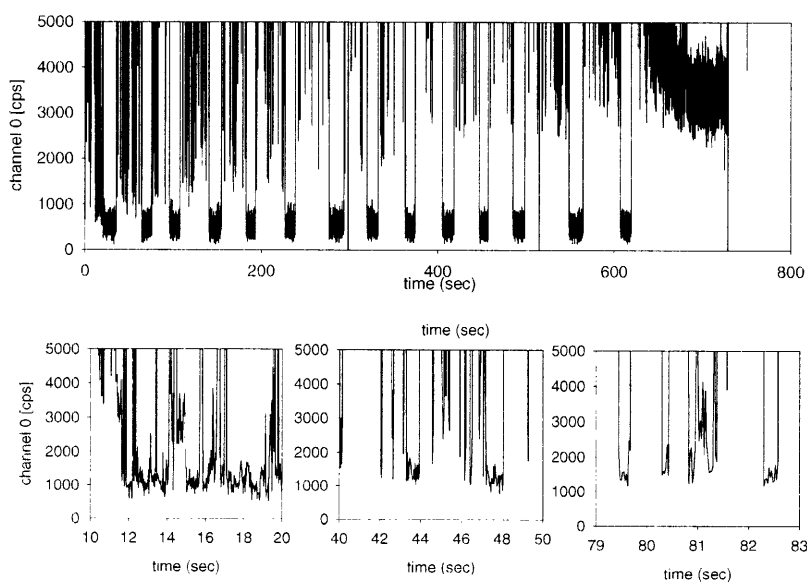


Figure A2.11 Blinking trace of single nanocrystal at various excitation powers. Note that between different powers, while not illuminated, the dark-count background signal is uniformly ~ 500 cps. In contrast, the intensity of the signal is higher while the dot is illuminated, but in the “off” state.

Based on these data (and assuming that the scattered excitation light is negligible) we conclude that the “off” intensity of the band-edge emission, even for relatively low powers is about 500cps ($500\text{cps} = 1000\text{cps observed} - 500\text{cps background}$). The “on” intensity during this period of illumination was about 50000cps. Hence the “off” state emission of the nanocrystal has a quantum yield of about 1% compared to that of the “on” state.

This is a surprising result because it implies that the Auger rate of a singly charged (i.e. one additional carrier) is significantly faster than the Auger rate of two- (biexciton) and four- additional carrier (triexciton) states. The quantum yields of the biexciton and triexciton relative to the single exciton are $\sim 10\%$ and $\sim 4\%$ for this sample (see chapters 4-6). Nevertheless, a hypothetically more efficient Auger decay for charged states compared to neutral states would be consistent with our observation of blinking by the triexciton emission.

The last piece of data that we present is the “off” state emission intensity as judged by eye at various excitation powers shown in figure A2.12. If the “off” state emission intensity actually is just the band-edge emission of a charged nanocrystal, then its power dependence ought to be approximately the same as for the “on” state – the “off” state quantum yield should be simply reduced by a factor of 100 as observed above. We can see that the power dependence depicted in A2.12 does indeed show some saturation, but the data is far from robust, and it is not clear that the ratio between “on” and “off” intensities remains the same at all powers. This implies the possibility that some of the

measured “off” state intensity, especially at higher powers, could be an artifact (perhaps laser scatter). More work is needed to truly understand the “off”-state intensity.

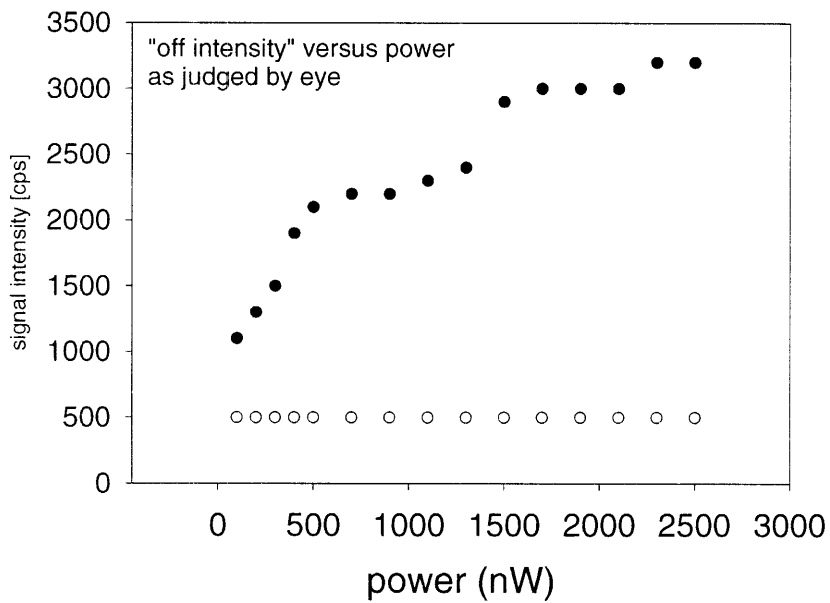


Figure A2.12 Power dependence of the “off intensity” as judged by eye as in the three small traces in figure A2.11.

Appendix 3: Effect of Fluorescence Intermittency (Blinking) on FCS Correlation Measurements

- A3.1 Introduction: FCS for fluctuations driven only by diffusion
- A3.2 Relate $G(t)$ to the autocorrelation of a solution containing a single molecule
- A3.3 Separate the contribution of blinking and diffusion
- A3.4 Re-assemble the pieces
- A3.5 References

A3.1 Introduction: FCS for fluctuations driven only by diffusion

The goal of this appendix is to show how blinking of individual nanocrystals can be incorporated into the formalism that has been developed to model the correlation functions measured in FCS experiments. Our reference point is the classic result that we referenced in chapter 9 for the autocorrelation of fluorescence intensity in an FCS measurement of a single component solution whose only dynamic fluctuation is driven by diffusion¹. In that work $G(t)$ is calculated beginning with the definition of the correlation function of the photon signal intensity ($n(t)$),

$$G(t) = \frac{\langle \delta n(0) \delta n(t) \rangle}{\langle n(0) \rangle \langle n(t) \rangle} \quad (\text{A3.1})$$

where the deviations of the signal from equilibrium, $\delta n(t)$, are defined as,

$$\delta n(t) = \Delta t \int d^3 \vec{r} I(\vec{r}) Q \delta C(\vec{r}, t) \quad (\text{A3.2})$$

or

$$n(t) = \Delta t \int d^3 \vec{r} I(\vec{r}) Q C(\vec{r}, t) \quad (\text{A3.3})$$

for a single component and are driven by a generalized diffusion equation,

$$\frac{\partial \delta C_j(r, t)}{\partial t} = D_j \nabla^2 \delta C_j(r, t) + \sum_{k=1}^m K_{jk} \delta C_k(r, t) \quad (\text{A3.4})$$

which simplifies to

$$\frac{\partial \delta C(r, t)}{\partial t} = D \nabla^2 \delta C(r, t) \quad (\text{A3.5})$$

for a single component.

If a gaussian point spread function (one radial gaussian and one longitudinal gaussian) is assumed for the excitation intensity function, $I(r)$, and diffusion (equation A3.5) is the only source of signal intensity fluctuation, then the autocorrelation of $n(t)$ is analytically derived to be¹,

$$G(t) = \frac{1}{N} \left(1 + \frac{t}{\tau}\right)^{-1} \left(1 + \frac{t}{\tau_z}\right)^{1/2} \quad (\text{A3.6})$$

A3.2 Relate $G(t)$ to the autocorrelation of a solution containing a single molecule

If blinking between the on and off states were governed by simple rate-constant kinetics then equation A3.4 would be sufficient to describe fluctuations of the signal intensity arising from switches between on and off states of individual nanocrystals. Unfortunately the probability distributions of on- and off- times of single nanocrystals are not given by simple exponentials. Instead, power laws govern these statistics, and we have to adopt a different approach to analytically include the effect of non-exponential blinking dynamics on $G(t)$ for FCS experiments.

Since blinking is a single nanocrystal (molecule) phenomenon, we can no longer use the bulk quantity of concentration to describe the system. Instead, we modify the definition of the signal intensity as an ensemble sum of the signal intensities of each individual molecule,

$$n(t) = \sum_i^{M_{tot}} n_i(t) \quad (\text{A3.7})$$

Writing the total signal intensity as the sum of many, independent single molecule signal intensities we can express the total correlation function in terms of the correlation function of individual nanocrystal signal intensities:

$$\begin{aligned}
G(t) &= \frac{\langle \delta n(0) \delta n(t) \rangle}{\langle n(0) \rangle \langle n(t) \rangle} = \frac{\langle n(0)n(t) \rangle}{\langle n(0) \rangle \langle n(t) \rangle} - 1 \\
&= \frac{\left\langle \sum_i^{M_{tot}} n_i(0) \sum_i^{M_{tot}} n_i(t) \right\rangle}{\left\langle \sum_i^{M_{tot}} n_i(0) \right\rangle \left\langle \sum_i^{M_{tot}} n_i(t) \right\rangle} - 1 \\
&= \frac{\sum_{i,j}^{M_{tot}} \langle n_i(0) n_j(t) \rangle}{\sum_i^{M_{tot}} \langle n_i(0) \rangle \sum_i^{M_{tot}} \langle n_i(t) \rangle} - 1 \\
&= \frac{\sum_{i,j}^{M_{tot}} \langle n_i(0) n_j(t) \rangle}{\sum_{i,j}^{M_{tot}} \langle n_i(0) \rangle \langle n_j(t) \rangle} - 1
\end{aligned} \tag{A3.8a-8d}$$

We assume that each molecule's signal is independent of one another, so that $\langle n_i(t) n_j(t') \rangle = \langle n_i(t) \rangle \langle n_j(t') \rangle$, which leads to:

$$\begin{aligned}
G(t) &= \frac{\sum_i^{M_{tot}} (\langle n_i(0) n_i(t) \rangle - \langle n_i(0) \rangle \langle n_i(t) \rangle)}{\sum_{i,j}^{M_{tot}} \langle n_i(0) \rangle \langle n_j(t) \rangle} \\
&= \frac{\sum_i^{M_{tot}} G_i(t) \langle n_i(0) \rangle \langle n_i(t) \rangle}{\sum_i^{M_{tot}} \langle n_i(0) \rangle \sum_i^{M_{tot}} \langle n_i(t) \rangle}
\end{aligned} \tag{A3.9a-9c}$$

where

$$G_i(t) = \frac{\langle n_i(0) n_i(t) \rangle - \langle n_i(0) \rangle \langle n_i(t) \rangle}{\langle n_i(0) \rangle \langle n_i(t) \rangle} \tag{A3.9d}$$

We make a further assumption that the statistics governing the dynamics are identical and that therefore their time averaged values are identical, $G_i(t) = G_1(t)$, $\langle n_i(t) \rangle = \langle n_1(t) \rangle$ for all i and all t . Therefore the sums become simple multiples of the total number of molecules in the entire solution (i.e. in the vial), M_{tot} ,

$$\begin{aligned}
G(t) &= \frac{M_{tot} G_1(t) \langle n_1(0) \rangle \langle n_1(t) \rangle}{(M_{tot} \langle n_1(0) \rangle) \times (M_{tot} \langle n_1(t) \rangle)} \\
&= \frac{1}{M_{tot}} G_1(t)
\end{aligned} \tag{A3.10a}$$

where

$$G_1(t) = \frac{\langle \delta n_1(0) \delta n_1(t) \rangle}{\langle n_1(0) \rangle \langle n_1(t) \rangle} \quad (\text{A3.10b})$$

Given the validity of our two assumptions (independent nanocrystal fluorescence dynamics and identical time averaged values for all molecules) we obtain the simple result that the autocorrelation of the total signal intensity (i.e. many molecules in the solution) should be the same as the autocorrelation of a single nanocrystal (i.e. a solution containing a *single* molecule only), but divided by the total number of molecules in the solution.

We note that this result is general: the autocorrelation of a quantity, A , that is itself defined as the sum of a series of independently varying quantities $a_i(t)$ is equal to the autocorrelation of one of the $a_i(t)$ divided by the number of $a_i(t)$ in the series.

A3.3 Separate the contributions of blinking and diffusion

At this point we can separately account for the contributions of diffusion and blinking to the dynamics of the fluorescence detected for a single nanocrystal in the solution. We define the signal intensity of each individual molecule as the product of a random variable $b_i(t)$ that varies continuously between 0 and 1 depending on the nanocrystal's blinking intensity, and another random variable $x_i(r,t)$ which varies continuously from 0 to x_{max} depending on the excitation intensity of the laser at its location in the solution. The variation of $x_i(r,t)$ accounts for diffusion. We have then,

$$n_i(t) = x_i(t)b_i(t) \quad (\text{A3.11})$$

and

$$n(t) = \sum_i^{M_{tot}} x_i(t)b_i(t) \quad (\text{A3.12})$$

Based on these, we also have the following:

Deviation of single nanocrystal fluorescence signal:

$$\delta n_1(t) = n_1(t) - \langle n_1 \rangle \equiv n_1(t) - \bar{n}_1 \quad (\text{A3.13a})$$

Fluctuations driven purely by diffusion:

$$\delta x(t) = x(t) - \langle x \rangle \equiv x(t) - \bar{x} \quad (\text{A3.13b})$$

Fluctuation driven purely by blinking:

$$\delta b(t) = b(t) - \langle b \rangle \equiv b(t) - \bar{b} \quad (\text{A3.13c})$$

Combining these equations we express the fluctuation of a single molecule's fluorescence in terms of its blinking and diffusion driven components,

$$\begin{aligned}
 \delta n_1(t) &= n_1(t) - \bar{n}_1 \\
 &= x(t)b(t) - \bar{x}\bar{b} \\
 &= (\bar{x} + \delta x(t))(\bar{b} + \delta b(t)) - \bar{x}\bar{b} \\
 &= \bar{x}\delta b(t) + \bar{b}\delta x(t) + \delta x(t)\delta b(t)
 \end{aligned} \tag{A3.14}$$

For notational convenience, we will define the following

$$\langle x(0) \rangle = \bar{x} \quad \delta b(0) = \delta b \quad \dots \quad etc.$$

To calculate the correlation function of the single molecule's fluorescence intensity, we substitute result of equation A3.14 into the equation A3.10b:

$$\begin{aligned}
 G_1(t) &= \frac{\langle \delta n_1(0) \delta n_1(t) \rangle}{\langle n_1(0) \rangle \langle n_1(t) \rangle} \\
 &= \frac{\langle (\bar{x}\delta b + \bar{b}\delta x + \delta x\delta b)(\bar{x}(t)\delta b(t) + \bar{b}(t)\delta x(t) + \delta x(t)\delta b(t)) \rangle}{(\bar{x} \cdot \bar{b}) \cdot (\bar{x}(t) \cdot \bar{b}(t))} \\
 &= \frac{\bar{x}\bar{x}(t)\langle \delta b\delta b(t) \rangle}{\bar{x} \cdot \bar{x}(t) \cdot \bar{b} \cdot \bar{b}(t)} + \frac{\bar{b}\bar{b}(t)\langle \delta x\delta x(t) \rangle}{\bar{x} \cdot \bar{x}(t) \cdot \bar{b} \cdot \bar{b}(t)} + \frac{\langle \delta x\delta x(t)\delta b\delta b(t) \rangle}{\bar{x} \cdot \bar{x}(t) \cdot \bar{b} \cdot \bar{b}(t)} \\
 &+ \frac{\bar{x}\bar{b}(t)\langle \delta b\delta x(t) \rangle}{\bar{x} \cdot \bar{x}(t) \cdot \bar{b} \cdot \bar{b}(t)} + \frac{\bar{b}\bar{x}(t)\langle \delta x\delta b(t) \rangle}{\bar{x} \cdot \bar{x}(t) \cdot \bar{b} \cdot \bar{b}(t)} + \frac{\langle \delta x\delta x(t)\delta b \rangle \bar{b}(t)}{\bar{x} \cdot \bar{x}(t) \cdot \bar{b} \cdot \bar{b}(t)} \\
 &+ \frac{\langle \delta x\delta b\delta b(t) \rangle \bar{x}(t)}{\bar{x} \cdot \bar{x}(t) \cdot \bar{b} \cdot \bar{b}(t)} + \frac{\langle \delta x(t)\delta b\delta b(t) \rangle \bar{x}}{\bar{x} \cdot \bar{x}(t) \cdot \bar{b} \cdot \bar{b}(t)} + \frac{\langle \delta x\delta x(t)\delta b(t) \rangle \bar{b}}{\bar{x} \cdot \bar{x}(t) \cdot \bar{b} \cdot \bar{b}(t)}
 \end{aligned} \tag{A3.15}$$

Time averages of products of uncorrelated variables can be separated into products of the time averages of the individual variables ($\langle \delta a \delta b \rangle = \langle \delta a \rangle \langle \delta b \rangle$). Since the time average of these deviations are zero, such terms are also zero. In our case, we assume that only like variables at different times are correlated (e.g. $\delta x(t')$ and $\delta x(t'+t)$). As a result, only the first three terms of the foregoing expression are non-zero. For instance, $\langle \delta x \delta b(t) \rangle = \langle \delta x \rangle \langle \delta b(t) \rangle = 0$ and $\langle \delta x \delta x(t) \delta b(t) \rangle = \langle \delta x \delta x(t) \rangle \langle \delta b(t) \rangle = 0$. We then have,

$$\begin{aligned}
 G_1(t) &= \frac{\langle \delta b\delta b(t) \rangle}{\bar{b} \cdot \bar{b}(t)} + \frac{\langle \delta x\delta x(t) \rangle}{\bar{x} \cdot \bar{x}(t)} + \frac{\langle \delta x\delta x(t) \rangle \langle \delta b\delta b(t) \rangle}{\bar{x} \cdot \bar{x}(t) \bar{b} \cdot \bar{b}(t)} \\
 &= G_{bb}(t) + G_{xx}(t) + G_{bb}(t)G_{xx}(t)
 \end{aligned} \tag{A3.16}$$

Combining this with our earlier result, we have an expression for the total correlation function, expressed in terms of the correlation functions of fluorescence dynamics of a single nanocrystal that driven by exclusively by either diffusion or blinking.

$$G(t) = \frac{G_{bb}(t) + G_{xx}(t) + G_{bb}(t)G_{xx}(t)}{M_{tot}} \quad (\text{A3.17})$$

A3.4 Re-assemble the pieces

We now need to know, what is $G_{xx}(t)$. Analogous to equation A3.3 above, we can define a quantity $X(t)$ which is proportional to the total fluorescence detected from a the focal volume of the FCS experiment, *independent* of blinking,

$$X(t) = \Delta t \int d^3\vec{r} I(\vec{r}) Q_{on} C(\vec{r}, t) \quad (\text{A3.18})$$

where Q_{on} is the product of the absorptive cross-section of the nanocrystals and their quantum yield for the on-state. By its definition, $X(t)$ can fluctuate on account of stochastic variations of concentration, *but it assumes no blinking*. Since it assumes no blinking it is formally equivalent to $n(t)$ as defined in equation A3.3 above and its autocorrelation is identical to that given in equation A3.6:

$$G_{xx}(t) = \frac{\langle \delta X(0) \delta X(t) \rangle}{\langle X(0) \rangle \langle X(t) \rangle} = \frac{1}{N} \left(1 + \frac{t}{\tau}\right)^{-1} \left(1 + \frac{t}{\tau_c}\right)^{1/2} \quad (\text{A3.19})$$

We re-iterate that this result assumes a 3D Gaussian focal volume for the excitation intensity profile ($I(r)$), and it does NOT include the phenomenon of blinking.

The question that remains is how equation A3.19 is related to the single molecule quantity, $G_{xx}(t)$. To derive this we consider the meaning of $C(r, t)$ at the microscopic level. $C(r, t)$ is not a continuous function, rather it is a field of delta functions corresponding to positions of individual molecules in solution.

$$C(r, t) = \sum_i^{M_{tot}} \delta(\vec{r} - \vec{r}_i(t)) \quad (\text{A3.20})$$

From this perspective, we see that the value $x_i(t)$, that is, the contribution of an individual molecule of the solution to the total fluorescence (based on whether it is in the focal region or not), can be written analogously to equation A3.18, with a delta function substituted for the bulk concentration,

$$x_i(t) = \Delta t \int d^3\vec{r} I(\vec{r}) Q_{on} \delta(\vec{r} - \vec{r}_i(t)) \quad (\text{A3.21})$$

Note that this definition has $x_i(t)$ behave exactly as we defined it to behave in section A3.2 – it varies continuously between 0 and $x_{max} = I_{max} * Q_{on}$. Comparing equations A3.18,

A3.20 and A3.21 it is simple to see that $X(t)$ is just the sum of all x_i , that is, over all molecules in the solution sample.

$$X(t) = \sum_i^{M_{tot}} x_i(t) \quad (\text{A3.22})$$

We assume that the values x_i are all independent of one another in time (a reasonable assumption) which allows us to conclude, analogous to equation A3.10, that,

$$G_{XX}(t) = \frac{1}{M_{tot}} G_{xx}(t) \quad (\text{A3.23})$$

When this result is plugged back into equation A3.17 we are left with,

$$\begin{aligned} G(t) &= G_{XX}(t) + G_{bb}(t)G_{xx}(t) + \frac{G_{bb}(t)}{M_{tot}} \\ &\approx G_{XX}(t) \times (1 + G_{bb}(t)) \end{aligned} \quad (\text{A3.24})$$

Equation A3.19 above gives the expression for the correlation function due to diffusion of the nanocrystals ($G_{XX}(t)$), and we can obtain the correlation function due to a single nanocrystal blinking ($G_{bb}(t)$) using the results of previous work².

$$\begin{aligned} G_{bb}(t) &\equiv \frac{\langle \delta b(0) \delta b(t) \rangle}{\langle b(0) \rangle \langle b(t) \rangle} = \frac{\langle b(0)b(t) \rangle}{\langle b(0) \rangle \langle b(t) \rangle} - 1 \\ &= (A(1 - Bt^{2-m})) - 1 \end{aligned} \quad (\text{A3.25})$$

where m is the power law constant ($m \sim 1.5$ for nanocrystals), and A and B are normalization constants based on the minimum and maximum on and off times (t_{min} , t_{max} , etc.)

The final result is simple. The correlation function of an FCS experiment on nanocrystals should be modified to account for blinking by multiplying the diffusion based correlation function with the correlation function of blinking by a single nanocrystal:

$$G(t) = \frac{1}{N} \left(1 + \frac{t}{\tau}\right)^{-1} \left(1 + \frac{t}{\tau_z}\right)^{-1/2} \times A(1 - Bt^{2-m}) \quad (\text{A3.26})$$

A3.5 References

- ¹ O. Krichevsky and G. Bonnet, *Reports on Progress in Physics* **65**, 251 (2002).
- ² R. Verberk, A. M. van Oijen, and M. Orrit, *Physical Review B* **66**, 233202 (2002).

Brent Fisher

77 Massachusetts Avenue
MIT Chemistry, 18-080
Cambridge, MA, 02139
617.252.1422(office) 617.253.8594(lab)

256 Brookline Street #2
Cambridge, MA 02139
617.909.9339
brentf@mit.edu

EDUCATION

Massachusetts Institute of Technology Cambridge, MA

Candidate for Ph.D in Physical Chemistry June 2005
"Single Molecule Spectroscopy of Semiconductor Nanocrystals and Devices" (tentative).
Thesis advisor: Prof. Mounji Bawendi.
GPA 4.4/5.0; *Publications:* 3 first-authored, 6 co-authored; NDSEG Fellow 2001 – 2005.

Northwestern University Evanston, IL

B.A. in Chemistry and B.A. in Integrated Science June 2000
GPA: 3.8/4.0, Cum Laude; *Publications:* 1 co-authored

EXPERIENCE

Massachusetts Institute of Technology Cambridge, MA

Research Assistant Dec. 2000 – Aug. 2005
Studied the optical and electronic properties of semiconductor nanocrystals. Developed and tested novel nanocrystal based semiconductor devices: photodetectors, LEDs and lasers. Fundamental spectroscopy discoveries include exciton lifetime fluctuations, multiexciton fluorescence, and non-classical light generation in *single* nanocrystals. Technical skills include optical spectroscopy and analysis of semiconductors; design of laser scanning confocal microscopes; ultrafast laser systems and optics; semiconductor device fabrication; scanning probe surface analysis techniques. Also developed novel quantum efficiency measurement techniques. Extensive computer programming and analysis skills include C, Matlab, and Labview and Visual Basic.

Credit Lyonnais Securities Asia (Hong Kong Office) Cambridge, MA

Research Assistant for Michael Rogol on "SunScreen" survey of Solar Industry May-July 2005

Patent Litigation Consultant Cambridge, MA

Collected and analyzed technical data for expert witness in pharmaceutical lawsuit Oct. 2003 – Jan. 2004

Massachusetts Institute of Technology Cambridge, MA

Teaching Assistant for Intro. Quantum Mechanics and Thermodynamics Fall 2000, Spring 2001

Technical University Munich Munich, Germany

Research Assistant in Theoretical Chemistry under Prof. Notker Rosch. Oct.1998 – Aug.1999
Used relativistic density functional theory to study the bonding of alkanethiol self-assembled monolayers on gold.

Northwestern University Evanston, IL

Theoretical and computational chemistry research under Prof. George Schatz Academic Year 1998
Adapted software for computation of gas-phase reaction dynamics relevant to combustion.

University of Minnesota Minneapolis, MN

Research Assistant in Computational Chemistry under Prof. Donald Truhlar Summer 1998
Developed and used semi-empirical theoretical chemistry model for the study of ground soil solvation properties.

Mayo Clinic Rochester, MN

Research Assistant in Cardiac Anesthesiology and Hematology Summer 1996, Summer 1997
Enrolled patients, collected blood samples and studied platelet function of patients undergoing cardiac surgery.

HONORS, AWARDS

National Defense Science and Engineering Graduate Fellowship (NDSEG) 2001 – 2004
Phi Beta Kappa; Northwestern University Chemistry Department Hypercube Award
Northwestern University Freshman Writing Award

SKILLS: Matlab, LabView, C, C++, Perl, Microsoft Office, Visual Basic. Design and Testing of Semiconductor Solid State Devices

LANGUAGES: Fluent in spoken and written German (ZDaF, 1999)

LEADERSHIP, ACTIVITIES: M.I.T. Energy Club; M.I.T. Varsity Men's Ice Hockey 2001 – 2004

REFERENCES

Moungi Bawendi
77 Massachusetts Ave, 6-221
Cambridge, MA 02139
(617) 253 9796
mgb@mit.edu

Hedi Mattoussi
4555 Overlook Ave., Code 5611
Washington, DC 20375
(202) 767 9473
hedimat@ccs.nrl.navy.mil

Andrei Tokmakoff
77 Massachusetts Ave, 6-225
Cambridge, MA, 02139
(617) 253 4503
tokmakof@mit.edu

List of Publications

1. Refereed Publications

Fisher BR, Caruge JM, Chan YT, Bawendi MG, "Multiexciton fluorescence from semiconductor nanocrystals." *Chemical Physics*, *Accepted and In Press*, June 2005.

Fisher BR, Caruge JM, Zehnder D, Bawendi MG, "Room temperature ordered photon emission from multiexciton states in single CdSe/ZnS nanocrystals," *Physical Review Letters*, 94(8): 087403, 2005.

Fisher BR, Eisler HJ, Stott NE, Bawendi MG, "Emission intensity dependence and single-exponential behavior in single colloidal quantum dot fluorescence lifetimes," *Journal of Physical Chemistry B*, 108 (1): 143-148, 2004

Jarosz MV, Porter VJ, **Fisher BR**, Kastner MA, Bawendi MG, "Photoconductivity studies of treated CdSe quantum dot films exhibiting increased exciton ionization efficiency," *Physical Review B*, 70 195327 2004

Clapp AR, Medintz IL, **Fisher BR**, Anderson GP, Mattoussi H, "Can luminescent quantum dots function as efficient energy acceptors with organic dye donors?" *Journal of the American Chemical Society*, 127(4), 1242-1250, 2005.

Clapp AR, Medintz IL, Mauro JM, **Fisher BR**, Bawendi MG, Mattoussi H, "Fluorescence resonance energy transfer between quantum dot donors and dye-labeled protein acceptors," *Journal of the American Chemical Society*, 126 (1): 301-310, 2004,

Medintz IL, Clapp AR, Mattoussi H, Goldman ER, **Fisher B**, Mauro JM, "Self-assembled nanoscale biosensors based on quantum dot FRET donors." *Nature Materials*, 2 (9): 630-638, 2003

Kim S, **Fisher B**, Eisler HJ, Bawendi M, "Type-II quantum dots: CdTe/CdSe(core/shell) and CdSe/ZnTe(core/shell) heterostructures," *Journal of the American Chemical Society* 125 (38): 11466-11467, 2003

Shimizu KT, Woo WK, **Fisher BR**, Eisler HJ, Bawendi MG, "Surface-enhanced emission from single semiconductor nanocrystals," *Physical Review Letters*, 89 (11): Art. No. 117401, 2002

Schatz GC, **Fisher B**, Grande W, Kumayama K, Pederson LA, "Reactive and nonreactive quenching of OH(A (2)Sigma(+)) in collisions with H atoms," *Journal of Physical Chemistry A*, 105 (12): 2515-2521 2001

2. Conference Proceedings

Fisher BR, Eisler HJ, Caruge JM, Bawendi MG, "On-going Studies of Excited State Dynamics in Single Quantum Dots," *Materials Research Society Conference*, Fall 2002.

Fisher BR, Eisler HJ, Caruge JM, Bawendi MG, "A study of the Emission Intensity Dependence of Fluorescence Lifetime in Single CdSe Quantum Dots," *Gordon Research Conference*, July 2003.

Fisher BR, Caruge JM, Zehnder D, Bawendi MG, "Room temperature ordered photon emission from multiexciton states in single CdSe/ZnS nanocrystals," *Materials Research Society Conference*, Fall 2004.

Acknowledgements

Note to reader (1): Terse and pithy this is not. Get comfortable.
 Note to reader (2): Apologies for the shameless switching between third and second person in the writing... it is unavoidable ☺

A thesis takes a long time to write and there are many sticking points. Strangely I am finding this section among the most difficult to write. I just don't know where to begin. I am currently preparing to move away from MIT and Cambridge, and this serves only to highlight even more vividly how much I have loved living in this city, going to this school and working in this lab – despite the many struggles and challenges that are a part of any thesis work. The people who have supported me in this endeavor are too many to list but I shall attempt to mention everyone that I can.

Of all the people who have been with me and supported me in my thesis the one who has a front row seat to it all and who is most deserving of thanks is my fiancée Rachel (soon to be wife in just 12 days!!). She has seen me at my best and at my worst as experiments have succeeded and failed, papers were accepted or rejected and most recently as I struggled through a challenging job search. The roller coaster I've put her on would have persuaded most anyone else to step off ASAP, but she has been the love and strength I've needed at every step. Any success I've had as a graduate student at MIT pale by comparison with the good fortune I've had to meet the lady of my life here in Boston and to have her stick with me continually, even when my promises to be out of lab by 8:00pm turn into 8:00am. Rachel, I'm so glad you took a chance on me at McCarthy's, and for you I am forever thankful.

The camaraderie and support of great friends and colleagues is a blessing that I have enjoyed since I first arrived at MIT. My class of P-Chem students especially Philip Sheehy, Craig Breen and Josh Vaughan made Bob Field's quantum homework even more exciting than it already was – lets do it in the library but you gotta be quiet! Only people like this could put together such a great set of parties [EPIDEMIC] to keep us sane all summer – thanks to all five of the party guys for that. Other members of my chemistry grad class that I must mention by name include Aaron Hoskins who has been a friend to me continually for all of the last five years. I also owe him thanks for introducing me to the fine dining options at the Whitehead Institute. My two roommates, Dave Krodell, a fellow NU alum, and Serhan Altunata, my 5.61 TA partner, helped make living in the cheapest rent-able building in Cambridge as fun as it could be. I'd also like to thank my teammates and coaches in the MIT men's varsity hockey program for giving me such an unexpected great opportunity for fun and competition outside of the lab. Coaches Mark, Jimmy and Froggy O'Meara taught me better than anyone how to communicate in Boston, and teammates like Etienne Parent, Martin Oiumet, and Nicolas Dulac taught me how to communicate in Montreal... Tabernac! All of these teammates – Johnny, Vokac, Lackner, Kyle, Studs, Coop, Smokey, Shabby, Richie, Glenn, T-Hop, VanHorn, Dagenais, Fahey, and everyone else helped give my life a dimension that kept me energized and positive while working on my thesis. Outside of MIT I have received constant support from innumerable other friends like old friends Aaron Johnson, Jeremy and Megan Fisher, and Will Grande, as well as new friends like Jyotsna and Gian Jagai,

Courtney and Brian Bassett, Sara Dinwoodie. I couldn't hope for more friendship and support...

.... And I haven't even begun to mention friends and colleagues in the Bawendi Lab. Ken Shimizu, Vikram Sundar and Wing Woo showed me all of the ropes and also where to eat Indian and Chinese – Punjabi Dhaba and Jumbo. Ken especially showed me everything I needed to detect single CdSe quantum dots by myself for the first time. I am also especially grateful to Hans Eisler for first introducing me to the Ti-Sapphire and OPO and providing sage-like guidance during my first two years. Hans' relentless attitude as well as his long rock-star hair inspired me to reach for great things. The same thanks goes for Jean-Michel Caruge, who showed me first how to set up a confocal microscope. Dr. Caruge has been a constant provider of thoughtful opinions and criticism of my research... and sometimes wonderfully heated arguments ☺ Jean-Michel has also endlessly lent his laptop to me and everyone else in the lab for group meeting – thank you for that! Each of my other laser lab comrades – Inhee, Mirna, Venda, Hao, Heather and Antoine – have contributed to my research and to sustaining a great work environment in those dark, dark rooms, and I'm grateful for their camaraderie as well... Many other Bawendi Lab members outside of the laser lab have been great colleagues to me at all times and made my experience memorable: Jonny Steckel for inspiring “innovation” and winning arm wrestling tournaments, “JZ” – John Zimmer for being my neighbor in the office as we endured the stupid telephone and door slamming that were immediately next to our desks; Yinthai Chan, for clearly distinguishing between different lab mates with the same name “jebus” as well as his relentlessly optimistic ☺ outlook that kept us all going strong; Brian Yen for his constant pursuit of emerging synergies to give our lab a competitive advantage in the emerging global scientific marketplace, “DCO” Dave Oertel for providing membership with the local 423 brothaahood – its been hahd doin all of thah reseaaachs and my knees ah killin me, but thanks fah all thah wicked good times brothah! we'll have a beah sometime...; Dr. Chicken (Preston Snee) for teaching me about the Nightrain and for his development of an entire language of new names for lab items that already have names (e.g. donkey dots); Big T – Joe Tracy for keeping the most extreme hours of anyone – no one ever had to feel like they were the only one in lab at 5 am; Dirk Weiss for being one of the most thoughtful and encouraging co-workers I've had; John Halpert for synthesizing rods *and* bringing some social events to the group like a few great golf outings and *finally* bringing me up to the roof deck; Xavier Brokmann for providing very thoughtful support of my research – even from France before joining our group; Numpon for the fabulous Thai treats; and finally to all the other members with whom I didn't always collaborate closely but made my experience great: Sungjee Kim, Sangwook Kim, Wenchao Sheng, Sonia Rao, Hideyuki Kamii, among others.... The newest additions to the laser lab with whom I've had the pleasure of working (and supposedly training) deserve special mention. August Dorn and Gautham Nair have been very fun to work with over the past year and have given me for the first time “collaborators” on my projects whereas previously I worked on most of my projects alone. Their contributions already and the ideas and experiments they are coming up with now make me feel like I'm leaving the party just as it is beginning. Lastly members of other groups at MIT who have helped me deserve a note of thanks – Justin Hodgkiss, Scott Miller (an old roommate as well!), Tom Liptay, Chris Fang-Chen, Joe Laporo and Eric Statz and Joe Gardecki, among others....I also wish to thank some of the many faculty members at MIT who have supported me including my thesis committee Silvia Ceyer and Andrei Tokmakoff, especially Andrei for being instrumental in my decision to

come to MIT, also Ramachandra Dasari, Bob Field, Keith Nelson, Vladimir Bulovic and Terry Orlando have all helped me at various steps of the way.

Of course the most important faculty member for me has been my advisor, Mounqi Bawendi. When I joined his group Mounqi warned me that I would have to take my own initiative to come and see him for support in my research, but that I should not be hesitant because he said that is the part of his job that he enjoys the most – interacting with and pushing forward the research of his students. I truly found this to be the case. In contrast to the stories of most grad students, I can't think of a single time that I felt overbearing pressure or micromanagement from Mounqi. Likewise I always felt that Mounqi's door was open for us grad students to visit and discuss our work, even if we weren't scheduled to be there. Indeed we all found that sometimes Mounqi's schedule (like our own) is more of a theoretical concept than an actual realization. In addition to the very constant support I have had from Mounqi in my research, I have also gained a great deal in being around him to see how he can evaluate problems in a very wide variety of research areas by honing in on the most important pieces of the a problem. This skill is perhaps one of the most important to begin learning as a doctoral student, and it is a privilege to be in a group with such diversity of science with an advisor which is so gifted at analyzing problems and teaching in disparate fields of research. Lastly, I have to thank Mounqi for being the kind of advisor that really lets us really take a hold of and guide our own research from beginning to end, including the complete writing of our own papers. It would appear that the only thing I haven't gained from Mounqi is his ability to say a lot in a small number of words – this acknowledgement section is getting pretty long... But it is worth re-iterating: I am very lucky and thankful to have known and had Mounqi as my advisor.

Last but not least I must thank my family – Mom, Dad, Brian and Brad – and again my lovely wife-to-be Rachel as well as her folks for all their emotional support. I love you all dearly. I'm not sure how they've been able to empathize with some of my complaints (“the time-correlated single photon counting instrument response sucks! It's way larger than the TTL jitter!!”) ... but they have, invariably. I feel like I've been blessed with the best family and best lady that anyone ever had, and I owe anything good that I've done to their support.

Thanks again everyone, I hope we will stay in touch.
I will miss you all... A lot.

8-23-2005



Room 14-0551
77 Massachusetts Avenue
Cambridge, MA 02139
Ph: 617.253.5668 Fax: 617.253.1690
Email: docs@mit.edu
<http://libraries.mit.edu/docs>

DISCLAIMER OF QUALITY

Due to the condition of the original material, there are unavoidable flaws in this reproduction. We have made every effort possible to provide you with the best copy available. If you are dissatisfied with this product and find it unusable, please contact Document Services as soon as possible.

Thank you.

Some pages in the original document contain color pictures or graphics that will not scan or reproduce well.